VNIVERSITAT DE VALÈNCIA

Departamento de Física Atómica, Molecular y Nuclear
Instituto de Física Corpuscular
Doctorado en Fisica

The Next Generation Nuclear Instruments: AGATA and NEDA, and Nuclear Structure Studies near N=Z line

TESIS DOCTORAL

Tayfun Hüyük

DIRIGIDA POR

Andrés Gadea

Mayo 2017

Declaration

Dr. Andrés Gadea, *Investigador cientìfico, CSIC*

CERTIFICA:

Que la presente memoria: "**The Next Generation Nuclear Instruments: AGATA and NEDA, and Nuclear Structure Studies near N=Z line**" ha sido realizada bajo mi dirección en el Instituto de Física Corpuscular (Centro-mixto del CSIC y de la Universidad de Valencia) por Don Tayfun Hüyük y constituye su tesis para optar al grado de Doctor en Física.

Y que así conste, firmo el presente Certificado.

Firmado:

Dr. Andrés Gadea

Declaration of Authorship

I, Tayfun Hüyük, declare that this thesis titled, 'The Next Generation Nuclear Instruments: AGATA and NEDA, and Nuclear Structure Studies near N=Z line' and the work presented in it are my own. I confirm that:

- This work was done wholly or mainly while in candidature for a research degree at this University.
- Where any part of this thesis has previously been submitted for a degree or any other qualification at this University or any other institution, this has been clearly stated.
- Where I have consulted the published work of others, this is always clearly attributed.
- Where I have quoted from the work of others, the source is always given. With the exception of such quotations, this thesis is entirely my own work.
- I have acknowledged all main sources of help.
- Where the thesis is based on work done by myself jointly with others, I have made clear exactly what was done by others and what I have contributed myself.

Signed: _____

Date: _____

*"Hayatta en hakiki mürşit **ilimdir, fendir**."*

*(The truest mentor in life is **science**.)*

Mustafa Kemal Atatürk

UNIVERSIDAD DE VALENCIA

Abstract

Departamento de Física Atómica, Molecular y Nuclear
Instituto de Física Corpuscular

Doctor of Philosophy

by Tayfun Hüyük

The first part of this thesis is devoted to the development of a large array of neutron detectors NEDA and their conceptual design using Monte-Carlo simulations. NEDA (NEutron Detector Array) aims to build a neutron detector array with high efficiency based on liquid scintillators. NEDA will be coupled to the high-purity γ-ray detector arrays, like AGATA, EXOGAM, to be used as a trigger or complementary detector in the contemporary nuclear physics experiments which aim to investigate the structure of the exotic nuclei. The importance of NEDA is related to its capability to filter the reaction channels including multiple neutron evaporation with high efficiency. The simulations of the conceptual design of NEDA for the near-future campaign at GANIL is presented. The NEDA detectors together with the Neutron Wall promise up to 7.62(11)% and 1.89(11)% efficiencies for two- and three-neutron detection comparing to the Neutron Wall standalone 3.93(10)% and 0.55(14)%, respectively. The results of this study has been published in The European Physical Journal - Section: A (2016) **52**: 55 and our study has been selected for the cover of the March 2016 issue. In the framework of NEDA, besides the simulations, I have been actively participating to the tests which aimed to characterize the prototypes and their functionality with digital sampling electronics. The preparation and the outcomes of these tests are also discussed.

The second part is devoted to the analysis of two experiments. The first experiment has been done at GANIL with EXOGAM - Neutron Wall - DIAMANT setup using fusion-evaporation reaction ^{32}S + ^{28}Si. The analysis of this experiment provided experience on the Neutron Wall, which the NEDA detectors will replace. The preparation, analysis and the results of this experiment are discussed. The second experimental activity has been done at GSI - Fragment Separator Facility (FRS) using the AGATA - PreSPEC setup to investigate the collectivity in ^{52}Fe above the isomeric state 12^+. The unstable ^{52}Fe beam at relativistic energies with an isomeric ratio of 16(2)% underwent Coulomb excitation by heavy ^{197}Au target. The reduced matrix element of the candidate for the $12^+ \rightarrow 14^+$ has been measured experimentally and compared with the LSSM calculations, suggesting a larger degree of collectivity in the involved states.

Acknowledgements

To The “Ministerio de Economia y Competitividad” of Spain for financing partially the experimental activities in the grants FPA2014-57196-C5 and FPA2011-29854-C04, and the “Generalitat Valenciana”, Spain, financed a PhD grant on the PROMETEO/2010/101 and partially the NEDA instrumentation on the grants PROMETEO/2010/101 and PROMETEOII/2014/019, and The European Regional Development Fund (FEDER) of European Commission.

I'm very grateful to Dr. Andrés Gadea for supervising this work with all his patience, understanding, and transferring me his knowledge on Physics and experimental techniques, also for his availability all the time, open for discussions and questions, not also on Physics but also for private matters. It has been a privilege to work with him and benefit his wisdom.

I would like to thank Javier Valiente for allowing me to work at Legnaro, in an elegant laboratory with great people, his availability for discussions and lading role on the NEDA project, transferring me his experience and being a great colleague and friend.

I'm thankful to Cesar Domingo for his availability, for being open for discussions and for his valuable help and opinions during the analysis of the ^{52}Fe experiment.

I'm thankful to Damian Ralet for helping me with the data analysis; and to Michael Reese for providing me the software for the “GSI experiment”.

A very special gratitude goes to the NEDA collaboration, especially to Grzegorz Jaworski, Antonio Di Nitto and Victor Modamio for their friendship, for being great colleagues to work with until late night at Legnaro and at GANIL, sharing ideas and leading enjoyable chats.

I appreciate the contributions of Johan Nyberg and Marcin Palacz on the EXOGAM - Neutron Wall - DIAMANT experiment and their help on NEDA, and the contributions of Silvia Lenzi on the Shell Model Calculations, Carlos Bertulani on the DWEIKO calculations, Takenori Furumoto on calculating the optical potential parameters.

I would like to thank to Maria Doncel for her availability always on Skype, sharing ideas and experiences, and for her hospitality -opening her house in Salamanca- for me and my wife; and to Rosa Perez for being always there to compare feelings, being my closest friend at IFIC!

My family deserves a special acknowledgement, my parents Gülden and Yüksel Hüyük and my brothers Tufan and Altan, for supporting me and believing in me all these years. Bana olan koşulsuz desteğiniz ve sevginiz için çok teşekkür ederim!

Last but not least, I'm very grateful to my wife, Seher, for her infinite support and love, for making my life better in all aspects.

Contents

List of Figures

List of Tables

Abbreviations

ADC	**A**nalog to **D**igital **C**onverter
AGATA	**A**dvanced **Ga**mma **T**racking **A**rray
CFD	**C**onstant **F**raction **D**iscriminator
CIME	**C**yclotron pour **I**ons de **M**oyenne **E**nergie
DESCANT	**De**uterated **Sc**intillator **A**rray for **N**eutron **T**agging
DESPEC	**De**cay **Spec**troscopy
DWEIKO	**D**istorted **W**ave **EIKO**nal Approximation
FOM	**F**igure-**o**f-**M**erit
FRS	GSI **Fr**agment **S**eperator
FWHM	**F**ull **W**idth at **H**alf **M**aximum
GANIL	**G**rand **A**ccelereteur **N**ational d'**I**ons **L**ourds
GSI	**G**esselschaft für **S**chwer**i**onenforschung
HPGe	**H**igh **P**urity **Ge**rmanium
HV	**H**igh **V**oltage
HISPEC	**H**gh-Resolution **I**n-Flight **S**pectroscopy
INFN	**I**stituto **N**azionale di **F**isica **N**ucleare
IReS	**I**nstitut de **Re**cherches **S**ubatomiques
ISOL	**I**sotope **S**eparation **O**n-**L**ine
LNL	**L**aboratori **N**azionali di **L**egnaro
LYCCA	**L**und - **Y**ork - **C**ologne **Ca**lorimeter
MH TDC	**M**ulti-**h**it **T**ime to **D**igital **C**onverter
MUSIC	**Mu**lti **S**ampling **I**onization **C**hambers
NEDA	**Ne**utron **D**etector **A**rray
NIM	**N**uclear **I**nstrumentation **M**odule

NW	The **N**eutron **W**all
PMT	**P**hoto**m**ultiplier **T**ube
PSA	**P**ulse-**S**hape **A**nalysis
PSD	**P**ulse-**S**hape **D**iscrimination
QVC	**C**harge-to-**V**oltage **C**onverter
RIB	**R**adioactive **I**on **B**eam
SPIRAL	**S**ystéme de **P**roduction d**I**ons **R**adioactifs en **L**igneé
Super-FRS	**Super**-conducting **Fr**agment **S**eparator
TAC	**T**ime-to-**A**mplitude **C**onverter
TDC	**T**ime to **D**igital **C**onverter
ToF	**T**imo **o**f **F**light
TPC	**T**ime **P**rojection **C**hamber
ZCO	**Z**ero **C**ross-**o**ver

for my wife, Seher...

Chapter 1

Introduction

This doctoral study is composed of two parts:

i) an instrumental study related to the large array of neutron detectors NEDA, including the design of the array by means of Monte-Carlo simulations.

ii) experimentation on nuclear structure with large γ-detector arrays based on semiconductor germanium detectors. In this second section, two experimental activities performed with γ-ray spectroscopy techniques will be presented, from the preparation to the completion of the data analysis and the discussion of the results.

The first part is devoted to development of the new generation high efficiency neutron detector arrays, based on liquid scintillators, to be used as trigger or complementary instrumentation in high-resolution nuclear structure experiments. I have been actively participating in a European project which aims to build such instrument, called NEutron Detector Array (NEDA) to be coupled to segmented high-purity γ-ray detector arrays, like AGATA [1], EXOGAM2 [2]. NEDA is currently in the production phase, is a collaborative effort of several European countries, including Spain, Turkey, Italy, France, Poland, Great Britain and Sweden. We aimed, with NEDA, to have high efficient neutron detector array for the needs of contemporary nuclear physics experiments, which aim to investigate the structure of exotic nuclei lying far from the valley of β stability. One of the most successful methods for producing such exotic nuclei is to use fusion-evaporation reactions with stable or radioactive beams and stable targets. The most exotic neutron-deficient nuclei are produced in extremely weak reaction channels after

the emission of two or more neutrons from the compound nuclei. In order to perform high resolution γ-ray spectroscopy of such exotic systems, as for instance in the case of ^{92}Pd [3], the identification of the reaction channel requires, in addition to the high efficiency and selectivity, the determination of the neutron multiplicity.

In the instrumental part of this thesis, the early conceptual design of the NEDA neutron detector array will be discussed, nevertheless, before entering the section of the conceptual design, it is essential to discussed the mechanism used to detect neutrons using liquid scintillators. Thus the second chapter is devoted to neutron interactions and neutron detection. During the development phase of NEDA, a test bench has been set up in Legnaro National Laboratories (LNL - INFN). The tests were carried out using four prototype detectors with identical sizes and two different scintillators - the conventional liquid scintillator and deuterated liquid scintillator. One of the conventional liquid scintillator detector was procured and mounted by us at IFIC-Valencia. With these tests, we aimed to characterize the prototypes and to test their functionality with digital sampling electronics. Of particular interest were the determination of relative efficiency of the two scintillators (G. Jaworski), time resolution (V. Modamio) [4], cross-talk evaluation (T. Hüyük) and the tests of the fast analog-to-digital boards (J. Egea and M. Jasztrab) [5–7]. The tests of the NEDA prototypes will be discussed in Chapter 4.

The second part of this thesis is devoted to the description of the preparation, realization, analysis and discussion of the results of two experiments. It will be preceded by a brief introduction to High-purity semiconductor Germanium detectors and the trigger/complementary detector systems. The first experiment was performed with the EXOGAM - Neutron Wall - DIAMANT setup at GANIL. The analysis of this experiment allowed me to gain experience on a setup which involves the neutron detectors. The Neutron Wall array is the ancestor of NEDA (see Chapter 3). More details on this experiment will be given in Chapter 6.

The second experiment was performed at the GSI Fragment Separator facility with the AGATA - PreSPEC setup. This experiment was done to study the collectivity in ^{52}Fe above the 12^+ isomeric state. In order to populate the low lying states above the isomeric state, we produced the unstable ^{52}Fe beam at relativistic energies and peformed Coulomb excitation by heavy ^{197}Au target. The physics motivation, the reaction mechanism and the analysis of the experiment together with the results and their evaluation will be discussed in Chapter 7.

Chapter 2

Neutron Detection with Liquid Scintillators

2.1 Introduction

In this chapter, the neutron detection with scintillator detectors will be discussed algonside with the fundamental background, such as, neutron interaction with matter and signal producing in scintillator based detectors. As it was emphasized in Chapter 1, this chapter has a character of introduction to the conceptual design study of the new neutron detector array, NEDA, using Monte-Carlo simulations. In NEDA, due to the characteristics of the reactions, the fast neutron detection is rather interesting. Therefore, in this chapter, the detection of the fast neutrons will be discussed, but, in order to provide knowledge to the reader, a general discussion on how the slow neutrons are detected will also be given.

This chapter is organized as the following: a brief introduction to the structure of neutron, its classification and its interaction with matter, the signal production inside the liquid scintillators and pulse shape analysis, the tests of neutron detectors in terms of relative efficiency, cross-talk and timing, and finally the digital-analog comparison of the electronics.

2.2 The Neutron

The neutron was discovered in 1932 by James Chadwick at Cavendish Laboratories. The neutron is a subatomic particle which carries no electrical charge and its mass is 1.674927351(74) x 10^{-30} g. Neutrons and protons are called together as "nucleons". The number of nucleons inside a nucleus determines its mass.

Neutrons are stable if they are bounded in a nucleus while the free neutrons are unstable and they suffer beta decay (see Eq. 2.1) with a lifetime of around 10.6 minutes.

$$n \rightarrow p + e^{-} + \nu_e \tag{2.1}$$

However, this does not mean that a neutron is composed of one proton, one electron and one electron neutrino. Neutrons are composed of smaller particles, quarks. Quarks carry electrical charges that are fractions of the elementary charge, which are $+\frac{2}{3}$e and $-\frac{1}{3}$e for up and down quark, respectively. The neutron is formed by *one* up and two *down* quarks, therefore electrical charge of a nuetron is $+\frac{2}{3} - 2(\frac{1}{3})$ = 0, while on the other hand, the proton is formed by two *up* and one *down* quarks, and its electrical charge is +1.

The free neutrons are produced during the fusion and fission reactions, neutron sources like research reactors. Also Neutron Spallation Sources produce free neutrons to be used in radiation and neutron scattering experiments. For practical reasons, neutrons are classified according to its energy range:

Neutron Energy	Energy range
Thermal neutrons	$\sim$ 0.025 eV
Epithermal	$\sim$ 1 eV
Slow neutrons	$\sim$ 1 keV
Fast neutrons	$\sim$ 100 keV - 20 MeV

TABLE 2.1: The classification of neutrons according to their energy range

The Energy of the neutron is the main factor determining its interaction with matter which will be discussed in the next section.

2.3 Neutron Detection

Unlike the charged particles, the neutrons don't leave traces when they pass through a material, for instance ionizing the atoms by means of Coulomb force, since they have no electric charge. As a result, the neutrons cannot be detected directly, and the detection of neutrons is based on observing the charged reaction products after letting the neutron interact with a material. In other words, it should undergo an interaction to transfer its energy to directly detectable particles. Depending on the type of the interaction, the neutron may leave all of its energy or lose its some of energy and change its direction.

The neutron interactions with matter can be summarized as:

- Elastic scattering
- Inelastic scattering
- Neutron capture
- Charged particle emitting reactions, i.e. (n,p), (n,d), (n,t), (n,α)

Detection mechanisms of slow and fast neutrons differ from each other. The reaction cross section at different energies will determine the type of mechanism that plays a role in the neutron detection.

2.3.1 Detection of Slow Neutrons

Slow neutrons can undergo elastic scattering with the absorbing material nuclei or neutron-induced nuclear reactions, mainly neutron capture. Elastic scattering causes slow neutron to lose its energy and very often the energy of the recoiling particle is not enough to be detected; on the other hand, the recoiling neutron will be at thermal equilibrium and is able to suffer neutron capture. Slow neutron interactions are detectable if they lead to a neutron-induced nuclear reaction, the conservation of momentum can provide enough energy to the recoiling nucleus either can be detected indirectly if there is a γ-ray emission or charged particles following the reaction. Since energy of a slow neutron is very low, the reaction should have positive Q-value in order to be energetically possible. In particular,

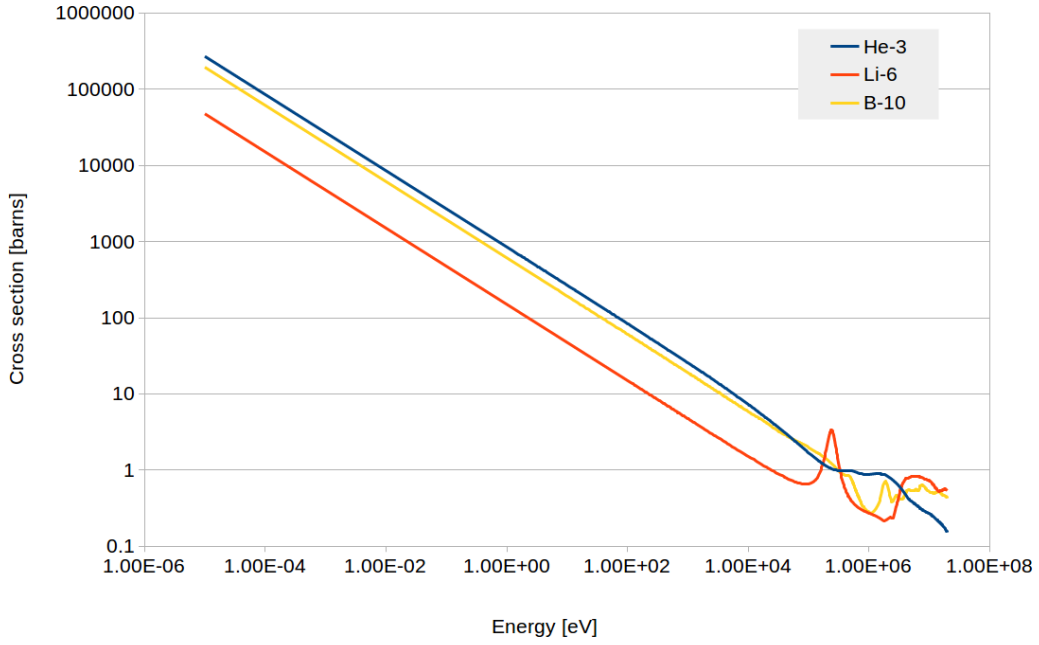

FIGURE 2.1: Cross-section as a function of neutron energy for some interesting reactions in slow neutron detection. Data taken from Refs. [8–11].

the (n,γ) reaction is the most probable one, but also less attractive due to the difficulties in direct detection of γ-rays. But, on the other hand, such reactions like (n,α), (n,p) and (n,fission) are more desired due to the secondary radiation released, that is easy to be detected directly.

The detection of slow neutrons rely on the very large cross section for slow neturon capture by certain isotopes. The probability of the above mentioned reactions drops dramatically down with increasing neutron energy (see Fig. 2.1), and different mechanisms play role in the detection of faster (i.e. more energetic) neutrons.

2.3.2 Detection of Fast Neutrons

The detection of fast neutrons can be based on two following methods: moderation of fast neutrons and observation of the recoil nuclei.

Detection of the fast neutrons by moderation is based on slowing down the fast neutrons using a moderating material so that the less energetic neutrons become detectable by means of reactions mentioned in Sec. 2.3.1. In such a case, the detector is surrounded by a moderating material, usually polyethylene or paraffin.

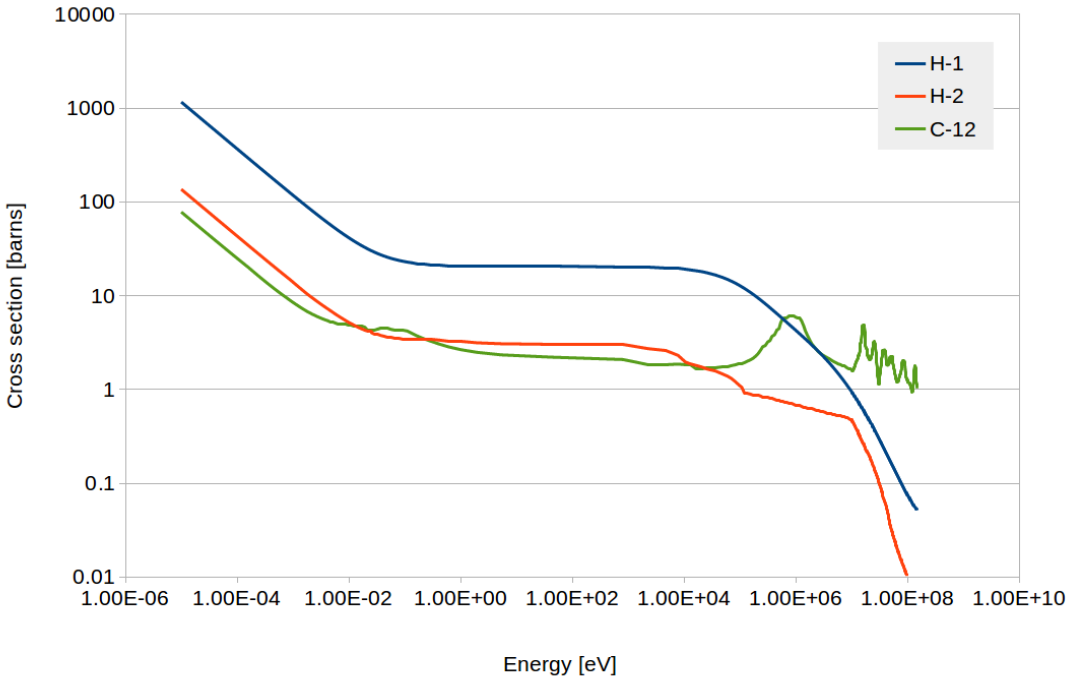

FIGURE 2.2: Cross-section as a function of neutron energy for some interesting reactions in fast neutron detection. Data taken from Refs. [8–11].

The moderation of neutron energy takes place by elastic scattering of neutrons inside the moderating material. Nevertheless, if the neutron has high enough energy, than, depending on the thickness of the moderating material, it will not slow down enough and the efficiency of it's detection will start to decrease.

The direct detection of fast neutrons is based on the detection of the charged recoiling products of the neutron scattering. Cross section of elastic scattering of neutrons does not decrease as dramatically as of slow neutron induced reactions does, as mentioned before (see Fig. 2.2). In most of the nuetron energy region of interest, cross-section for the elastic scattering of neutron on hydrogen is very large with respect to those on ^{2}H, ^{3}He, ^{4}He and ^{12}C [12]. In this interaction, the neutron transfers a part or all of its energy to the recoiling particle. The energy of the recoiling particle is high enough to ionize the surrounding molecules.

The energy transferred to the recoiling nucleus with mass A by an incoming neutron with non-relativistic energy can be calculated in the laboratory frame as:

$$E_R = \frac{4A}{(1+A)^2}(cos^2\theta)E_n \tag{2.2}$$

where, E_R is the kinetic energy of incoming neutron in laboratory frame, A is the mass of target nucleus, θ is the scattering angle of recoiling nucleus in laboratory frame and E_n is the incoming neutron energy in the laboratory frame. If θ angle is zero, than the maximum energy is transferred to the recoiling particle. In such a case, Eq. 2.2 becomes:

$$E_R|_{\max} = \frac{4A}{(1+A)^2} E_n \tag{2.3}$$

Maximum energy fraction can be transferred to the various recoiling nuclei are listed in Table 2.2.

Target	A	$\frac{E_R}{E_n}\|_{max}$
^{1}H	1	1
^{2}H	2	0.889
^{3}He	3	0.750
^{4}He	4	0.640
^{12}C	12	0.284
^{16}O	16	0.221

TABLE 2.2: Maximum fractional energy transferred to the recoiling nucleus in neutron elastic scattering.

The most used target nucleus in neutron detectors is the hydrogen since neutron can transfer up to 100% of its energy to the recoiling proton (see Table 2.2).

2.4 Neutron Detection Using Scintillators

An ideal scintillation detector would require all energy of an incoming neutron is converted into light with no loss, without allowing neutron to be scattered away and deposit its remaining energy at another detector. This energy conversion should be linear so the light production should be proportional to energy left by neutron. The decay time of the light produced should be short enough that the fast signals can be generated and the detector material should be transparent for a good light collection.

Since real detectors don't fulfil all these conditions simultaneously, the detector material should be chosen for what is best in the application. In the case of NEDA, fast neutron detection with neutron - γ discrimination capability is the

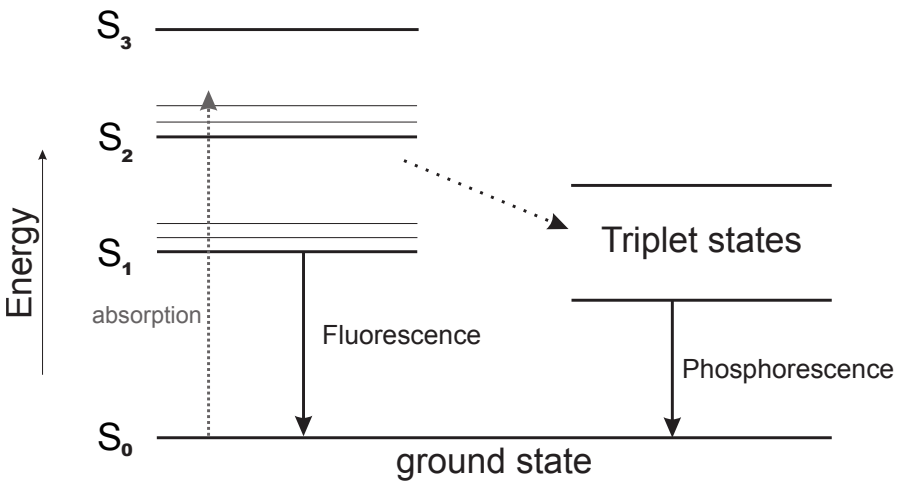

FIGURE 2.3: Schematic view of the light production mechanism in an organic scintillator

main requirement. Therefore, organic liquid scintillators become interesting with their fast response, i.e. few nanoseconds, and their availability to perform pulse shape analysis, which will be described later in this section.

The light production in scintillators is possible from transitions in the energy level structure of a single molecule (see Fig. 2.3). In a liquid scintillator, the fast neutron might transfer part or its whole energy to the target nucleus in the scintillator in the interaction, causing it to recoil, which results in raising molecules to their excited states, i.e. singlet (S_1, S_2, ...) or triplet (T_1, T_2, ...) states. The light production occurs when the molecules de-excite to the ground level, this emission is called *fluorescence*. This process occur within few nanoseconds. As can be seen in Fig. 2.3, the de-excitation of the molecule not only takes place via fluorescence but also to the T band, i.e. triplet states, without light emission, and from the excited states of the T band to the ground state via *phosphorescence*. Contrary to the prompt fluorescence emission, the delayed fluorescence and phosphorescence have decay time from several hundred nanoseconds to microseconds. The probabilities to populate triplet and singlet states are 75% and 25%, respectively [13]. However, the excitation energy might be transferred to the neighbouring molecules before the light emission. Such interactions are explained with *Förster* (dipolar interaction) and *Dexter* (charge exchange) mechanisms and no light output occurs during the energy transfer [15]. The energy transfer efficiency of Förster mechanism is proportional to the distance between the molecules with an inverse sixth power law. Dexter mechanism occurs within 10 Å between the molecules. Therefore, the

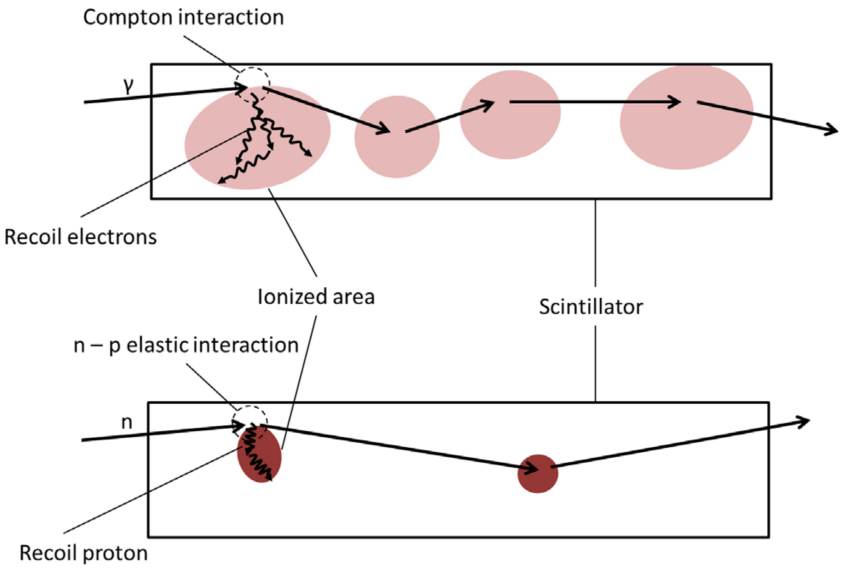

FIGURE 2.4: An artistic illustration of the ionization caused by γ-rays (electrons) and neutrons (protons) in the scintillation material. Courtesy of Ref. [13].

probability of occurrence of these mechanisms increases as the distance between the interacting molecules decreases.

The γ-rays interact with the electrons via Compton scattering and the neutrons interact with the protons via elastic scattering in the case of liquid scintillator. Recoiled charged particles, i.e. electrons and protons, ionize the surrounding material. The mass of electrons are smaller than the one of protons thus their mean free path is larger than of protons. The protons, on the other hand, can release more energy in a very limited area (see Fig. 2.4). The prompt fluorescences show no discrepancy in γ-ray and neutron de-excitation paths. The high density of excited states in neutron interaction increases the probability of a special case of Dexter energy transfer where two triplet excited states of two nearby molecules annihilate each other, one of them reaches to its ground state S_0 and other remains in singlet excited state S_1. Finally, the latter de-excites by radiating delayed fluorescence, which results in a footprint of a neutron interaction, in such a way that at equivalent deposited energy, the light pulse of a fast neutron has a longer decay time than that of a γ-ray.

The decay of the fluorescence light is not a simple exponential decay, but a superposition of two exponential decays. These decay components have different decay time constants and are called slow and fast components. The fast component

is due to the prompt fluorescence flash while the slow component is due to the delayed flashes of fluorescence which was explained above. As a consequence of what was mentioned before the fraction of light corresponding the slow components depends on the incident particle: for γ-rays and neutrons, less and more light appears in the slow component, respectively (see Fig. 2.5). Therefore, one can understand the nature of the incident particle by analysing the pulses, and this process is called *pulse shape analysis* (PSA).

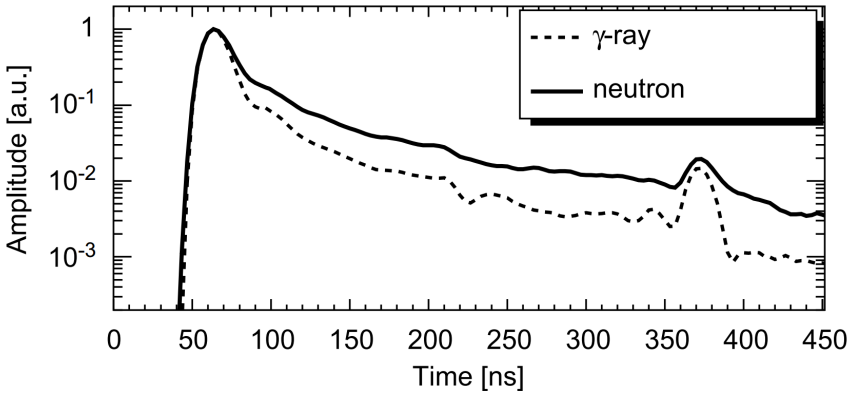

FIGURE 2.5: Pulse shapes from a liquid scintillator produced by a γ-ray and a neutron interaction. Courtesy of Ref. [14].

Several different PSA methods are available to be used in n-γ discrimination. Two widely known are *zero cross-over* (ZCO) and *charge comparison* (CC). The former is based on the shaping of the signal into a bipolar pulse and the information on the particle type is extracted from the zero-crossing. The latter is based on the comparison of the charge (light) of fast and slow components of the pulse.

Another method, that is not based on the PSA tecnique, to discriminate neutrons from γ-rays is the Time-Of-Flight (TOF). Since neutrons are massive particles, if the source to detector distances are large enough, it is possible to measure the time differences due to the velocities. Using one of two PSA techniques together with the Time-Of-Flight (TOF) information, a good n-γ discrimination can be done. Figure 2.6 shows a comparison of the ZCO PSA and TOF for neutrons and γ-rays. The TOF is represented on y-axis and ZCO is on x-axis, both in arbitrary units.

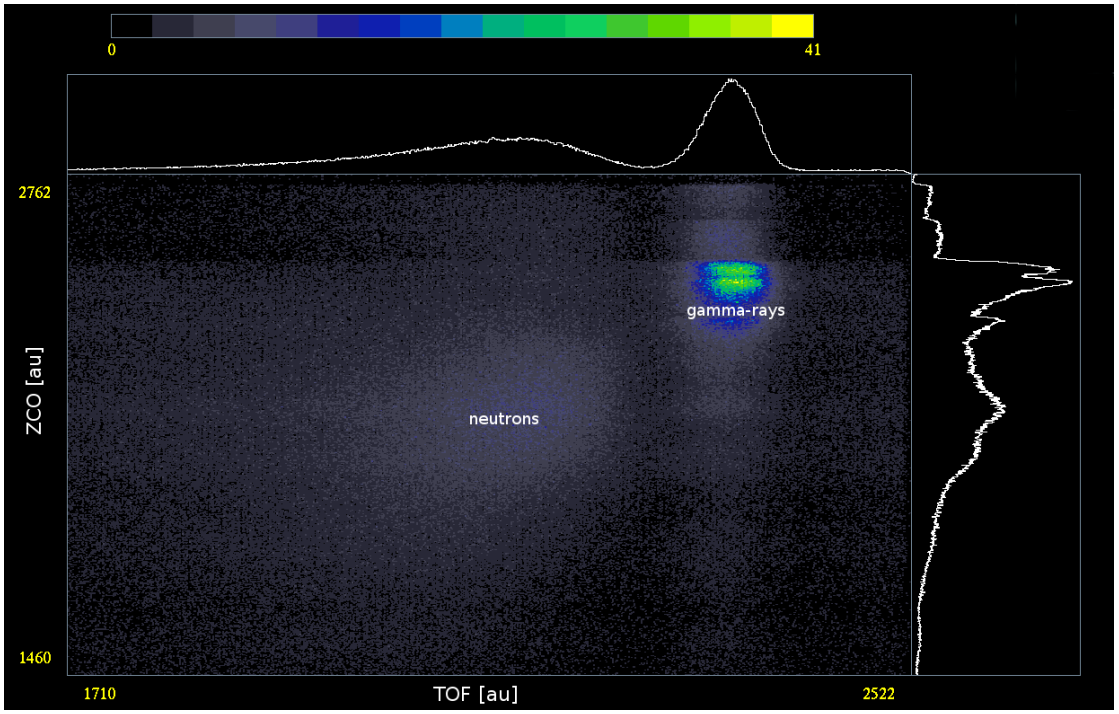

FIGURE 2.6: ZCO vs. TOF comparison for the neutron and γ-ray discrimination. Units are arbitrary.

Chapter 3

NEutron Detector Array (NEDA)

Contemporary nuclear physics experiments aim to investigate the structure of exotic nuclei lying far from the valley of β stability. One of the most successful methods for producing such exotic nuclei in the proton-rich side is to use fusion-evaporation reactions with stable or radioactive beams and stable targets. The most exotic neutron-deficient nuclei are produced in extremely weak reaction channels after the emission of two or more neutrons from the compound nuclei. In order to perform high resolution γ-ray spectroscopy of such exotic systems, as for instance in the case of ^{92}Pd [3], the identification of the reaction channel requires high neutron efficency and capability to determine the neutron multiplicity. NEDA will be an ancillary detector, to be coupled to a set of germanium-based gamma detectors (e.g. AGATA, EXOGAM2) intended to fulfill these requirements. It will be used in different studies of nuclear structure of both neutron-rich and neutron-deficient nuclei. NEDA will present a high detection efficiency for one-, two- and three-neutron events with a good neutron-gamma discrimination.

In neutron detectors like NEDA, one of the critical issues in the determination of the neutron multiplicity is the scattering of neutrons between the different detectors of the array. The neutron scattering gives rise to signals in more than one detector, creating an ambiguity in the actual number of neutrons detected (neutron cross-talk). One important goal in the design of new neutron detection filters, such as NEDA, is to minimise the neutron cross-talk and to increase the efficiency for detecting 2 or 3 neutrons compared to existing arrays, e.g. the Neutron Wall [16, 17] and the Neutron Shell [18].

Moreover, NEDA will make use of digital electronics and state-of-the-art digital signal processing based on NUMEXO2 cards [5, 6]. With this in mind, considerable effort has been expended recently in studying digital timing [4], fast digital data acquisition cards [7] and digital pulse shape discrimination [19, 20].

The size of the single detector unit and the scintillation material used for the neutron detection are important factors in order to optimise the performance of the full array. A detailed study in which I have participated, using Monte Carlo simulations of a detector unit filled with liquid scintillator, reported the optimum size that is sufficient for the detection of neutrons typically emitted in fusion-evaporation reactions [21]. The outcome of that work was used to decide the dimensions of a single NEDA detector.

In this chapter the description of the NEDA detectors will be presented in more detail, the simulations to evaluate the performance of the first implementation of NEDA together with the Neutron Wall will be discussed. The geometry will be defined and the simulations performed to determine the neutron efficiency for the cases of isotropic emission from the ^{252}Cf source and for a fusion-evaporation reaction.

3.1 Design of the NEDA detectors

NEDA is conceptually designed as a flexible array with identical detector units able to adapt to different experimental setups. It is expected to be coupled with complementary Ge detector instrumentation like AGATA [1], EXOGAM2 [2] or GALILEO [22]. A regular hexagon was chosen as the starting point for the design of the NEDA geometry since it is the most suitable polygon for both clustering detectors and coupling to a circularly shaped photomultiplier tube (PMT), minimising the uncovered area by the PMT. NEDA detectors will have the shape of a uniform hexagonal prism, see Fig. 3.1. The optimum depth of the detector units, evaluated using GEANT4 simulations, is 20 cm as discussed in Ref. [21]. The side length of the hexagon is 84 mm, suitable for the largest commonly available photomultiplier tubes with 5 inch diameter. The volume of each detector is 3.23 litres. An aluminum canning with a thickness of 3 mm is used in order to provide sufficient mechanical stability of the detector.

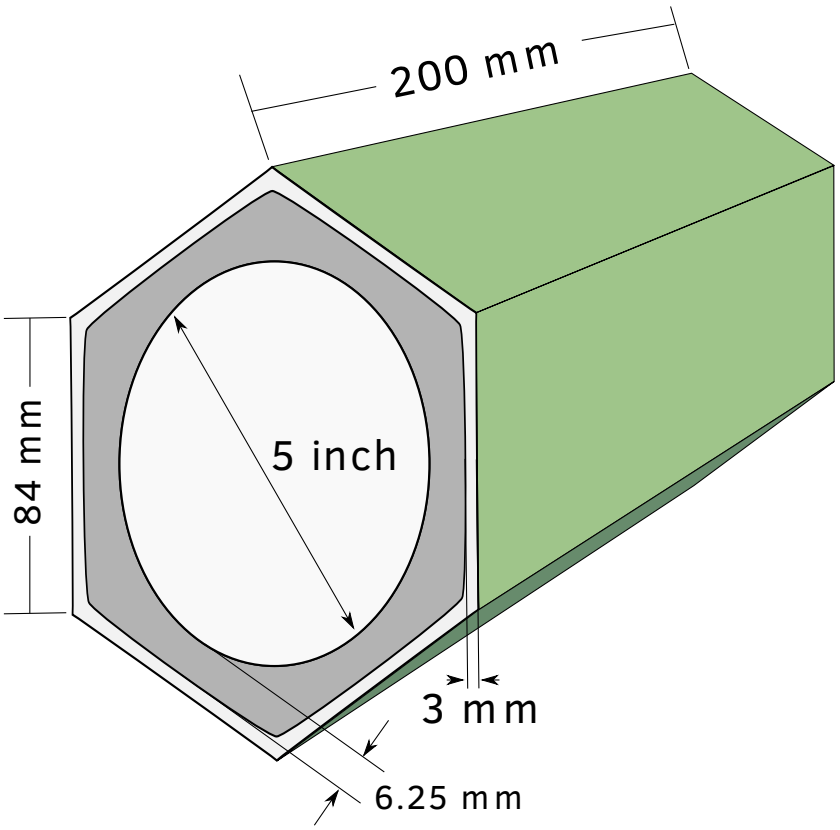

FIGURE 3.1: Schematic picture of the NEDA detector unit.

The broad experimental conditions expected for NEDA, using both stable and radioactive high intensity beams, require a modular concept of the overall design. In addition to modularity, three basic conditions are to be considered for the design of the array, that have implications in the design of the detectors:

1. Efficiency: to be maximised within the geometrical coverage.
2. Target-to-detector distance: large enough for neutron-γ discrimination by Time-Of-Flight (TOF)
3. Granularity: to maximize the discrimination efficiency for the reaction channels with neutron multiplicity larger than 1.

The possibility to have a flexible array that can change the distance between the target and the detectors, make this array more adaptable to the needs of the different physics cases. It allows to improve the neutron-γ discrimination based on TOF measurements, but also to increase the neutron energy resolution. Clearly, increasing the distance to the target would require a sizeable number of additional detectors for the same angular coverage.

3.2 Monte Carlo simulations and analysis procedure

The main goal of the simulations is to evaluate the performance figures of an early implementation of NEDA combined with the Neutron Wall and AGATA. The evaluation of such figures requires the use of Monte Carlo techniques. The Monte Carlo simulations presented in this chapter were carried out using GEANT4 [23] and the AGATA Simulation Package (ASP) [1, 24]. The ASP was chosen since it is compatible with the existing simulations of AGATA and other γ-ray detector arrays. With the ASP, it is possible to implement different geometrical configurations into the simulations and to select a number of essential parameters, e.g. detector material, source position, angular distribution of emitted particles, etc. The performance of the proposed array has been simulated for a ^{252}Cf source that emits neutrons isotropically and for the fusion-evaporation reaction ^{58}Ni + ^{56}Fe in which the neutrons are distributed according to the reaction kinematics. In GEANT4 the physical conditions of the simulations are mimicked by the so called "event generator", which will be introduced in the next subsection.

3.2.1 Event generators

In order to simulate the performance figures of the detectors, two different event generators have been used to produce neutrons, one corresponding to a ^{252}Cf source and the other to reproduce the emission of neutrons in a realistic fusion-evaporation reaction.

The neutron energy distribution of a ^{252}Cf source was produced by the built-in event generator of GEANT4 an by using the expression (see Eq. 3.1) deduced in Ref. [25] with T = 1.42 MeV and E given in MeV.

$$N(E) = E^{1/2} e^{-E/T}. \tag{3.1}$$

The simulations with the ^{252}Cf source can be compared directly with the measurements with a radioactive source, thus are interesting to calibrate the response of the detector to the neutrons. Regarding the realistic fusion-evaporation reaction events, the Monte Carlo Hauser-Feshbach code `LILITA_N97` [26] has been used to calculate the physical parameters of the neutron emission on an event-by-event

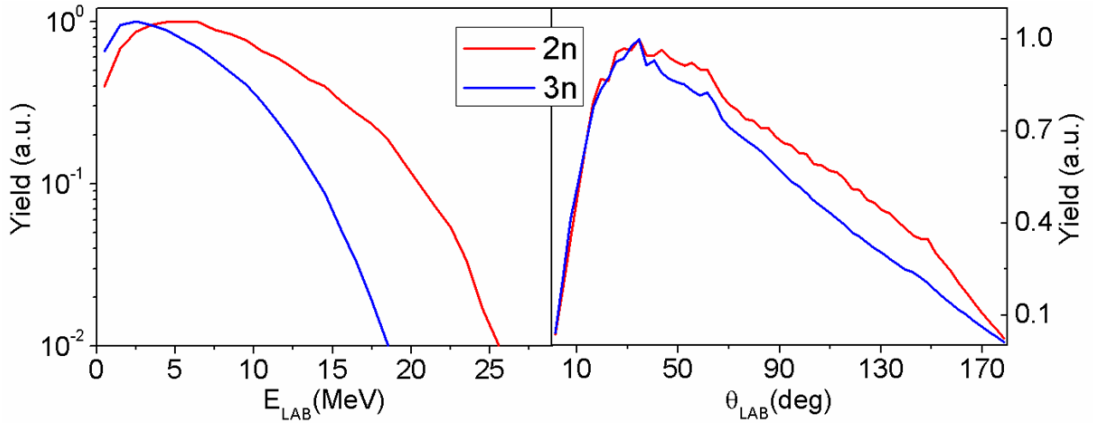

FIGURE 3.2: Angular distribution and energy spectra of neutrons emitted in the 2n and 3n reaction channels following the decay of the compound nucleus ^{114}Xe at an excitation energy of around 54 MeV.

basis. In `LILITA_N97`, the de-excitation of the compound nucleus is modelled through a multistep emission of light particles (neutrons, protons and α-particles) adopting the Hauser-Feshbach formulation of the statistical model in conjunction with the Monte Carlo method. The program produces energy spectra and angular distributions in the laboratory frame for light particles and evaporation residues. Furthermore, for this work, a new prescription for the transmission coefficients based on the Optical Model (OM) was implemented in the code. The event generator optimization has been performed by A. Di Nitto, has been explained in detail in Ref. [27], and is not the main focus in the conceptual design of NEDA.

3.2.1.1 Simulations for the selected fusion-evaporation reaction

In Ref. [27], the competition between the neutron and proton invovling channels have been discussed. In the same work, the two parametrizations described in the previous section suggest similar results at low energies. Although, the proton-neutron competition is modified by the large differences in proton transmission coefficients at low energy. The one-, two- and three-neutron channels are the most interesting ones for the future nuclear structure experiments to be performed with NEDA.

The angular and energy distributions of 2n and 3n channels are shown in Fig. 3.2. Obviously, the mean energy of the neutrons emitted in the 2n channel is higher than in the 3n channel in the center-of-mass(CoM) system, which implies that

when passing to the laboratory system the neutrons of the 3n channel are more focused in the forward direction due to the kinematics, which can be seen when comparing the yield ratios at small and large angles. The knowledge of the spatial distribution of the emitted neutrons is essential in order to be able to define the angular coverage of the detector array and its efficiency for a given reaction. The validation of this second event generator will be discussed in terms of neutron efficiency and angular distribution in the following subsection.

3.2.2 Verification of the fusion-evaporation reaction event generator

The modeling of a fusion-evaporation reaction is complex and depends on several parameters that are not always known. In order to validate our simulations, the event generator has been verified by comparing a Neutron Wall measurement with a simulation of the same setup. A representation of the GEANT4 model of the Neutron Wall system is shown in Fig. 3.3. In order to get a realistic comparison between the real data and the simulations, most of the materials between the target and the Neutron Wall were included, namely two concentric beam pipes of stainless steel with a thickness of 2 mm and a length of 250 mm together with a standard CF100 vacuum flange which were used as a beam dump in the experiment (see inset in Fig. 3.3). The energy loss inside the target was also taken into account. A data set measured with the Neutron Wall in which a ^{58}Ni beam at 220 MeV impinging on a ^{56}Fe target with a thickness of 10 mg cm^{-2}, was used for comparison. The choice of this reaction was motivated by the existence of a data set used earlier for the characterisation of the Neutron Wall detector array [17]. Moreover, the characteristics of this reaction are quite similar to those that we intend to use in future experiments with NEDA.

In the experiment, the Neutron Wall was coupled to the EUROBALL γ-ray spectrometer [34]. The trigger condition required at least two Compton-suppressed γ-rays in the HPGe detectors and there was no trigger condition on the Neutron Wall. The experimental energy threshold of the neutron detectors were determined using the calibration runs performed with a ^{207}Bi γ-ray source collected just before the experiment. The thresholds were determined for each Neutron Wall detector. The average value of the thresholds of the 43 operational detectors was determined to be 150 keVee. In order to validate the event generator we will

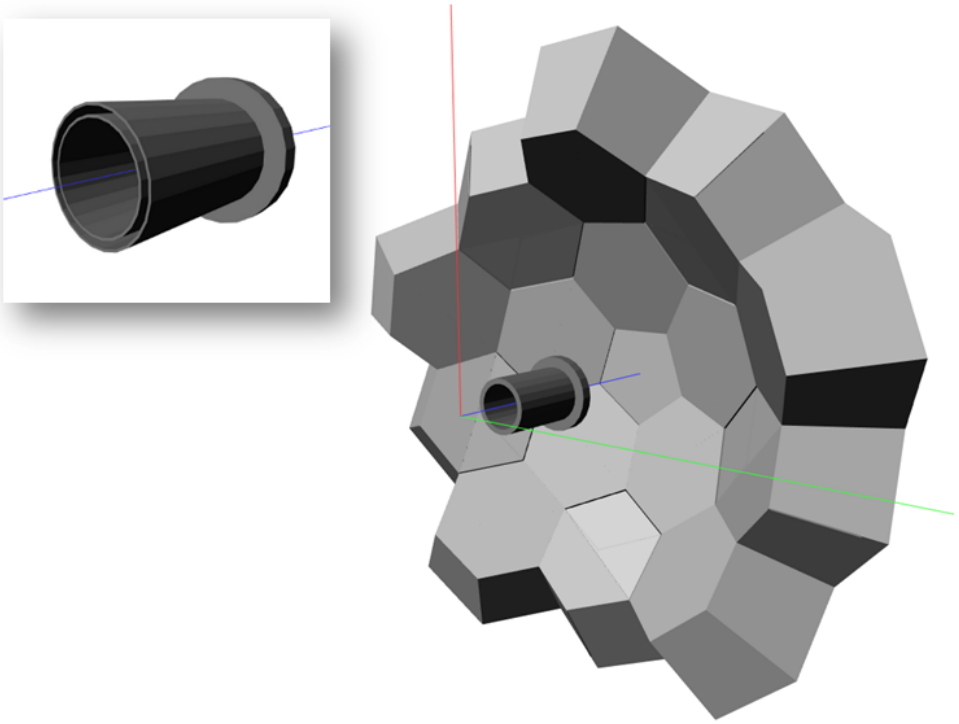

FIGURE 3.3: View of the Neutron Wall (light grey) with the beam pipe and beam dump after the target (dark grey) as modelled by GEANT4. The inset in the upper left corner shows in some detail the steel mechanical elements used in the beam pipe and beam dump.

make a comparison of the experimental TOF distributions measured in the aforementioned experiment for the various polar angles of the Neutron Wall with the GEANT4 simulations.

Figure 3.4 shows the measured and simulated TOF spectra for the six different θ angles of the Neutron Wall, see Table 3.1. The experimental data were collected using a common stop for the neutron detectors, therefore the time axis runs from right to left. The center of the γ-ray time distribution has been taken as time reference (t = 0 ns in the spectra). The rescaling between experimental and simulated data was performed using the ratio between the total number of neutrons in the experimental and simulated TOF spectra.

The simulated spectra are obtained: *i*) using the measured experimental thresholds and *ii*) taking into account the seven detectors that were inoperative during the experiment. However, the presence of the inoperative detectors were taken into account to simulate the real setup, since they influence, in particular, the events including scattering. In order to reproduce this particular set of experimental data, several values of the level density parameter a in the range from $A/12$ to

TABLE 3.1: Grouping of the Neutron Wall detectors according to their polar angle θ.

Group	n. Detectors	n. Working Detectors	θ [deg]
0	5	4	57.21
1	20	17	47.20
2	5	3	34.87
3	5	5	30.30
4	10	10	18.54
5	5	4	6.90

$A/6$ were considered in the `LILITA_N97` code. The best agreement was obtained with $a = A/8$. Prescriptions with a dependency of the parameter a and of the symmetry energy on the neutron-proton mass asymmetry were not considered, because their effects are negligible on the inclusive neutron energy spectra and angular distributions. Nevertheless, these dependencies may be important for the determination of the neutron energy spectra for very exotic nuclei and the cross sections of the evaporation residues are predicted to be more affected [33]. However, these are beyond the scope of this thesis and will be studied in a future work.

Large discrepancies between experimental and simulated data with plain results of `LILITA_N97` are shown in Fig. 3.4. The discrepancy is especially large for the detectors at forward angles ($\theta < 20°$). The reason for this is the simulated neutrons (dark grey spectra) have lower mean energies than the experimental ones (black spectra) as can be seen in Fig. 3.4 where the maximum of the experimental distribution is shifted to higher TOF values. Furthermore, the ratio between detected -simulated and experimental- number of neutrons is rather different at the smaller and larger polar angles. The ring at 6.9° shows the largest disagreement. In order to improve the agreement of the simulated and experimental data, the center-of-mass energy of the evaporated light particles had to be increased by 800 keV in `LILITA_N97`. This energy was subtracted from the excitation energy of the nucleus after each neutron emission, in order to keep the correct competition between different decay channels. The physical reason behind the disagreement, concerning the energy of the evaporated neutron, between the measurement and the statistical model is not fully understood. The statistical model parameter a, the transmission coefficients and the yrast lines cannot produce such a large effect on the energy of the emitted neutrons. One possibility could be a different distribution of the decay channels between experiment and simulations, but this

could not be verified using the present data set, due to low statistics. This remains an open question, that goes beyond the goal of the present work and is planned to be investigated in future experiments. In Fig. 3.4, the simulated TOF distributions are shown also after applying the 800 keV correction discussed above (light grey spectra). The standard deviation of the γ TOF distribution in the experimental data was found to be σ=2.21 ns, thus the Gaussian smearing function has been applied to the simulated data. As seen in the figure, the agreement is quite good and therefore we conclude that the event generator can be used to determine the performance figures of NEDA for the fusion-evaporation reaction.

Figure 3.5 shows the experimental and simulated neutron differential detection efficiency as a function of the polar angle θ for the Neutron Wall. This relative neutron detection efficiency was calculated according the expression:

$$\varepsilon_{\mathrm{rel},\theta} = \varepsilon_{1\mathrm{n}} \frac{N_\theta}{N_{\mathrm{NW}}} \frac{1}{\Omega_\theta}, \tag{3.2}$$

where $\varepsilon_{1\mathrm{n}}$ is the efficiency to detect at least one-neutron, N_{NW} the number of detected neutrons in the whole array, N_θ the number of detected neutrons in the ring at angle θ and Ω_θ the solid angle covered by the detectors at that angle. The solid angle correction in Eq. 3.2 is necessary since the detector volume at every polar angle varies, and this effect needs to be excluded for a clearer comparison.

In the case of fusion-evaporation reactions, one would expect a monotonic decrease of the neutron efficiency as a function of the θ angle due to the neutron angular distribution in the laboratory reference system. However, as a result of the neutron scattering with the material of the beam dump shown in Fig. 3.3, there is a clear reduction of the relative efficiency at the forward angles both experimentally and in the simulations. The simulated and experimental curves show the same behaviour as a function of θ. The experimental data points are, however, lower than the simulated ones by a constant factor for the whole angular range. The origin of this mismatch might be due to several factors, e.g. from different events close in time (pile-up) depending on the structure of the beam pulses as well as from the same event in case of multiple hits of γ-rays in high multiplicity cascades, causing sum up of the signals, which makes neutrons undistinguishable from γ-rays.

In order to obtain an acceptable level of agreement between simulations and experiment, a correction factor with a value of $0.772(1)$ has been introduced. This factor was calculated using the experimental neutron detection efficiency of the

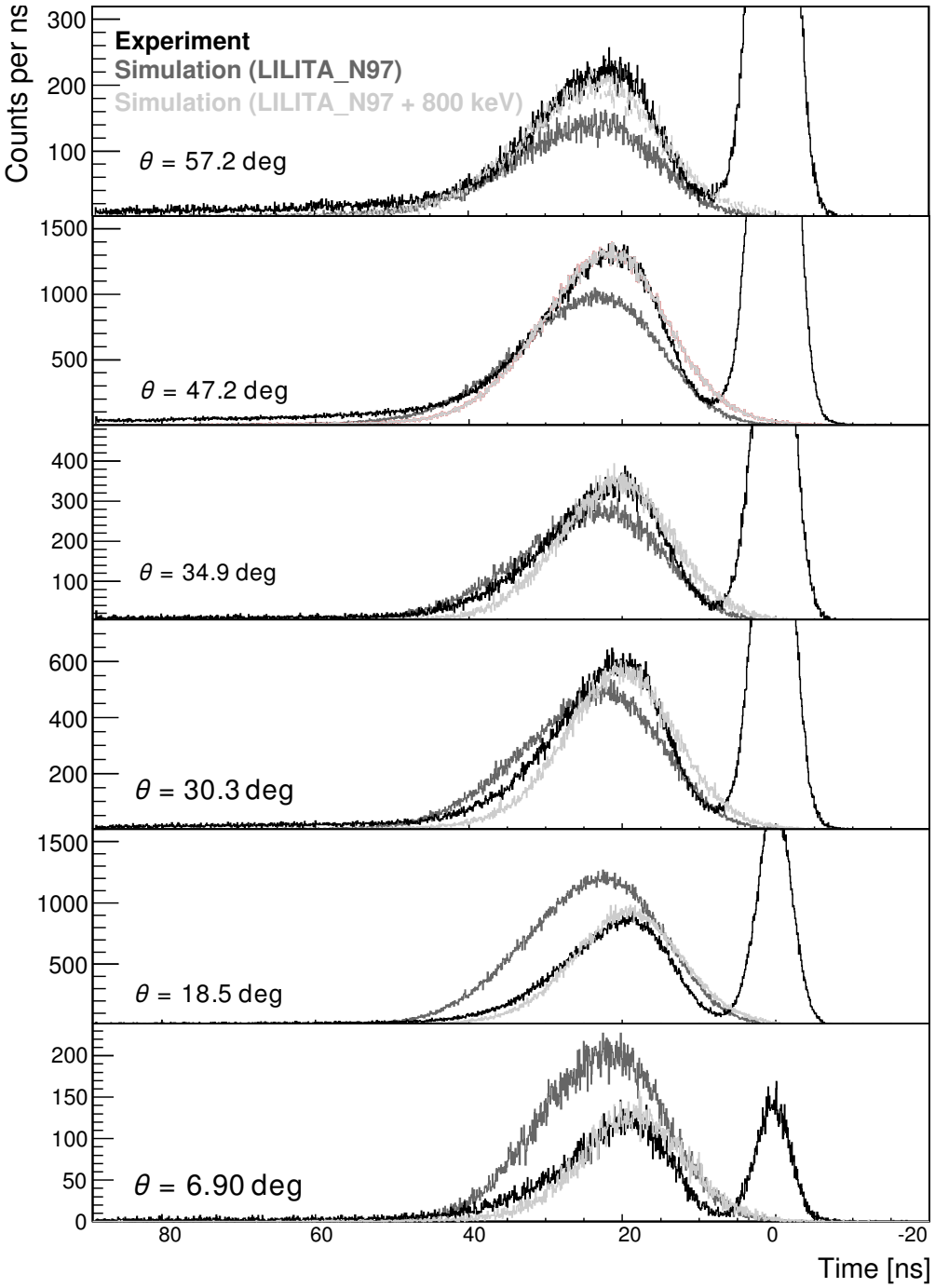

FIGURE 3.4: Simulated and experimental TOF spectra for the six different θ angles of the Neutron Wall. TOF increases from right to left. Gamma rays were not included in the simulations. The large Gaussian-shaped peak in the experimental spectra, centered at time 0 ns and with a width of $\sigma = 2.21$ ns, is due to γ rays. For the comparison of the simulated and experimental data, the former were smeared with a Gaussian distribution with the same width as the γ-ray peak. The initial simulated TOF spectra are shown in dark grey colour. The simulated TOF spectra after the center-of-mass energy of the evaporated neutrons was increased by 800 keV are shown in light grey colour. The experimental data are shown in black colour.

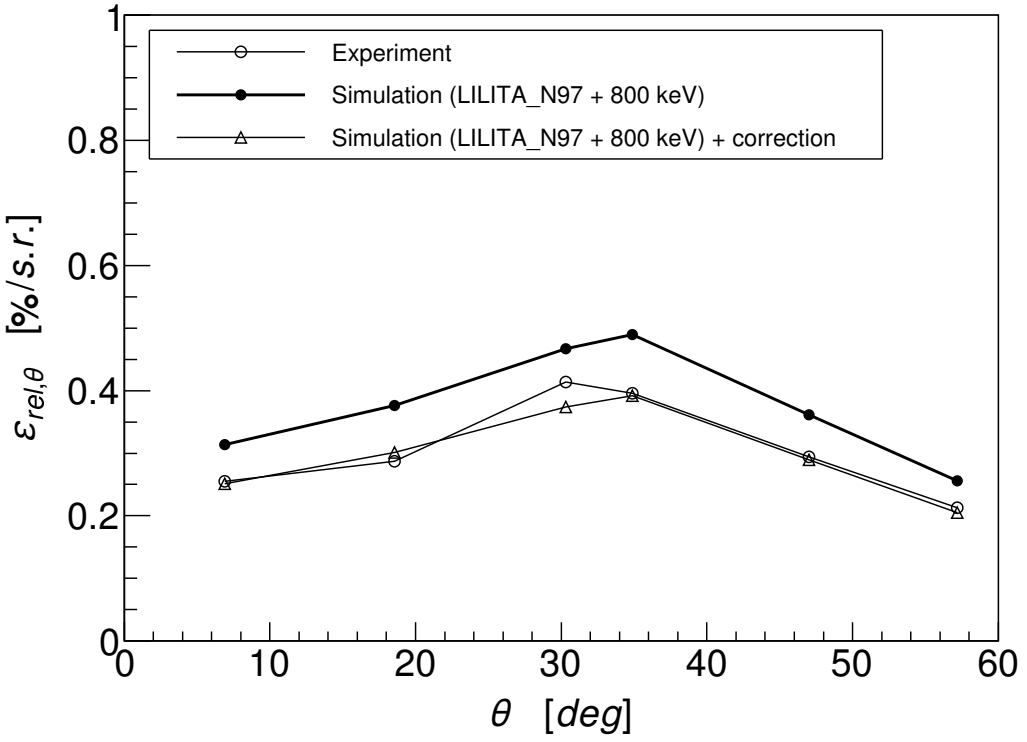

FIGURE 3.5: Experimental and simulated neutron detection efficiency per solid angle as a function of the polar angle θ of the Neutron Wall. The efficiency at the forward angles decreases due to the stainless steel beam dump shown in Fig. 3.3.

full Neutron Wall, reported to be 26(6) % in Ref. [17], and the simulated neutron efficiency, which was 33.7(1) % according to the present work. Figure 3.5 shows a perfect overlap for the whole angular range when the correction factor is used.

3.2.3 Handling of the scattered events

As mentioned before, in a neutron detector array with a compact geometry, such as NEDA, the probability of neutron cross-talk between detectors is rather large. For the Neutron Wall detector array, the simulated neutron cross-talk is estimated to be 12% in fair agreement with the previous estimates [16, 17]. This leads to an ambiguity regarding the real number of neutrons interacting in the array. In order to decrease this ambiguity and to optimise the two- and three-neutron efficiency, a method based on the correlation among the distance between the detector centroids (Δr) and the TOF (Δt) difference of two fired detectors in the array is commonly used [17, 35]. Each pair of coincident neutron signals is

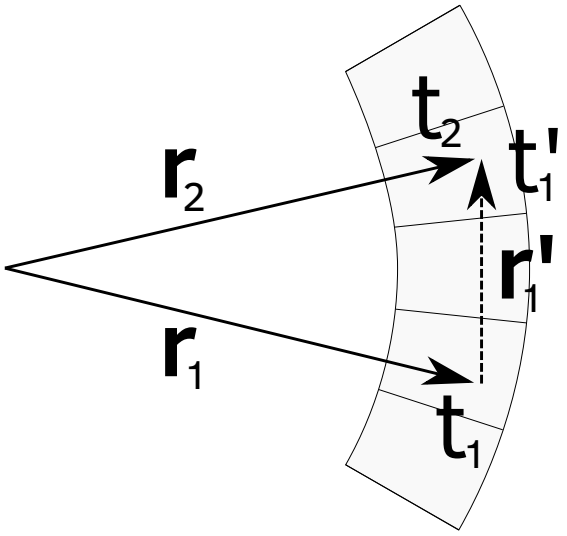

FIGURE 3.6: Schematic view of the Neutron Wall, showing two real neutron events with an associated time t_1 and t_2 and a scattered event t'_1. The difference $t_1 - t_2$ is smaller than a scatter event $t_1 - t'_1$, in average, for the vast majority of events.

evaluated to determine whether they are produced by two different neutrons or by the scattering of a single one (See Fig. 3.6). If the difference Δt is large enough to cover the distance Δr, assuming a realistic range for the neutron energy, the two signals are assigned to the neutron cross-talk category, i.e. a single neutron was detected. Otherwise, they are assigned to the real two neutron events. This procedure can be extended to all possible combinations of two pairs of detectors fired in each event.

Figure 3.7 shows the distribution of Δr versus Δt for simulated single neutron events emitted in a fusion-evaporation reaction. By definition, all these data points are associated to neutron cross-talk events and the observed distribution in Δt is due to the differences in the neutron velocities, and the velocities are independent from the geometry of the detector system. Events in which real two neutrons are detected should give counts inside the gate. The edge of the gate represents the largest neutron velocity for which a crosstalk event is defined and therefore for a given neutron energy spectrum the form of the gate is independent of the geometry. It can be seen that the gate is not symmetric around the $\Delta t = 0$. This is because detectors are sorted with a criterion that the interaction which left more energy in the detector should be the one that occurs first. A few events are observed inside the higher multiplicity gate, even if they don't exist in the simulation. These events are due to neutrons with a very large energy. They correspond to events

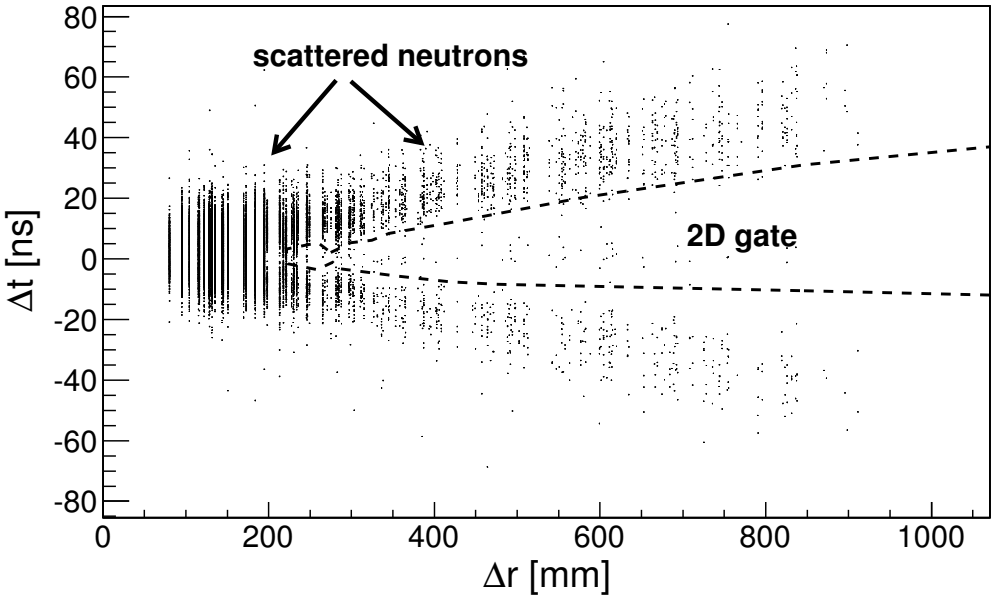

FIGURE 3.7: Δr-Δt plot for simulated one neutron events from the fusion-evaporation reaction, described in the text. The two dimensional gate shown with a dashed line corresponds to the position where the real detection of two- and three-neutron events would be located. The edge of the gate represents the largest neutron velocity for which a crosstalk event is defined.

with velocities larger than the one defined by the gate, therefore they cannot be discriminated from the real events. This events amount to about 0.05%.

The accuracy of such a gate depends on the granularity of the detector array since the Δr and Δt parameters would be determined with better accuracy for higher granularity. NEDA is conceptually designed expected to be suppressing the cross-talk events better than the Neutron Wall.

3.3 Early implementation of NEDA to be coupled with AGATA: Design and results of the simulations

An early implementation of NEDA, together with the Neutron Wall, is proposed to be coupled to AGATA at GANIL. The use of the Neutron Wall detectors in combination with NEDA detectors has been considered in order to maximise the number of detectors and therefore the efficiency of the setup. The coupling of both

arrays will provide the best achievable performance compared to the case of the Neutron Wall standalone. Two configurations have been proposed that are shown in Fig. 3.8. The reason to consider these two configurations are related to the geometry of the Neutron Wall detectors - these are more compact in the configuration shown in Fig. 3.8-a and in a "ring" at ninety degrees in the configuration shown in Fig. 3.8-b. The basic properties of both configurations, together with those of the Neutron Wall alone are listed in Table 3.2.

In the setup shown in Fig. 3.8-a, the Neutron Wall is translated 180 mm away from its nominal position in the downstream beam direction, i.e. the front faces of the pentagonal detectors are at 690 mm from the target position. The 50 NEDA detector units are placed at 510 mm, 17 are at 60.5°, 16 are at 74°, and 17 are at 87.5° with respect to the beam direction, in order to cover a larger solid angle in the forward direction. On the other hand, we considered another setup, in contrast to the previous configuration, where NEDA is placed at the forward position and the Neutron Wall detectors surround it. There are few possibilities for such configuration, nevertheless, the setup shown in Fig. 3.8-b is selected in order to maximize the number of the Neutron Wall detectors due to the geometry of the array. In this configuration the hexagonal units of the Neutron Wall are placed at θ angles between 60° and 90°. The target-to-detector distance of the Neutron Wall is kept at its original position, i.e. 510 mm. The 51 NEDA unitary cells are placed at between $\theta = 0°$ and $\theta = 60°$, covering a solid angle of about $\approx 0.7\pi$ sr in the forward position. The central detector unit of NEDA is placed at 570 mm from the target position.

TABLE 3.2: Summary of the basic properties of the Neutron Wall and the NW + NEDA.

Geometry		**Granularity**	**Solid angle [sr]**	**Volume/unit [litres]**	**Total volume [litres]**	**Radial distance to target [m]**
Neutron Wall (NW)		50	$\approx 1.00\pi$	(*)	149.5	0.51
NW + NEDA	NEDA	50	$\approx 1.63\pi$	3.23	311.0	0.51
	NW	50		(*)		0.69
NW-ring + NEDA	NEDA	51	$\approx 1.60\pi$	3.23	308.7	(**)
	NW-ring	45		3.20		0.51

(*) Volume of each segment of the Neutron Wall detectors is 1.1 l for the segments of the pentagonal detector and 3.2 l for the segments of the hexagonal detectors.
(**) The distance between the central detector of the NEDA array and the target position is 0.57 m.

Tables 3.3 and 3.4 show the simulated one-, two- and three-neutron efficiencies for neutrons emitted from a ^{252}Cf source and from the fusion-evaporation reaction ^{58}Ni + ^{56}Fe, respectively. The efficiencies are calculated according to the following expression:

$$\varepsilon_{\mathrm{n}} = \frac{N_{\geq m}}{N_{\mathrm{emitted}}}, \tag{3.3}$$

where $N_{\geq m}$ is the number of events that includes neutrons identified with multiplicity at least m. This specific definition of efficiency assumes that multiplicities m bigger than the number of neutrons emitted n is only due to scattered neutrons which is valid in the experiments performed in proton rich region of the Segré chart. The numbers listed have been determined using the 2-dimensional gate described before. The final values of the efficiencies have been scaled by the correction factor that has been explained in Sec. 3.2.2, in such a way that $\varepsilon'_{mn} = \varepsilon_{mn}\ f^m$, where m is the multiplicity of neutrons and f stands for the correction factor. The correction factor is deduced $f = 0.772(1)$.

TABLE 3.3: One-, two- and three-neutron detection efficiencies obtained from simulations of a ^{252}Cf source for the different detector configurations. Errors quoted are statistical.

Geometry	$\varepsilon'_{1\mathrm{n}}$ [%]	$\varepsilon'_{2\mathrm{n}}$ [%]	$\varepsilon'_{3\mathrm{n}}$ [%]
Neutron Wall (NW)	8.81 (*6*)	0.50 (*4*)	0.021 (*13*)
NW + NEDA	13.55 (*5*)	1.371 (*23*)	0.125 (*12*)
NW-ring + NEDA	14.68 (*5*)	1.743 (*21*)	0.182 (*11*)

TABLE 3.4: One-, two- and three-neutron efficiencies obtained from simulations of a fusion-evaporation reaction ^{58}Ni + ^{56}Fe at 220 MeV for the different detector configurations. Errors quoted are statistical.

Geometry	$\varepsilon'_{1\mathrm{n}}$ [%]	$\varepsilon'_{2\mathrm{n}}$ [%]	$\varepsilon'_{3\mathrm{n}}$ [%]
Neutron Wall (NW)	26.00 (*5*)	3.93 (*10*)	0.55 (*14*)
NW + NEDA	28.70 (*5*)	6.37 (*11*)	1.66 (*12*)
NW-ring + NEDA	31.30 (*5*)	7.62 (*11*)	1.89 (*11*)

According to the results of the simulations, this early NEDA - Neutron Wall implementation will provide a substantial improvement in terms of efficiency. The numbers listed in Table 3.3 show the results of the simulations using a ^{252}Cf source. The fission of ^{252}Cf results in emission of fast neutrons - which are in the same energy range as the neutrons emitted from a fusion-evaporation reaction. The average multiplicity of neutrons from spontaneous fissions of the ^{252}Cf source is 3.10(0.18) according to Ref. [36], which makes it interesting for the verification

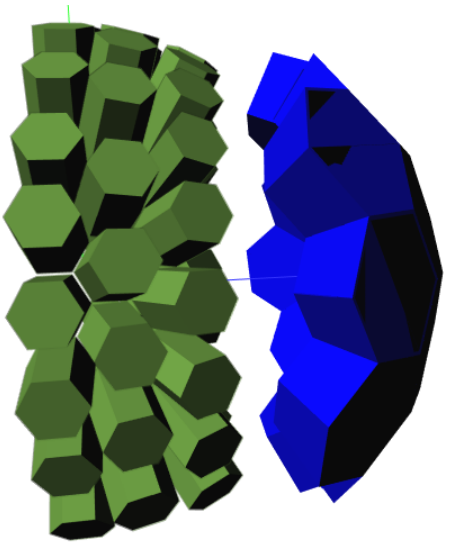

(a)

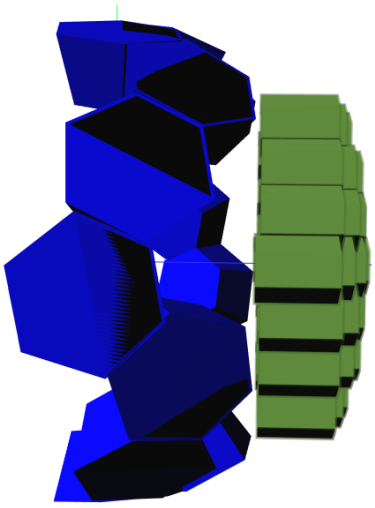

(b)

FIGURE 3.8: The proposed geometries of the NEDA array - left-hand-side in (a), right-hand-side in (b) - coupled to the Neutron Wall - right-hand-side in (a), left-hand-side in (b) - for the AGATA campaign at GANIL. See text for details.

of the neutron multiplicity counting. The results show the advantage of the configurations, in particular, the efficiency increment in the cases where the NEDA detectors are used, especially for two- and three-neutron multiplicities. For an isotropic distribution of neutrons, the increase of efficiency should be proportional to the increase in solid angle coverage, but the configurations involving the NEDA detectors show better performance figures. The results of the fusion-evaporation simulations in Table 3.4, show that the two-neutron efficiency for the *NW + NEDA* and *NW-ring + NEDA* configuration is predicted to be a factor 1.63(5) and 1.95(1), respectively, larger than what is obtained with NW alone. For the three-neutron

efficiency the increase is a factor of 3.0(1.7) and 3.4(1.9) for *NW + NEDA* and *NW-ring + NEDA*, respectively, compared to NW alone. The NEDA detectors have a larger intrinsic neutron detection efficiency due to their larger depth (20 cm compared to 15 cm for NW). The measured number of photoelectrons per MeV is about 3 times larger for the NEDA detectors compared to the NW detectors [4], which will provide a better neutron-γ discrimination performance. Therefore, in order to benefit from the better performance of the NEDA detectors compared to the NW detectors, the best configuration is the one with the NEDA detectors placed at the forward angles, *NW-ring + NEDA* shown in Fig. 3.8-b, where the energy and intensity of the neutrons is largest.

3.4 Summary and Outlook

The identification of rare neutron-deficient evaporation residues produced by fusion-evaporation reactions requires a high efficiency for detection of multiple neutrons. This can be achieved by using a detector array with a large solid angle coverage, high granularity and high efficiency. The optimisation of these quantities drove the design of the new NEutron Detector Array, NEDA. The conceptual design of an early implementation of NEDA together with the Neutron Wall, to be coupled to AGATA at GANIL has been described in this work. Two configurations have been discussed: one consists of 50 NEDA detectors and 50 Neutron Wall detectors covering 1.63π sr solid angle and the other consists of 51 NEDA detectors and 45 Neutron Wall detectors covering 1.6π sr solid angle. The performance figures of these two configurations were studied by using a fusion-evaporation event generator that has been discussed an validated in this paper with experimental data. The results of the present work show that the proposed *NW-ring + NEDA* setup will provide a sizeable improvement compared to the Neutron Wall alone for the detection of multiple neutrons emitted in fusion-evaporation reactions.

Nowadays, the goal of the NEDA collaboration is to build an array covering up to 2π sr solid angle at 1 m distance from the target position. In this configuration, named NEDA 2π, the detector units which are positioned between $\theta = 0^o$ and $\theta = 60^o$ with respect to the beam were translated in the upstream direction in order to increase the solid angle of the peripheral detectors. Moreover, the detectors located between $\theta = 60^o$ and $\theta = 90^o$ were oriented towards the target position

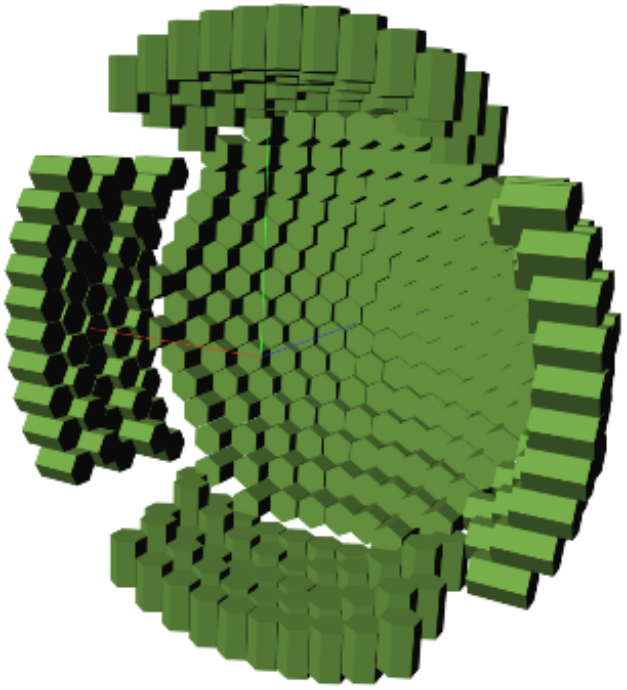

FIGURE 3.9: The proposed geometry of NEDA 2π consisting of 331 detector units and covering a solid angle of 1.88π sr at a distance of 1 m from the target position.

to maximise the exposition to the emitted particles. Such a geometry with 331 detector units covers a solid angle of 1.88π sr in the forward direction.

The efficiencies foreseen for the NEDA 2π geometry are about 0.36, 0.10 and 0.03 for one-, two- and three-neutron channels. The conceptual design for the final NEDA configuration is still ongoing and the best geometry is not decided yet for NEDA. The final geometry will be designed considering the best detection efficiency with lowest cost. Nevertheless, the philosophy behind the modular geometry of NEDA is promising in the sense of flexibility as well.

Chapter 4

Tests of Neutron Detector Prototypes

In the previous chapter, detailed information on the NEDA project has been discussed. In order to optimize the selection among different types of neutron scintillator detectors in the preparation phase of the NEDA project, a test bench has been deployed in Legnaro National Laboratories (LNL). In this chapter, the structure of a scintillator based neutron detector, its signal processing and data acquisition systems will be described, following by the reports on the tests and results.

Within this task, the evaluation of several commercial prototype detectors has been done. These sample detectors have been chosen with the dimensions which are similar to those of the Neutron Wall detector segments. The reason lies behind the fact that the final size was not decided yet for the NEDA single detectors by the time the tests were initiated, but it was foreseen that it would be similar to the size of one segment of the hexagonal detectors of Neutron Wall. Therefore, prototypes with 5 inch diameter and 5 inch depth were chosen. The four vessel prototypes (without photo-multiplier tubes), two filled with the liquid scintillator (BC501A) and two with deuterated liquid scintillator (BC537), have been evaluated for their basic characteristics, like time resolution, relative efficiency and probability of neutron cross-talk. The time resolution evaluation task has been lead by V. Modamio and published in Ref. [4]. The relative efficiency evaluation task has been lead by G. Jaworski. A brief explanation of these tasks will be given

later in this chapter. The cross-talk evaluation task has been done by myself and the discussion will also be given later in this chapter.

The four neutron detector vessel prototypes were coupled to four different PM tubes (Hamamatsu R4144, Hamamatsu R11833-100, Photonis XP4512, ET Enterprises ET9390kb) in turn. In addition to the detector prototypes, the setup was also consisted of a BaF_2 detector to be used as the time reference.

A ^{252}Cf source has been used in the tests. This source has several advantages in this particular application, like it emits fast neutrons with an average multiplicity of 3 per fission in coincidence with γ-rays. The source had an activity of 2.12 GBq by April 2011.

4.1 Structure of the Scintillator Based Neutron Detector Prototypes

The liquid scintillator based neutron detector prototypes consist of two main parts: i) the aluminium container which holds the liquid scintillator, and ii) the PMT which converts the light produced in the scintillator liquid into an electrical signal. The two parts are separated from each other with a transparent glass window (see Fig. 4.1). The glass window is attached tight and secure to the first part as it forms also one of the walls of the liquid scintillator container.

Since the scintillator liquid is chemically poisonous and has relatively low flash point temperature (about 26°C), it should be handled with care. Therefore, the first part of the detector should be sealed well to avoid any liquid leak. There should be an extra room for excess liquid taking into account the expansion of volume in case of temperature increase. This part is so called the expansion chamber and it contains also *backup* liquid in order to fill back up the detector container in case the temperature decreases to avoid creating bubbles. The air bubbles are not desired since they make light to disperse, reducing the amount of light arriving to the cathode layer of PMT. It is also important to assure not to create air bubbles during the filling of the detector. The inner walls of the container should be painted with a special paint that is dispersive following a Poisson distribution which helps the light to avoid absorption but also produces a more uniform response of the detector.

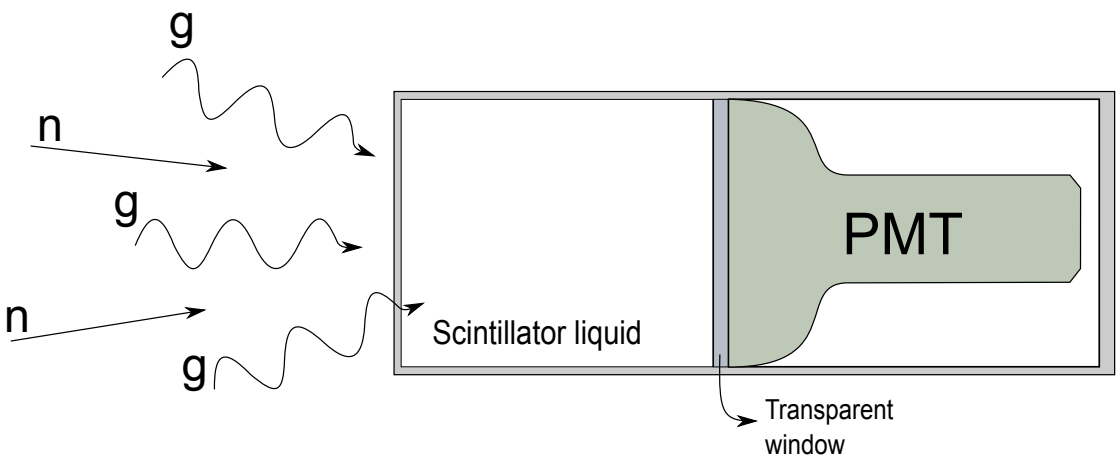

FIGURE 4.1: An artistic view of the scintillator detector prototypes used in the NEDA tests. See text for details.

The neutron detection efficiency of a detector depends strongly on the liquid scintillator volume. The efficiency of a proton recoil based detector, e.g. the liquid scintillator, is defined as in Eq. 4.1:

$$\varepsilon = 1 - e^{N\sigma_s d} \tag{4.1}$$

where N is the density of target nuclei, σ_s is the cross section of neutrons and the target nuclei, and d is the distance that the neutron travelled inside the detector [12]. As one can see from the equation above, the efficiency is proportional to the distance d, therefore, the thicker the detector is the more efficient the neutron detected. Nevertheless, the constraint in the thickness of the detector arises from the energy resolution desired due to the difficulties to have a uniform light collection. Another constraint in the detector size is the counting rate due to γ-rays. If the detector is large enough than the time difference between any two consecutive events will be small so that the pulses will superpose, *i.e.* pile-up.

The optical grease should be applied on the surface of the glass window that touches to the PMT. The optical grease is important to fill up the spaces due to the imperfections on both surfaces (i.e. the glass window and the PMT window), maintaining the refraction index compatible, to make the maximum quantity of photons pass through without any reflection and interact with the electrons in the cathode surface of the PMT.

PMT is an electron tube which convert light into electrical signal. It consists of a vacuum tube, a photo-cathode layer, dynodes, and anode. The cathode, dynodes

and anode are connected to a small circuit - a voltage divider, which basically distributes the high voltage to the dynodes providing the necessary voltage difference to accelerate the electrons. The released electron from the cathode by a photon coming from the scintillator, is accelerated through the applied electric field and hits to first dynode. When an electron hits, it transfers some of its energy to the electrons in the dynode. Secondary electrons will be emitted and accelerated towards the next dynode, where upon strike, more electrons will be emitted and further accelerated. Finally, this electron cascade will create a sizeable electrical signal at the anode which then can be processed and analysed.

4.2 Signal Processing and Data Acquisition

The electronic signal produced in the detector, requires generally a signal processing and finally a data acquisition. The signal processing may involve as well the application of analog signal treatments to infer the timing, amplitude and even to discriminate the nature of the interacting particles. Finally, the data acquisition (DAQ) system digitizes the processed signals and stores the relevant information in a computer.

The signal processing electronics and DAQ system of the prototype detectors work roughly as the following: The signal is created on the anode of the PMT following the decay time and light amplitude produced in the liquid scintillator.

In the past, the only way to disentangle the γ-ray or neutron nature of the particle interacting, was the on-line analog processing, generally based on the charge comparison or timing processing. With the advent of the sampling fast analog-to-digital converters (FADCs), it is possible to store the signal pulses provided by the detector, allowing to perform off-line PSA based on digital signal processing. The former has been used for n-γ discrimination in many detector systems, like the Neutron Wall. The latter is planned to be used in new detector systems, like NEDA.

As an example of analog signal processing like the Neutron Wall, there are several modules to process the signal. Not every signal that comes from the detector carries information on the nature of the detected radiation. There is low amplitude noise along with "real" signal that needed to be discriminated. This is done by a module called *constant fraction discriminator* (CFD). CFD discriminates analog

signals that have an amplitude larger than the determined threshold producing logic signals. CFD also suppresses the time walk present in threshold discriminators when working with signals of different amplitude. Thus they also provide a time reference independent on the amplitude and mostly the shape of the signal. The BARTEK NDE 202 module [37] that has been especially designed for the Neutron Wall has the PSA capability alongside with the CFD capability. Therefore, the PSA output is sent directly to an *analog-to-digital converter* (ADC) module to be to be recorded and undergo the off-line data analysis on the computer based system. The CFD output is sent to *time-to-amplitude converter* (TAC) module to measure the arrival time of the signal with respect to a reference. This module allows to produce a spectrum of the time difference between its inputs *start* and *stop*. As mentioned in Chapter 2, the neutron-γ discrimination process involves as well the ToF measurement. For the determination of the ToF, the measurement of time of the events in the neutron detector with respect to another fast detector, preferably a BaF_2, is crucial. The time difference between the events in the neutron detector and in BaF_2 is converted in pulses and directed to the ADC's (see Fig. 4.2). In digital signal processing, the signals from the detectors are directed to the ADC's.

The signals are digitized by sampling ADC / FADC and the data are transferred to computers. The data are stored and further samples processing can be performed off-line in a computer.

An example for a DAQ system for digital and analog signal processing that has been used in NEDA prototype tests at LNL can be seen in Fig. 4.2. These tests will be explained in the next section with more detail.

4.2.1 Triggering

In nuclear physics experiments, a particular reaction or some events, which occur in the same reaction with a number of competing channels, should be selected. In order to select specific events, one requests a criteria which identifies, e.g. a reaction, depending on the discrimination capabilities of the detector setup. Events that satisfy the criteria activate other systems, for instance the data recording on the disks. The electronic logic to select events under certain criteria is called *trigger*.

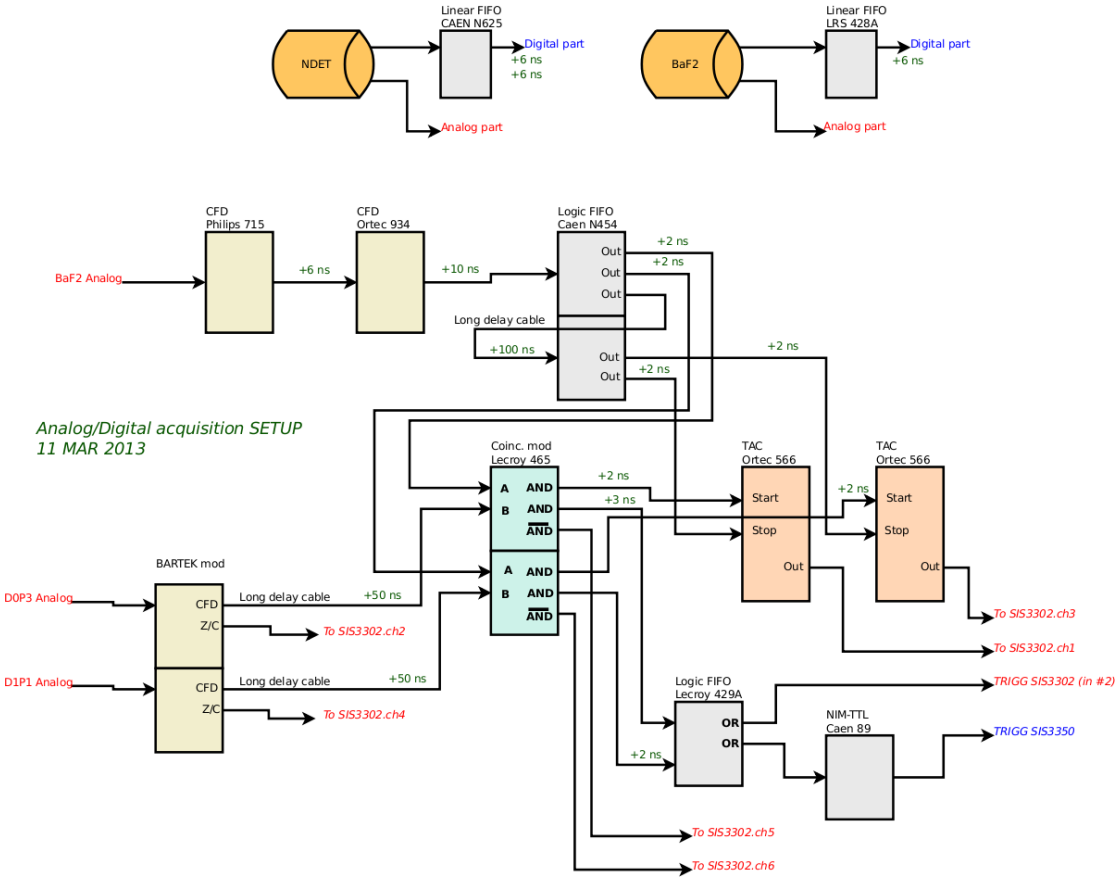

FIGURE 4.2: Electronic scheme of the data acquisition system for a typical neutron-γ coincidence setup. This setup has been used for the NEDA tests performed at LNL.

In the test bench we are describing the trigger condition was the coincidence between a γ and a neutron signal. In order to fulfill this condition, any signal received from the fast detector BaF_2 is accepted after CFD with any signal from the CFD of any of the neutron detectors. Therefore, there are two type of coincidence events recorded: one is γ-γ and the other is γ-n, from the BaF_2 and the neutron detectors.

4.3 Neutron Cross-talk measurements

The concept and the consequences of the neutron cross-talk have been discussed in detail in Chapter 3. In this section, the evaluation of the neutron cross-talk of the prototype detectors will be presented. Since the detection of the neutrons is highly dependent on the scattering reactions inside the detector it is important to know the neutron cross-talk characteristics as a parameter to choose the best

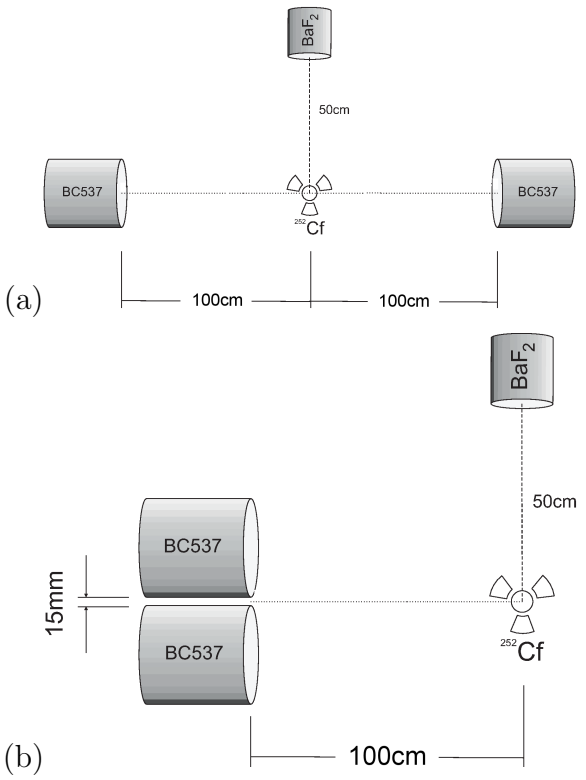

FIGURE 4.3: Drawing of the setup that is used for the cross-talk measurement: upper panel- 2n multiplicity background with the cross talk events; below panel - 2n multiplicity background.

suited liquid scintillator for NEDA. In order to find out the neutron cross-talk characteristics of the prototype detectors, a two-step measurement has been realized. The measurement lies on a simple idea in which the subtraction of two TOF spectra, one from the *real* events and the other from the *real + cross-talk* events. The first spectrum has been acquired placing the two neutron detectors where they face each other.

The source has been located at the half way of the distance between the two detectors, so the solid angle will be the same for both. In this way, only any two coincident neutrons that are emitted with 180^o to each other will be recorded by two detectors, and there will be almost no cross-talk event since back scattering of a neutron from one detector to the other is less probable due to very small solid angle (see Fig. 4.3 - upper panel). The second has been obtained by placing the detectors next to each other at equal distance to the source (see Fig. 4.3 - below panel).

The TOF spectra measured in the two mentioned setups are compared (see Fig. 4.4). Since the detector-to-source distance is large enough, a good separation in

flight times of fast neutrons and γ-rays is expected. A ToF spectrum of γ-rays with common start will produce *ideally* a delta function. This is because γ-rays will arrive to both BaF_2 and the neutron detectors with very small time difference and due the trigger condition selected. Nevertheless, due to the inevitable imperfections on the detection system, the shape of the γ-γ coincidence peak will have a normal distribution. On the other hand, the neutrons will arrive to the NEDA prototypes well delayed with respect to the γ-rays arrive to the BaF_2. Since the neutron time-of-flight depends on its energy which varies between 0 MeV to 20 MeV with a distribution that is studied in Ref. [36], the ToF spectrum of the neutrons will have a form that will follow the velocity distribution rather than a normal distribution.

The experimental results suggest 15.51% neutron cross-talk events over the number of detected neutrons. In order to evaluate better this result, the Monte-Carlo simulations of the cross-talk tests have been done. The cylindrical prototypes are created in the GEANT4 environment with 127 mm diameter and 127 mm depth. The volume material is chosen as the liquid scintillator.

The neutrons were emitted in 4π s.r. solid angle with isotropic distribution. Therefore, the experimental conditions were kept realistic as much as possible in the simulations, except the background radiation, the scatterings of neutrons and γ-rays due to the walls and table which were present during the measurements. The γ-rays emitted from a ^{252}Cf source were also not simulated.

The simulation results were analyzed with 2n multiplicity assumption in the emitter. The cross-talk neutrons are determined as in the similar way the test bench, i.e. the ToF spectrum of the configuration that the detectors stand separate from each other was subtracted from the ToF spectrum of the configuration that the detectors stand next to each other. The probability of the detection of the neutrons in both detectors with only one neutron emitted, was found to be 15.58% over all detected neutrons in the simulations. The simulation results are in very good agreement with the experimental results and also agree with the neutron cross-talk probability in the Neutron Wall, in which the similar detector units are used [35].

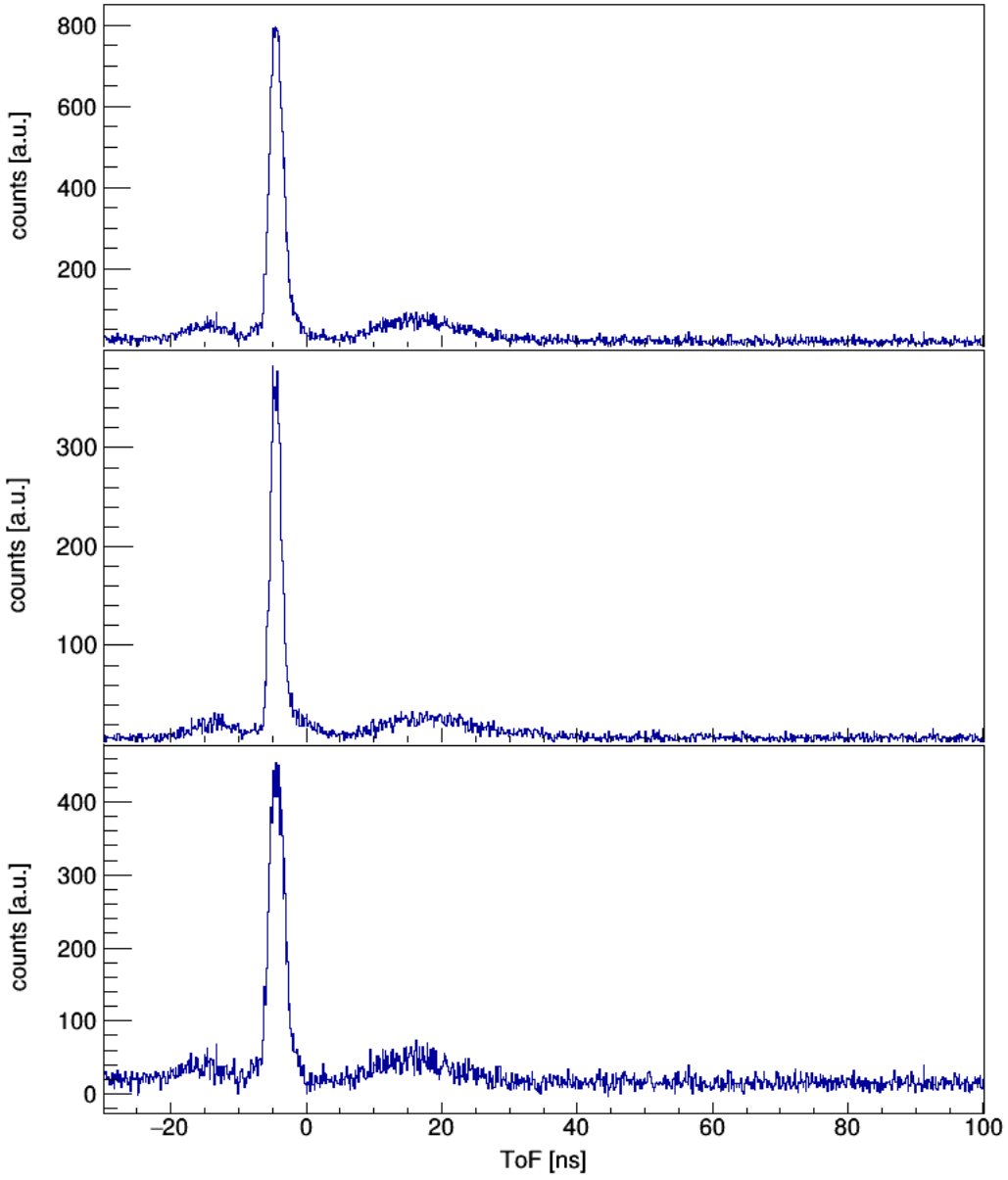

FIGURE 4.4: Experimental results of the cross-talk tests. Upper panel: data obtained where the detectors put aside (left panel of Fig. 4.3); middle panel: data obtained where the detectors put separate (right panel of Fig. 4.3); lower panel: the subtraction of the two spectra. The spectra have been obtained with the condition where both detectors are fired.

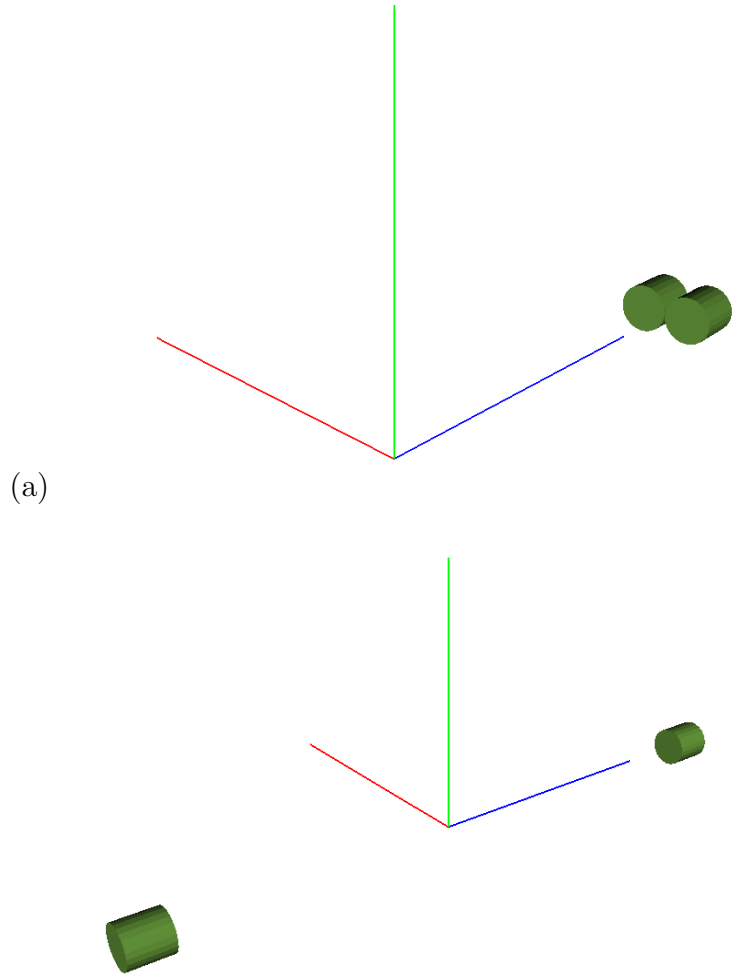

FIGURE 4.5: GEANT4 visualization of the setup that is used for the cross-talk measurement in the simulations: left panel- 2n multiplicity background with the cross talk events; right panel - 2n multiplicity background.

Chapter 5

γ-ray Spectroscopy with Segmented HPGe detectors and Ancillaries

5.1 Segmented HPGe detectors

5.1.1 Introduction

In the last decades, the γ-ray spectroscopy using Ge detector arrays has become an essential tool in experimental nuclear structure studies. They are an improvement with respect to the scintillator based detectors due to the high energy resolution, i.e. frequently less than 2 or 3 ‰ in a detector in good conditions. Despite the fact that detector volumes are limited, the peak-to-total ratio (P/T) is improved by using veto detectors (anti-Compton shields) [38–41] or by tracking techniques in position sensitive [42, and references therein] segmented Ge arrays. Efficiency of the detectors can also be improved using composite detectors [42].

The advent of the new generation radioactive ion beam (RIB) facilities will open new chances the investigation of the regions that are far from the β-stability. These facilities will provide heavy ions with large intensities and large energies, thus extending our knowledge to more exotic nuclei. Nevertheless, the production decreases as the the nuclei of interest become more exotic, the investigation of such nuclei will be more challenging and brings the necessity to have efficient and

sensitive detectors. The γ-ray detectors should provide high detection efficiency and high peak-to-total ratio (P/T). New detectors are being built to respond these needs based on pulse shape analysis (PSA) and tracking, covering 4π s.r. solid angle with high granularity. The escape suppression methods [38–41] will no longer be needed thanks to these techniques and the geometric efficiency of the high purity Ge (HPGe) will be as large as 80% [1].

The use of segmented Ge crystals make possible the identification of the position and deposited (released) energy of each interaction point of the γ-rays. Such segmented Ge crystals require digital sampling electronics to disentangle the energy, position and time information out of the detector's signal using PSA methods.

In this chapter, two of the widely known segmented and high purity Ge arrays in Europe are going to be introduced namely EXOGAM and AGATA. These arrays were used also in the experiments discussed in this thesis. Therefore, it is worth to discuss their design, status and performance figures.

5.1.2 Advanced GAmma Tracking Array (AGATA)

AGATA is a highly segmented, encapsulated coaxial n-type high purity Ge crystal array with PSA and tracking capabilities that has been developed in participation of 13 European countries and more than 40 institutes.

AGATA is designed to be a close-packet array which consists of 180 crystals when it is completed (see Fig. 5.1). The crystals are grouped in three to form clusters (AGATA triple cluster - ATC) and each cluster is cooled down by one cryostat. The geometry has been decided by extensive Monte-Carlo simulations among other configurations [47] optimizing the performance on new generation in-flight facilities for RIB, like FAIR [43]. The inner radius of the AGATA shell is 225 mm and the outer radius is 315 mm. Therefore, one AGATA crystal length is measured 90 mm. The geometry was optimized to minimize the solid angle not covered by detector and to maximize the overall detection efficiency. The performance figures of AGATA were determined for 1 MeV γ-rays in Monte-Carlo simulations and listed in Table 5.1.

Each AGATA crystal is divided in thirty six segments. The segmentation is done in azimuthal and longitudinal axes (see Fig. 5.2). With such detector geometry

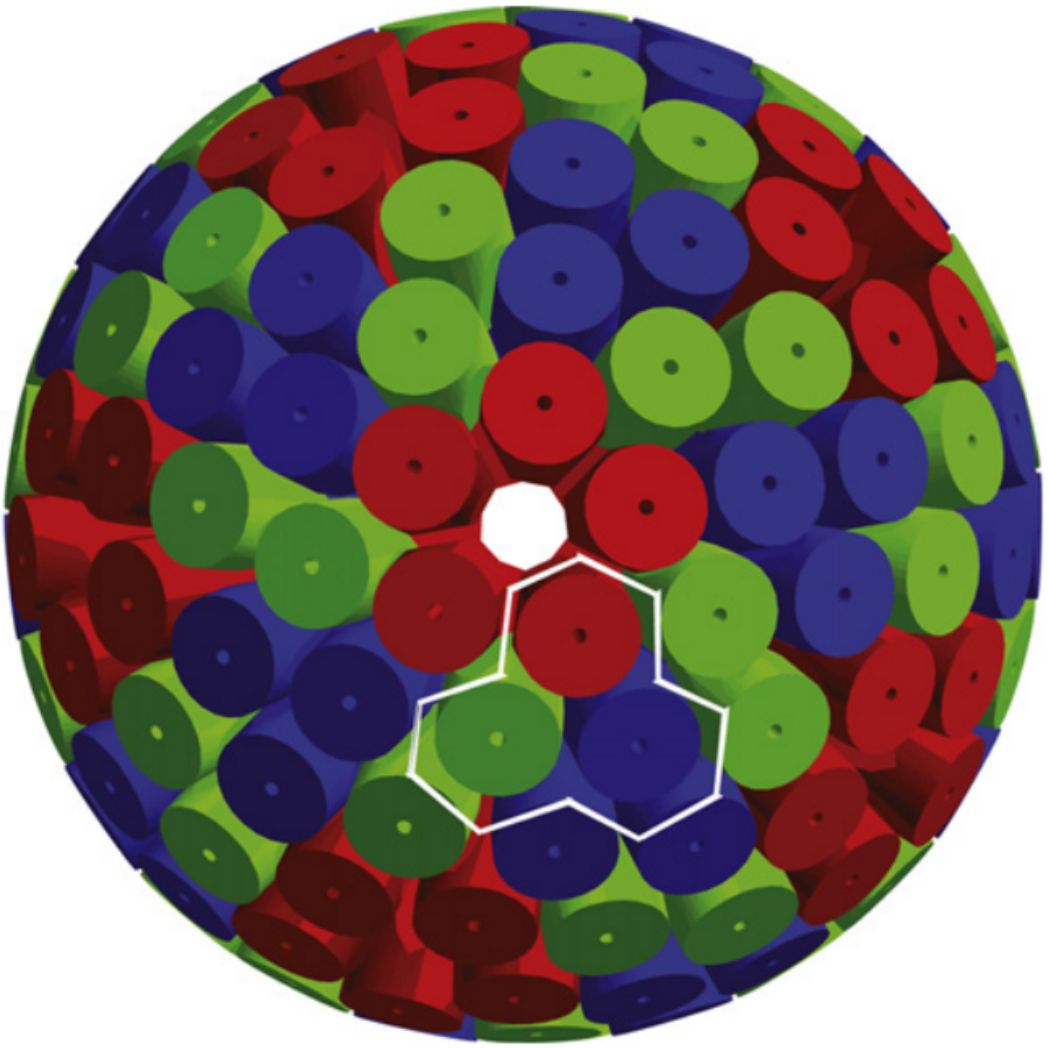

FIGURE 5.1: The figure of the AGATA 4π s.r. geometry generated in GEANT4 simulations. The white polygon represents how three crystals form a triple cluster.

and segmentation, the PSA provides nowadays a position resolution below 5 mm FWHM [44].

Each AGATA crystal has a readout of 38 channels. The 36 channels are allocated to the 36 segments and the remaining channels are allocated to the central contact. The central contact is also known as the core signal and corresponds to the total energy deposited in each crystal. Thus, the ATC detector contains 114 spectroscopy channels. The signals from the channels are amplified by the core preamplifier. The preamplifier has low noise with large range of energy detection, important characteristics for good timing properties and for PSA, and high

TABLE 5.1: AGATA performance figures determined in Monte-Carlo simulations [1].

Performance Figure	**Value**	**γ-ray multiplicity**
Solid angle	82%	N/A
Full energy efficiency	43%	1
	28%	30
P/T ratio	59%	1
	43%	30

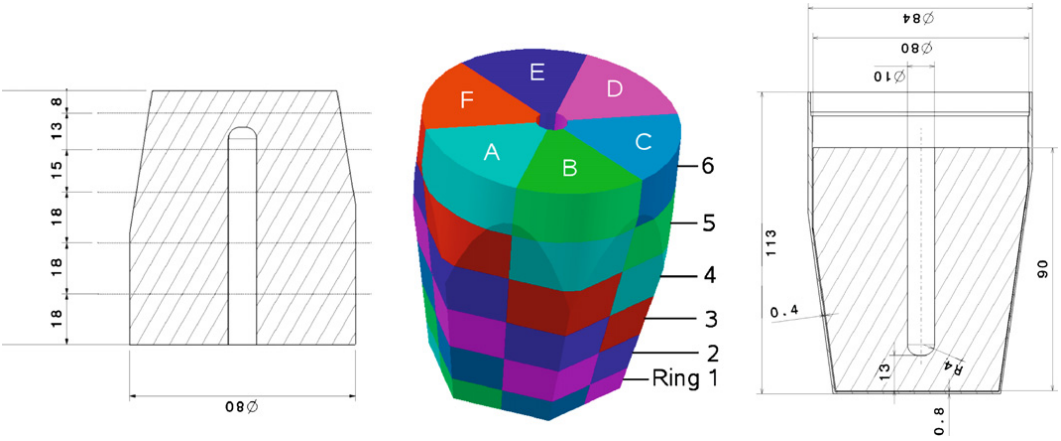

FIGURE 5.2: Drawing of one AGATA crystal showing the segmentation in two axes, the crystal cross-section and the dimensions (figure taken from ref. [1]).

counting rate capability. The preamplifiers have been developed by the AGATA collaboration to fulfill these requirements [48–50].

The pre-amplified signals then pass through the flash digitizers which were built specially for AGATA [1]. The signals are digitized at a rate of 100 MHz and a resolution of 14 bits while the effective number of bits (ENOB) is 12.2. The AGATA digitzer serializes the ADC data using FPGAs and transmits them through optical fibre cables to the pre-processing electronics, implementing digital CFD, Moving Window Deconvolution, compression, etc. algorithms. The AGATA digitzer has a synchronization feature which is done with a signal from the Global Trigger and Synchronizaton system of AGATA (GTS) [1].

The sampled signals are then transferred to the pre-processing electronics that reduces the data by a factor of 100. This reduction is due to the selection of samples from detectors with real signals discriminated by a signal threshold, as well as by limiting the length of the samples to be transferred to the acquisition system to about 1 μs (i.e. 100 samples). The triggering can be done optionally -nevertheless it is necessary in most experiments due to the high counting rate- within the

GTS from which a clock for the digitizer and the timestamp are derived. If the data reduction is not needed, then the system can work on the trigger-less mode. In this case, the data are sent directly to the PSA farm and an offline selection can be applied later. The maximum delay that the pre-processing electronics should provide is limited by specifications to 20 μs. This is the time that the pre-processing hardware waits for the trigger decision.

There are two triggering mechanisms in AGATA pre-processing: local and global. The local trigger checks if there is pulse in the core signal. If it finds pulse then it generates a local trigger request which makes all segment electronics to save to a buffer the trace from the data stream. Traces are held in each channel's local memory for a maximum of 20 μs while the GTS makes a decision. In case the event is validated by the trigger processor, the traces of the segment and core are stored and sent to the PSA farm.

The pre-processing electronics also implements the moving window deconvolution (MWD) algorithm [45] on the incoming data to extract the γ-ray energy in each segment and the cores. After the local trigger detects a signal in the segments or in the core data, by using the response function of the pre-amplifier, the MWD algorithm reconstructs the deposited charge. Once the MWD algorithm is applied, the signal amplitude, that is proportional to the energy deposited, is stored and sent together with the samples.

The GTS system and the data analysis have been explained in Chapter 7. In that chapter, also the merging of the data with the ancillary detectors at GSI has been explained.

The first five AGATA triple clusters were ready and AGATA became operative in 2009 at INFN-LNL. This configuration, so called the AGATA demonstrator (see Fig. 5.3), has been operative between 2009 and 2011, coupled to PRISMA mass spectrometer and DANTE reaction product detectors, leading to significant results (see the web page of the AGATA collaboration - https://www.agata.org/).

Afterwards, it has been moved to GSI in 2012 to be coupled with the Pre-SPEC setup, to be used with the Fragment Separator facility until 2014 (see description of the PreSPEC setup in Chapter 7).

The AGATA configuration used at GSI has significantly been modified with respect to the previously used at INFN-LNL due to the large diameter of the beam pipe.

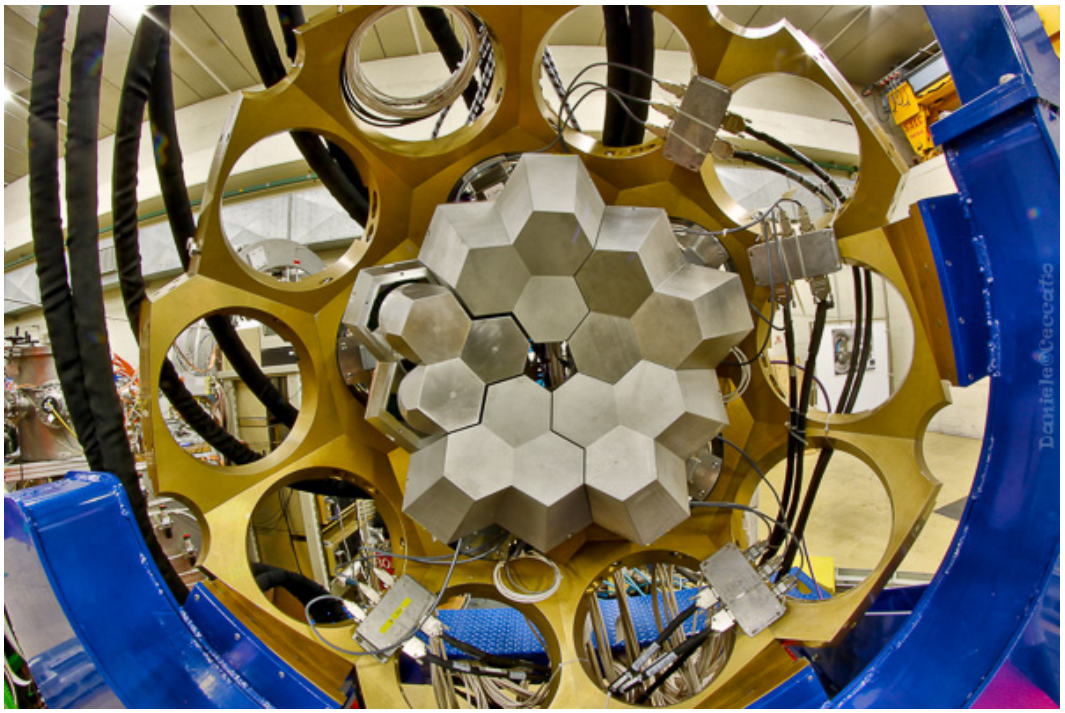

FIGURE 5.3: A view from the AGATA demonstrator at INFN-LNL.

It was necessary to convert three triple clusters into double clusters, removing the RED (A) type capsule at the inner circle to enlarge the gap that allows the beam pipe to be mounted surrounded of encapsulated detectors. Three AGATA double clusters and five AGATA triple clusters were operative during the GSI campaign in 2012, but one of the triple clusters missing one crystal and one of them had one crystal inoperative. Thus, 19 crystals were operative in 2012 and our experimental activity described in Chapter 7 has been performed with such configuration (see Fig. 5.4). The performance figures will be mentioned in this section as we move forward describing the detector's properties. AGATA has moved to GANIL in the second half of 2014. It has been using coupled to VAMOS mass spectrometer and is planning to be coupled with the Neutron Wall - NEDA - DIAMANT detectors starting from 2018. Currently, there are 35 AGATA channels operative at GANIL.

5.1.2.1 PSA techniques

The tracking arrays and in particular AGATA, functionality requires the reconstruction of the trajectories of the γ-rays detected inside the array. In order to reconstruct the trajectories, one needs the accurate position, time and energy information of each scattering point of the γ-rays. This is done by the analysis of

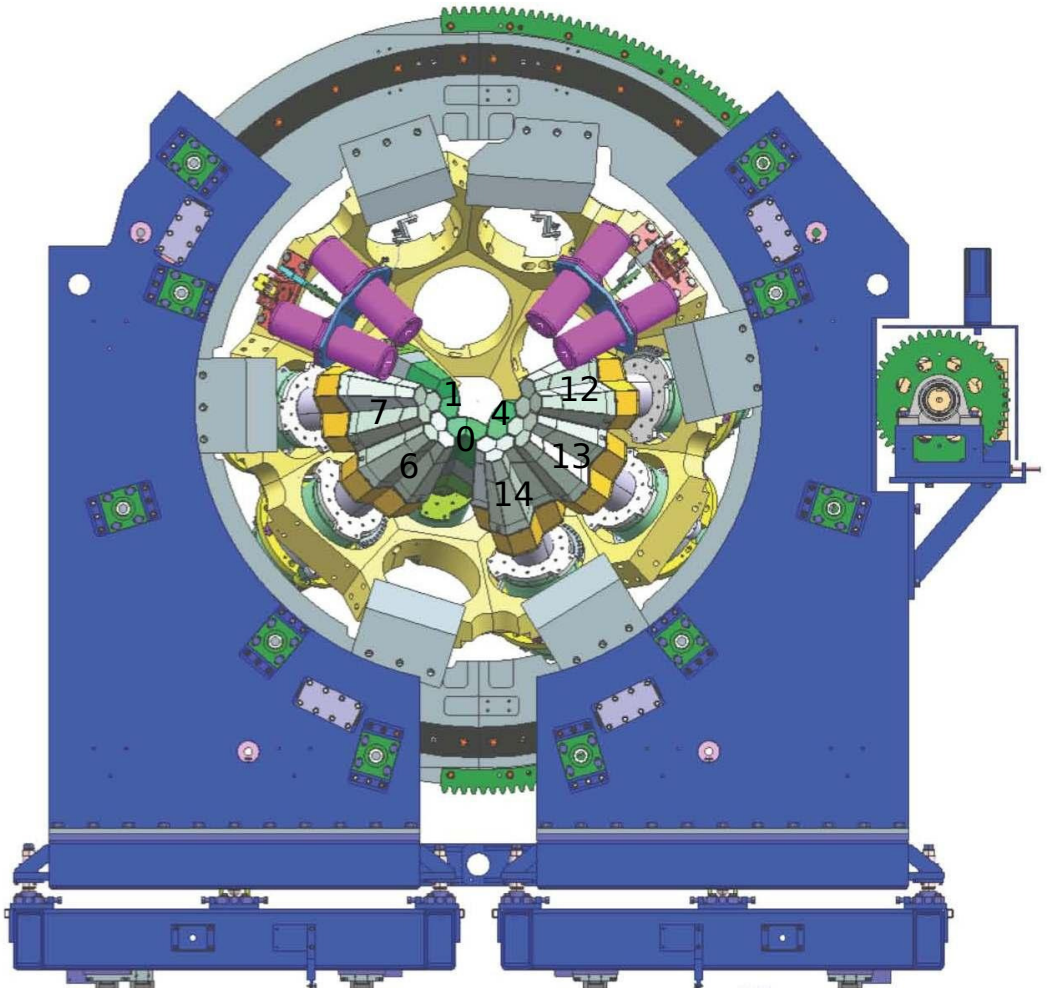

FIGURE 5.4: CAD drawing of AGATA and the holding structure at GSI. Clusters numbered 0, 1 and 4 are the double clusters. Clusters numbered 6, 7, 12, 13 and 14 are the triple clusters. Two crystals, one from each cluster 7 and 6, were inoperative.

the signal shapes for the segments with a net charge as well as the neighboring ones with mirror signals in each AGATA crystal, i.e. Pulse Shape Analysis.

A γ-ray would normally have sequential interactions in a Ge array until it exhaust all the energy in subsequent interactions or escapes finally from the detector material. The path of a γ-ray can be limited in a single crystal or it can scatter from one crystal to another. It is important to locate the interaction points with the best accuracy possible to reconstruct the path of the γ-ray inside the array. The algorithm to determine the position and energy of the γ-ray needs to be fast enough to be applied in real time for the online data processing. Data from the samples are reduced by PSA to few parameters of interest. To do that, the PSA

algorithm compares the real pulse, for the charge as well as for the signals induced in the neighbor contacts, to the references which presently are calculated by simulations.

There are several PSA algorithms that have been developed, such as, grid search [51, 52], genetic algorithms[53], wavelet decomposition and a matrix method [54]. In this thesis, only the grid search algorithm will be mentioned, since it was used during the online data processing, *i.e.* adaptive grid search and the offline data processing, *i.e.* the full grid search. The comparison of the measured and calculated signals is done by the interpretation of their residuals [51]. The residual is defined as the sum of square of signal differences over sampled times (i) and segments (j - see Eq. 5.1).

$$R = \sum_{ij} \left(S_{ij}^{m} - S_{ij}^{c}\right)^2 \tag{5.1}$$

The grid search evaluates the $R_{r\phi z}$ in a cylindrical volume defined by $r\phi z$ coordinates [51]. The full grid search algorithm evaluates the all points in the segment, i.e. considering the unit volume as the real segment. The adaptive grid search makes a two step evaluation: first the R values in a wider grid is searched. The smaller R defines a unit volume, i.e. a voxel, and in the second step, this voxel is searched with a full grid search, making the algorithm works more efficient.

The optimum grid size of the coarse grid is chosen 8 mm, which is obtained by the comparison with the full PSA. The advantage of the adaptive grid search algorithm is due to the fact that it is faster and more accurate than the genetic algorithm [1]. Therefore, the short processing time makes the adaptive grid search favorable to use it for the online data processing.

5.1.2.2 GRID computing

The AGATA collaboration has adopted GRID as final storage and backup for the data. Moreover, GRID computing [56] provides as well a good platform. The idea behind GRID computing is the use of hundreds of processing units (CPUs) and data storage elements in parallel to process large amount of data in shorter time. The AGATA collaboration has its storage elements in the Bologna and Strasbourg sites. The processing units are available in the Valencia and Strasbourg sites. The

data are directly transferred to the GRID storage elements and are accessible to perform replay from any institute with GRID access.

A test has been done to compare how the GRID processing and a normal computer processing in terms of data replay time. A data set of the ^{60}Co calibration data with the acquisition time of 14 hours is replayed on an Intel Xeon CPU E5-2630 v4 2.20 GHz computer and on GRID. The data replay on the Intel computer has been done using the adaptive grid search algorithm in 120 hours. On the other hand, the data replay using the full grid search algorithm has been done in 3 hours on the GRID computing system.

5.1.2.3 Tracking

The tracking algorithm reconstructs the γ-ray trajectory and energy deposited inside the array by using the interaction points and energy releases determined by the PSA algorithm. There are few algorithms that could be used for AGATA that can be grouped in two, as the forward and the backward tracking. The code used to analyze the experimental data in this work, MGT, uses the forward tracking technique. The tracking of the low energy γ-rays (i.e. of the order of hundred keV) is frequently not possible, since the main detection mechanism is the photoelectric absorption (see Fig. 5.5). The γ-rays that are energetic of order of 1 MeV are

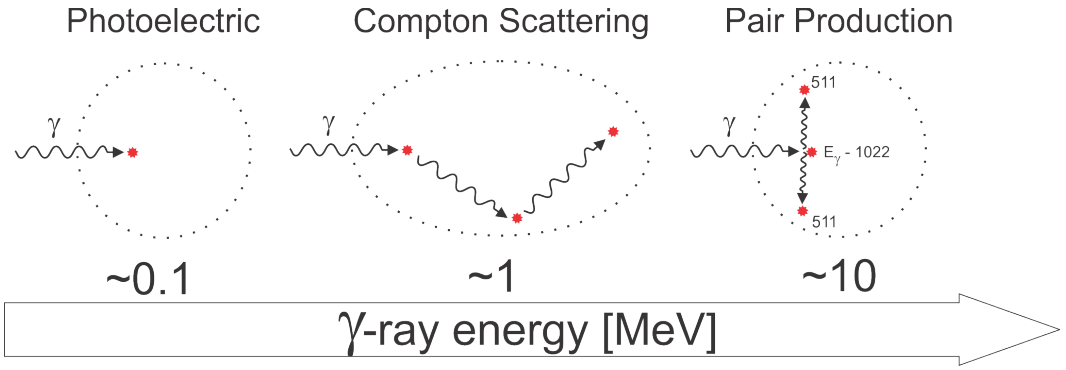

FIGURE 5.5: The most probable γ-ray detection mechanisms at different ranges of E_γ. See text for details.

more likely to lose energy by Compton scattering before they either escape the array or or the secondary γ-ray of the Compton process has low energy and suffers photoelectric absorption. In this case, the γ-ray trajectories are reconstructed using χ^2 minimization process with a figure of merit as indicator of how well the scattering angles from the interaction positions fit in to the Compton formula.

In forward tracking, the γ-ray reconstruction is done by determining the first interaction point with an educated guess provided from the ancillary detectors, i.e. the trajectory of the ion emitting γs or in the case of conventional experiments, by the position of the beam in the target. The probability of pair production for the γ-rays that are as energetic as 8 MeV is considerably high (see Fig. 12.17 in Ref. [12]). Therefore, the γ-rays with several MeVs are more likely to be detected with in a single interaction with the energy of the $E_\gamma - 2m_e c^2$ which is the energy needed to create the e^- - e^+ pair. The two photons produced in the annihilation of the e^+ with an e^- of the medium are then detected in the vicinity of the first interaction point creating their own clusters [55].

The tracking efficiency is determined by the ratio of the full energy peak efficiency of the array in calorimetric mode and the efficiency determined using the tracking algorithm. The most convenient way to determine the tracking efficiency is the use of the ^{60}Co data, as the calculation of the efficiency of the calorimetric mode is easier. The tracking efficiency with the present version of the algorithms and with an AGATA sub-array of about 19 capsules has been found to be between 72 to 75%.

The absolute detection efficiency of the array in close geometry (i.e. with the array closer to the target by 14 cm in the central axis) has been found to be 4.26% for 1 MeV γ-rays from the calibration data of the experiment discussed in Chapter 7.

5.1.3 EXOGAM

EXOGAM is a European collaboration project which built a γ-ray detector array. The EXOGAM array is situated at GANIL and used to perform experiments with beams provided by both the GANIL and SPIRAL facilities. The array consists of segmented Clover detectors [57] and a coverage maximized in 4π s.r. solid angle (see Fig. 5.6-a). Segmentation is important for several performance figures of the detectors, for instance, the energy resolution and minimization of multiple-hits. The detectors are separated by the BGO shields for the Compton suppression. The Compton suppression shields help to reduce the background events and increase the Peak-to-Total (P/T) ratio. The P/T ratio obtained for the full EXOGAM in experimental conditions is of 47% [59]. The Ge crystals forming the Clover detector are cylindrical from the backward, but tapered to have almost a square shape from the front surface (see Fig. 5.7). The clover detectors have 60 mm of diameter and

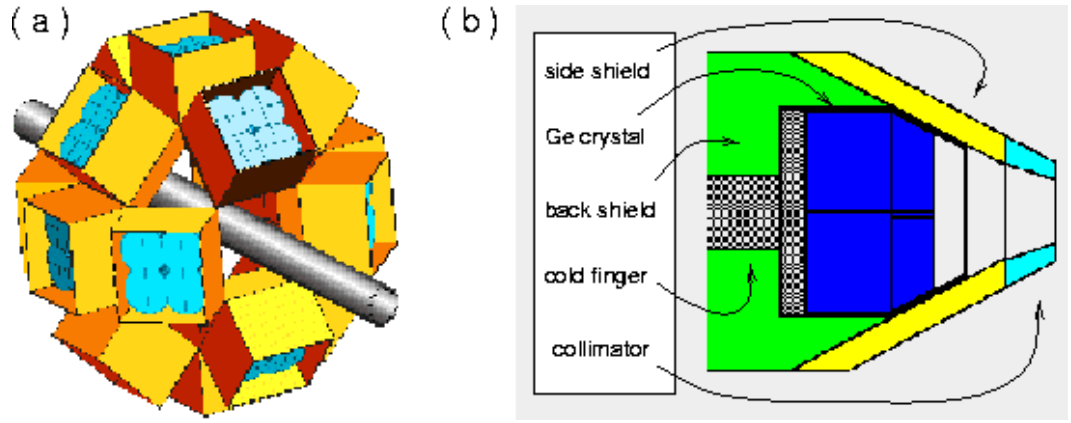

FIGURE 5.6: (a) The EXOGAM array with 16 clover detectors. (b) The cross-section of the clover detectors.

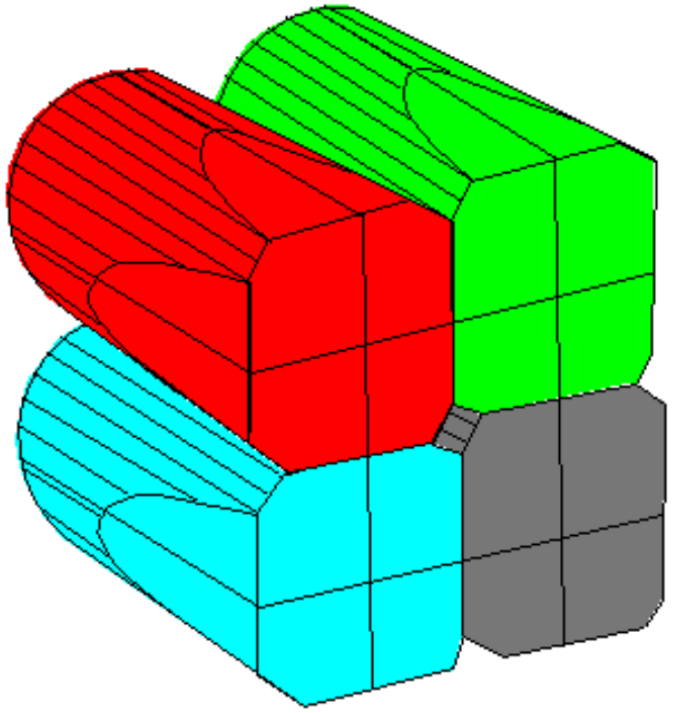

FIGURE 5.7: A drawing of the clover detectors.

90 mm of length before the tapering process. The efficiency is increased when the signals from the adjacent segments, produced during the scattering process of the γ-ray, are added, i.e. addback. The photopeak efficiency at 1.3 MeV. for the complete EXOGAM array is estimated to be 20% for γ-ray multiplicity = 1 in the close configuration geometry. The four Clover detectors placed downstream in the beam line haven't been mounted during the experiment discussed in Chapter 6. This is due to the coupling of EXOGAM with the Neutron Wall and was necessary

in order to give space to the neutron detector array. Nevertheless, the absolute efficiency of EXOGAM in the configuration coupled with the Neutron Wall and DIAMANT was estimated to be more than 10%.

The segmented crystals also help to obtain better resolution in case of the Doppler broadening. This becomes important when the ions emitting γ-rays travel with velocities are a sizeable fraction of the speed of light. The EXOGAM array is effective particularly since it has 8 clover detectors at $\theta = 90^o$, at which the Doppler broadening reduces significantly.

The EXOGAM detector array uses VXI (VME eXtension for Instrumentation) modules to transfer the data. There are five modules in the EXOGAM system:

- Ge detector cards for center and outer contacts [60]
- Compton suppression cards; six shields per card
- Master Trigger (one card) [61]
- Resource managers (one per crate) [62]

In case of the usage of the ancillary detectors, the following VXI modules could be added:

- ADCs for ancillaries
- Purpose built cards for ancillaries

For EXOGAM the energy signals are amplified and converted with high and low gains allowing the spectra ranges 6 MeV and 20 MeV, respectively. The time parameter is recorded from a TAC which has CFD output of the crystals at START and the beam pulse at STOP inputs. The read-out of energy and time parameters are transferred to the buffer in the crate read-out controller over the VXI back-plane. When all VXI modules finish transferring the data to the buffer, they are ready for acquiring data of the new event. During this cycle, the EXOGAM electronics cannot accept any new event, i.e. the EXOGAM system uses a common-dead-time.

Triggering in the EXOGAM system has two steps. The first step provides good timing for stopping TACs and a quick decision. The second step confirms that if

the event is good and must be read-out, or is bad and must be rejected. Therefore the global trigger signals issued by the master trigger are the Fast Trigger (1^{st} step) and either Validation or Rejection (2^{nd} step). The 2^{nd} level trigger Validation/Rejection processing is programmed in the FPGA of the Trigger Card.

The data acquisition system (DAQ) of EXOGAM is based on MIDAS (Multiple Instance Data Acquisition System) which is developed initially for Eurogam [63]. MIDAS provides GUI on UNIX systems to make possible the user interaction between the VXI, CAMAC and VME modules remotely. All VXI crates have Resource Managers that contain a processor with ethernet interface. The VXI modules have a read-out of 32 bits data bus (DT32) into a VME event builder crate in which the data are formatted to be recorded on the disks. Online data analysis is done with actors running on the workstations that observe the data flow on the network and making histograms.

5.2 Ancillary detectors to the segmented high-purity Ge-arrays

5.2.1 Introduction

In this section, two complementary detectors of interest for us, that have been coupled to the HPGe detectors will be described: The Neutron Wall and DIAMANT. The Neutron Wall is a neutron detector array that has been mentioned earlier in this work. It has been installed at GANIL during the experiment which will be explained in the next Chapter coupled to EXOGAM and DIAMANT detectors. The Neutron Wall is currently situated at INFN-LNL, but is planned to be moved back to GANIL to be coupled with AGATA - NEDA - DIAMANT in 2018. DIAMANT is a light charged particle detector array which consists of CsI scintillator detectors. More details on these two ancillary detectors will be discussed in the next two sections.

5.2.2 The Neutron Wall

The Neutron Wall is a neutron detector array that is mainly used to select and identify very weakly populated reaction channels associated with neutron emission

by efficiently detecting the neutrons from the fusion-evaporation reactions. It is situated at GANIL since 2004 and coupled to EXOGAM γ-array and DIAMANT particle detector. It has been used in many experiments and lead to many exciting discoveries in the Nuclear Structure Physics. The Neutron Wall consists of 15

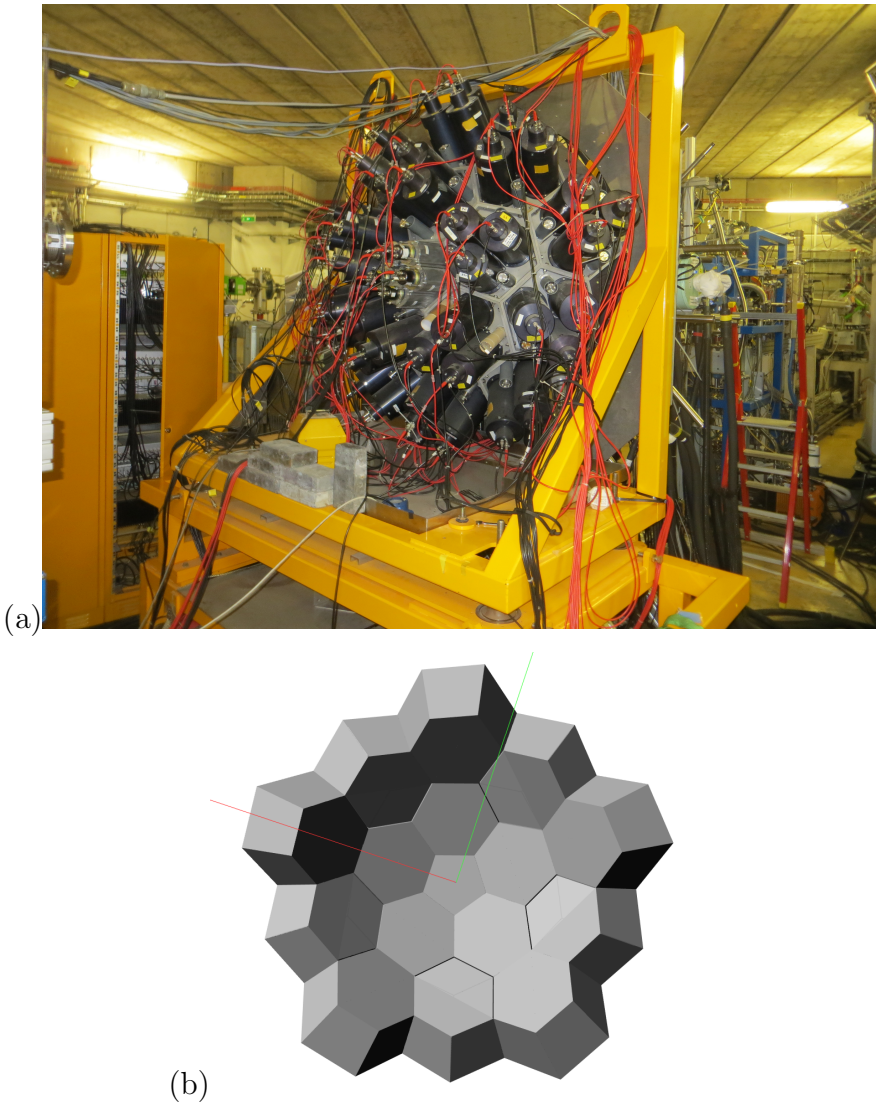

(a)

(b)

FIGURE 5.8: The Neutron Wall array at GANIL, photo of the view from the beam downstream (a) and 3D computer model of the view from the beam upstream (b).

hexagon and 1 pentagon shaped detector blocks and covers 1π s.r. solid angle at 510 mm from the target position to the detector surfaces. In Fig. 5.8, the Neutron Wall could be seen from the beam downstream (Fig. 5.8-a) and the beam upstream (Fig. 5.8-b).

The hexagonal detector blocks are subdivided into 3 detectors and each one containing approximately 3.2 liters of liquid scintillator, while the pentagonal block

is subdivided into 5 detectors and each one containing approximately 1.1 liters of liquid scintillator. Thus the whole array consists of 50 detectors and the total scintillator volume is about 150 liters. The detectors could be seen in Fig. 5.9 where the hexagonal and pentagonal blocks are shown dismounted. The detectors could be noted by the photo-multiplier tubes (PMT) mounted. The detectors of

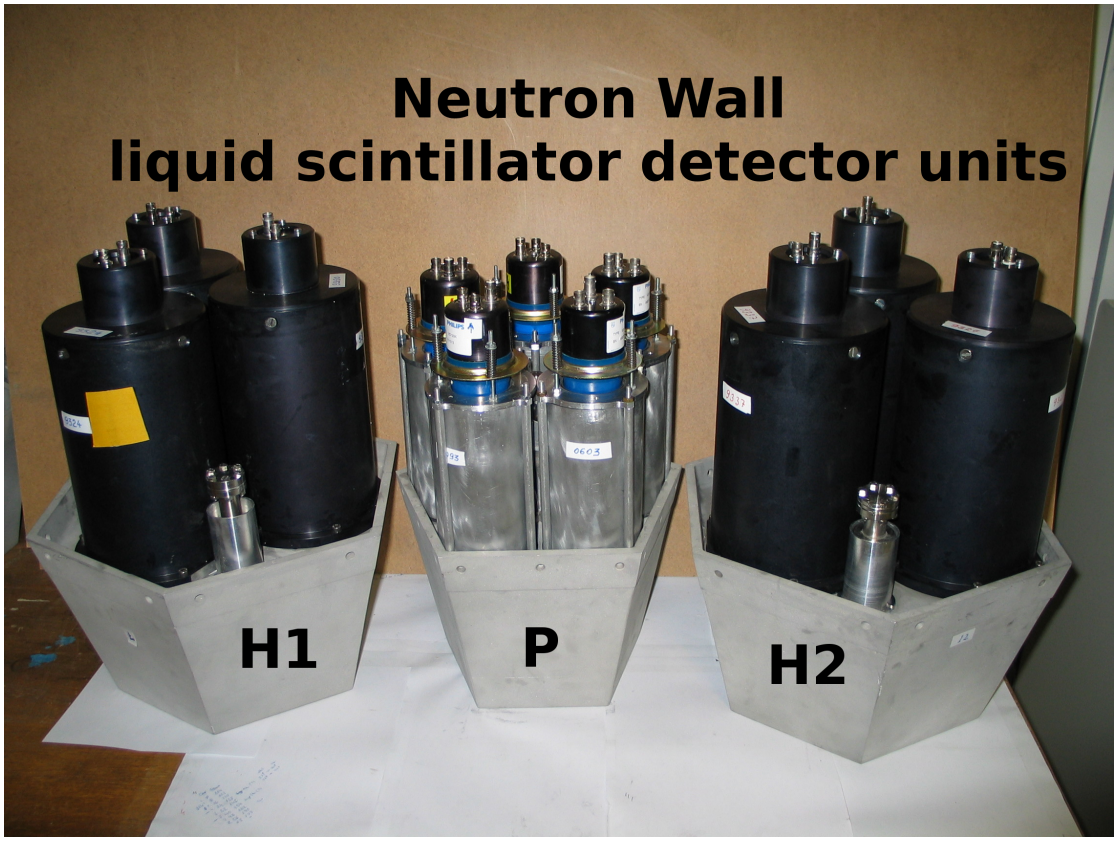

FIGURE 5.9: Hexagonal and pentagonal segments of the Neutron Wall.

the array are filled with the liquid scintillator (BC501A). This scintillator material provides so far the best performance with considerably low cost with respect to the other scintillators. Nevertheless, its properties like chemically poisonous and flammable at 30°C makes it very dangerous and an extra care should be taken while working with it. The detection mechanism of neutrons and the neutron-γ discrimination using liquid scintillator detectors have been discussed in Chapter 2. Especially, the neutron-γ discrimination by PSA and ToF is explained in Sec. 2.4 in the same chapter. It is worth to mention that the PSA is done by an electronic card specially designed for the Neutron Wall, the BARTEK NDE 202 module [37].

5.2.3 DIAMANT

DIAMANT is a light charged particle detector array consists of 3 mm thick 80 CsI(Tl) scintillators, covering 90% of the 4π s.r. solid angle (see Fig. 5.10). The

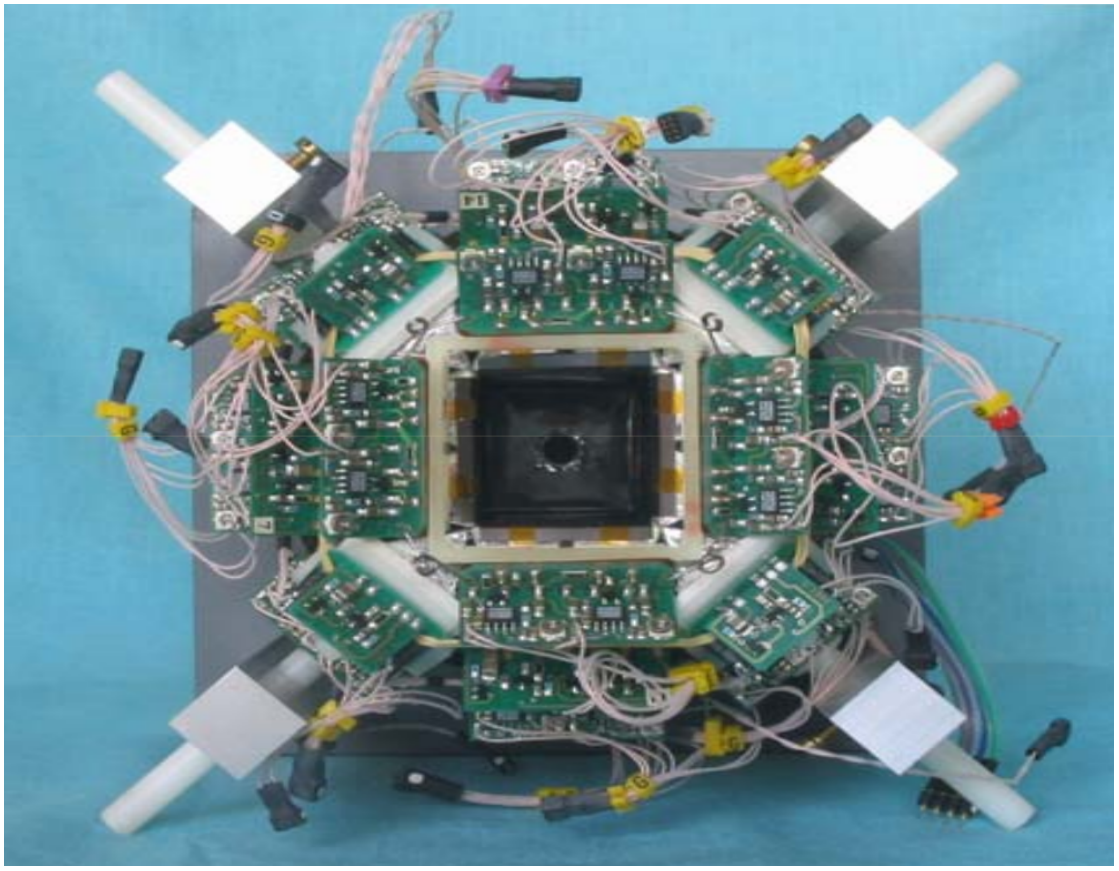

FIGURE 5.10: DIAMANT detector array.

energy resolution is 2% at 5.5 MeV for the α-particles which is insignificant in our application, *i.e.* our experiment described in Chapter 6, since the determination of the existence of a particle is sufficient to disentangle the reaction channels in a compound nucleus decay.

The DIAMANT array is packed in a small volume since it has to fit into the reaction chamber. The reason why DIAMANT is small, is because we need the array to be used inside compact Ge arrays with small detector-to-target distances. The compact design of the DIAMANT array makes impossible to use the photo-multiplier tubes with the scintillators, but photo-diodes are used instead. The depth of one CsI(Tl) scintillator is 3 mm. The scintillators are two types in terms of their shape: square and triangular. The square scintillators have a 14.5 mm

of the edge length and the triangular ones have 29 mm (see Fig. 5.11). The geometrical shape of the array is called *rhombicuboctahedron*.

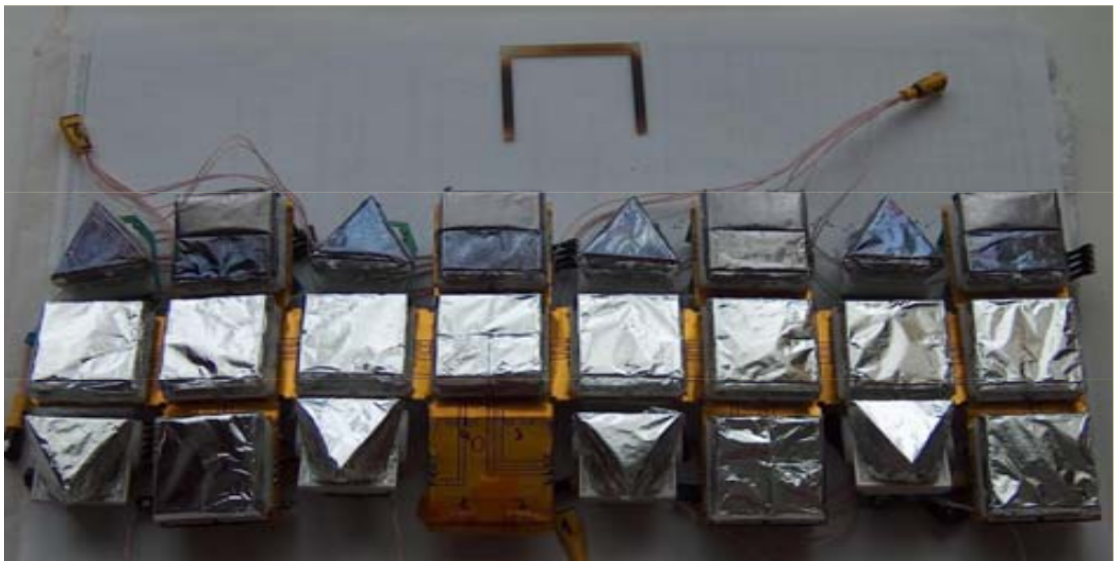

FIGURE 5.11: DIAMANT detector array unrolled. The square and triangular shaped scintillators are shown.

DIAMANT has 70% and 50% efficiency for proton and α-particles, respectively. It can be used either particle veto mode or particle channel selection mode, coupled to large γ-ray detection arrays, like EUROGAM and EXOGAM. Nevertheless, considering such efficiencies for the particle detection, DIAMANT is not a good veto detector. The CsI crystals are covered by a foil, which its material and thickness -e.g. 5 μm Thallium in our experiment described in Chapter 6- depends on the beam material and energy, in order to avoid the damage of the CsI crystals by irradiating with the beam. The particle detection efficiency of the array depends also on the thickness and the material of the protective foil.

The signal processing is done with VXI based electronics. The DIAMANT electronics provide three output parameters: time, particle-type and energy. The energy parameter is read-out after the amplifier and the stretcher by the ADCs. The particle-type parameter is obtained using two pulse shape discrimination techniques: the ballistic deficit method [65–67] and the zero-crossing method [68]. The zero-crossing method is better concerning the α-proton particle discrimination figure-of-merit. The VXI cards are integrated with the Euroball environment. The data syncronization is done thgrough Fast Trigger and Validation generated by Master Trigger. Each CsI channel the Local Trigger checks if the delayed signal is in coincidence with Fast Trigger and, in case, the channels are involved into

particle-γ coincidence. The control of the VXI cards are done through the MIDAS interface, as it is in the EXOGAM case (see Sec. 5.1.3).

Chapter 6

Experimental activity at GANIL with EXOGAM, Neutron Wall and DIAMANT

6.1 Introduction

The experiment has been done at GANIL in 2009, as a part of the EXOGAM - Neutron Wall - DIAMANT campaign. The primary goal of this experiment was to populate nuclei in the vicinity of N=Z in the region of ^{56}Ni. The preferable reaction mechanism -with stable beams and targets- for the population of such nuclei is the Fusion-Evaporation. In this reaction mechanism the accelerated projectile hits on the stationary target. If the impact parameter is sufficiently small, the compound nucleus might be formed and, in case it does not suffer fission, it will follow a de-excitation process. The compound nucleus is in a highly excited state and thus, shortly after the formation -in about 10^{-19} seconds- it will evaporate nucleons and small fragments, as α particles. The particle evaporation is always competing with the γ-ray emission during the cooling process, and when the resulting recoiling product is close or below the threshold for particle emission, the de-excitation will continue by emitting γ-rays till the nucleus reaches the ground state.

As the interest moves to more exotic nuclei in the proton rich side of the Segrè chart, trying to improve the knowledge on the nuclear structure, the accurate determination of the reaction channels became more important. In particular

when the nuclei of interest are populated by Fusion-Evaporation reactions, those involve one or more neutrons. In this context, highly efficient neutron detector arrays, like Neutron wall and in the future NEDA are an effective tool to determine the neutron multiplicity corresponding to a given reaction product. On the other hand, it was mentioned already in Chapter 4 that the Neutron Wall is going to be used together with NEDA in the initial phases of the project, and in the near future AGATA campaign at GANIL with NEDA - Neutron Wall - DIAMANT. The similarities between two neutron detector arrays make the Neutron Wall a unique platform to understand the concept of neutron detection and the data analysis in a real environment on the way to NEDA. Analysis of an experiment in which the Neutron Wall is used has been a useful study of a case where a neutron detector array is involved, in particular considering the work performed on the conceptual design for NEDA.

6.2 Reaction Mechanism

The scattering of a projectile from a target in the framework of nuclear reactions is visualized in Fig. 6.1. The distance between the trajectory of a projectile and the target is called the impact parameter (represented by "b" in Fig. 6.1). Smaller is the impact parameter -compared with the sum of both nuclear radius- higher is the probability that the projectile interacts with the target. In a Fusion-Evaporation reaction both the projectile and target nuclei merge in a intermediate system called the Compound Nucleus (CN). The energy of the reaction will be shared among the nucleons of the new combined system. When the compound nucleus is formed, it *forgets* the previous process, i.e. the fusion of projectile and target. After possible pre-equilibrium phenomena, the CN thermalizes, the energy excess is shared by the CN and in the de-excitation process it will behave as a single system. The CN is unstable and undergoes a series of decays, it first *evaporates* nucleons and/or α-particles then the final, but excited, reaction product nucleus will start to de-excite emitting γ-rays.

The decay probability depends only on the total energy given to the system. The CN decays are governed primarily by statistical rules. Close to the stability, the charged particle (protons and α-particles) evaporation is less probable than the neutron evaporation due to the contribution of the Coulomb barrier. Further the nuclei are on the proton-rich (neutron-deficient) side, the neutron separation

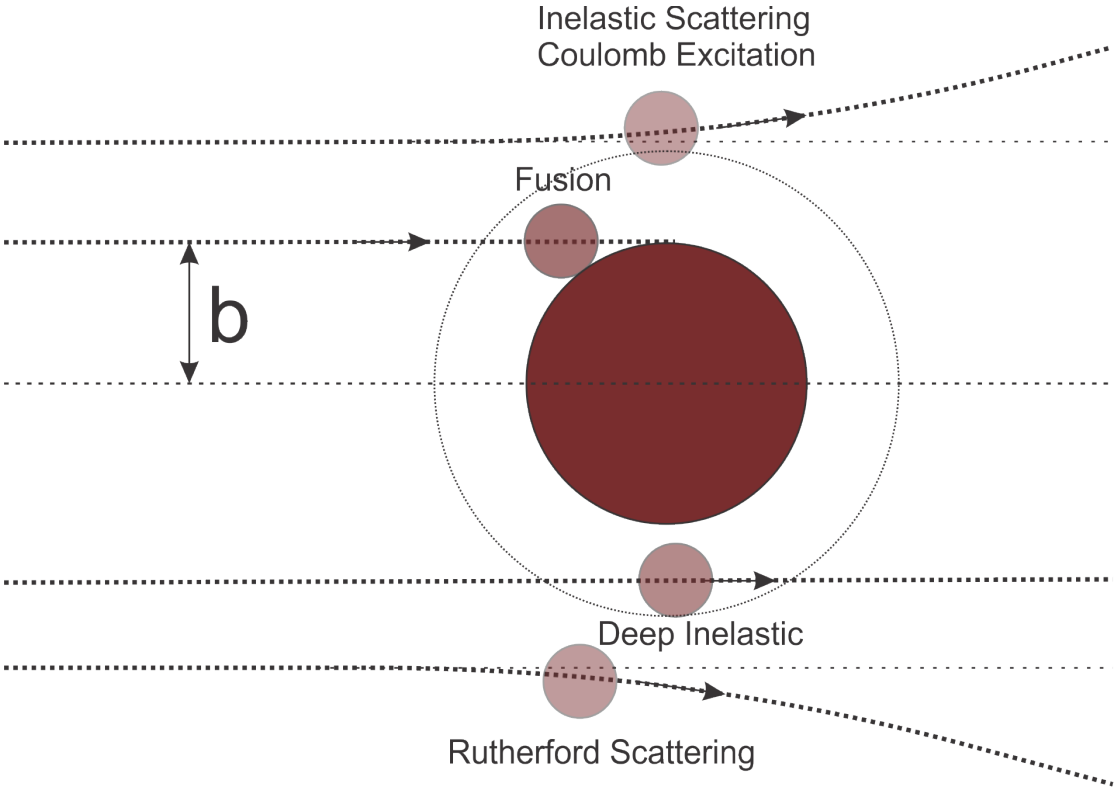

FIGURE 6.1: Two nuclei scattering. The type of reaction depends on the impact parameter, b. In the case of the present work, the impact parameter is small enough that the nuclei interact with each other by the strong force.

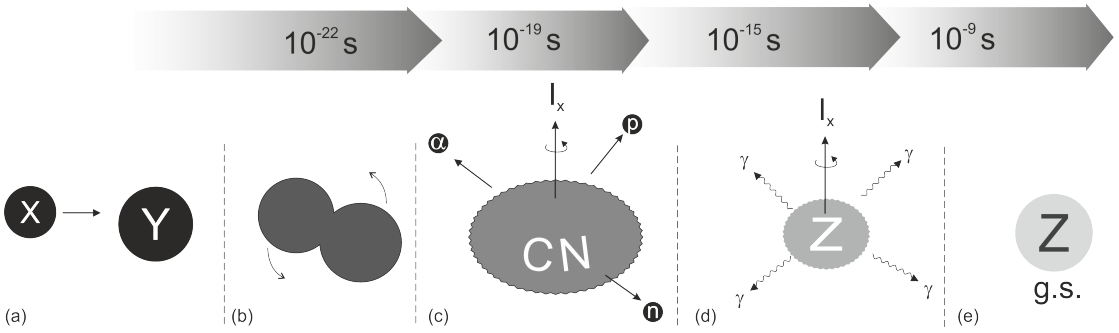

FIGURE 6.2: Visualization of the fusion-evaporation reaction. (a) Two nuclei collide and (b) fuse together. Thermal equilibrium is occured and (c) a compound nucleus is formed. This is an intermediate state and the CN forgets what nuclei formed by. It is highly unstable and undergoes the evaporation of the light particles. Finally, (d) it forms a daughter excited nucleus and suffers γ-ray emission until (e) it reaches to the ground state.

energy increases. The residual nucleus will be even more neutron deficient and then charged particle (mainly proton and alpha particles) evaporation will become competitive. The maximum angular momentum of the residual nucleus is related to the beam energy and to the maximum impact parameter that will allow the formation of the CN at that energy. On average, it is considered that evaporation of a nucleon (proton or neutron) decreases the angular momentum of the compound nucleus by 1 to 2 $\hbar$. Particle evaporation will continue until the excitation energy is below the particle separation energy above the yrast line. Residual nuclei formed after the evaporation of fewer particles will have higher angular momentum. Therefore, a reaction with limited number of evaporated particles -in particular of neutrons- is preferable when the residual nucleus is to be studied at high angular momentum.

6.3 Experiment

The experiment was done at Grand Accélérateur National d'Ions Lourds, Caen, France (GANIL). The ^{32}S beam accelerated at an energy of 79.8 MeV by the Intermediate Energy Heavy Ion cyclotron accelerator CIME impinged a ^{28}Si target with a thickness of 0.5 mg/cm^2 on a 8 mg/cm^2 ^{90}Zr backing.

The evaporated charged particles were detected by DIAMANT (see Sec. 5.2.3) and the neutrons by the Neutron Wall (see Sec. 5.2.2). These detectors were coupled to the γ-ray detector EXOGAM, an array of Clover composite HPGe detectors described in Sec. 5.1.3.

The experiment was performed with two trigger conditions simultaneously, i.e. gamma-neutron coincidence and gamma-gamma coincidence. The two conditions were in "OR". Higher fold in gamma multiplicity in coincidence with the neutrons were not excluded.

The experiment was originally designed to study the structure of the ^{58}Zn nucleus, nevertheless even at an early stage of the experiment it was clear that the results were compromised by the insufficient purity of the primary beam, that was contaminated at the level of 1% with ^{40}Ar -with a charge state that provided the same magnetic rigidity for the same energy-. Nevertheless, the energy of the beam was selected to maximize the relative cross section of the most exotic nuclei possible with such reaction, reducing as much as possible the beam energy to reduce the

channels with several particles evaporated. The cross sections for such channels have been calculated with the Statistical Model code `HIVAP` [69, 70]. As already mentioned in Sec. 6.2, the beam energy is definitive on how many and what type of particles will be evaporated and what will be the final angular momentum of the residual nuclei after the compound nucleus is formed. The Coulomb barrier for such a reaction is calculated as 36 MeV using the below formula [71],

$$V_C = \frac{e^2}{4\pi\varepsilon_0}\frac{Z_B Z_T}{1.4(A_B^{\frac{1}{3}} + A_T^{\frac{1}{3}})}, \tag{6.1}$$

where Z_B and Z_T are the proton numbers of the beam and the target, respectively, while A_B and A_T represent the mass numbers of the beam and the target, respectively.

The relation between the beam energy and the excitation energy of the recoiled compound system can be derived using the conservation of energy and momentum, thus the center-of-mass energy of the system will be,

$$E_{CM} = E_B \left(\frac{M_T}{M_B + M_T}\right), \tag{6.2}$$

where E_B is the beam energy. Thus the needed beam energy just to be at the limit of the Coulomb barrier would be $E_B = 77.25$ MeV, which is around 2.41 MeV/A.

The beam energy was selected as 2.5 MeV/A, just above the Coulomb barrier, such that the evaporation of charged particles is as small as possible and the relative cross section of the "only-neutron" evaporation channels is maximized.

The beam intensity was selected 10 pnA and the target thickness was 500 µg cm^{-2}, and 8 mg cm^{-2} ^{90}Zr backing was placed behind the target material to stop the recoil nucleus, to avoid broadening of the γ-rays due to the Doppler effect. The efficiency for detecting two-neutron inside the Neutron Wall is around 1.4%, and particle detection efficiencies of DIAMANT are of the order of 65% and 35% for protons and α-particles, respectively. The gamma efficiency of the EXOGAM array for our experimental configuration that includes Neutron Wall is expected to be around 10% for 1.3 MeV γ-rays.

6.4 Analysis

As mentioned in previous paragraphs, we are dealing with a complex system of detectors that will provide information on the evaporated particles in the reaction as well as provide information on the γ-ray cascade de-exciting the residual nucleus after the evaporation. The information of all these detectors has to be sorted and organize such that we can set conditions (gates) that will help to identify the specific reaction channels and associated gamma-ray cascade. The first step on the analysis of such complex instruments is the time alignment. One has to be sure that all particles and γ-rays are in time coincidence, *i.e.* belong -more likely- to the same event. A correct time calibration and alignment maximizes the sensibility of the detection system. There are four time-to-amplitude converters (TACs) and three groups of TACs corresponding to each Neutron Wall, each DIAMANT and each Ge detector in the setup to help defining the time coincidence windows. Their configuration is shown in Table 6.1. One of them is particular since it is integrated in the BARTEK module of the Neutron Wall detector system (see Sec. 5.2.2).

TABLE 6.1: TAC configuration in the EXOGAM - Neutron Wall - DIAMANT setup at GANIL. RF stands for the radio frequency which is the external time reference coming from the accelerators. FT stands for the fast trigger (see Sec. 5.1.3). CFD-OR is the OR of the CFD modules in the Neutron Wall. CFD n represents the individual detectors of the Neutron Wall. CFD g represents the individual EXOGAM detectors. "Time DI" represents the time reference of the DIAMANT detectors. CFD p represents the individual DIAMANT detectors.

TAC	**START**	**STOP**
TAC 0	BaF_2	RF
TAC 1	FT	RF
TAC 2	FT	CFD-OR
TAC 3	CFD-OR	RF
ToF NW	CFD-OR	CFD n
Time Ge	CFD g	FT
Time DI	CFD p	FT

The time calibration of the TACs was done by determining two calibration points. First, 16 ns delay was added and then 10 ns removed in the RF signal. This information is used to find ns calibration of the TAC channels. As explained in Chapter 2, in order to maximize the neutron-γ discrimination capability of the neutron detector arrays, we use condition in two parameters, namely the Pulse Shape Discrimination, provided by the liquid scintillator, and the Time-of-Flight,

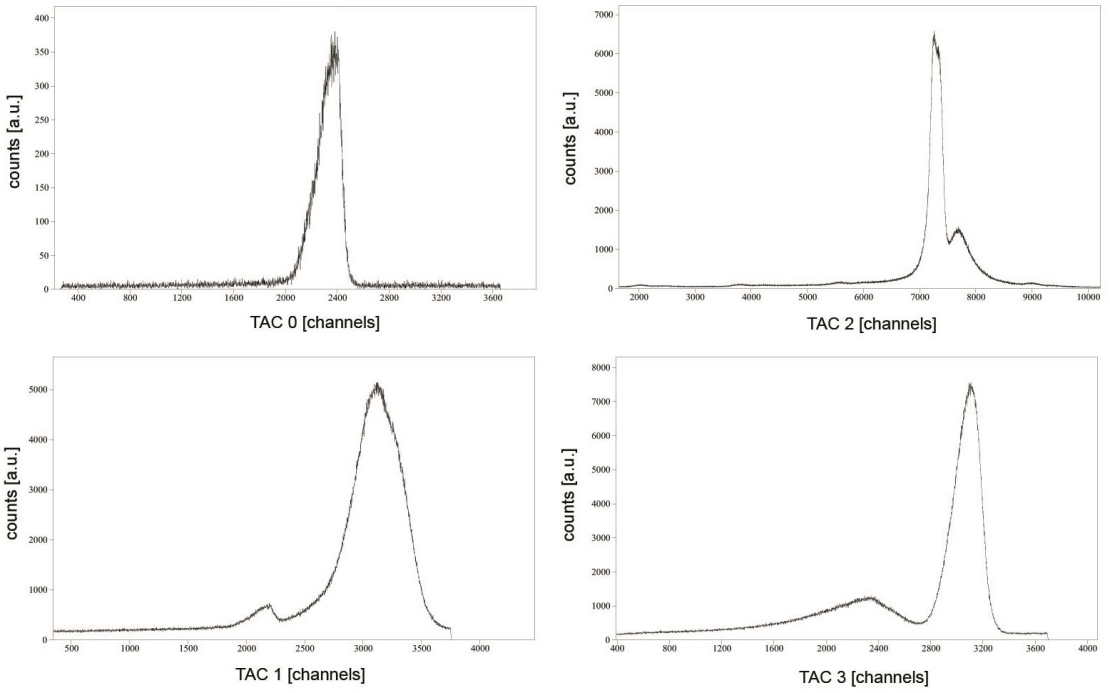

FIGURE 6.3: The TAC-0, -1, -2, -3 spectra listed in Table 6.1.

provided by the good timing of the neutron detectors and a time reference, in general given by the accelerator system or other detectors.

The performance of the ToF is best when it is referenced to a external time reference. In our case this time reference is the radio-frequency signal provided by the accelerator (RF), that is synchronous with the acceleration of the ion packages in the cyclotron. The evaluation of the ToF is done in two steps, first the individual electronics of the neutron detectors provides a TAC amplitude referenced to the logical "OR" of all the Neutron-Wall Constant Fraction Discriminator logical signals (CFD-OR). In a second step and only when a trigger happens, a TAC provides the measurement between the already mentioned CFD-OR and the accelerator RF. In order to reference the time of the Neutron Wall detectors to the RF signal, the information in the *TAC 3* is used (see Tab. 6.1). If one multiplies *TAC 3* with *-1* and adds to *ToF NW*, then the result will be *CFD n - RF* which will provide the information on the ToF for each neutron signal taking as reference the radio-frequency pulse of the accelerator.

$$[\text{CFD n} - \text{CFD OR}] - [\text{RF} - \text{CFD OR}] = \text{CFD n} - \text{RF} \tag{6.3}$$

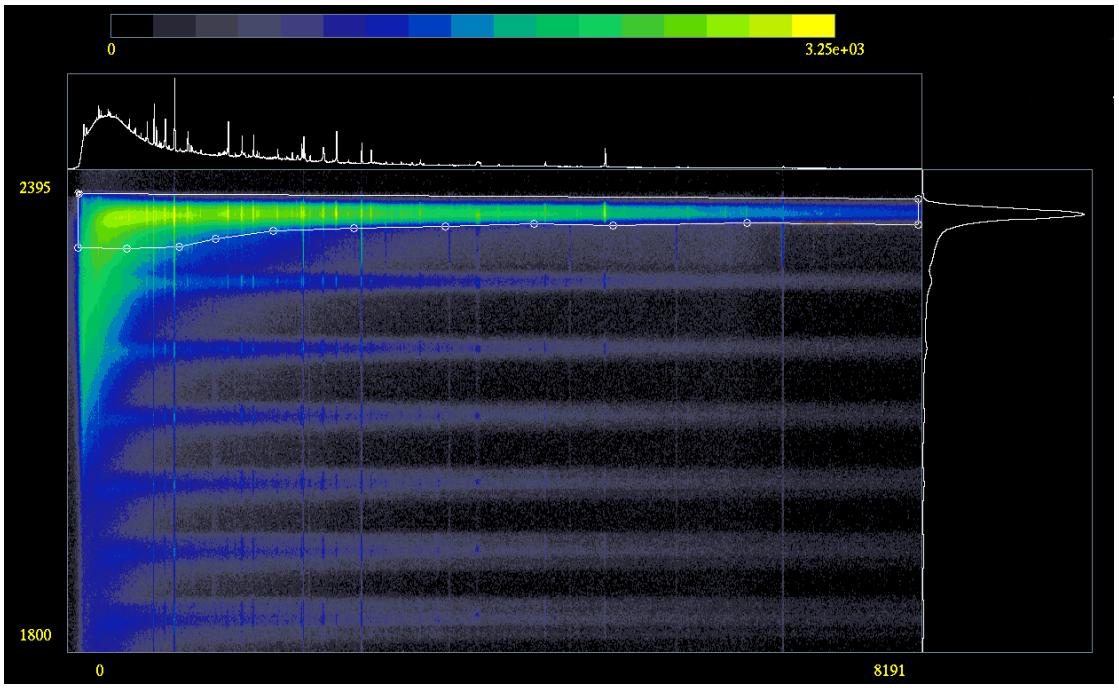

FIGURE 6.4: EXOGAM eenrgy vs. time after FT correction (see Eq. 6.4). The 2D gate is shown. The horizontal axis represents the EXOGAM energy in keV. The vertical axis represents the EXOGAM time after FT correction in ns. The γ-rays in coincident with previous and next to the prompt peak are also visible, are parallel, and are above and below the prompt peak selected with the 2D gate.

The time information on the TAC of the EXOGAM detectors are treated in a similar way to get proper timing. The TAC 1 is needed to be subtracted from the Time Ge detectors to get the Ge detector signal time references the RF signal (see Eq. 6.4).

$$[\text{CFD g} - \text{FT}] - [\text{RF} - \text{FT}] = \text{CFD g} - \text{RF} \tag{6.4}$$

The time alignment of the EXOGAM detectors is important in order to request a narrow time window for the γ-ray and particle coincidence. Once the alignment is done, a 2-dimensional gate (see Fig. 6.4) is set on the Energy vs. Time matrix to the region that is in coincidence with the prompt γ-peak in order to minimize as much as possible the background events produced by random coincidences.

The time information of the DIAMANT detectors are processed in a very similar way to the EXOGAM detectors. In the case of DIAMANT, the TAC 1 is needed to be subtracted from the Time DI signal to get the particle time references to the RF signal (see Eq. 6.5). The alignment of the time signals of the DIAMANT

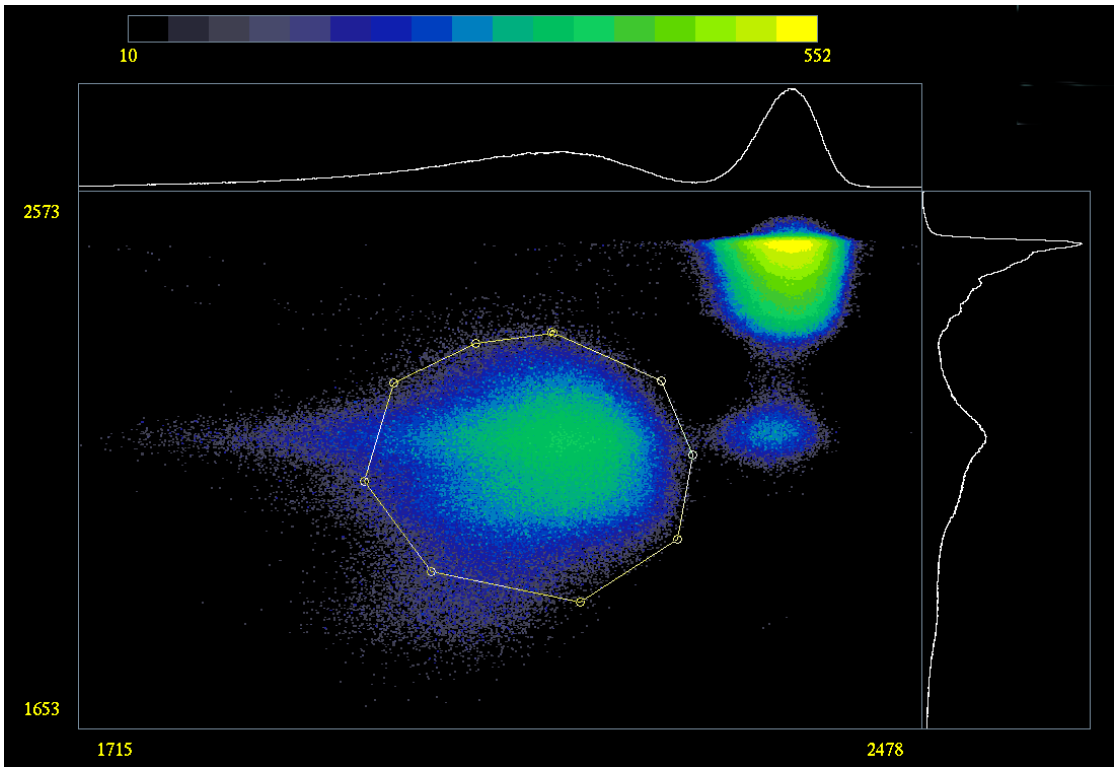

FIGURE 6.5: An example to the 2-dimensional neutron selection gates on the Neutron Wall data. Such matrix is produced for each Neutron Wall detector with ToF and PSA parameters on the horizontal and vertical axes, respectively. Units are arbitrary.

detectors has been done after such operation.

$$[\text{CFD p} - \text{FT}] - [\text{RF} - \text{FT}] = \text{CFD p} - \text{RF} \tag{6.5}$$

As mentioned before, neutron-γ discrimination is done by combining two different information from the neutron wall which has been explained in detail in Chapter 2. The 2-dimensional gates were determined for each Neutron Wall detector individually (see Fig. 6.5). The reader is referred to see Chapter 2 for more details.

The DIAMANT detector array is used for the light charged-particle detection. The DIAMANT detectors built from CsI scintillator, provide the particle identification as well via PSA. The 2-dimensional spectra of particle energy and particle identification parameter for each DIAMANT detector are created. Particle identification parameter is determined by the pulse shape analysis. The technique used in DIAMANT -similar to the one used in the Neutron-Wall BARTEK electronics- is the called Zero Cross-Over (ZCO) technique. This technique measures the time

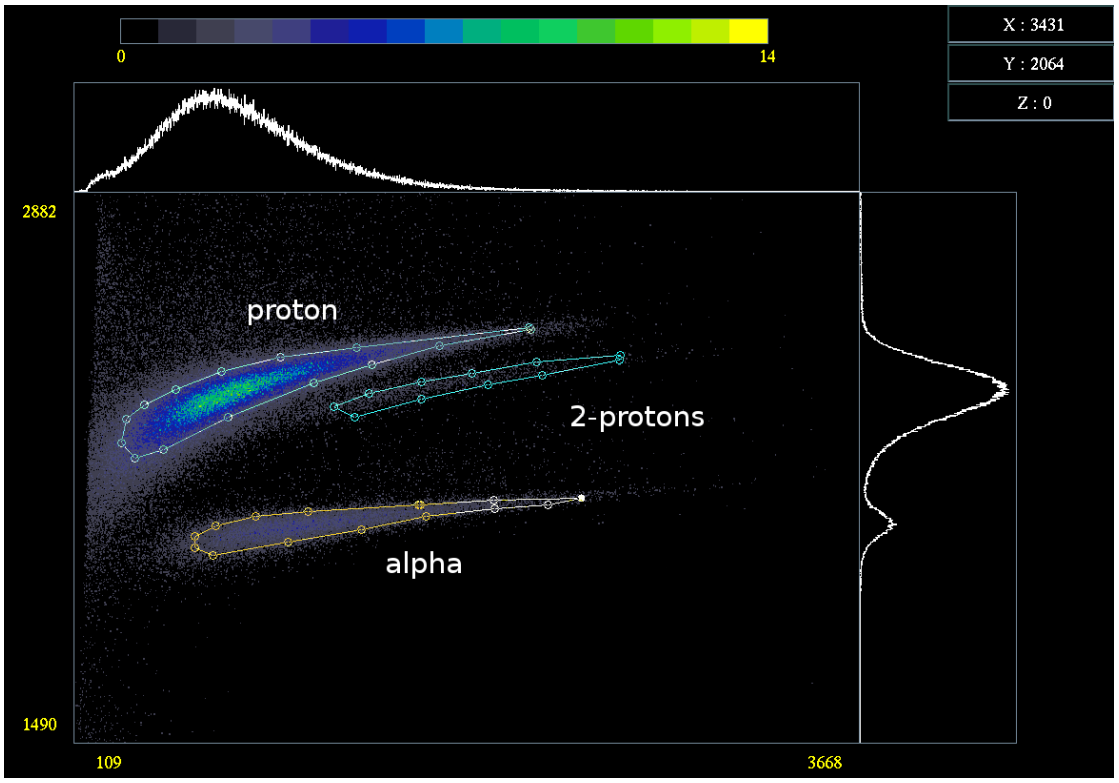

FIGURE 6.6: The particle selection gates on the DIAMANT data. The matrices are formed by the energy parameter on one axis and the PID parameter on the other. Units are arbitrary.

difference between the time determined with the CFD and the time when a bipolar signal -generated by differentiation with an appropriate time constant- crosses the zero amplitude. The ZCO spectrum has different location for the different particles detected in DIAMANT. Drawing this spectrum in one axis and the energy spectrum of the particles on the other axis, will produce a 2-dimensional particle discrimination matrix. Then 2-dimensional gates are defined to select proton and α particles (see Fig. 6.6). It is important that the time of each DIAMANT CsI crystal is aligned and calibrated. The calibration and the alignment are done in the same way as the Neutron Wall time calibration and the EXOGAM time alignment.

Energy and relative efficiency calibrations of EXOGAM were done with ^{152}Eu source and with the activity of ^{56}Co implanted during the measurement. The ^{152}Eu source provides up to 1.4 MeV energy and together with the activity of ^{56}Co, which provides a data point at 2.6 MeV, and thus they are convenient to perform such calibration. The energy calibration was done together and separately for the two rings of EXOGAM, $\theta = 90^o$ and $\theta = 135^o$ with respect to the beam axis, taking

TABLE 6.2: The final values of the parameters used in the HPGe efficiency calibration fit function in Eq. (6.4).

Parameter	**Overall**	**90^o**	**135^o**
A_1	44.31±0.196	41.84±0.3227	44.99±0.2032
A_2	-9.068±0.056	-4.302±0.2048	-7.797±0.7398
A_3	0.7549±0.0096	-0.4468±0.05103	0.3408±0.2016
A_4	4.871±0.284	-2.647±0.1042	1.005±0.825
A_5	-5.32±0.27	1.917±0.04774	-1.194±0.7572
A_6	1.753±0.067	-0.09874±0.004934	0.6112±0.1844

as reference the downstream direction. The relative efficiency calibration was done by fiting the data points to the second degree polynomial function described in Ref. [72] (shown in Eq.(6.4)). The fit parameters after the successful fit are listed in Table 6.2.

$$Q(E_\gamma) = exp\left[\frac{2(A_4) + log(E_\gamma).A_5 + [log(E_\gamma)]^2.A_6}{\pi.Arctan(Q\prime)}\right]$$
$$\text{where } Q\prime(E_\gamma) = exp[A_1 + log(E_\gamma).A_2 + [log(E_\gamma)]^2.A_3] \quad (6.6)$$

Once all the energy and time calibrations are done and the time signals are aligned, the single γ-ray spectra and the γ-γ matrices are created with different particle detection conditions. The analysis of such an experiment requires to identify the γ-rays with particle and neutron coincidences. The reaction channel selection of the setup depends highly on the effective detection efficiency of the detector arrays. The information -regarding the evaporated particles- is the number of particles detected, no the ones emitted. The probability that a number "X"' of particles from the total number "N" emitted is detected, follows a binomial distribution (see Eq. 6.7).

$$P(x) = \frac{n!}{(n-x)!x!}p^x(1-p)^{n-x} \quad (6.7)$$

One can, in principle, calculate what will be the probability to detect, for example, one-proton in a two-proton channel, or two-proton in a two-proton channel depending on the proton detection efficiency using the binomial distribution.

In order to identify the new reaction channels by analyzing the γ-ray spectra, it is crucial to know the detection efficiency of the setup. It has been mentioned that the

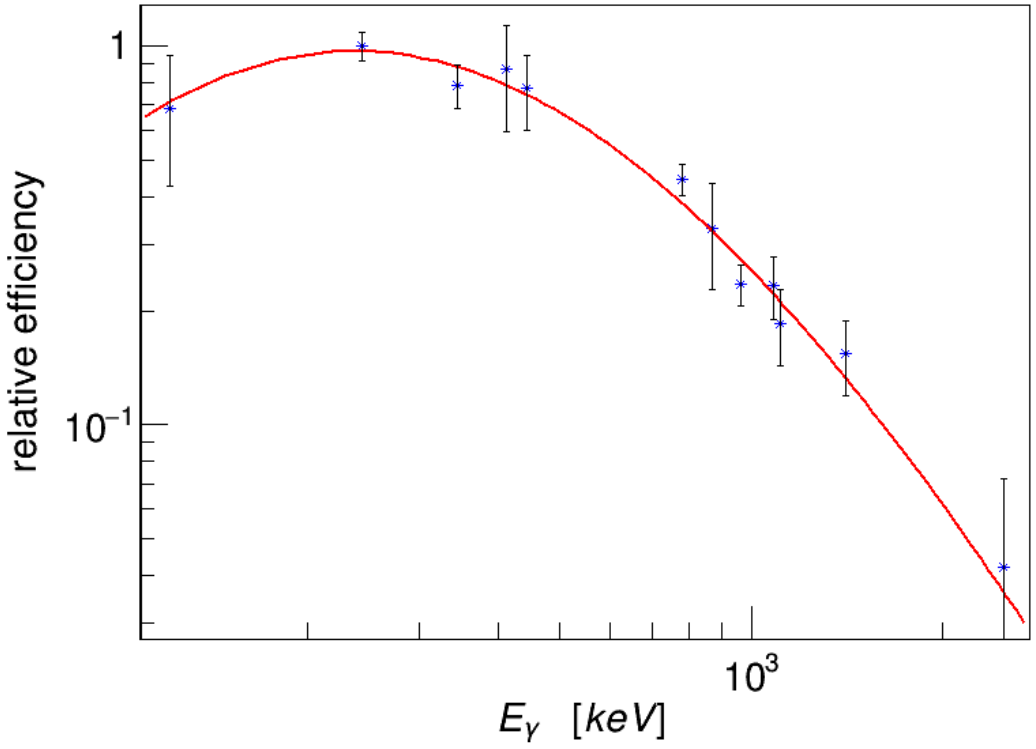

FIGURE 6.7: The fit curve and data points after successful fit.

probability to have the γ-ray from a nucleus in coincidence with in a certain channel is determined by the binomial distribution. Therefore, the determination of the proper channel in which the γ-ray is in coincidence with, is done by comparing the intensities of the γ-rays with different conditions. Let me remind the reader that the proton detection efficiency was found 65% and the α detection efficiency was found 35%.

The Neutron Wall efficiency, on the other hand, does not fulfill the binomial distribution due to the certain conditions applied to increase the accuracy of the two-neutron selection, e.g. the ΔToF condition, which will be mentioned later in this section. Before applying such conditions the one-neutron detection efficiency can be calculated using the number of counts of the transitions that are in coincidence with channels including one-neutron and two-neutron evaporation. For such test, we have selected the 2577 keV and 191 keV peaks which are in coincidence with one-neutron and two-neutron, respectively. The area of a peak from a nucleus in coincidence with two-neutron channel in the two-neutron gated spectrum can

TABLE 6.3: The areas of the 2577 keV and 191 keV peaks with one-neutron and two-neutron coincidences to calculate the one-neutron detection efficiency. See text for details.

Transition	**Detected neutron coincidence**	**Area [counts]**
191 keV	1n	14900±700
191 keV	2n	4600±430
2577 keV	1n	7900±600
2577 keV	2n	1200±110

be deduced as:

$$A_{2n}^{2n} = I_{2n}\left[\varepsilon_{NW}^2 + \{2 \times CT \times \varepsilon_{NW} \times (1-\varepsilon_{NW})\} - (CT \times \varepsilon_{NW}^2) - (CT^2 \times \varepsilon_{NW}^2)\right] \tag{6.8}$$

where I represents the intensity of the transition, ε_{NW} is the Neutron Wall one-neutron detection efficiency, CT represents the neutron-cross-talk factor which can be deduced as:

$$CT = \frac{A_{2n}^{1n}}{A_{1n}^{1n}} \tag{6.9}$$

where the A_{Yn}^{Xn} notation represents the area of a peak in the Yn gated spectrum emitted from a nucleus in the Xn channel. On the other hand, the area of a peak from a nucleus in coincidence with two-neutron channel in the one-neutron gated spectrum can be deduced as:

$$A_{1n}^{2n} = I_{2n}\left[\{2 \times \varepsilon_{NW}(1-\varepsilon_{NW})\} - \{2 \times CT \times \varepsilon_{NW} \times (1-\varepsilon_{NW})\}\right] \tag{6.10}$$

The one-neutron detection efficiency than can be deduced using the Eq. 6.8 and Eq. 6.10 as:

$$\varepsilon_{NW} = \frac{2R_{2n/1n}(1-CT) - 2CT}{(1-3CT-CT^2) - 2R_{2n/1n}(CT-1)} \tag{6.11}$$

where,

$$R_{2n/1n} = \frac{A_{2n}}{A_{1n}} = \frac{\varepsilon_{NW}(1-3CT-CT^2) + 2CT}{2\varepsilon_{NW}(CT-1) + 2 - 2CT} \tag{6.12}$$

The efficiency of the Neutron Wall can be calculated using the areas determined from the related spectra and listed in Table 6.3. The one-neutron detection efficiency has been deduced as 21.1(2.1)%.

As it has been mentioned in Chapter 3, it is possible to increase the 2n Neutron Wall (or in the future NEDA) selectivity by applying ΔToF condition on the neutron detection time. The ToF difference between two-neutron events is more

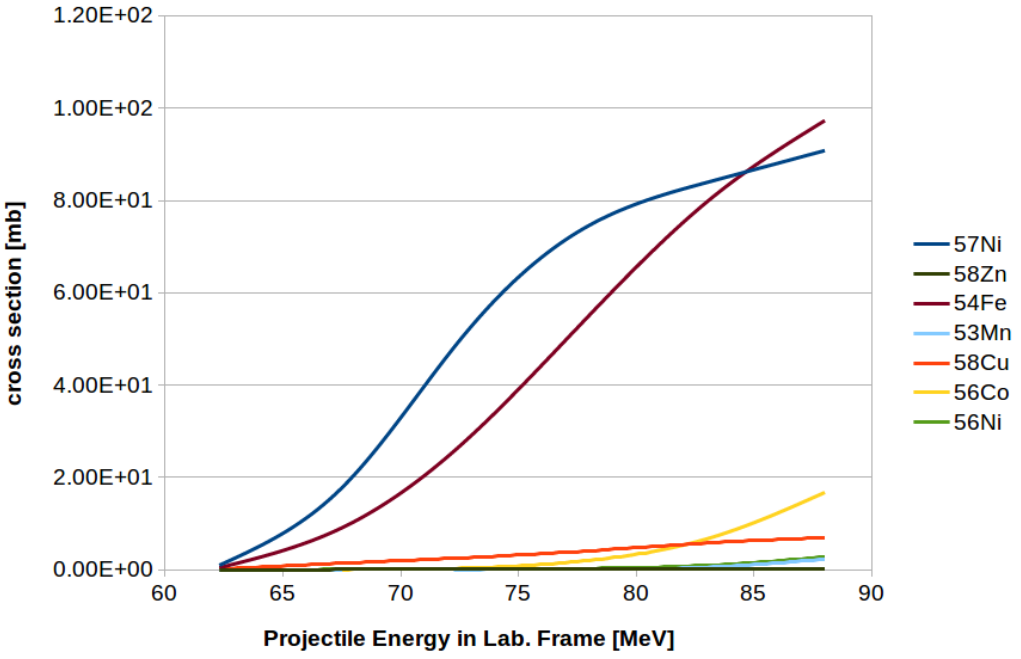

FIGURE 6.8: The HIVAP estimations of the cross-sections of various channels in ^{60}Zn compound nucleus decay.

likely less than one-neutron event firing two detectors due to the neutron-cross-talk. Nevertheless, at the time of the analysis we had only possibility to use the neighbor canceling technique. In this technique, the neighboring detectors to the detector that gives the signal are ignored thus the neutron-cross-talk events are substantially reduced at the cost of efficiency.

6.5 Cross-section Predictions

The probabilities to populate the daughter nuclei after the compound nucleus formation in a fusion-evaporation reaction can be predicted using `HIVAP`[[69, 70]], for different combinations of projectile and target, and different projectile energies. The use of this code provides fair predictions, in general is used before the experiment in order to choose the best combination of projectile and target and the best energy for the population of the channel of interest.

The HIVAP estimations of the various channels in the compound nucleus decay are seen in Fig. 6.8. It is foreseen that the 2p1n channel will be dominant with respect to the other channels for the selected beam energy.

6.6 Angular Correlations of the γ-rays

Information of the multipolarity of the γ-ray transitions is obtained using the the angular distribution from oriented nuclei (i.e. ADO) ratios [80–82]. In this technique, the γ-ray intensities at different detection angles are compared to find out if the γ transition has a pure quadruple, a pure dipole character or has a mixing of the two multipolarity. The EXOGAM array allows to perform such measurement on the detected γs since the array has three "rings" with polar angles $\theta = 90^o$, 135^o and 145^o. Therefore, the ADO ratios of the detected γs were calculated as in Eq. 6.13.

$$R_{ADO} = \frac{I_\gamma^{145}}{I_\gamma^{90}} \tag{6.13}$$

In order to get proper results, the relative efficiency calibration of the EXOGAM array has to be done separately for each angular ring, depending on the detector solid angle coverage at given polar angle range. The efficiency calibrations of the EXOGAM rings have been done using the ^{152}Eu source and the decay of ^{56}Co, i.e. the same data set used to make efficiency calibration of the whole array (see Sec. 6.4), except in this case, with ring conditions. The ADO ratios depend as well on the degree of alignment obtained in the reaction and how the alignment is preserved in the decay cascade. The alignment is frequently represented as σ(J)/J.

6.7 Results

The γ-γ coincidence matrices have been created with several different charged particle and neutron detection conditions (see Fig. 6.9). The aim is to assign γ-ray transitions to the different reaction products. In the de-excitation process of the reaction products, the gamma-ray emission drives the nucleus towards yrast states -minimum excitation energy for a given angular momentum-, therefore, low lying yrast transitions concentrate larger intensity than the ones happening at larger excitation energy and/or angular momentum. Once the main transition have been assigned to a reaction channel, a practical way to proceed is the identification of the rest of transitions by analyzing the γ-γ matrix and establishing coincidence relationships. This procedure allows us to build the de-excitation level scheme with the obtained information. In order to complete the information of the de-excitation

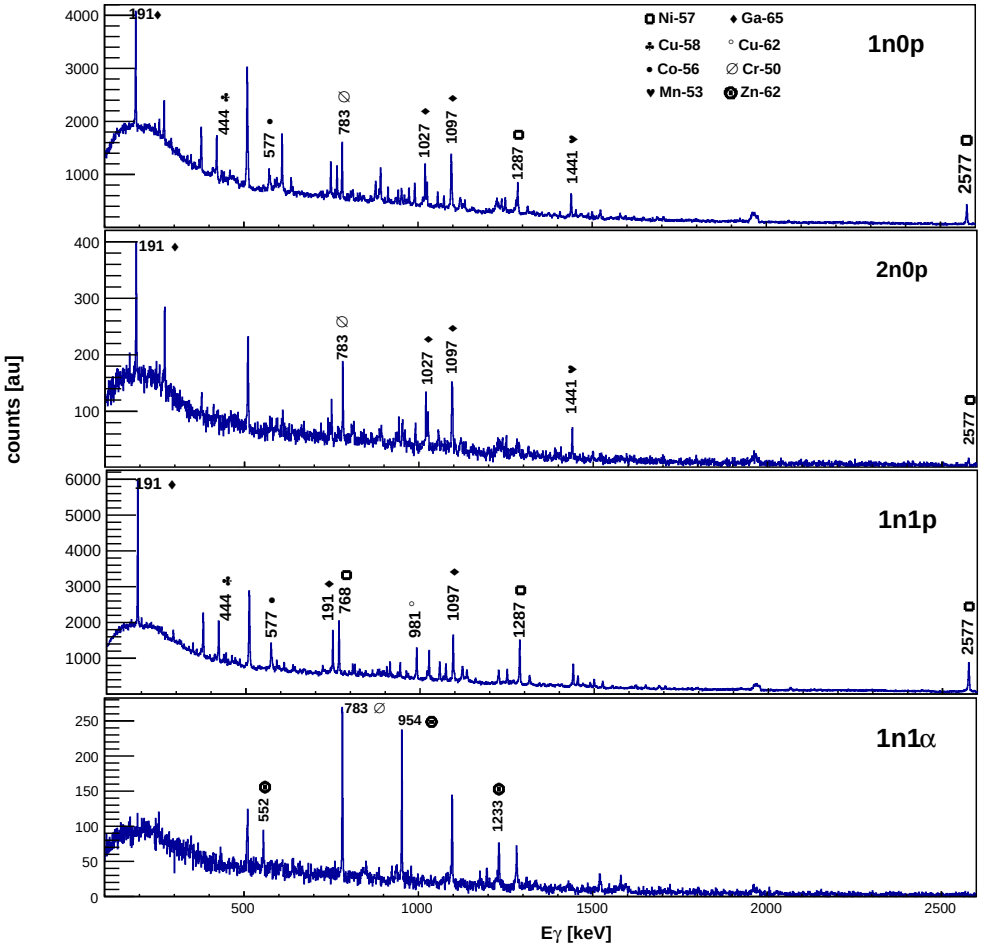

FIGURE 6.9: γ-ray spectra with different charged particle and neutron conditions.

level scheme, it is necessary to determine as well the relative intensities of the γ-rays. The relative intensity is calculated by correcting the area of a peak with the relative γ-ray detection efficiency at its energy. The efficiency determination has been discussed in the previous section.

The area of a transition in a spectrum with conditions in charged particles and neutrons depend on several factors. First its intensity, then the probability that the reaction channels product to which this transition belongs fulfills the conditions in charge particles and neutrons.

It was mentioned before that the probability to have the γ-ray from a nucleus in coincidence with in a certain detection particle multiplicities is determined by the binomial distribution. Therefore, the determination of the proper channel in which the γ-ray coincidence with is done by comparing the intensities of the γ-rays

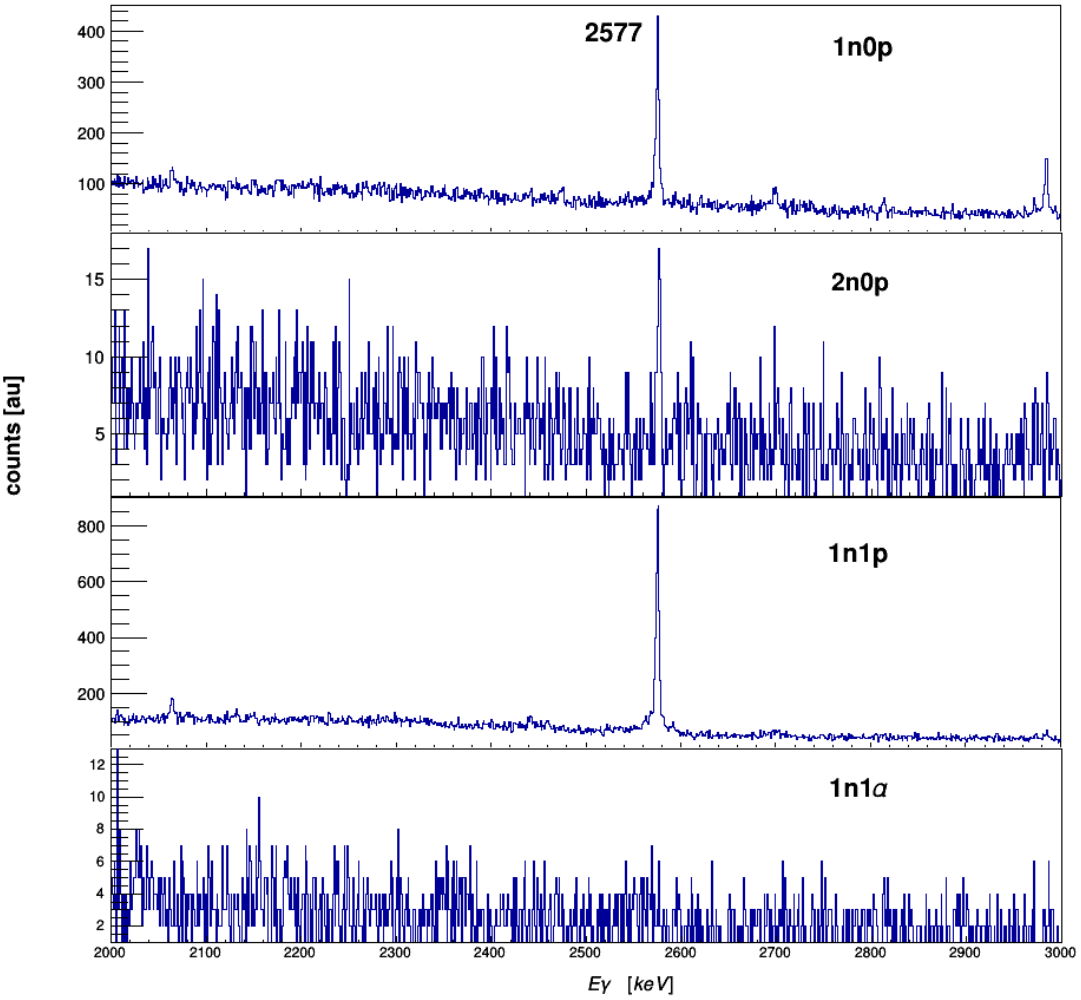

FIGURE 6.10: 2577 keV ($7/2^- \rightarrow 3/2^-$) transition in ^{57}Ni with different neutron and charged-particle conditions.

with different conditions. Nevertheless, the discrepancy of the neutron detection efficiencies with the binomial distribution are taken into account.

6.7.1 $\gamma - \gamma$ coincidence analysis for ^{57}Ni

The level scheme of the ^{57}Ni nucleus was previously investigated by D. Rudolph and collaborators, and published in Ref [83]. The first excited state in the yrast band of this nucleus is $\frac{7}{2}^-$ with the excitation energy of 2577 keV. The $\frac{7}{2}^-$ decays to the ground state level with an angular momentum and parity of $\frac{3}{2}^-$. This transition is clearly seen in the γ-ray spectrum in coincidence with 1n (see Fig. 6.10). The peak is the most intense in the spectrum in coincidence with one-neutron and one-proton. The spectrum in the bottom panel of Fig. 6.10 is in

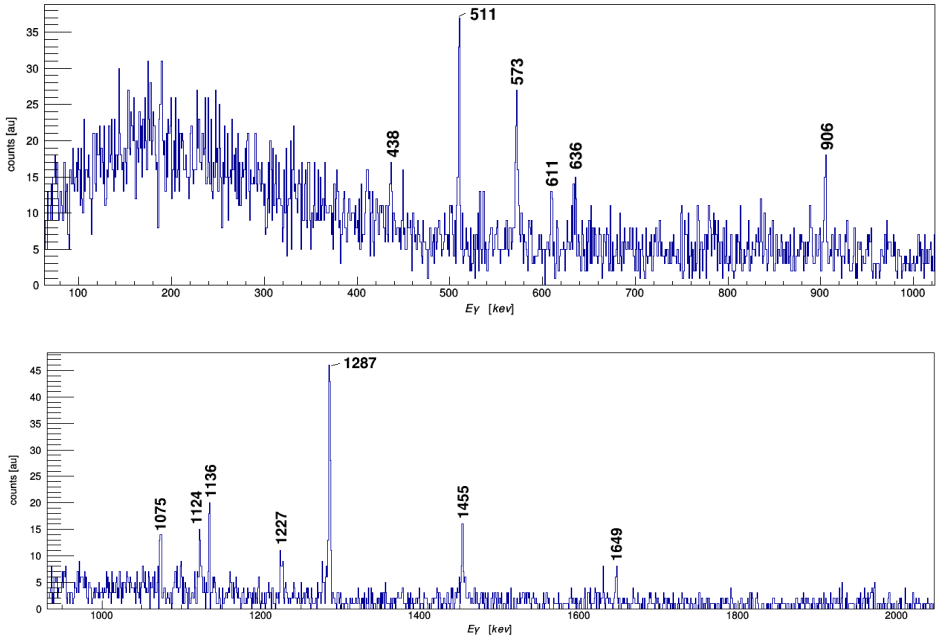

FIGURE 6.11: The 2577 keV gated γ-ray spectrum with one-proton and one-neutron conditions. The γ-ray transitions that are in the yrast band and the ones in coincidence with the yrast band transitions are shown.

coincidence with one-neutron and one-α-particle. In this spectrum, the peak has disappeared, suggesting that the transition is not in coincidence with α-particles. A detailed analysis can be done by gating on the transitions go down to the $3/2^-$ ground state, for example, on the 2577 keV peak and producing the γ-ray spectrum in coincidence with ^{57}Ni nucleus. The 2577 keV gated gamma spectrum can be seen in Fig. 6.11.

The level scheme built with the current experimental information is shown in Fig. 6.14.

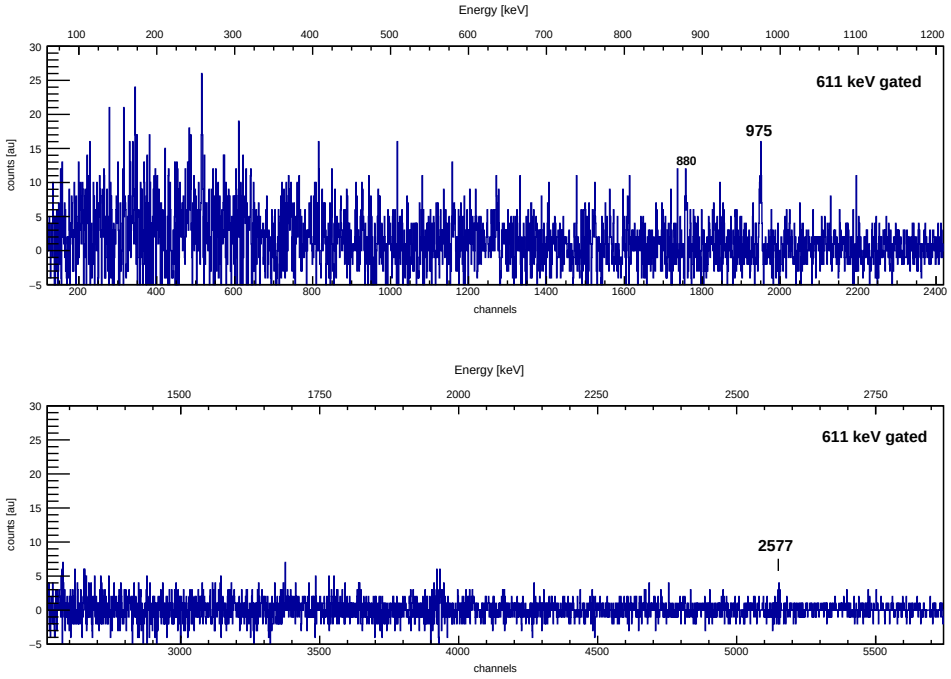

FIGURE 6.12: 611 keV gated spectra showing the coincidences with 880 keV, 975 keV and 2577 keV transitions.

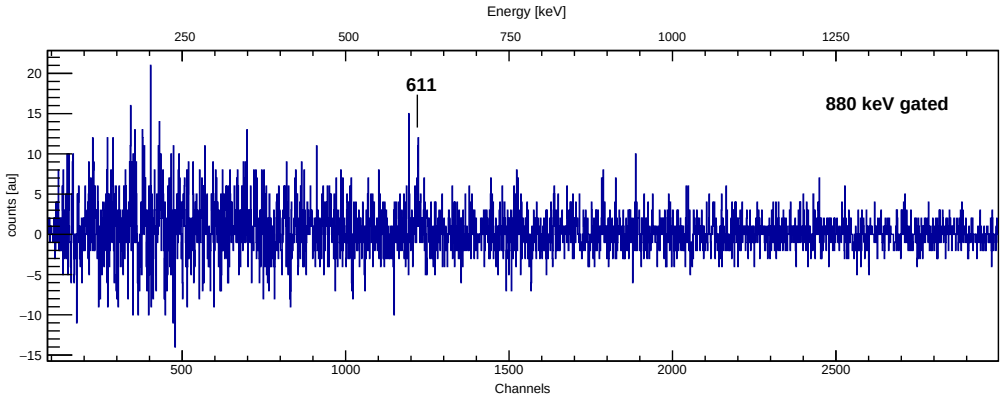

(a-1)

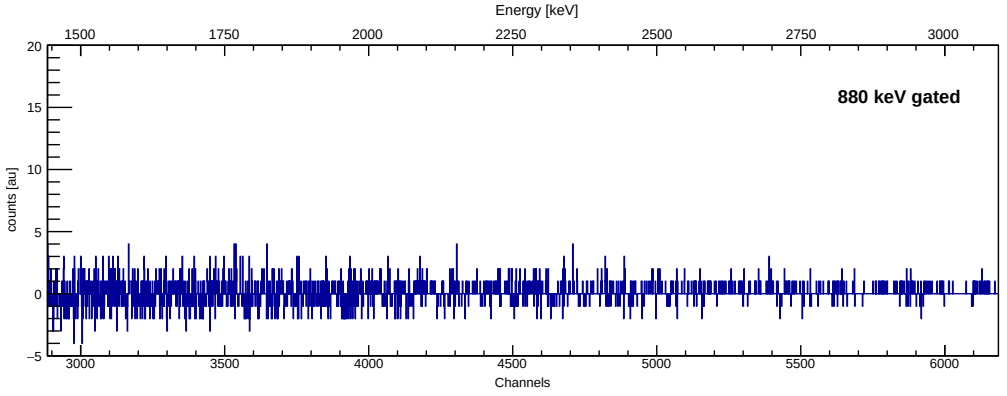

(a-2)

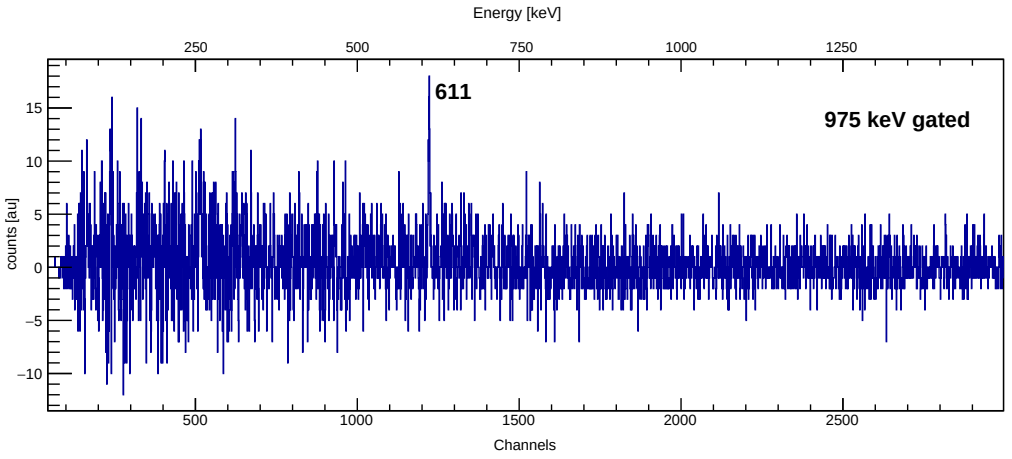

(b-1)

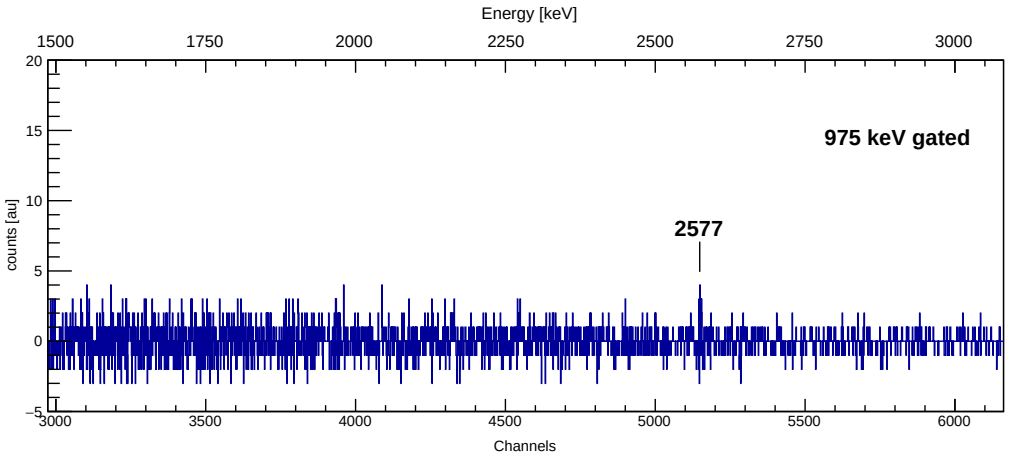

(b-2)

FIGURE 6.13: 880 keV (upper panels - a-1 and a-2) and 975 keV (below panels - b-1 and b-2) gated spectra showing the coincidence with the 611 keV transition.

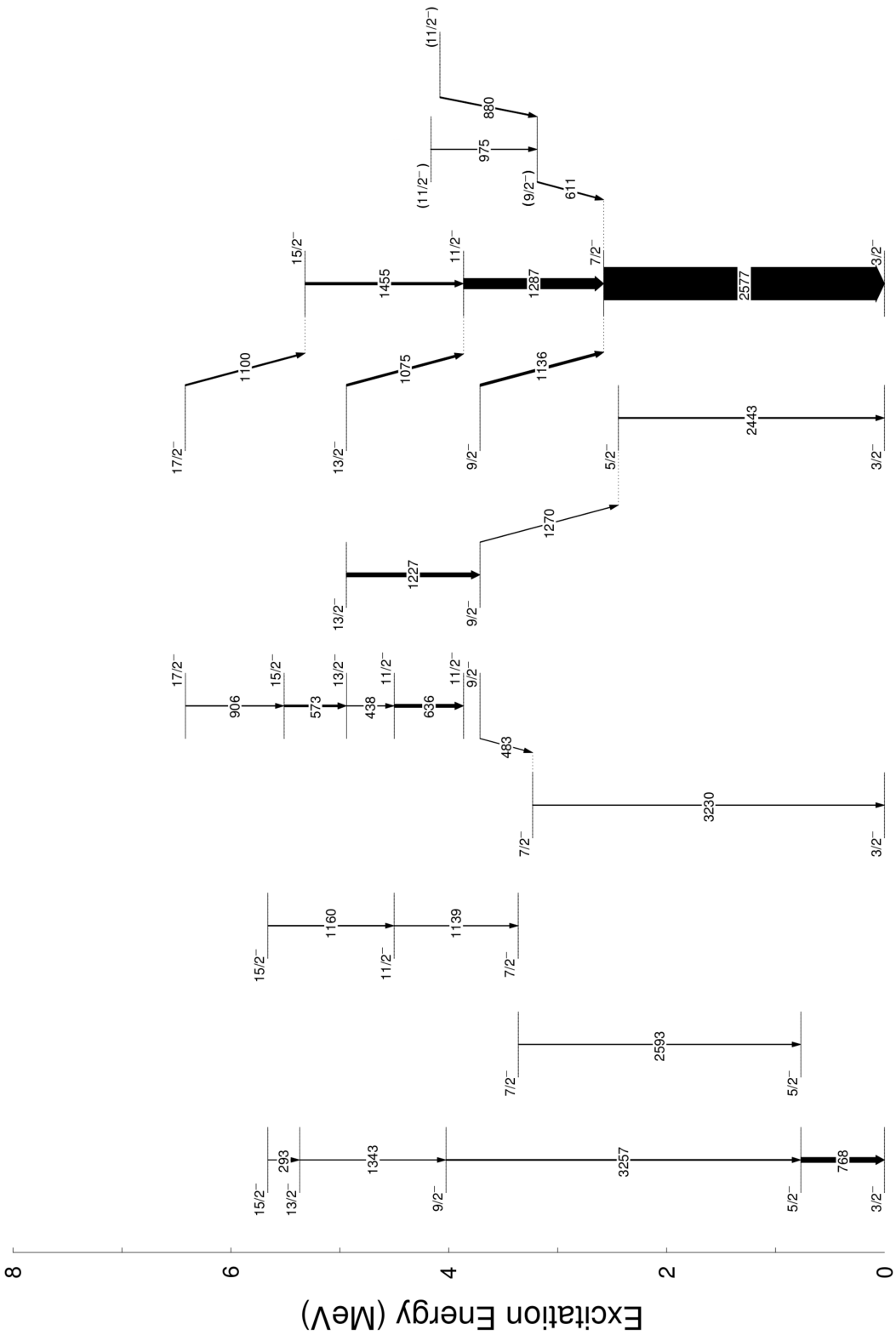

FIGURE 6.14: Level scheme of ^{57}Ni deduced in the current work.

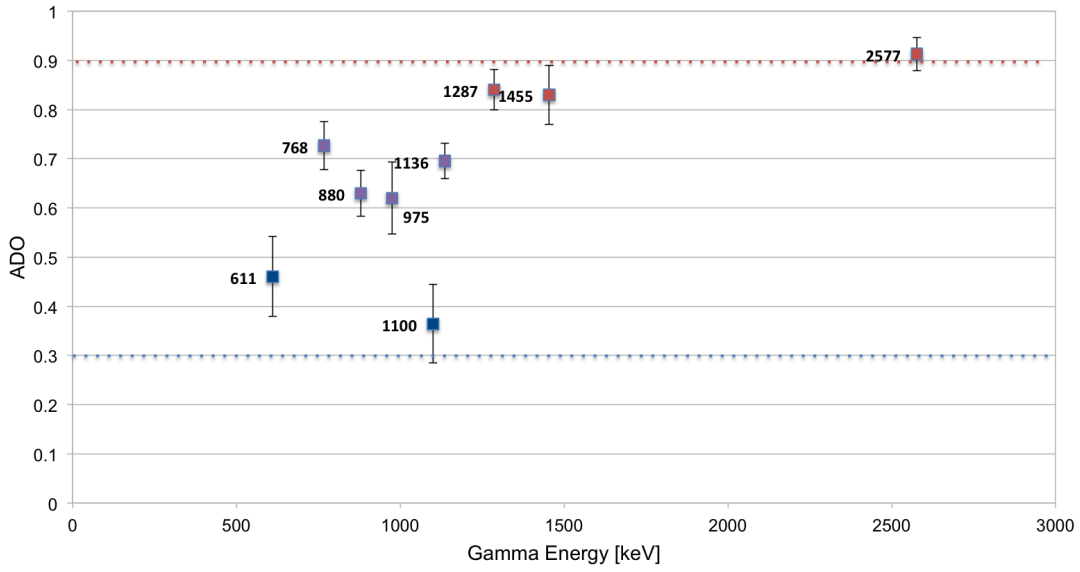

FIGURE 6.15: ADO ratios for several known transitions and the new transitions. Transitions with quadrupole character shown in red. Purple represents quadrupole/dipole mixing. Blue represents the transitions with dipole character but probably with electric quadrupole mixing.

As it is possible to see in the level scheme of ^{57}Ni, shown in Fig. 6.14, I have identified three new transitions that are de-exciting three new levels in ^{57}Ni. In order to suggest the angular momentum and parity of the new states is is necessary first to assign a multipolarity to the transitions. The ADO ratios of the new transitions along with the ratio of the already known ones -to be used as calibration- have been determined. The EXOGAM array, having the detectors relatively close to the target, in order to gain efficiency, has a large angular coverage for each single detector. In a theoretical calculation with the given angles, one would expect ADO of about 0.5 for pure dipoles and larger than 1.5 for pure quadrupoles with a usual $\sigma(J)/J \sim 0.3$. The integration over broader angular ranges makes more practical a calibration with transitions of known multipolarity. Such calibrations results on a value of 0.3 for pure dipoles and larger than 0.9 for pure quadrupoles (see Fig. 6.15). In Tab. 6.4, one can see the ADO ratios of the known E2 and M1/E2 transitions in ^{57}Ni, together with the ones of the newly identified transitions. With the present results we assigned M1/E2 character to the three new transitions. In Tab. 6.4, there is a summary of the observed transitions in ^{57}Ni.

The interpretation of the newly assigned levels to ^{57}Ni in the framework of the Shell Model is ongoing.

TABLE 6.4: The ADO ratios and the multipolarities of the known and the newly identified transitions in ^{57}Ni. The known multipolarities have been taken from Ref. [83]. Proposed multipolarities of the new transitions are shown in parenthesis. See text for details.

$\mathbf{E}_{ex}$ [keV]	$\mathbf{E}_{\gamma}$ [keV]	$\mathbf{I}_{rel}$	$\mathbf{R}_{ADO}$	Multipolarity	$\mathbf{I}_i^{\pi}$ [$\hbar$]	$\mathbf{I}_f^{\pi}$ [$\hbar$]
768.7(2)	768.7(2)	15(1)	0.69(4)	M1/E2	$5/2^-$	$3/2^-$
2443(4)	2443(4)	1.6(1)		M1/E2	$5/2^-$	$3/2^-$
2577(1)	2577(1)	100(4)	0.93(3)	E2	$7/2^-$	$3/2^-$
3188.1(2)	611.1(2)	3.6(3)	0.40(4)	(M1/E2)	$9/2^-$	$7/2^-$
3230(1)	3230(1)	2.0(3)			$7/2^-$	$3/2^-$
3361(2)	2593(2)	1.0(2)			$7/2^-$	$5/2^-$
3713(2)	483(1)	2.1(2)		M1/E2	$13/2^-$	$11/2^-$
	1136.2(2)	10.1(5)	0.66(3)	M1/E2	$9/2^-$	$7/2^-$
	1270.1(4)	3.1(2)			$9/2^-$	$5/2^-$
3864.4(6)	1286.4(6)	32.2(3)	0.85(3)	E2	$11/2^-$	$7/2^-$
4025.7(8)	3257.2(7)	2.2(4)			$9/2^-$	$5/2^-$
4068.6(6)	879.7(6)	1.9(2)	0.63(5)	(M1/E2)	$11/2^-$	$9/2^-$
4168.3(4)	975.2(4)	2.0(2)	0.62(5)	(M1/E2)	$11/2^-$	$9/2^-$
4500(2)	636.1(2)	3.5(1)			$11/2^-$	$11/2^-$
	1139.3(3)	3.5(1)			$11/2^-$	$7/2^-$
4940(4)	437.6(7)	1.1(1)		M1/E2	$13/2^-$	$11/2^-$
	1075.1(3)	9.9(4)		M1/E2	$13/2^-$	$11/2^-$
	1227.0(3)	13.1(5)		E2	$13/2^-$	$9/2^-$
5319.0(5)	1455.0(5)	8.1((7)	0.85(5)	E2	$15/2^-$	$11/2^-$
5368(1)	1343(1)	0.8(2)			$13/2^-$	$9/2^-$
5513(2)	573.6(2)	2.4(2)		M1/E2	$15/2^-$	$13/2^-$
5661(1)	293.4(4)	2.1(3)		M1/E2	$15/2^-$	$13/2^-$
	1159.6(5)	6.2(5)		E2	$15/2^-$	$11/2^-$
6419(3)	905.9(3)	1.5(1)		M1/E2	$17/2^-$	$15/2^-$
	1100.2(3)	9.7(8)	0.43(3)	M1/E2	$17/2^-$	$15/2^-$

6.7.2 $\gamma - \gamma$ coincidence analysis for the ^{65}Ga nucleus produced in the reaction with the ^{40}Ar contamination in the beam

Even if the ^{65}Ga is produced only in the fusion-evaporation reaction with the ^{40}Ar contamination of the beam (1%), nevertheless, the characteristic 190.8 keV peak is one of the most intense peaks on the spectrum (see Fig. 6.16). The analysis of the 190.8 keV peak shows that it is in coincidence with the 2n1p channel (see Tab. 6.5). The 190.8 keV gated γ-ray coincidence spectrum shows that this transition is in coincidence with 751, 1027, 1096, 1501 and 1526 keV transitions (see Fig. 6.17). The γ-ray coincidence search within the region that is expected to be populated

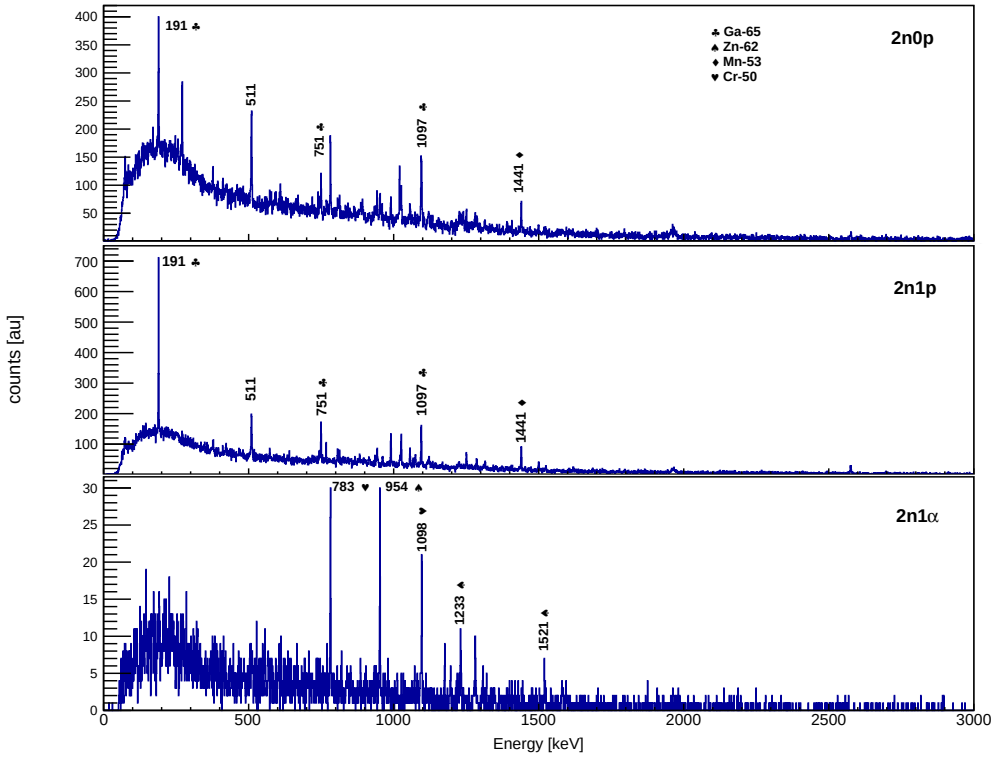

FIGURE 6.16: The spectra with various reaction channels gated. The 191 keV peak disappears completely on the spectrum in coincidence with α-particles.

TABLE 6.5: The areas of the 190.81 keV peak with no-particle and one-proton coincidences. The proton detection efficiency of the DIAMANT array can be found as 65%.

Condition on particle detection	**Area [counts]**	**Percentage [%]**
1n0p	2604	35
1n1p	4838	65

in the ^{32}S + ^{28}Si reaction turned with no results. Extended search of the region for the $\gamma - \gamma$ coincidence database lead us to ^{65}Ga.

In order to populate ^{65}Ga as the daughter nucleus in 2n1p channel, the compound nucleus should be ^{68}Ge. The only way to form ^{68}Ge as the compound nucleus, the beam should have been contaminated with ^{40}Ar. The ^{40}Ar is due to the identical rigidity of the ^{32}S 4^+ beam with the contaminant ^{40}Ar 5^+. The presence of ^{40}Ar in the ion source was unknown to us during the experiment. The energies of both the beam and the contaminant were about 2.5 MeV/u. The ^{40}Ar contamination in the beam was found 1%.

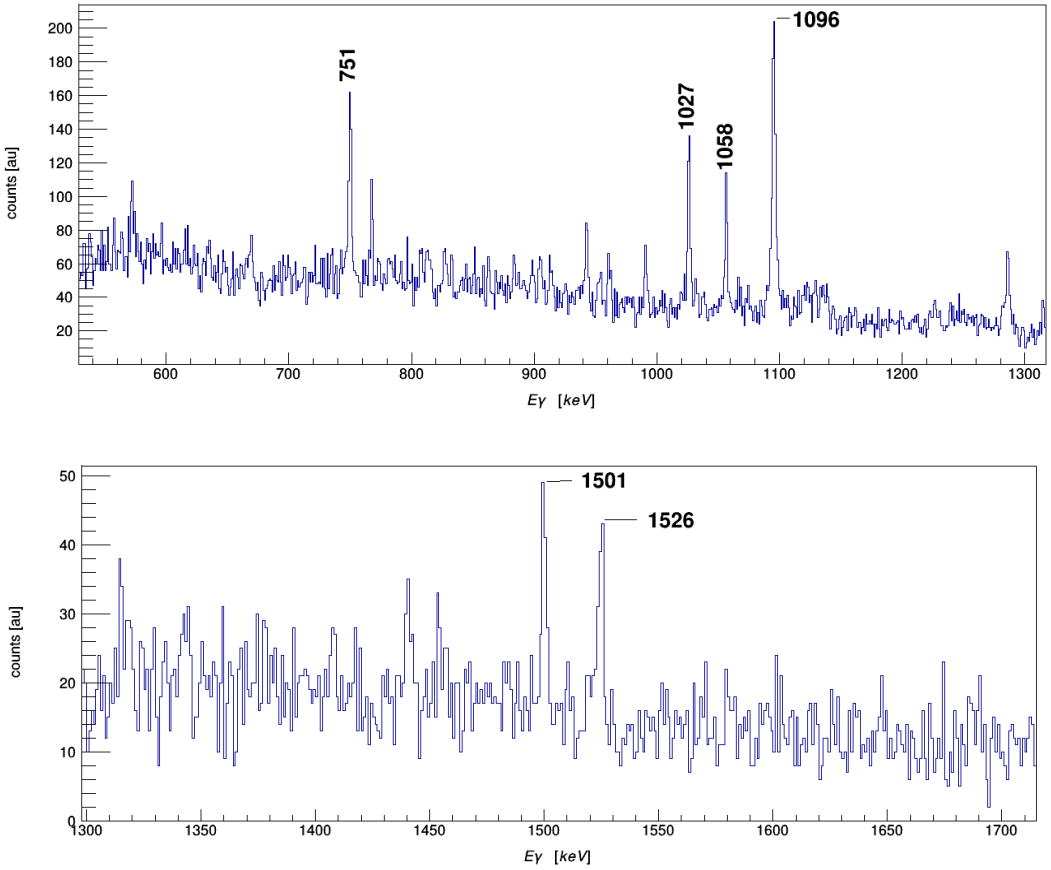

FIGURE 6.17: The two regions of the 191 keV gated $\gamma-\gamma$ coincidence spectrum showing some of the peaks of ^{65}Ga.

The level scheme of ^{65}Ga built with the data of the current work is shown in Fig. 6.18 and Tab. 6.6.

6.7.3 Other nuclei observed in the present experiment in the reactions ^{32}S + ^{28}Si and ^{40}Ar + ^{28}Si

In this section, the level schemes of the rest of nuclei that have been populated in the experiment will be presented. The identification of the rest of the transitions observed on the spectrum has been done by analyzing the $\gamma-\gamma$ and γ-particle coincidence matrices. The angular momentum and parity of the states were taken from previous works, therefore the reader is advised to see the related publications cited.

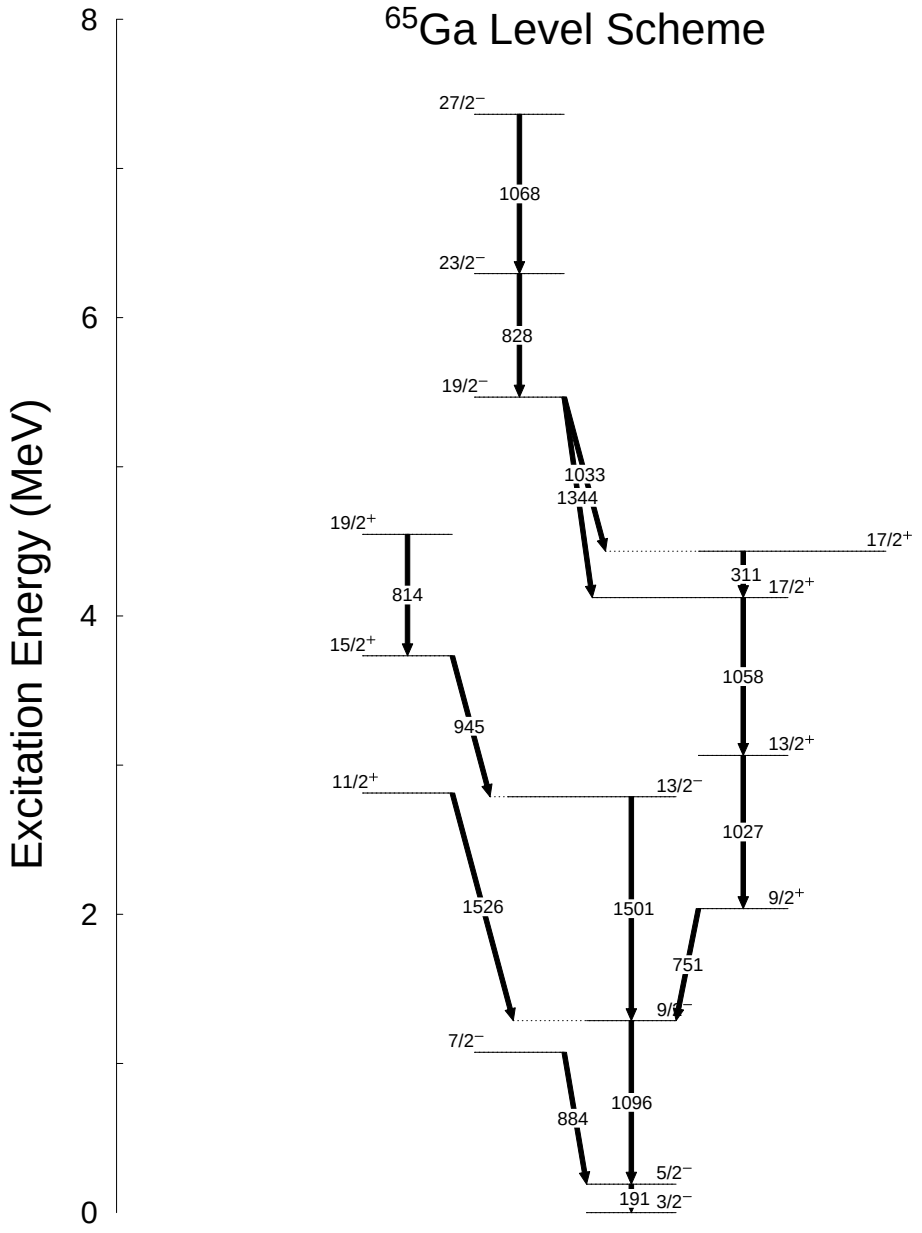

FIGURE 6.18: Level scheme of ^{65}Ga as measured in the present work.

TABLE 6.6: Transitions belonging to ^{65}Ga observed in the present experiment. The level angular momentum and parity data have been taken from Ref. [84].

$\mathbf{E}_{ex}$ [keV]	$\mathbf{E}_{\gamma}$ [keV]	$\mathbf{I}_{rel}$	$\mathbf{I}_i^{\pi}$ [$\hbar$]	$\mathbf{I}_f^{\pi}$ [$\hbar$]
190.8(1)	190.8(1)	100(5)	$5/2^-$	$3/2^-$
1075.2(2)	884.2(3)	9.5(8)	$7/2^-$	$5/2^-$
1287.1(1)	1096.1(1)	85(5)	$9/2^-$	$5/2^-$
2037.9(1)	750.9(1)	70(5)	$9/2^+$	$9/2^-$
2788.1(3)	1501.0(3)	15(1)	$13/2^-$	$9/2^-$
2812.6(6)	1525.8(4)	5.2(8)	$11/2^-$	$9/2^-$
3064.8(2)	1027.2(2)	60(3)	$13/2^+$	$9/2^+$
3732.9(2)	945.1(2)	14(1)	$15/2^+$	$13/2^-$
4122.9(5)	1057.9(1)	50(3)	$17/2^+$	$13/2^+$
4434.1(6)	311.2(4)	7.3(9)	$17/2^+$	$17/2^+$
4546.8(6)	813.7(3)	10.1(1)	$19/2^+$	$15/2^+$
5467(1)	1033.4(3)	6.8(2)	$19/2^-$	$17/2^+$
	1344.1(4)	4.5(4)	$19/2^-$	$17/2^+$
6295(1)	827.9(3)	14(2)	$23/2^-$	$19/2^-$
7363(1)	1068.1(2)	11.3(9)	$27/2^-$	$23/2^-$

6.7.3.1 Reaction products populated by the compound nucleus ^{60}Zn

The nuclei with the higher population following the evaporation in the compound nucleus ^{60}Zn in the experiment are presented in this section. The level schemes of each nuclei are presented in the corresponding reaction channels listed in Tab. 6.7. The intensities are relative to the most intense transition.

TABLE 6.7: The most populated nuclei by evaporation of the compound nucleus ^{60}Zn. The level schemes can be seen in corresponding figures.

Channel	Nucleus	Level Scheme	Reference
1n1p	^{58}Cu	Fig. 6.19	[85]
1n3p	^{56}Co	Fig. 6.20	[86]
2n4p	^{54}Fe	Fig. 6.21	[87]
2n5p	^{53}Mn	Fig. 6.22	[88]

6.7.3.2 Reaction products populated by the compound nucleus ^{68}Ge

The compound nucleus ^{68}Ge is produced due to the ^{40}Ar contamination in the ^{32}S beam. The nuclei populated with large probability within different reaction channels are listed in Tab. 6.8. The level schemes of the populated nuclei are presented in the corresponding figures listed in Tab. 6.8.

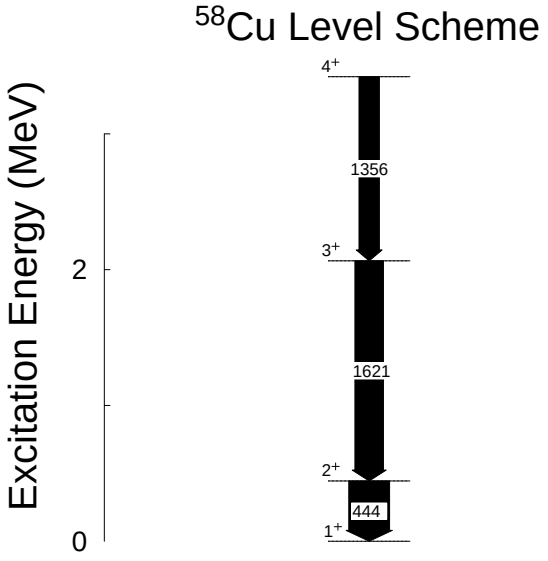

FIGURE 6.19: Level scheme of ^{58}Cu as measured in the present work.

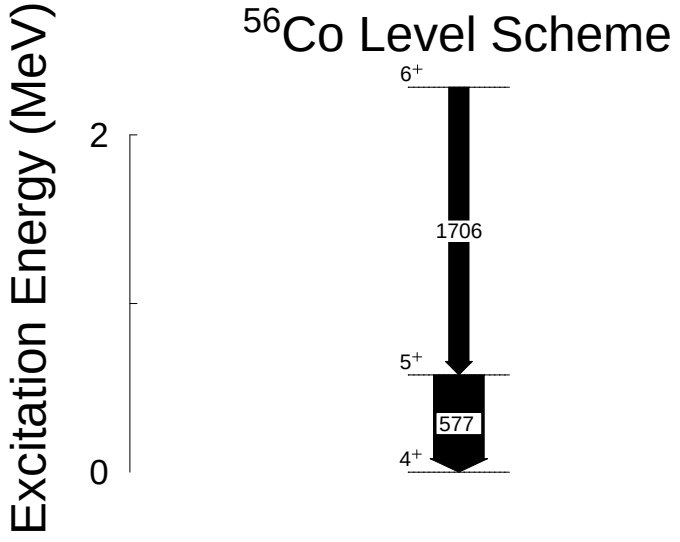

FIGURE 6.20: Level scheme of ^{56}Co as measured in the present work.

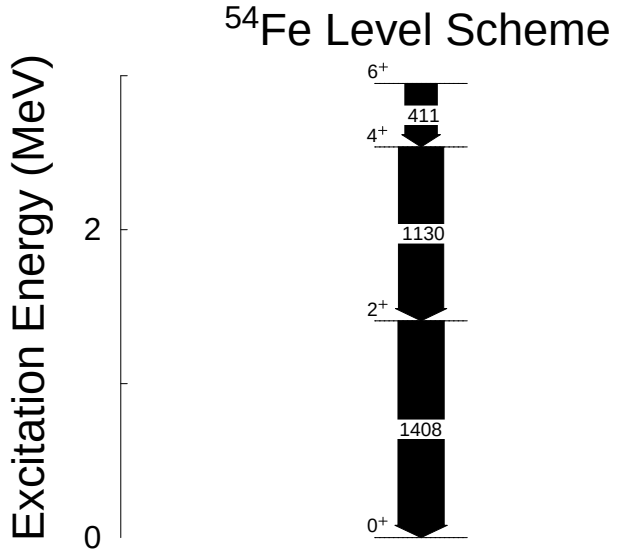

FIGURE 6.21: Level scheme of ^{54}Fe as measured in the present work.

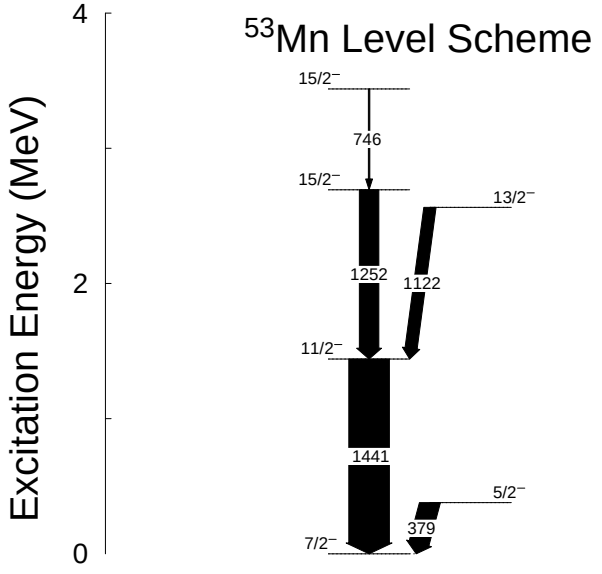

FIGURE 6.22: Level scheme of ^{53}Mn as measured in the present work.

TABLE 6.8: The mostly populated nuclei by evaporation of the compound nucleus ^{68}Ge. The level schemes can be seen in the corresponding figures.

Channel	**Nucleus**	**Level Scheme**	**Reference**
1n2p	^{65}Zn	Fig. 6.23	[89]
2n2p	^{64}Zn	Fig. 6.25-(a)	[90]
2n1α	^{62}Zn	Fig. 6.25-(b)	[91]
1n1p1α	^{62}Cu	Fig. 6.24	[92]

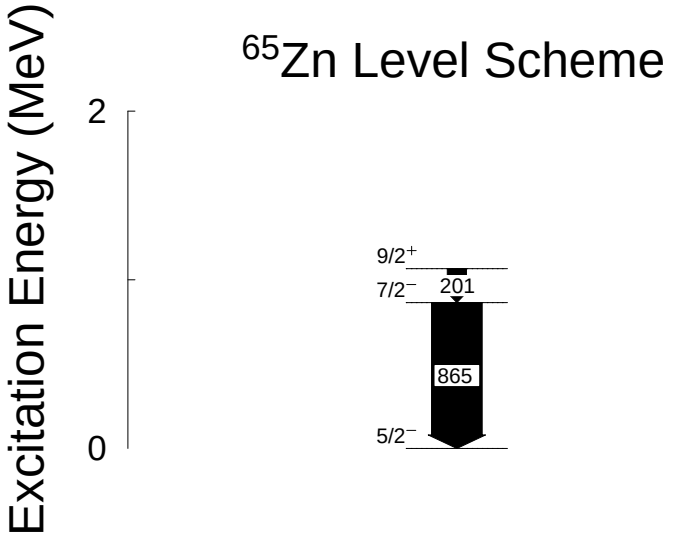

FIGURE 6.23: Level scheme of ^{65}Zn as measured in the present work.

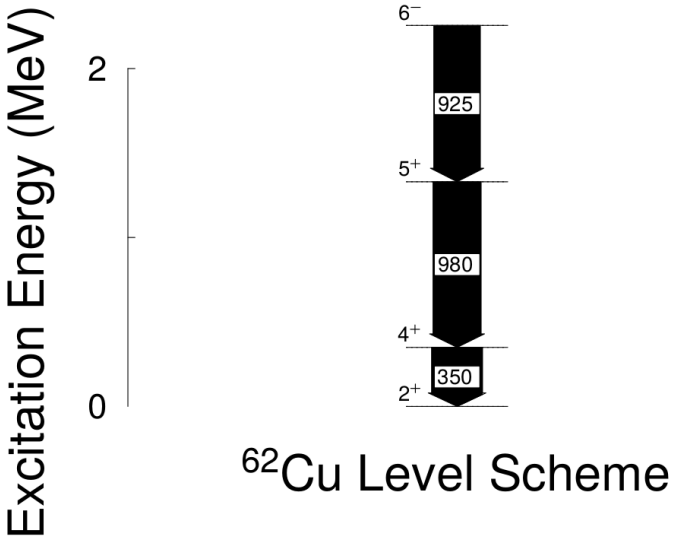

FIGURE 6.24: Level scheme of ^{62}Cu as measured in the present work.

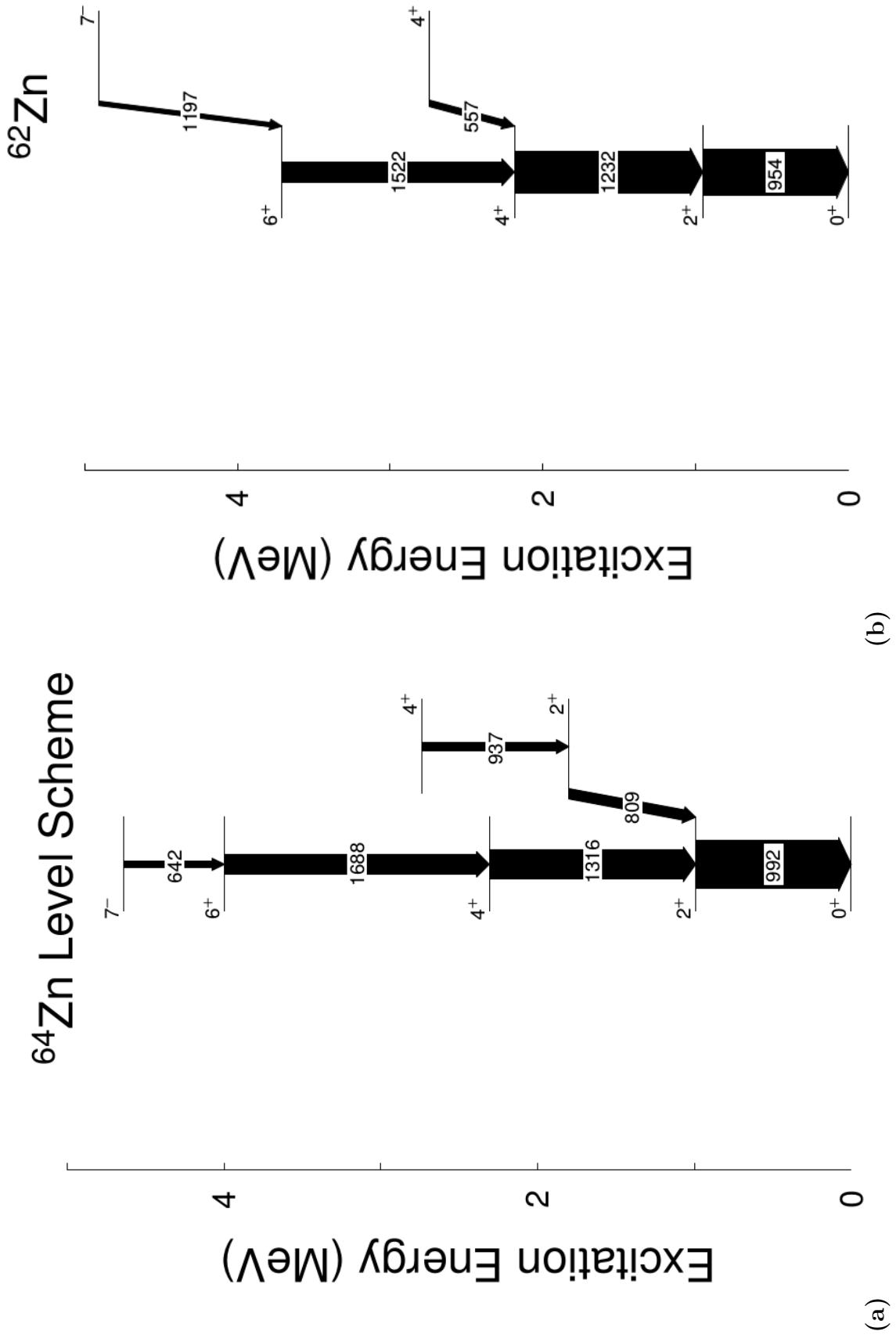

FIGURE 6.25: Level schemes of (a) ^{64}Zn and (b) ^{62}Zn as measured in the present work.

6.7.4 Comparison of the experimental and calculated yields

The yields of the populated nuclei obtained experimentally for the ^{32}S + ^{28}Si and ^{40}Ar + ^{28}Si reactions relative to the most intense detected reaction channel. The theoretical cross-sections have been calculated using the `HIVAP` code, previously mentioned in Sec. 6.5. Since the experimental transition intensities have been determined relatively, the calculated yields have also been normalized to the same nucleus as in the experimental cross-sections (see Fig. 6.26 and Fig. 6.27).

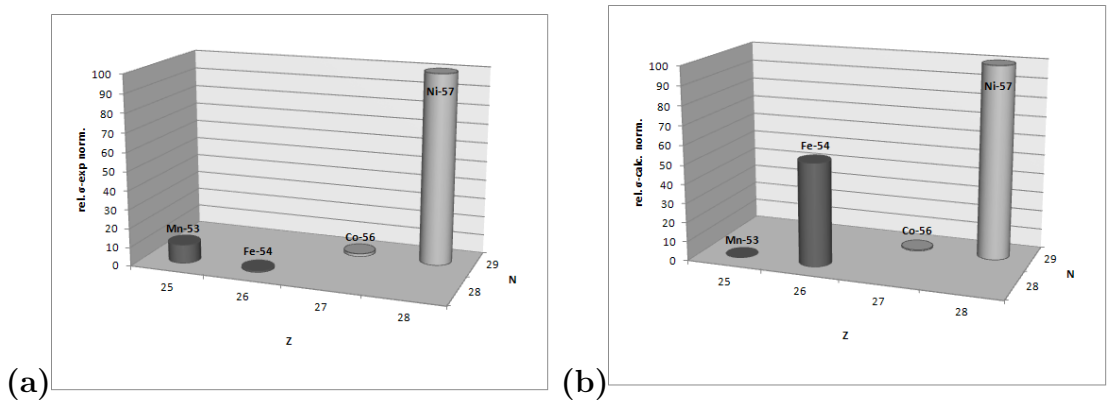

FIGURE 6.26: Relative intensities normalized to the cross-section of the ^{57}Ni nucleus, experimental (a) and calculated (b).

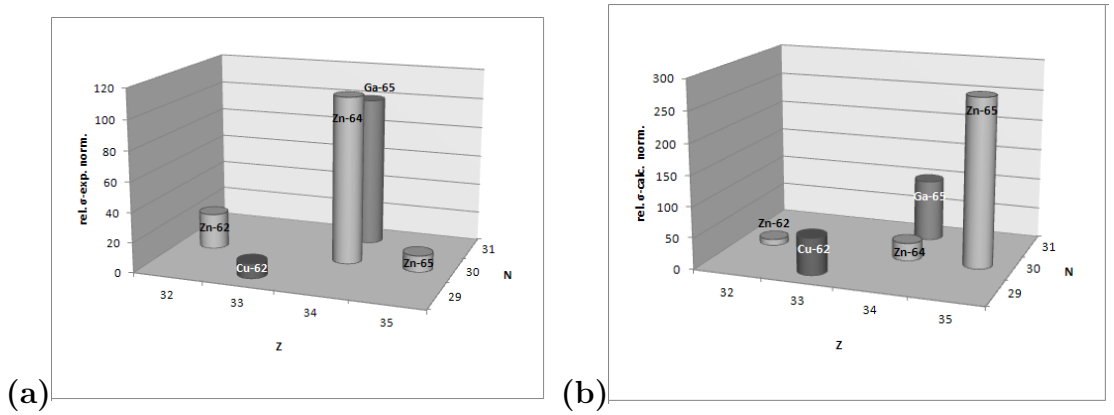

FIGURE 6.27: Relative intensities normalized to the cross-section of the ^{65}Ga nucleus, experimental (a) and calculated (b).

The neutron detection has been requested by the single γ trigger, thus reaction channels emitting less or no neutrons will be suppressed with respect to the ones emitting several neutrons. Some channels can be populated using more than one reaction channel. For example, ^{54}Fe can be populated using either 2n4p or 1α2p channels. The discrepancy between the calculations and the measurements arises

mainly due to only the fraction going through neutron channels will be represented in the experiment.

6.8 Summary and Conclusions

The analysis of this experiment was useful to understand and practice on the use of neutron and light charged-particle detectors for the selection of the reaction channels in fusion-evaporation reactions. The experience acquired has been applied to the design of NEDA (see Chapter 3).

The beam contamination, even if small, prevented us to reach the initial goal of this experiment.

The performance of the Neutron Wall was satisfactory in terms of one-neutron detection efficiency, i.e. 21.1(2.1)%. Fifty segments of the Neutron Wall have been active and working giving ∼10% neutron cross talk probability, which is expected (see Chapter 4). The Neutron Wall has been used in multiplicity filtering mode and provided good channel selection. The two-neutron efficiency was found ∼1.4%. The two-neutron efficiency depends on the neighbor canceling technique to distinguish the event whether it is a real two-neutron event or a one-neutron event fired two detectors (see Chapter 3). The efficiency of this technique depends highly on the granularity of the array. This outcome has been one of the starting points on the conceptual design of the NEDA array (see Sec. 3.1) to make the design in favor of the efficiency of multiple-neutron detection.

The level structures of the populated nuclei are in good agreement with previous works. The new levels discovered in ^{57}Ni nucleus and the multipolarities of the new transitions have successfully been determined.

Chapter 7

Experimental activity at GSI with AGATA-PreSPEC: Collectivity in ^{52}Fe

7.1 Introduction

The experiment has been performed at the PreSPEC setup of the FRS in-flight radioactive ion beam facility at GSI. GSI is one of the leading nuclear physics laboratories in Europe providing in-flight Radioactive Ion Beams (RIBs) at relativistic energies. The importance of having this experiment performed at GSI is that the production of secondary beams at highly relativistic energies, allows a sizeable population of isomeric states [93, 94]. This in principle provides an opportunity to study the collectivity in both the ground state and the isomeric state simultaneously. The physics motivation of the experiment will be explained in more detail in the next section.

After the physics motivation, this chapter will discuss: the reaction mechanism, experimental setup, realistic Monte Carlo simulations, isomeric ratio determination, data analysis and results.

7.2 Physics Background

In the last decade the $1f_{7/2}$-shell nuclei have become a very successful test-bench for nuclear models and interactions. On one side, nuclear structure experiments in the region have benefited from the use of the large γ-arrays, on the other side there was an impressive progress in the shell-model approach due to the appearance of the large-scale shell-model (LSSM) calculations [95, 96]. Near the middle of the shell, nuclei show collective properties similar to those observed in heavier nuclei, such as rotational-like bands, band termination, and back-bending phenomena. Presently this is the unique region where it is possible to describe deformed nuclei within both the mean-field and the shell-model descriptions [96, 97]. The ^{52}Fe nucleus (N=Z=26), with two proton and two neutron valence holes in the doubly magic ^{56}Ni, has been a particular experimental challenge. Most of the known excited states, observed in (^{3}He,n) [98–100] (α,2n) [101] and (p,t) [102] reactions (see also ref. [103]), were at relatively low spin (below 6^+). Many attempts to extend the ^{52}Fe yrast structure to higher spins in fusion-evaporation reactions induced by heavy ions have failed due to the presence of a 12^+ isomer, which acts as a "trap" for the de-exciting γ ray flux. In recent works [104, 105] with high efficiency γ ray detectors the level scheme of ^{52}Fe was extended up to the 10^+ state, thereby confirming the predicted inversion [106, 107] of the yrast 10^+ and 12^+ states and measuring the two E4 γ-branches connecting the 12^+ state to two 8^+ states. Thus the long-lived yrast 12^+ state, with a measured half-life of 45.94±0.60 s [106, 107], was accurately placed at the excitation energy of 6493 keV. In one of the previous in-beam works [104], lifetimes and excitation energies of several states in ^{52}Fe up to I = 8^+ were measured with the GASP spectrometer at LNL (INFN). The B(E2) values, calculated with the code ANTOINE [109] and the KB3 [108] interaction were in rather good agreement with the experimental ones. The shell model calculations also provided the spectroscopic quadrupole moments Q_S; large negative values were obtained for the first two excited states. As already pointed out in Ref. [110], ^{52}Fe behaves as a rotor below I=6, consistently with a K=0 band. Using the rotational model prescription, an intrinsic quadrupole moment $Q_0 \sim 90$ efm^2 was obtained for the lowest 2^+ and 4^+ states from both the theoretical B(E2) values and the quadrupole moments. The deduced quadrupole deformation parameter is rather large ~ 0.23. A recent measurement of the $2_1^+ \rightarrow 0^+$ B(E2) value in ^{52}Fe, using Coulomb excitation techniques [111], is in excellent agreement with the calculation performed in Ref. [104]. A drastic change is noticed at I=6

where Q_S changes sign and becomes very small. Such a behavior can be related, in terms of a deformed Nilsson model, to a crossing between the ground state K=0 band and an excited K=6 band. The K=0 band corresponds to an intrinsic state obtained by filling the $[330]\frac{1}{2}^-$, $[321]\frac{3}{2}^-$, $[312]\frac{5}{2}^-$ Nilsson orbitals with protons and neutrons. The intrinsic state of the K=6 band is constructed by exciting one proton or one neutron from the $[312]\frac{5}{2}^-$ to the $[303]\frac{7}{2}^-$ orbital. This also explains the presence of two 6^+ levels close in energy. The intraband transitions show that the structure of the two rare 6^+ and 8^+ states is strongly mixed with the K=0 ground state band so that we cannot speak of a pure intrinsic state but only give an intuitive image. The LSSM calculations show that the structure of the two K=0 and K=6 bands is largely dominated by a $(f_{7/2})^4$ configuration. In a naive interpretation the change at I=6 might also be viewed as a termination in the subspace of the protons or the neutrons as the spin 6 is the maximum value that can be produced by two holes in the $f_{7/2}$ shell. The nucleons with aligned spins gain energy as their residual interaction is stronger due to the large overlap of their wave functions. This has the effect of lowering the energy of the corresponding excited states that are usually associated with oblate deformation and 'single-particle' rotation.

As shown in Fig. 7.1 the change of regime at I=6 is also reflected in the fractional occupation numbers; the occupation of the $p_{3/2}$ orbit has a marked drop at this point. It is well known that the development of quadrupole coherence giving rise to rotational-like bands in the fp-shell comes from the mixing of the $f_{7/2}$ and $p_{3/2}$ orbits [96, 97]. In the most deformed nuclei of the region, the $p_{3/2}$ occupation number stays almost constant at low spins while at the maximum spin that can be constructed with the valence particles in the $f_{7/2}$ shell, the $p_{3/2}$, $f_{5/2}$, and $p_{1/2}$ occupation numbers vanish for ^{44}Ti (I=12) and become insignificant for ^{48}Cr (I=16). The $f_{7/2}$ becomes the only relevant orbit in these cases where the fully aligned band-terminating states are of non-collective character. The situation is different in ^{52}Fe, where above I=6, all contributions remain almost constant and different from zero as a function of spin even at I=12, thus keeping a residual collectivity predicted for the yrast trap.

The comparison with ^{44}Ti is relevant in this sense. The N=Z ^{44}Ti nucleus has 2 protons and 2 neutrons in the $f_{7/2}$ shell being the self-conjugated partner of the ^{52}Fe at the other end of the shell. Its band termination at 12^+ has almost purely $f_{7/2}$ character and it leads to a lowering of the state's excitation energy

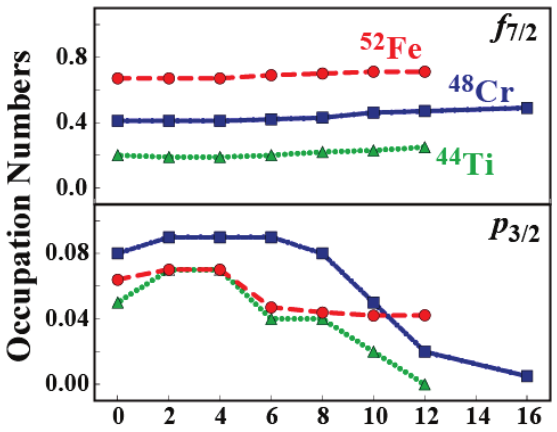

FIGURE 7.1: Calculated ocupation numbers as function of the angular momentum in ^{52}Fe . The LSSM calculation has been performed with the KB3G interaction and the code ANTOINE.

due to the gain in energy of the aligned configuration owing to the large overlap of the wave functions but without going below the yrast 10^+ state. In ^{52}Fe the $(f_{7/2})^4$ configuration accounts only for 60% of the structure of the terminating state and the lowering of the state might be the result of the residual quadrupole collectivity induced by the presence of the $p_{3/2}$ orbital. In ^{52}Fe [104] as well as in ^{52}Mn [112], the observed 3^- state (lying at 4.4 MeV excitation energy in ^{52}Fe), cannot be reproduced by the LSSM calculation including only orbitals from the sd-shell. Already in this two works it is suggested that the contribution of the $g_{9/2}$ intruder orbital could be an important factor. If this is the case it is very likely to find an increase of collectivity in the high spin states of these nuclei due to $(g_{9/2})^2$ configurations. Another clear fingerprint can be found in a high-sensitivity experiment performed at Gammasphere in which a $g_{9/2}$ band in ^{51}Mn was identified [113] with the $\frac{15}{2}^+$ bandhead lying at 7296 keV excitation energy. Recent experimental studies brought strong evidence for the role of the $g_{9/2}$ orbital at medium spins in Z=28 nuclei. In a recent work studying the structure of ^{56}Ni it was pointed out that the contribution of the $g_{9/2}$ orbital, in the configuration of the yrast and first yrare 8^+ states, can justify the fact that LSSM calculations, with state of the art interactions, do not succeed to describe their de-excitation pattern [114]. In ^{54}Ni has been recently identified the particle decay of the 10^+ isomer by emitting a $g_{9/2}$ proton [115].

It also was reported by our group [105] the measurement of the E4 γ de-excitation of the 12^+ yrast trap in ^{52}Fe to the two known 8^+ states. The experiment was performed at the GSI on-line mass separator. The evaluated intensities reflect

very low E4 transition probabilities: $4.6(17)\times10^4$ W.u. and $3.5(13)\times10^3$ W.u. for the $12^+ \rightarrow 8_1^+$ and $12^+ \rightarrow 8_2^+$ transitions, respectively. If one compares the ^{52}Fe data with the B(E4) observed in other $f_{7/2}$ shell nuclei, to obtain the lowest value, corresponding to ^{52}Mn (0.138 W.u.), partial de-excitation branches that are $\sim$300 and $\sim$40 times higher than those observed for the $12^+ \rightarrow 8_1^+$ and $12^+ \rightarrow 8_2^+$ transitions, respectively, would be required. In order to interpret these results calculations in the shell model framework with the code ANTOINE [109] in the full pf model space were performed. Three different residual interactions have been used, namely the FPD6 [116], the KB3G [117], and the GXPF1 [118] interactions. All calculations overestimate the experimental values. The best description is achieved by the FPD6 interaction while both the KB3G and GXPF1 calculations fail in reproducing even the order of magnitude of the B(E4). The FPD6 calculation in turn is not especially good calculating the ^{52}Fe energy spectra, as it fails largely to reproduce excitation energies and transition probabilities from the low-lying states. The only reason to explain the huge difference and better agreement found between the B(E4) calculated with FPD6 and the other two interactions is that FPD6 predicts a more than 50% larger collectivity for the 12^+ state while KB3G and GXPF1 predict comparable values for the $f_{7/2}$ occupation number. This fact was also discussed by B. Castel and L. Zamick in Ref. [119], where it is mentioned that hexadecapole of electric character show significant retardation with respect to the corresponding shell model calculation in the pf-shell. In this work it is pointed out that effect due to deformation can be very important, in particular the fact that a quadrupole deformation will alter a hexadecapole moment.

A frequently employed method to investigate the collectivity of the states is the measurement of the transition probabilities. Large B(E2) values are expected in collective states. The first step to understand if such measurement can be performed in the isomeric states of ^{52}Fe is to calculate where the 12^+ and 14^+ yrast or near-yrast states are predicted. In our case this has been achieved performing LSSM calculations in the pf-shell model space, with the GXPF1 interaction and the code ANTOINE. The preliminary calculations limited to 8 particle excitation (truncated calculation) and effective charges $e_p = 1.5$, $e_n = 0.5$. The resulting states above the yrast 12^+, transitions and calculated B(E2) are shown in Tab. 7.1.

The structure of the 12^+ yrast trap in ^{52}Fe is still largely not understood. The investigation of this state by Coulomb excitation can provide excitation energies

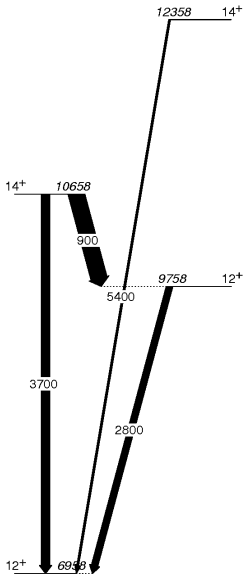

FIGURE 7.2: Calculated level scheme for the yrast and near yrast states in ^{52}Fe above the 12^+ yrast trap. The LSSM calculation has been performed with the GXPF1 interaction and the code ANTOINE. Intensities are proportional to the emission probability.

TABLE 7.1: Calculated B(E2) above the 12^+ yrast trap.

$\mathbf{E}_i$ [keV]	$\mathbf{I}_i$ [$\hbar$]	$\mathbf{E}_\gamma$ [keV]	$\mathbf{E}_f$ [keV]	$\mathbf{I}_f$ [$\hbar$]	**B(E2)** [$\mathbf{e^2fm^4}$]
9758	12_2^+	2800	6958	12_1^+	21
10658	14_1^+	3700	6958	12_1^+	27
10658	14_1^+	900	9758	12_2^+	53
12358	14_2^+	5400	6958	12_1^+	6

of the higher-lying states beyond the 12^+ as well as transition probabilities. The information gained will be a strong constraint for the LSSM calculations in the full fp-shell and will contribute to the understanding of build-up of the collectivity and the role of the $g_{9/2}$ orbital in stabilizing the structure of the nuclei from the upper half of the $f_{7/2}$ shell in the vicinity of ^{56}Ni. Additionally physics with isomeric beams is still at an early stage of development. While the recent success obtained at the REX-ISOLDE [120] ISOL-facility on producing and Coulomb exciting a purified isomeric beam of ^{68m}Cu at low energy has opened new perspectives for the nuclear structure studies, isomeric beams have been very seldom use at fragmentation facilities despite that in several occasions it was stressed the importance of using such beams for nuclear structure experimental studies [121]. The ^{52}Fe isomer with its high excitation energy of 6957 keV, high spin of $12\hbar$ and

long half-life of 45.94 s has characteristics that only multi-quasiparticle isomers in the mass region 180-200 can offer. Our study will provide important information on the population of high-spin/high excitation energy isomeric states and the isomer-to-ground state ratio in fragmentation reactions.

7.3 Reaction mechanism

In the present study we aim to investigate the collectivity in the ^{52}Fe states employing relativistic Coulomb excitation. In order to perform such reaction, the radioactive ^{52}Fe beam has to be produced at relativistic energies. This has been done at GSI where the primary ^{58}Ni ions are accelerated by the UNIversal Linear ACcelerator (UNILAC) and SchwerIonen Synchrotron (SIS18) with 600 MeV/u. The secondary RIBs are produced following the fragmentation of the primary beam with ^{9}Be target with a thickness of 4 g/cm^2. A schematic view of the fragmentation process can be seen in Fig. 7.3. Fragmentation reactions are peripheral nuclear

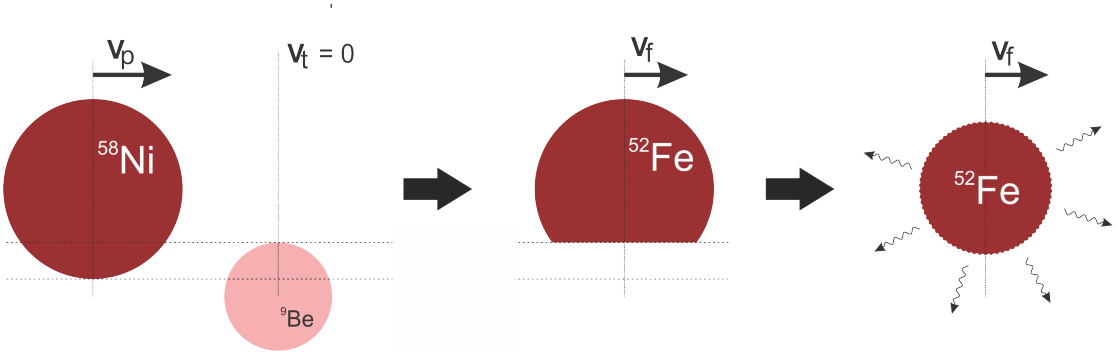

FIGURE 7.3: The schematic explanation of how the ^{52}Fe ion fragments were produced at GSI.

collisions between heavy projectiles and light targets at relativistic energies. The process could be described by using the *abrasion* - *ablation* model [122]. Fragmentation is done, as well, with a light target to keep lower angles in the forward kinematic of the reaction. This particular primary reaction has been previously studied at similar energy and the ^{52}Fe production cross-section has been measured to be about 2.1 mb (see Table 1 in Ref.[123]). After the primary reaction, the secondary beam is selected in flight using the FRagment Separator (FRS). The selection mechanisms and the components of the FRS will be discussed later in this chapter (see Sec. 7.4.1).

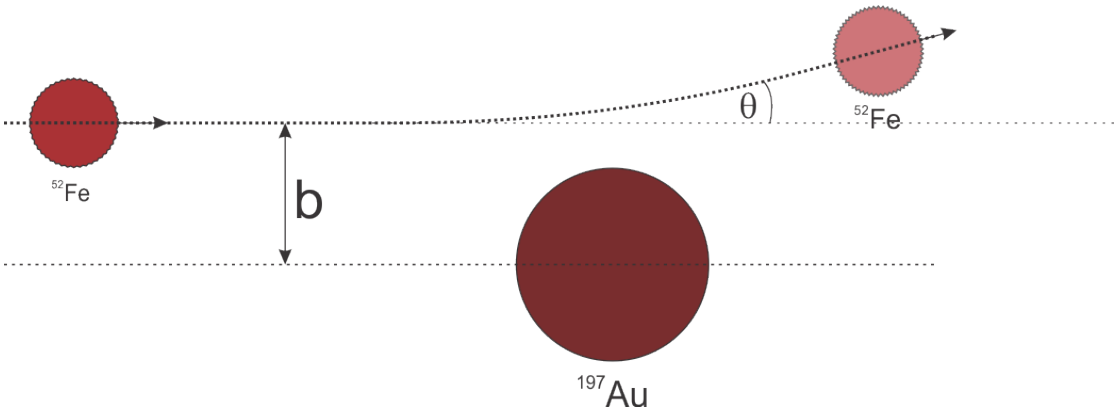

FIGURE 7.4: The schematic explanation of the inelastic scattering of two nuclei.

The Coulomb excitation is an inelastic scattering reaction which allows energy transfer through the electromagnetic field (see Fig. 7.4). This technique is used to populate the excited states in exotic nuclei and to study the corresponding electromagnetic transition matrix elements - B(Eλ) and B(Mλ).

Non-relativistic Coulomb excitation can be performed at energies below the Coulomb barrier, such that the interactions of nuclear origin are suppressed. On the other hand, in relativistic Coulomb excitation, the ions are at high energies (30-300 MeV/nucleon), and the energy of the projectiles are largely above the Coulomb barrier, then the projectile and target might interact through the nuclear forces in addition to the Coulomb one. In order to make sure that nuclear contributions are small, one needs to keep the projectile and target nuclei separated during the scattering process. The Sommerfeld parameter gives an approximate condition for the classical behaviour in the scattering process:

$$\eta = \frac{a}{\lambda\!\!\!^{-}}, \text{ where } a = \frac{Z_1 Z_2 e^2}{m_0 c^2 \beta^2} \tag{7.1}$$

where a is half the distance of the closest apporach and $\lambda\!\!\!^{-}$ is the reduced wavelength. Z_1, A_1 and Z_2, A_2 are charge and mass numbers of projectile and target nucleus, respectively. The Sommerfeld parameter, η, ensures that one may form a wavepacket containing several waves and still having a size which is small compared to the dimensions of the classical trajectory with the condition $\eta \gg 1$ [124]. The semi-classical approach is appropriate for a relatively heavy projectile scattered on a heavy target, like in our case, a Au target, since the Sommerfeld parameter is still $\gg 1$. The scattering angle of the projectile ions is related to the minimum

distance between the projectile and the target (b_{min}) which becomes identical with the maximum closest approach D:

$$b = \sqrt{D^2 - \frac{2 \times a \times D}{\gamma}} \tag{7.2}$$

$$D(\theta_{cm}) = \frac{a}{\gamma} \times \left[1 + sin^{-1}\left(\frac{\theta_{cm}}{2}\right)\right] \tag{7.3}$$

Larger angles will correspond to larger Coulomb force, thus smaller distance b. In our case, we selected the impact parameter b = 18 fm, 6.3 fm larger than the distance of the closest approach to be conservative. Thus the nuclear matter distributions of the two interacting nuclei would not overlap at any time. This is crucial for calculating the Coulomb excitation cross section accurately.

The relativistic Coulomb excitation cross section is a function of the electromagnetic matrix elements B(Eλ) and B(Mλ). Thus, measuring the cross-sections via Coulomb excitation the following basic nuclear structure properties are obtained:

- The excitation energy of a low lying excited state of a nucleus
- Electromagnetic transition matrix element B($\mu\lambda$).

The relation between the Coulomb excitation cross section and the sum of the allowed multipole matrix elements is explained in Ref. [125] as:

$$\sigma_{i \to f} = \sum_{\pi\lambda} \sigma_{\pi\lambda} \tag{7.4}$$

where,

$$\sigma_{\pi\lambda} \approx \left(\frac{Z_p e^2}{\hbar c}\right)^2 \frac{B(\pi\lambda, 0 \to \lambda)}{e^2 R^{2\lambda}} \pi R^2 \begin{cases} (\lambda - 1)^{-1} & \text{for} \quad \lambda \geq 2 \\ 2ln(\rho_a/R) \geq & \text{for} \quad \lambda = 1 \end{cases} \tag{7.5}$$

where ρ_a denotes the impact parameter at which the adiabatic cutoff of the Coulomb exciation process sets in. This occurs when the time of internal motion in the nucleus $\hbar/E_\gamma$ equals the collision time $\rho_a/(\gamma c\beta)$, where E_γ is the energy of the excited state $< f \mid$ relative to the initial state $\mid i >$. Thus the maximum

energy of final states that can be excited in collisions with impact parameter b is of the order of;

$$E_{\gamma}^{\max} \approx \frac{\gamma \hbar c \beta}{b} \tag{7.6}$$

In our case, the maximum excitation energy is 6.5 MeV. The Coulomb excitation cross-section as a function of the projectile energy is discussed by Glasmacher in Ref. [126]. In Figure 1 of Ref. [126], it is shown how the cross-section of the Coulomb excitation of the first excited state, the giant dipole resonance (GDR) and the giant quadrupole resonance (GQR) changes with different ^{40}S projectile energies. The Coulomb excitation of the first excited state is dominant below the energy of the projectile of 100 MeV/nucleon, while for the giant resonances, energies above 300 MeV/nucleon become ideal.

In short and on view to the previous discussion, the relativistic Coulomb excitation will allow to excite low-lying states in ^{52}Fe both above the ground and isomeric state. The determination of the Coulomb excitation cross-section will allow to deduce the electromagnetic transition matrix elements, thus gaining information on the collectivity of the states.

7.4 Experiment

It was mentioned earlier in this chapter that the experiment has been performed at GSI, the PreSPEC setup of the FRS. In Fig. 7.5, a schematic drawing of the GSI is shown. In this figure, the location of the ion sources, the linear accelerator, the synchrotron and the FRS are indicated.

The ^{52}Fe ions have been produced by the fragmentation of a ^{58}Ni primary SIS beam at 600 MeV/u impinging on a 4 g/cm^2 ^{9}Be primary FRS target. The primary beam intensity was of the order of 10^9 ions per spill with spill-on and spill-off periods of 3 and 2 seconds, respectively. The secondary beam after the fragmentation reactions of the primary beam on the primary target, is simply a mixture of radioactive isotopes, and the isotope of interest has to be separated, i.e. ^{52}Fe in this case. The selection is done by means of the FRS and after separation, the ions of interest are impinging into the secondary target, i.e. in our case a 400 mg/cm^2 ^{197}Au target.

The FRS uses the $B\rho$ - ΔE - $B\rho$ technique to separate the reaction products (see Fig. 7.6). Change of direction of the velocity vector of a charged particle inside a magnetic field is a known fact, the Lorentz force and widely used in similar experiments and applications, like magnetic spectrometers or separators (see Eq. 7.7).

$$\mathbf{F} = q(\mathbf{E} + \mathbf{v} \times \mathbf{B}) \tag{7.7}$$

Note that the charged particle would experience the Lorentz force only when it is moving. The deviation from the initial trajectory of the moving ion inside a magnetic field depends on its mass and charge,

$$B\rho = \left(\frac{A}{Q}\right).\frac{m_0 c}{e}.\beta\gamma \tag{7.8}$$

where A is the mass number, Q is the charge state, m_0 is the mass at rest, $\beta\gamma$ is the relativistic reduced momentum with β=v/c, being v the velocity.

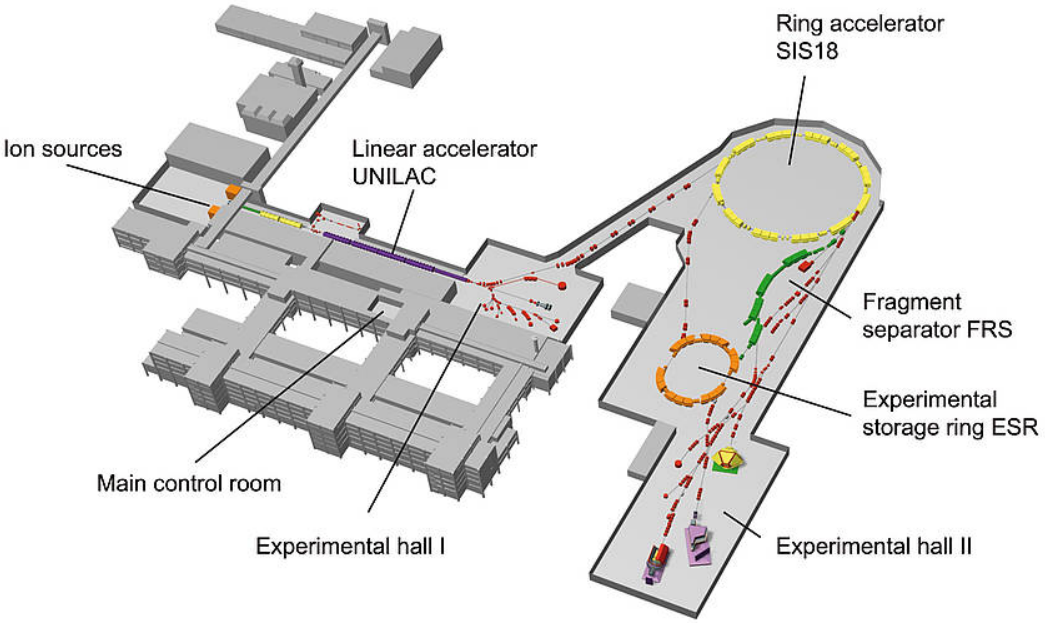

FIGURE 7.5: A schematic drawing of the GSI accelerator facility.

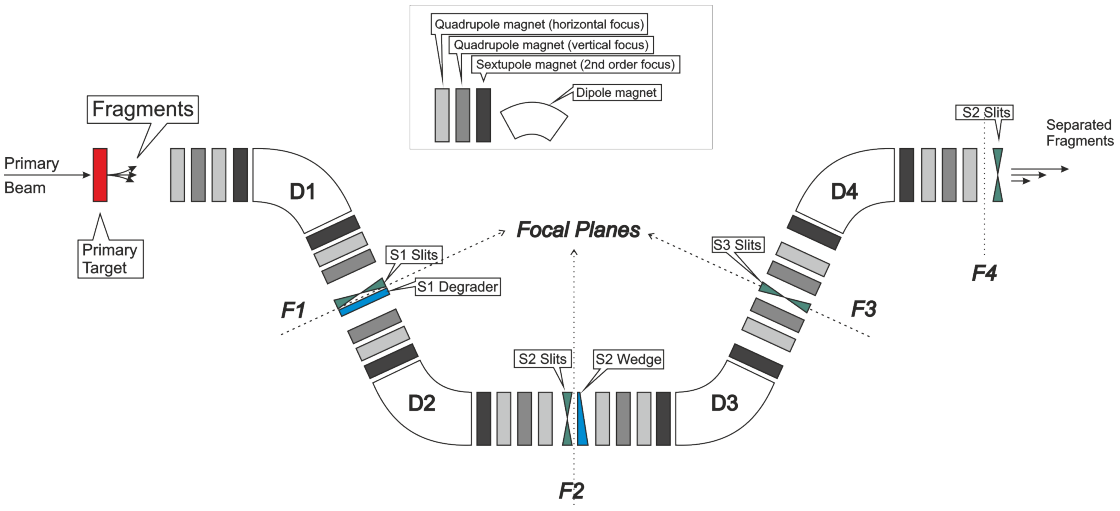

FIGURE 7.6: Illustration of the optic elements of the FRS for the ion separation process. The secondary beam which consisted of the fragment residues of the primary beam after the fragmentation reactions, is produced in the primary target and then the ions are separated in flight. The settings of some of the elements are given in Table 7.2.

The fragment selection is done in two stages in FRS. The first stage includes all optical elements from the entrance to the F2 focal plane shown in Fig. 7.6. The velocity of the residual ions after the fragmentation reactions is largely preserved. The magnetic fields and curvature radii of the dipoles D1 and D2 distribute the secondary beam in F2 as a function of the magnetic rigidity $B\rho_2$, that depends largely on the A/Q ratio (see Eq. 7.8).

The second stage of FRS goes from the F2 focal plane to the F4. A noticeable amount of ions with A/Q ratio similar to the reference one are going through the first stage with the selected ions. The energy distribution of the ions is modified using an Al wedge degrader. The ions distributed at S2 depending on their magnetic rigidity, lose their energy in the wedge, therefore reduce their velocity, depending on their trajectories, i.e. depending on the thickness of the section of the wedge they go through (see Fig. 7.7).

The FRS has been operated in the achromatic mode in the current experiment. In this mode, the resulting transversal position of the ions at F4 is independent from their momentum at the exit of the degrader.

The D2 and D4 dipoles are adjusted to fullfill Eq. 7.9.

$$B\rho_4 = \frac{p_f}{p_i}.B\rho_2 \tag{7.9}$$

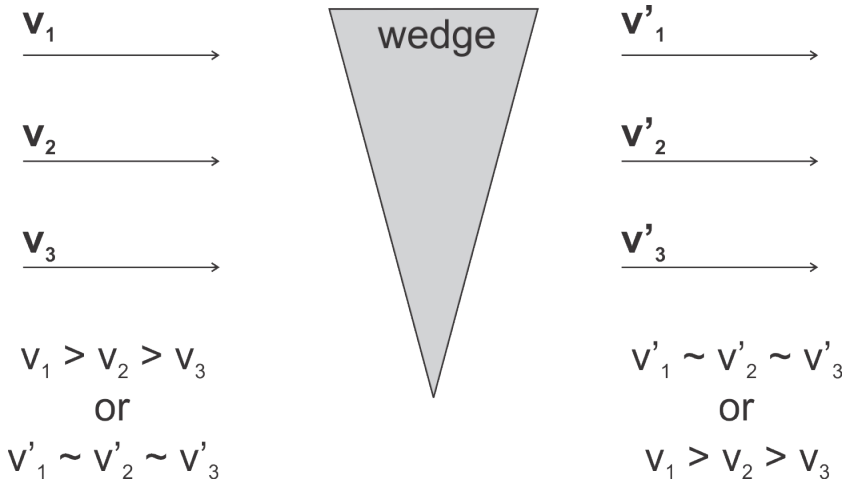

FIGURE 7.7: A schematic view of how the velocities of the ions are equalized or spread in the energy loss process.

The MOCADI [127, 128] and LISE++ [129] simulations were done before the experiment to determine the best possible settings for the FRS elements. LISE++ is a powerful and user-friendly tool to simulate the transmission efficiency of the ions at several different laboratories, like GSI, GANIL, RIKEN or NSCL. This tool allows the user to use different blocks that represent the optical elements and matter and to be able to define their settings and material composition. Such flexibility makes possible to quickly optimise the setting for a particular fragment. LISE++ also provides tools to calculate and plot the energy loss of a beam before, inside or after a material, time of flight between two given points, etc... The suggested settings in the simulations to select the ^{52}Fe ions with best accuracy can be seen in Table 7.2. The counting rate was 1.7×10^{6} at S2 area and 1.03×10^{5} at S4 with the listed settings. On the other hand, the MOCADI Monte-Carlo code, more accurate simulating the transmission through FRS, was used to obtain the settings of the FRS magnetic elements.

7.4.1 The FRagment Separator (FRS) detectors

The FRS is divided into 4 areas which are separated by 4 dipole magnets after the primary target, and are called S1, S2, S3 and S4. The FRS detectors are distributed in two focal planes, S2 and S4 areas.

The FRS detectors consist of plastic scintillators for time-of-flight measurements, time projection chambers for the position determination and ionization chambers

TABLE 7.2: Settings of the FRS elements during the experiment. These settings were determined with LISE++ simulations before the experiment. The horizontal settings of the S2 slits were modified for this experiment, the reason for such change will be given later.

FRS element	**Setting**	**Material/Orientation**
S1 Slits	±20 mm	Horizontal
S1 Degrader	2 g/cm^2	Aluminium
S2 Slits	-10, +70 mm	Horizontal
S2 Slits	±100 mm	Vertical
S2 Wedge	4 g/cm^2	Aluminium
S3 Slits	-30, +10 mm	Horizontal
S4 Slits	±20 mm	Horizontal

for the energy loss measurement. These detectors and their use in FRS will be described in the following subsections.

7.4.1.1 Time Projection Chambers (TPCs)

The time projection chamber (TPC) is a position sensitive detector [130, 131]. It has a vertical drift space with respect to the beam direction, it is filled with Ar gas at atmospheric pressure and works at room temperature. The drift space has cathode and anode in upper and lower ends, respectively. The structure of the lower end of the drift space includes, a shielding grid (Frisch grid), anode and four proportional counters with C-pad cathodes. The drift space is surrounded by mylar strips of 20 μm thick which are coated with aluminium of 0.5 μm thick. A schematic drawing of the TPC could be found in its manual provided by GSI, and can be seen in Fig. 7.8.

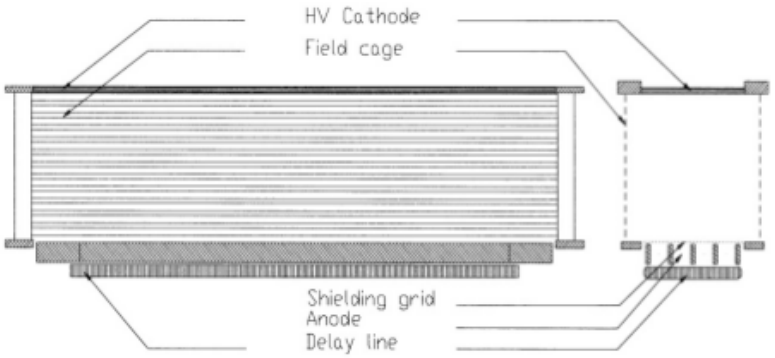

FIGURE 7.8: Schematical view of the TPC.

A high voltage is applied on the cathode to create electric field. The mylar strips are connected to the voltage divider and a voltage up to 400 V/cm is applied to the divider to form a uniform electric field. The proportional part is placed underneath the drift space and is separated by a shielding grid which is kept at negative potential (-80 V). The proportional part consists of four anode wires of 20 μm in diameter and placed inside C-shaped pad formed cathodes. Each C-pad is connected to an integrated passive delay line.

The vertical position of an incident particle is proportional to the drift time of the ionized electron. The horizontal position is determined by the measurement of the time difference between the arrival of the signals at the left and at the right end of the delay line. Another way to determine the y-coordinate is by the measurement of the sum of the arrival time of the signals on both sides of the delay line. Then the sum will consist of the length of the delay line and double of the drift time. The TPC provides a two dimensional position measurement.

Four TPCs were placed during the experiment: Two of them at the S2 and the others at the S4 focal plane. The TPC read-outs are acquired by conventional TDCs.

7.4.1.2 MUlti Sampling Ionization Chambers (MUSICs)

The MUlti Sampling Ionization Chamber (MUSIC) is used to determine the energy loss of the particles. The detector has a chamber which filled with pure CF_4 gas at atmospheric pressure (see Fig. 7.9). The chamber is covered with anode strips at the top and cathode at the bottom. The gas is ionized as the charged particles pass through and the electrons and ionized molecules give rise of the signals at the anode strips and cathode, respectively.

The ions inside the beam are *ideally* striped off of their electrons, if the beam consists of light nuclei like in our case, therefore they are positively charged ions. As the beam passes through the gas, its Coulomb field will displace electrons from the gas molecule, creating an ion-electron pair. The number of ions produced is proportional to the energy loss and also is proportional to the charge of the incoming ion. The mean energy loss per distance of an ion inside a material is described by the Bethe formula [132]. According to the Bethe formula the energy loss per distance is related to the square of the charge of the incoming ions, *the*

Z number. Ions with different Z numbers will lose different amount of energy and the energy spectrum will represent the Z number distribution of the ions inside the beam.

The gas counters are quite efficient allowing to detect up to 90% of the ions. On the other hand, they are relatively slow detectors, i.e. the electron collection in a gas detector is of the order of several microseconds and the ion collection is of the order of milliseconds. If the counting rate is too high, like in the case of the current experiment, one could suffer from pile-up. This is partially overridden by using digital read-outs with pile-up suppression capabilities. A comparison of two energy loss spectra, one obtained using the pile-up module and the other with the conventional module is shown in Fig. 7.10.

The pile-up counts of the conventional output of the MUSIC are most likely overflowed and are not within the ADC range. The digital read-out with pile-up suppression is more efficient as seen on the same figure.

7.4.2 ToF detectors

Time-of-flight (ToF) of the ions are recorded in two ways in FRS, using two different detectors, standard and finger, in the S2 area and a standard detector in the S4 area (see Fig. 7.11). The finger ToF detectors are better, on high counting rate conditions, than the standard plastic scintillator detectors due to their segmented structure (see Fig. 7.12-b). Therefore they are more useful in the current experiment due to high counting rates at the S2 area.

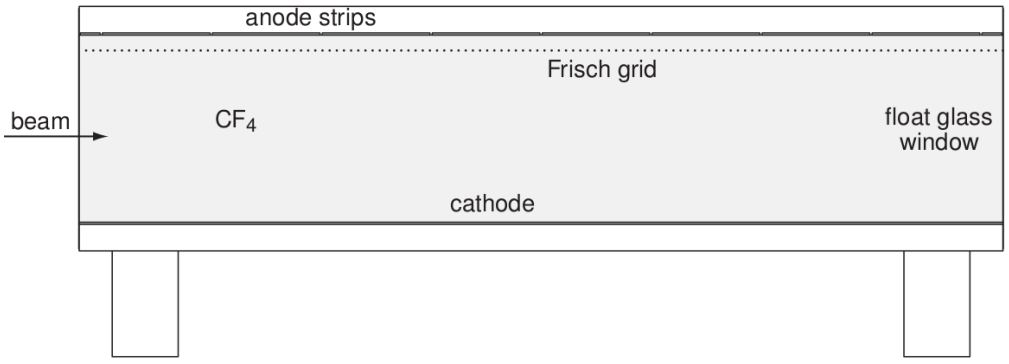

FIGURE 7.9: An artistic view of the MUSIC detector showing its parts. Drawing taken from the technical manual of MUSIC.

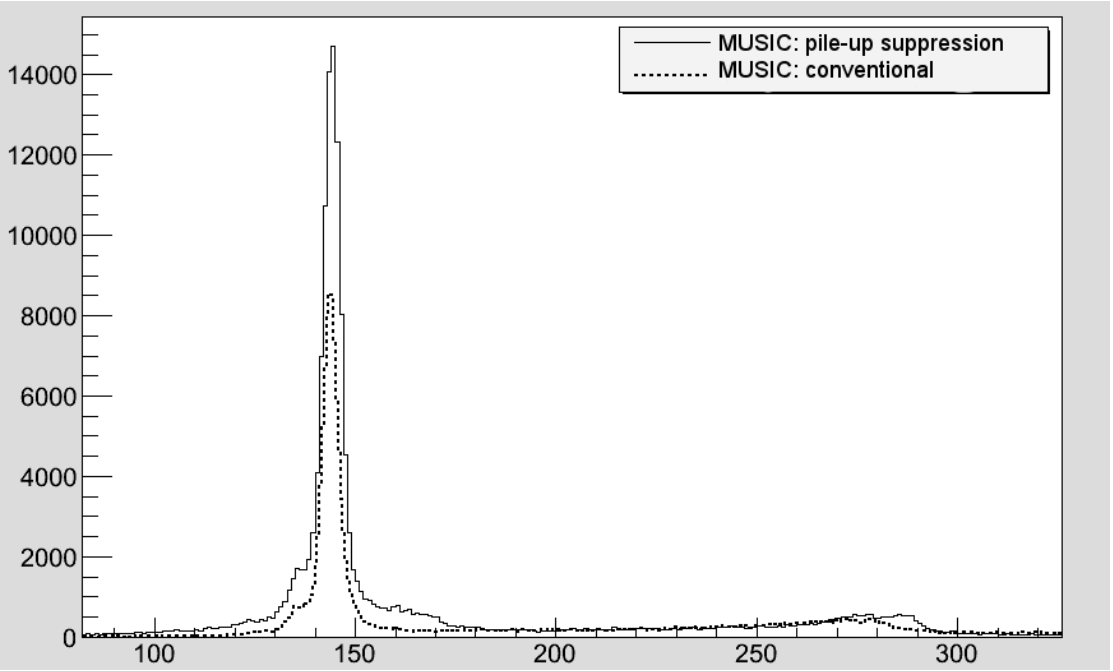

FIGURE 7.10: Comparison of pile-up suppressed and unsuppressed spectra of the MUSIC detectors.

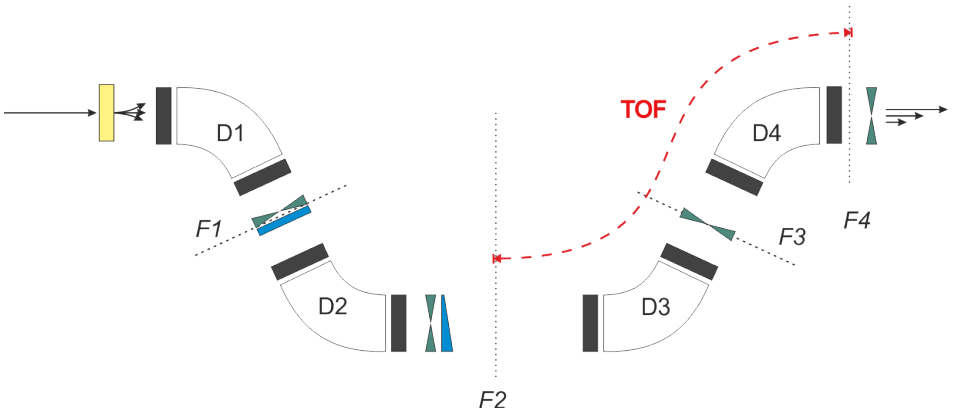

FIGURE 7.11: Illustration of the FRS. The drawing in Fig. 7.6 is simplified to focus on the ToF measurement.

Finger detectors are consisted of 15 segments, attached to 16 photomultiplier tubes (PMTs) at the top and the bottom. While, the standard detectors have two PMTs at their left and right sides (see Fig. 7.12-a).

There are three more ToF detectors for measuring the times before and after the secondary target, and they are located as; one in the S4 area, one inside the target chamber, and the last one in LYCCA. Two of these detectors (see Fig. 7.13) are identical in size and material (BC-420), which are located in S4 and in LYCCA.

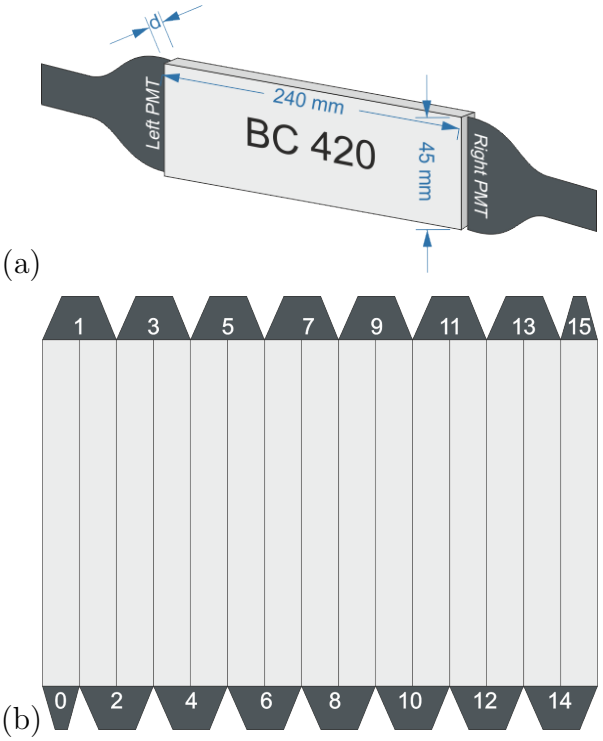

FIGURE 7.12: Schematic views of the Standard (a) and Finger (b) detectors. The thickness d in the standard scintillator is 2.765 mm and 3.15 mm for the S2 and S4 area ToF scintillators, respectively. The thickness of the finger detectors is 4.4 mm.

The one inside the target chamber is made of the same material except its size is smaller.

These detectors are also position sensitive. The position of the ion inside the detector could be re-constructed using the time difference between the fired PMTs for each event.

The high counting rates at S2, mentioned previously in Sec. 7.4, i.e. of the order of 10^6 per spill, makes the standard S2 ToF scintillators to function with relatively low performance. Since the Finger ToF scintillators show a better performance (see Fig. 7.12), the determination of the ion velocities is done using the ToF between S4 standard ToF scintillator and the S2 Finger scintillator.

The standard scintillators at S2 and S4 are attached to three TDC modules with multihit capabilities on FRS, LYCCA and USER crates (see Sec. 7.5). The Start, Target and Stop ToF detectors are connected to the multhit TDC modules on the LYCCA crate. The Finger detector is connected to the multihit TDC on the FINGER crate.

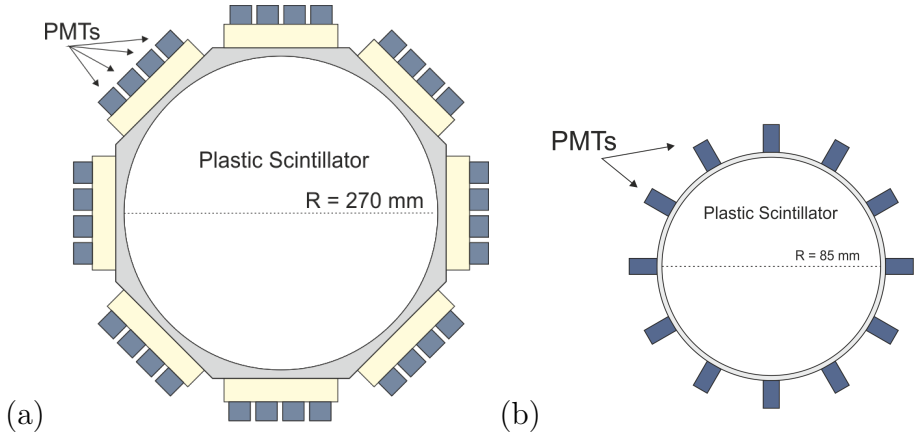

FIGURE 7.13: The position sensitive ToF detectors. Two large detectors with 32 PMTs (a) are positioned in S4 area and 3712 mm away from the target chamber in the beam downstream. The small detector with 12 PMTs (b) is positioned inside the target chamber.

7.4.3 The LYCCA detectors

The Lund-York-Cologne CAlorimeter (LYCCA) detector system [134] is located approximately 3.7 m away in the beam downstream after the target chamber, and is composed of Double-Sided Si-Strip Detectors (DSSSD), Cesium-Iodide (CsI) detectors and plastic scintillators for the ToF measurements. LYCCA can discriminate the ions using their total energy, energy loss and time-of-flight information. A schematic overview of LYCCA together with the ToF detectors can be seen in Fig. 7.14.

One can see from the figure that the LYCCA detectors are not used only to detect the released energy by the ions, but also to detect the scattering angles of each event. The angle determination is done in two stages: first the trajectory of the ions before hitting the secondary target is determined using the xy positions on the TPC and Target-DSSSD detectors, and second the trajectories after hitting the secondary target are calculated using the xy positions on Target-DSSSD and wall-DSSSD detectors. Angular difference between two trajectories, i.e. before and after the target, gives the scattering angle of the ions in the secondary target.

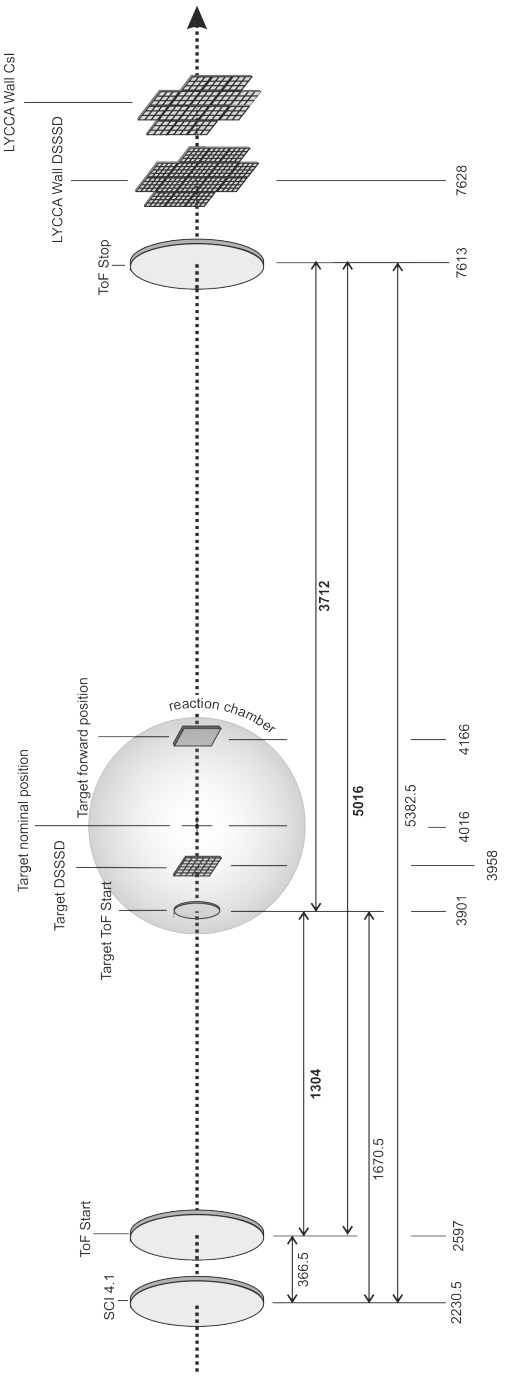

FIGURE 7.14: A schematic view of the focal point F4, target chamber and the LYCCA detector system. The distances are given in mm.

7.4.3.1 Double-Sided Si-Strip Detector (DSSSD)

The DSSSDs are position sensitive detectors which determine the energy loss of the ions. There are two types of DSSSDs used in LYCCA: Target DSSSD and Wall DSSSD. Target DSSSD consisted of one single Double-Sided Silicon Strip Detector which has 32 strips on each side. Considering that size of the detector side is 58 mm, the Target DSSSD has 1.8 × 1.8 mm^2 accuracy in the position determination. The Wall DSSSD system consisted of 16 modules with the same size as in the Target DSSSD, but with 16 strips on each side. Thus it has 3.6 × 3.6 mm^2 position accuracy. The thickness of one DSSSD module is 303(3) μm. The distance between the Target DSSSD and the Wall DSSSD was 3712 mm.

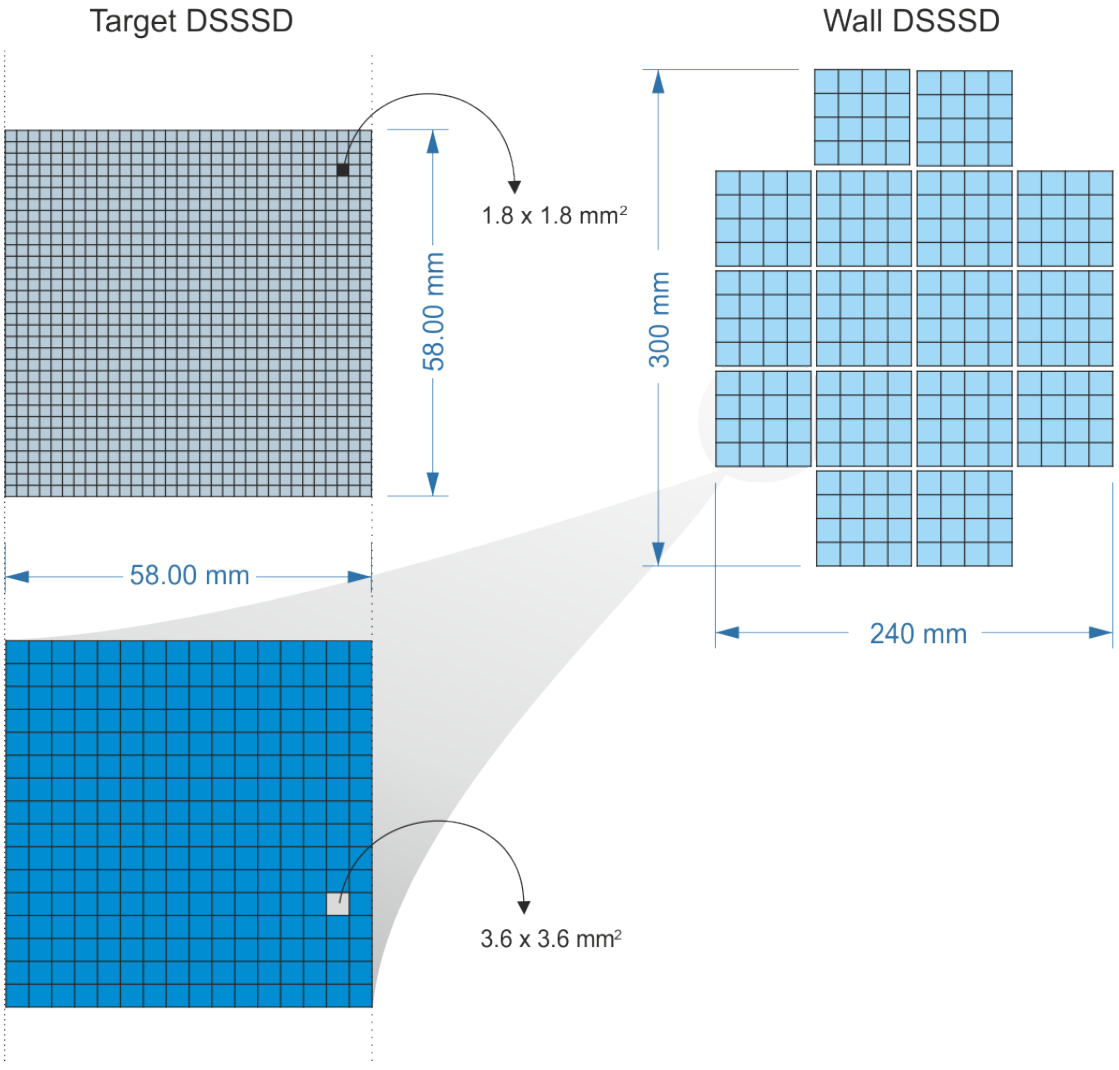

FIGURE 7.15: The two DSSSDs of LYCCA. The Target DSSSD consisted of one module with 32 strips on each side. The whole Wall DSSSD array consisted of 16 modules and each module has 16 strips on each side.

7.4.3.2 Cesium-Iodide Detector (CsI)

The CsI detectors are used to measure the residual energy of the arriving ions. They are square shaped and nine of them fit behind one of the Wall DSSSD modules. Their active size is 20 × 20 mm^2 with a wrapping of 0.25 mm VM2000/ESR foil to improve surface light reflection properties. Their depth is 13 mm plus a 7 mm thick pyramidal light guide that adapts de dimension of the detector to 10 × 10 mm^2 for the coupling with the light-readout photodiode. The full CsI array is built up 16 of nine-packed modules.

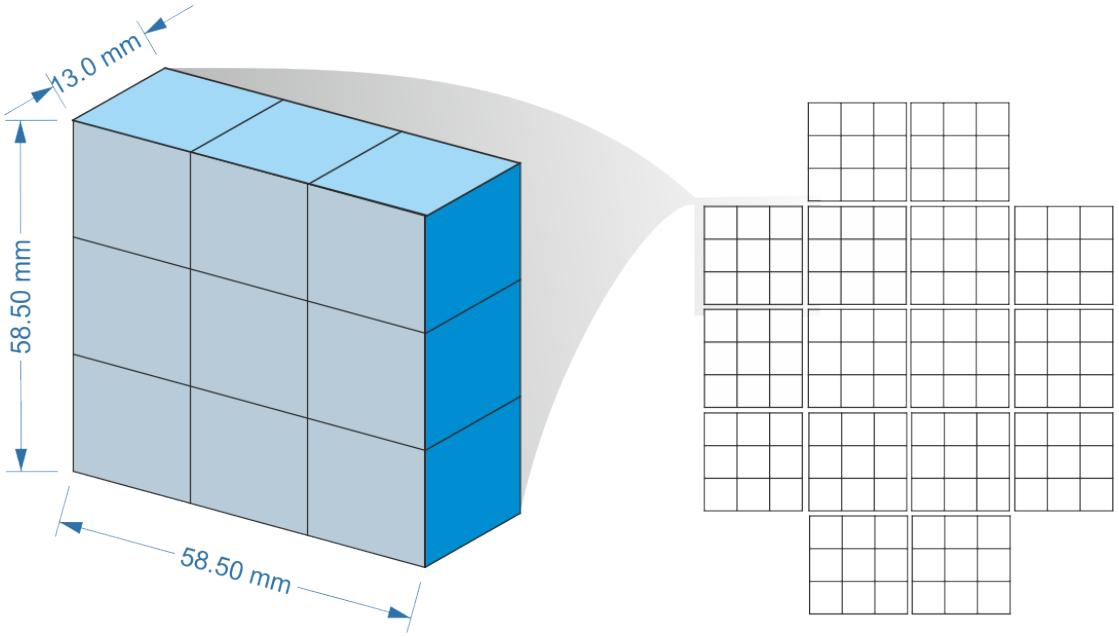

FIGURE 7.16: The CsI detector array is made of 16 modules (right-hand side) and each module is built up 9 CsI crystals (left-hand side). The CsI array fits behind the DSSSD array in the beam downstream.

7.4.4 The AGATA configuration at GSI

The AGATA geometry has been described in Chapter 5. There were 19 AGATA crystals operative by the moment that the experiment has been performed. It also has been mentioned that the geometry of the AGATA array has been modified for the FRS - PreSPEC setup at GSI. The diameter of the beam pipe at GSI is larger than the gap in the AGATA geometry. In order to mount the beam pipe, it was necessary to convert three triple clusters in to double clusters. There were also one crystal inoperative and one crystal missing in two different triple clusters.

In order to increase the γ ray detection efficiency, the secondary target has been located at 158 mm forward position in the beam downstream axis. This increased the AGATA solid angle coverage by factor of 2. Another advantage of the use of such close geometry to increase the efficiency is to make use of the angular distribution of the γ rays. The angular distribution of the quadrupole transitions in ^{52}Fe is forward focused with respect to the beam downstream axis (see Sec. 7.10). Such distribution has been calculated using `DWEIKO` [133] and Monte-Carlo simulations have been done to obtain the increment in efficiency. The contribution due to the anisotropic angular distribution of γ rays to the AGATA efficiency is found to be an increase of 22(2)%.

7.5 Data Treatment

7.5.1 Signal Processsing and Data Acquisition System (DAQ)

The Signal Processing and Data Acquisition System is in charge of processing the analogue signals provided by the detectors, converting them into the digital format and finally storing them for subsequent data analysis. The DAQ is important for recording the events from tens of detectors in a synchronized way. The setup of the current experiment consists of three main instruments: FRS, PreSPEC and AGATA (also the HECTOR detector array was present but it was of no use for our measurement). Therefore the systems to acquire the data from the two mentioned instruments are;

- MBS (Multi Branch System) for FRS and PreSPEC
- The AGATA sampling electronics and NARVAL (Nouvelle Acquisition temps Réel Version 1.2 Avec Linux) for AGATA

7.5.1.1 Multi Branch System (MBS)

The MBS is responsible for recording the data coming from the FRS, LYCCA and HECTOR detectors. In addition, it is also responsible for acquiring an analogue version of the AGATA detector timing. The MBS consisted of 11 branches, and each branch corresponds to a VME crate. Each crate has a trigger module which

are interconnected and ensure the system to run synchronously on an event by event basis [135]. The MBS can be divided into three subsystems:

- FRS
- LYCCA
- GAMMA

Four of the eleven branches (crates) of the MBS are dedicated to the FRS subsystem. For a description of how FRS works the reader can refer to Sec. 7.4.1. These crates are; USER, FRS, TPC and FINGER. The USER crate is of use in case of higher beam intensities or in case of inhomogeneous spill structure. It has a flash ADC based module (SIS3301) with pile-up disentanglement capabilities for the readout of one of the two MUSIC detectors (see Sec. 7.4.1.2). Likewise, the TDC modules in this crate have multi-hit capabilities, allowing to have all timing signals (TPCs, S2/S4 scintillators, etc.) with pile-up determination support which makes the system to recover the data loss as much as possible.

The time-to-digital converters (TDC) with multi-hit (MH) capabilities were fed with four reference signals; left and right signals of S2 and S4 standard ToF scintillators. The clock of MH-TDCs was synchronised with two BuTis timing system [136].

The LYCCA subsystem is composed of four crates. The LYCCA-time crate housing 3 MH-TDC modules, which are acquiring the signals from 32 PMTs of the Start ToF, 16 PMTs of the Target ToF and 32 PMTs of the Stop ToF scintillators (see Sec. 7.4.3), and are synchronised with one of the FINGER crate via BuTis [136].

The GAMMA subsystem has two ADCs, one TDC and one MH-TDC modules, which the two ADCs and one TDC are engaged to the HECTOR crate, and one MH-TDC is the AGATA crate. The HECTOR crate modules are connected to the eight $LaBr_3$ detectors which record the high energy γ rays, energy and time, and to eight BaF_2 detectors which record two time components (slow and fast) in order to use their good intrinsic time resolution. Nevertheless, HECTOR is not used in the present experiment, because the angular distribution of the quadrupole transitions of interest (see Section 7.10.1) foresees extremely small effective detection efficiency for the HECTOR detector position in the setup.

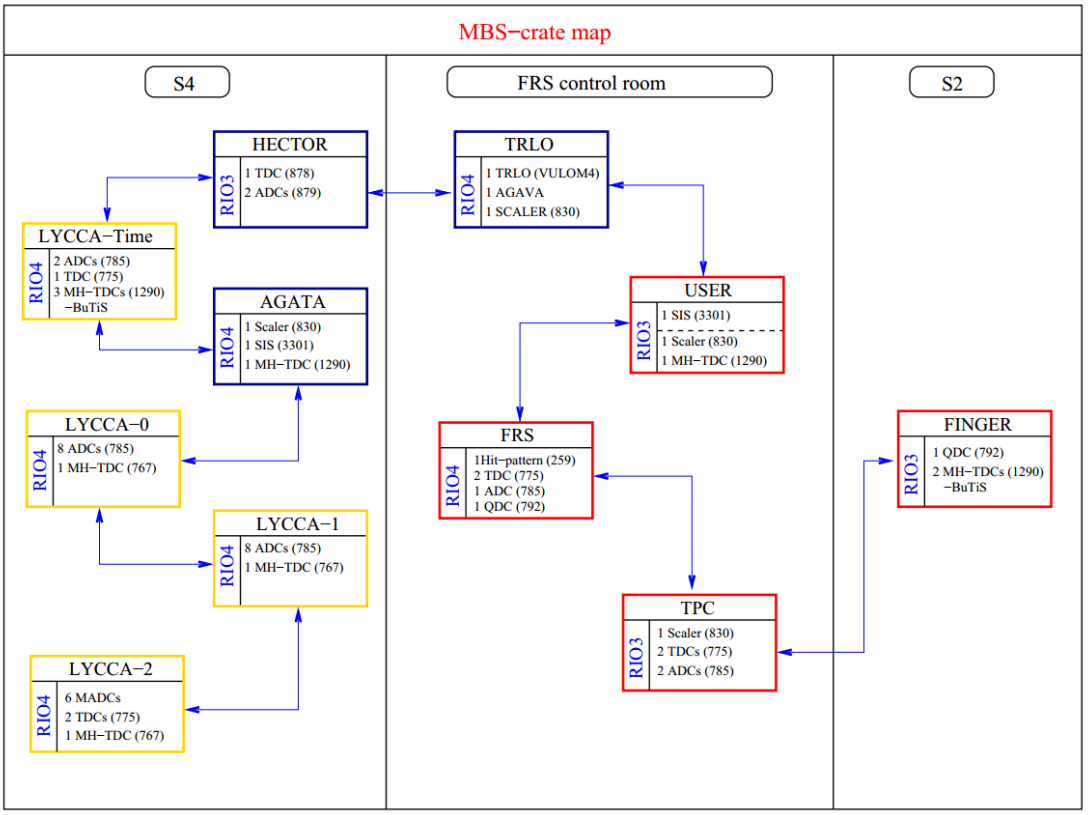

FIGURE 7.17: Schematic view of the MBS crate map at AGATA-PreSPEC campaign at GSI. Courtesy of Ref. [139]

The AGATA crate module has a MH-TDC and a scaler module which record the data from each Ge core signal after a Timing Filter Amplifier (TFA) and CFD stage.

Apart from these subsystems, there is one more crate which is called TRLO crate. It performs synchronous read-out of all crates with a given Master Trigger. The Master Trigger is generated by a TRigger LOgic (TRLO) module that assures the dead-time locking and read-out decision made according to the user defined scheme.

Coupling of the VME-based system to AGATA and the GTS time-stamp information for any MBS event, the AGAta Vme Adaptateur (AGAVA) is used. AGAVA is inside the TRLO crate.

The AGATA data processing and the triggering mechanism in AGATA have been described in Chapter 5.

7.5.1.2 Nouvelle Acquisition temps Réel Version 1.2 Avec Linux (NARVAL)

The NARVAL system works differently from the MBS. The coming signals after sampling by the Digitizer and pre-processing on the AGATA pre-processing electronics are sent to the computing farm following the GTS validation and with the energy information, time-stamp and short traces from the core and 36 segments of each crystal. The signals are processed by actors and each actor represents a different step. The signals are read by the Producer actor, and then sent to the Preprocessing actor. The data are calibrated and aligned in this step. Then the data are sent to Pulse Shape Analysis (PSA) actor where a grid-search algorithm is used to extract the position information of the γ ray from the pulse shapes [137]. The data are then sent to the tracking actor in order to reconstruct the γ ray energy by tracking the interaction points inside the crystal following the Compton scattering formula [138]. The NARVAL system process the data with Event Builder and Merger actors after the Tracking actor. The data are gathered together from all crystals by the Event Builder actor, and then are merged with the ancillary data by the Merger actor.

The data could be written at any step by the Consumer actor. In our case, the data were written after the PSA actor in addition to the raw traces. Moreover, since the trajectory information is needed in the tracking procedure the merging with the FRS data is performed at an early stage in the off-line analysis.

7.6 Realistic Simulations

The realistic simualtions of the experiment have been done in the GEANT4 environment, using the Agata Simulation Package with the realistic geometry of the array and the target chamber (see Fig. 7.18). These simulations aim mainly to the understanding of the experimental observations and to optimize the results of the data analysis. The events were produced using the dedicated code inside the package. When producing the events, a Gaussian distribution was considered for the distribution of the beam hits in the secondary target, in agreement with the FRS beam structure at GSI. The velocity and the intensity distributions of the secondary ions were tuned to reproduce the experimental conditions.

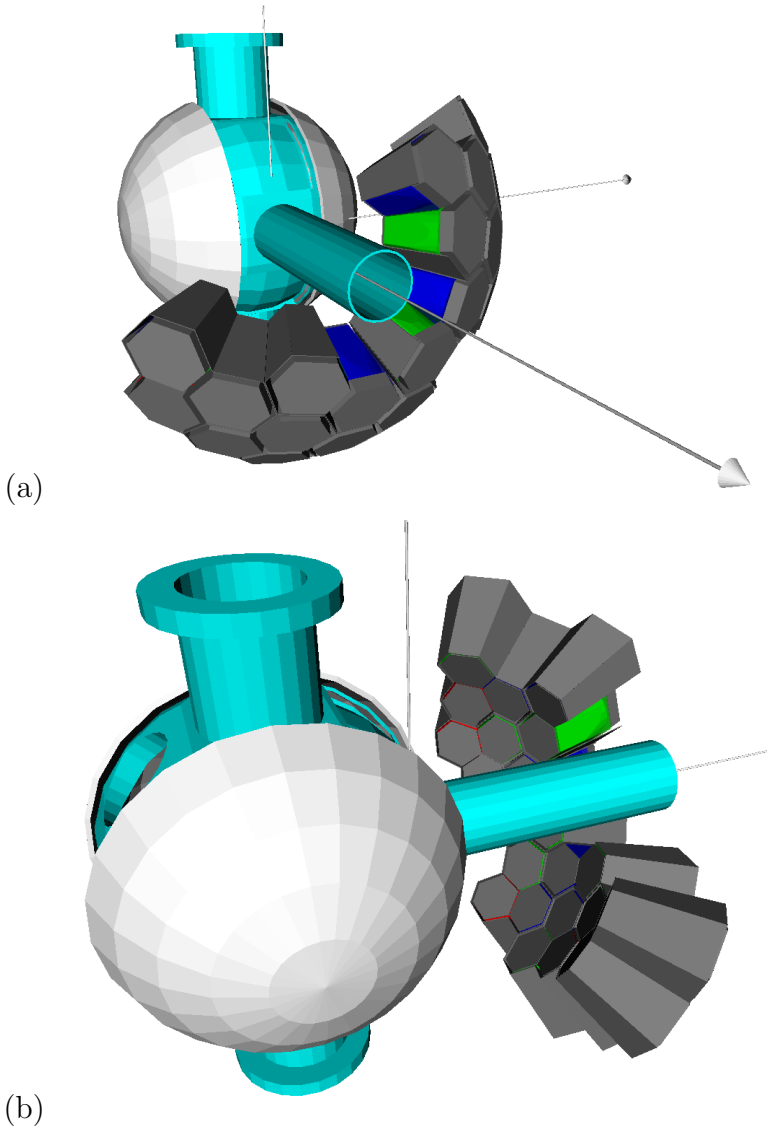

FIGURE 7.18: Realistic geometry used in the simulations from different points of view. Turquoise and ligth grey structures represent the target chamber at GSI. Dark grey structure represents AGATA.

In Figure 7.2, the expected transitions from the high angular momentum states of ^{52}Fe for the pure Shell Model calculations are shown around 4 MeV. Therefore, in the simulations, a hyptothetical state at 4 MeV emitted by an ion traveling at a velocity of 0.51c was considered.

Regarding simulations, two main tasks have been performed: *i*) determination of the ratio of the recovered events due to pair-production for high energy γ rays, and *ii*) determination of the expected resolution of the transitions of ^{52}Fe.

Additionally, in order to evaluate the efficiency of detection in the event of a pair production, we have used a code which tests the interaction points in the AGATA

array for pair-production events, developed by our collaborators from INFN and University of Milano [140]. The code finds the interaction point with maximum energy deposited at each event, and assumes a hypothetical sphere with growing radius at every iteration, then sum up the recorded energies of the interaction points inside the sphere. Then, the code creates spectra for each iteration of the radius and make possible to judge which radius maximize the efficiency for the reconstruction of the γ ray, minimizing the double escape and single escape peaks. A simple macro has been written to process the simulated data in the `root` environment, since the pair-production recovery code uses the root interface. The interaction points in the simulated data were clustered reproducing what is observed in reality, i.e. in the data acquisition of AGATA after PSA. Therefore, the interaction points were grouped in each segment of each crystal, considering the interaction type and the time. The position of each cluster determined as the barycenter and the time determined as the first interaction point. Then the sum energy has been written with the corresponding position and time information in the root tree.

The γ ray spectrum for the summing radius of 9 cm - optimized for the reconstruction efficiency of such simulation - is shown in Fig. 7.19. Even with the optimization on the analysis, the number of recovered events amounted to about 8% of the peak area, to be compared with the standard reconstruction of pair-production events included in MGT that amounted to 4%.

Our final decision considering this meager gain, was not to proceed with a particular analysis of such events, that would have make much more complicated the data processing of the experiment.

The second batch of simulations were performed to help us on understanding and improving the response of the setup to our particular experimental conditions.

The simulations were performed for the line shape and Doppler shift of the $2_1^+ \rightarrow 0^+$ transition in ^{52}Fe, the only transition with sufficient experimental statistics to be able to compare with simulations with different angular conditions. The simulations have been done taking into account the excitation and de-excitation through the target and the decay curve previously determined by Yurkewicz, et al. [111] with half-life of 7.8 ps. In the analysis of the simulated data, the smearing in the γ ray detection positions in AGATA (FWHM: 5 mm) is considered. In addition, the γ ray emission positions in the beam downstream axis is considered as the

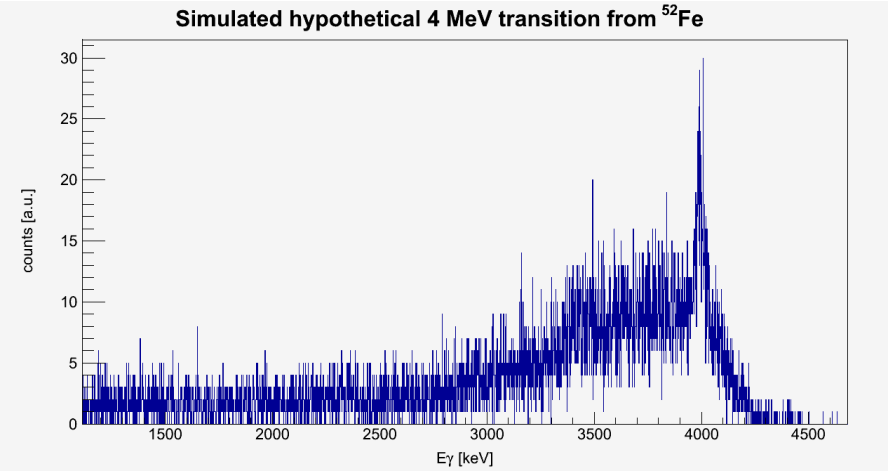

FIGURE 7.19: A simulated hypothetical 4 MeV transition in ^{52}Fe (Doppler corrected). The recovered events due to pair production are shown.

surface of the target, which is another constraint in the experimental conditions. The simulated γ ray spectrum is found to be as in Fig. 7.20.

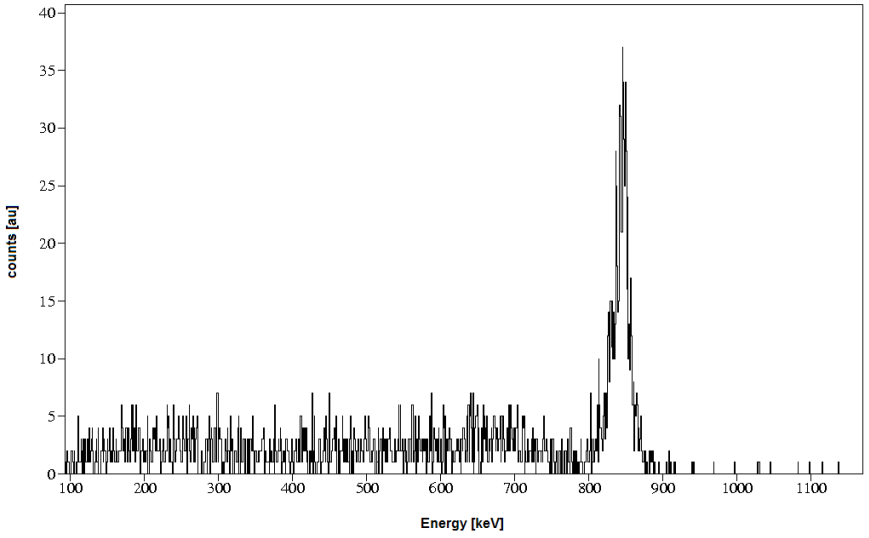

FIGURE 7.20: Simulation of the $2_1^+ \rightarrow 0^+$ transition in ^{52}Fe.

The overall result of this simulation is that for the $2_1^+ \rightarrow 0^+$ transition, the expected FWHM, considering the best possible conditions, is 30 keV.

7.7 Data Analysis

In this section, the data analysis procedure will be described. The particles are tracked starting soon after the production in the primary target in FRS all way down until are finally stopped in the LYCCA wall. In the following sections, the secondary beam separation in FRS and the identification of the secondary reaction products in LYCCA will be described.

7.7.1 Trigger configurations

The triggering at AGATA-PreSPEC setup was crucial since the counting rate at S4 was of the order of 10^5 particles per second (as S4 Standard ToF scintillator) and it was not possible to record every event. The complexity of the setup requires a complex trigger system where different detectors contributed. The trigger configuration at the AGATA-PreSPEC setup is shown in Tab. 7.3. Trigger condition

TABLE 7.3: The trigger configuration and reduction rates at the AGATA-PreSPEC setup.

Trigger number	**Detector systems included**	**Reduction factor**
3	AGATA (calibration)	2^{10}
8	FRS + HECTOR + LYCCA	-
9	FRS + AGATA + LYCCA	-
10	FRS (Scintillator S4)	2^{10}

3 has been used for the energy and efficiency calibration of the Ge crystals. The trigger conditions 8, 9 and 10 have been used during the experiment. A reduction factor of 2^{10} has been applied to Trigger condition 10 due to the high counting rate at the focal plane of S4.

7.7.2 Production, separation and identification of the secondary beam in FRS

The detectors located in the FRS allow us to determine the energy loss, velocity and position of the ions as described in Section 7.4.1. The determination of the mass to charge ratio using the FRS is described in Sec. 7.4. The FRS uses the Bρ - ΔE - Bρ technique to distinguish the reaction products after the fragmentation

reaction of primary ion (^{58}Ni) with the primary target (^{4}Be). The selection of secondary beam is done using the magnetic rigidity B_ρ (see Eq. 7.8) as well as by the trajectory selection elements in FRS. The first stage of the ion selection in FRS is done using the transmission through the magnetic elements (see Fig. 7.6). The horizontal position of the beam depends on the magnetic rigidity and the beam is selected through its x-position using slits. Therefore the magnetic field at the first stage of the FRS determines the acceptance on magnetic rigidity of the fragments. In the second stage of the FRS, the deviation of the ion trajectories due to the magnetic field depends on the energy distribution of the ions. This deviation is corrected by the wedge.

The ion identification in FRS, i.e. determination of their charge (Q) and mass (A), is done by measuring their velocity, position and charge (or atomic number). In order to determine the velocity, the ToF of the ions should be measured. The ToF measurement has been done between focal planes S2 and S4, using the S4 ToF plastic scintillator and S2 Finger ToF detectors. Then the velocity is calculated using Eq 7.10.

$$\beta = \frac{v}{c}; \quad \text{where} \quad v = \frac{d}{ToF} \tag{7.10}$$

As already mentioned in Sec. 7.4.1.1, the TPCs allow the position determination of the ions. Once the positions are determined, the magnetic rigidity can be calculated using;

$$B\rho_2 = (B\rho_0)_2 \left(1 + \frac{x_2}{D_2}\right) \tag{7.11}$$

and

$$B\rho_4 = (B\rho_0)_4 \left(1 + \frac{x_4 - Mx_2}{D_4}\right) \tag{7.12}$$

where $(B\rho_0)_2$ and $(B\rho_0)_4$ are magnetic rigidities of the fragments at focal planes S2 and S4, respectively. The dispersion D_2 and D_4 are for S2 and S4, respectively, and M stands for the magnification between two focal planes. If we replace $(B\rho)$ and β in Equation 7.8, the mass to charge ratio (A/Q) of the ions are:

$$\frac{A}{Q} = \frac{B\rho e}{\beta\gamma cu} \tag{7.13}$$

where u is the mass unit. Once we have the FRS data, the selection of the ions of interest among all arriving to the focal plane of FRS is performed with the help of the FRS detectors described in the previous sections. We have chosen the Atomic Number (Z) identification as starting point. The energy loss of a charged particle

inside a matter is defined by the Bethe-Bloch equation [141]:

$$\frac{dE}{dx} = f(\beta)Z^2, \tag{7.14}$$

where Z the atomic number and $f(\beta)$ a function defined of the beam velocity. According to the Bethe-Bloch equation, the energy (ΔE) released in the MUSIC detectors is proportional to the square of the ion atomic number Z:

$$Z = \sqrt{\frac{\Delta E}{f(\beta)}} \tag{7.15}$$

The high counting rate required in the present experiment and MUSIC detectors provided poor Z resolution and efficiency.

The separation of different ions can be done by applying condition on a 2D plot of Z vs. A/Q, as in Fig. 7.21.

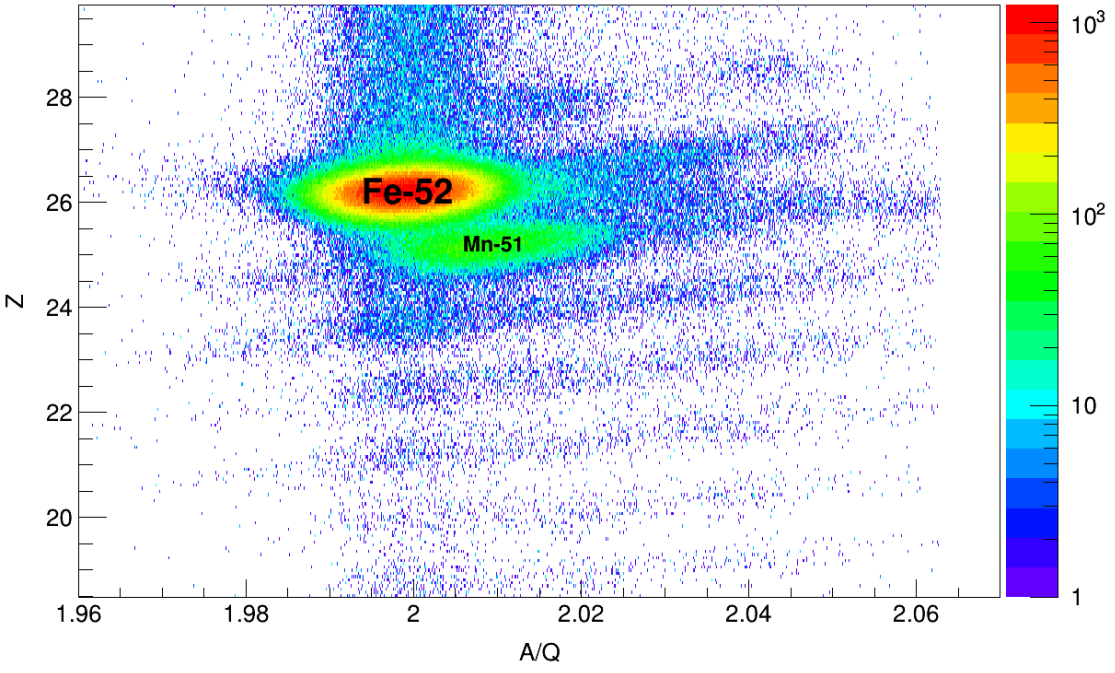

FIGURE 7.21: A/Q vs. Z separation in the FRS with trigger condition 10, i.e. not requiring coincidence with γ rays.

The separation between ions seen on Fig. 7.21 is relatively poor due to the pile-up in the MUSIC detectors, even if we include all the trajectory corrections to the energy losses in the detectors. Nevertheless, the separation capabilities of FRS is sufficient in the region of interest. In addition the purity of ^{52}Fe at S4 is of 99%.

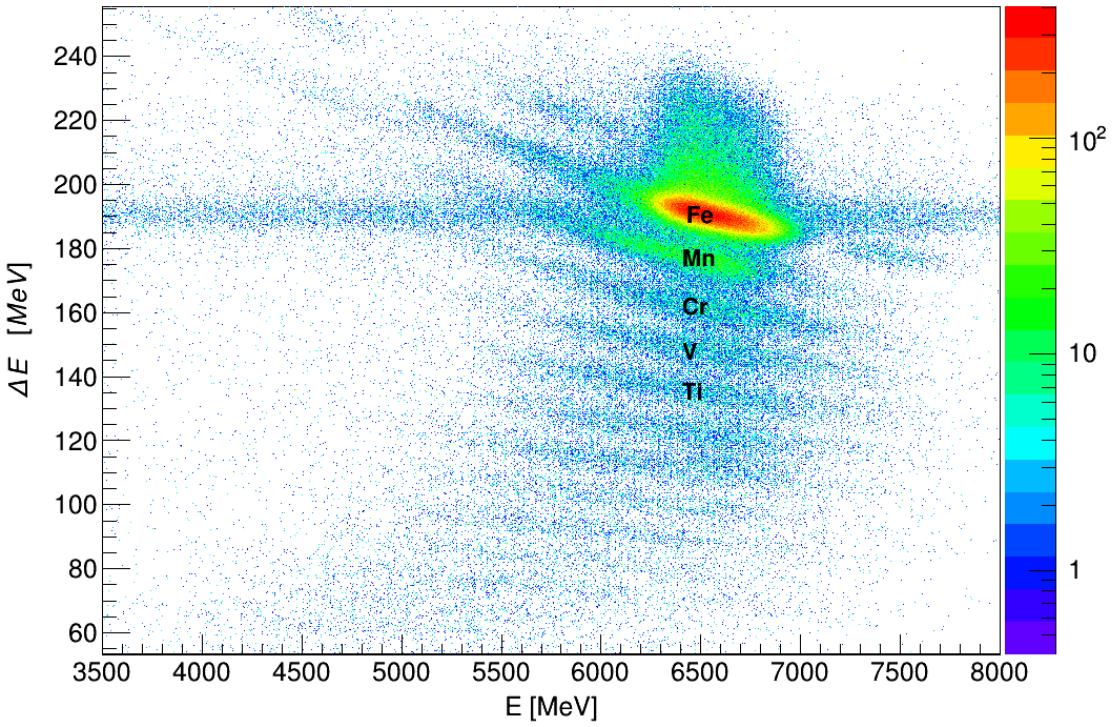

FIGURE 7.22: Total kinetic energy vs. energy loss matrix produced with the DSSSD and the CsI arrays at the LYCCA-wall with trigger condition 10, i.e. not requiring coincidence with γ rays.

The efficiency loss due to the high rate in the MUSIC detectors has been found of the order of 30%.

7.7.3 Identification of the secondary reaction products in LYCCA

Once the secondary beam exits from FRS, it might still suffer reactions with the active and passive materials placed in S4 and in the PreSPEC setup. This includes the ToF scintillators, DSSSD detectors and the target materials. Our goal is to identify the ^{52}Fe ions that might have suffered relativistic Coulomb excitation in the secondary ^{197}Au target.

The identification of the secondary reaction products is performed with the LYCCA setup, described in Sec. 7.3.

The Wall DSSSD and the CsI detector array of the LYCCA detector system allows us to measure the energy loss and total energy of the incoming ions. The DSSSD detectors are thin and the ions deposit a part of their energy. On the other hand,

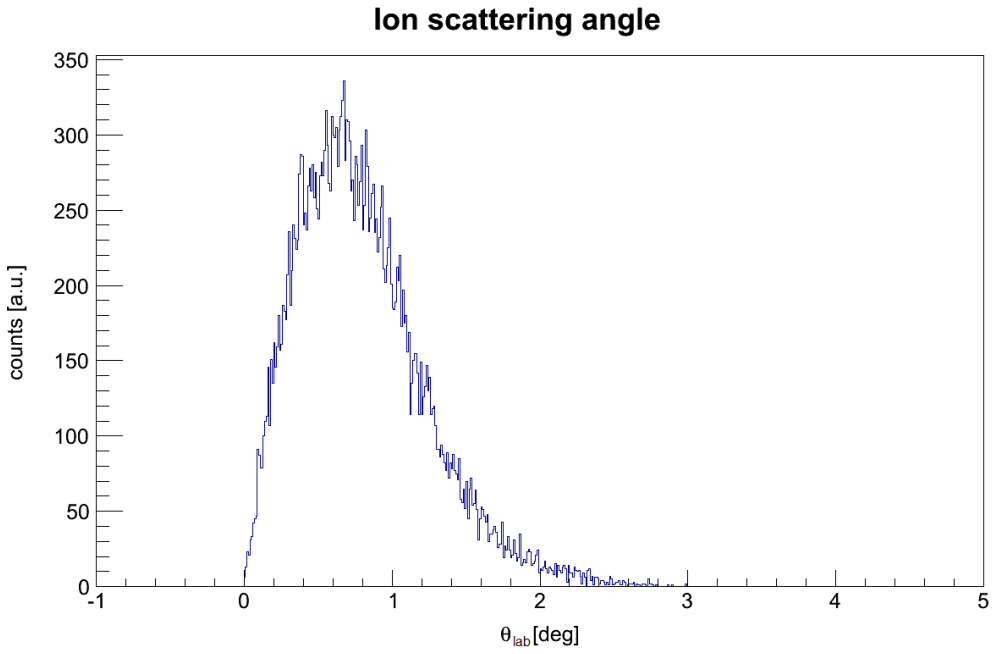

FIGURE 7.23: Angular distribution of the ions after scattering due to the secondary target, measured with both DSSSD detector systems of LYCCA with trigger 9.

the CsI detectors are thick enough to stop the ions and provide the total kinetic energy of the ions. The matrix of the energy loss in the DSSSD array and the total kinetic energy deposited in the CsI array provide ΔE-E discrimination allowing to identify the different Z of the ions arriving to LYCCA (see Fig. 7.22).

The LYCCA detector system allows us to determine particle positions in *xy*-plane via the DSSSD detectors both at the reaction chamber, close to the secondary target position, and at about 3.7 meters away from the reaction chamber in the beam downstream direction (see Fig. 7.14). The DSSSD information allows to calculate the trajectories of the ions after the secondary target, distinguishing the ones suffering scattering. This information is necessary to perform the Doppler correction (see Sec. 7.8) and to determine reaction cross-section (see Sec. 7.3). The distribution of the scattering angles of the excited ions, selecting the ones on Trigger 9 with γ rays in coincidence, can be seen in Fig. 7.23. In order to select the Coulomb excitation and suppress the nuclear reaction events the impact parameter is selected b = 18 fm (distance of the closest approach + 6.3 fm) which is translated to 1.28^o in the ion scattering angles in the laboratory system. This allows us to have a calculated nuclear contribution of ∼0.17 mb.

The energy loss of the secondary beam inside the target is found to be 7%. Therefore, the average ion velocity after the target is v/c = 0.51.

It is possible to see from the hit map of the DSSSD's shown in Fig. 7.24, that the secondary beam is centered in the target and with a FWHM of about 28 mm. Nevertheless, one can point out that the beam center is shifted few mm in the -x axis, and this might be due to the settings of the slits (see Tab. 7.2) to higher momentum transfer -in the primary reaction- part of the secondary beam. The reason to select a part of the beam is to increase the probability to have the ^{52}Fe ions at the isomeric state [94], as it will be explained in Sec. 7.9 .

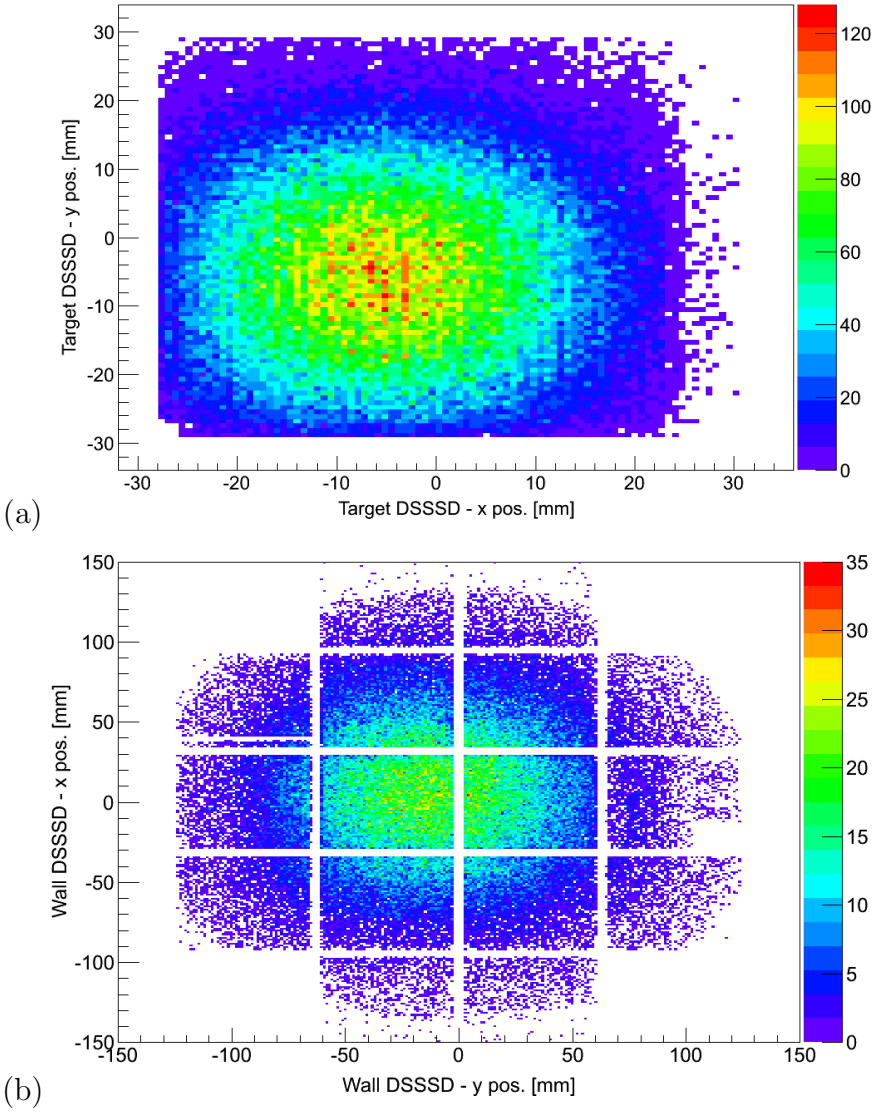

FIGURE 7.24: Hit positions on the target DSSSD (a) and the wall DSSSD (b) arrays of LYCCA.

7.7.4 Particle-γ time

The γ ray background in experiments like this one has a sizable contribution from the atomic background due to the interaction of the relativistic ions, the annihilation radiation peak, the de-excitation of the target and the naturally occuring radioactivity, like the decay of ^{40}K. The background suppression is usually done by putting a tight condition on the time difference between the ions and γ rays.

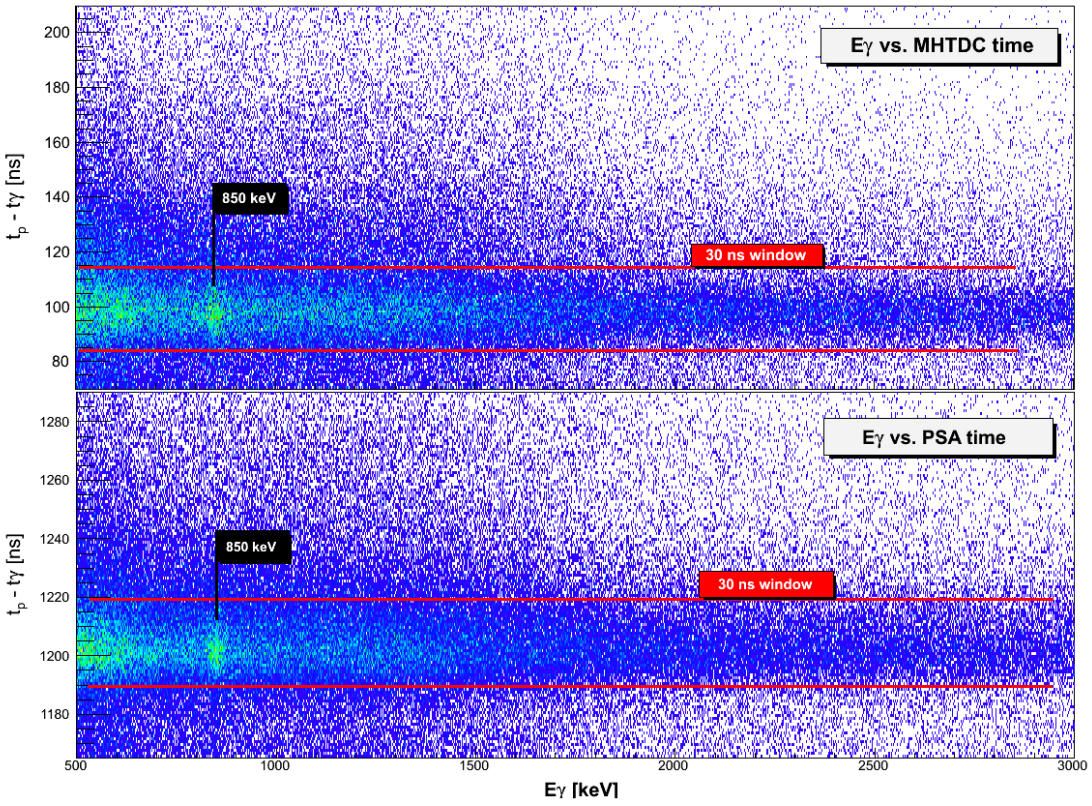

FIGURE 7.25: Particle-γ ray time coincidence as a function of γ ray energy plots. See text for details.

In the case of the present work, there are two methods to calculate the time between γ rays and ions. The particle-γ time spectrum shown in the lower panel of Fig. 7.25 is produced by the time difference between the AGAVA accepted trigger time-stamp and the AGATA core time-stamp with walk correction [139]. The other method to generate the time is done with the TDCs with multi-hit capabilities, where the START is the FRS scintillator Sci4.1 (see Sec. 7.4.2) and the STOP is the Ge time determined as well with TDCs from the inspection signals of the AGATA Digitizers. In the upper panel of Fig. 7.25, the former timing method is shown in the form of the particle-γ time coincidence as a function of

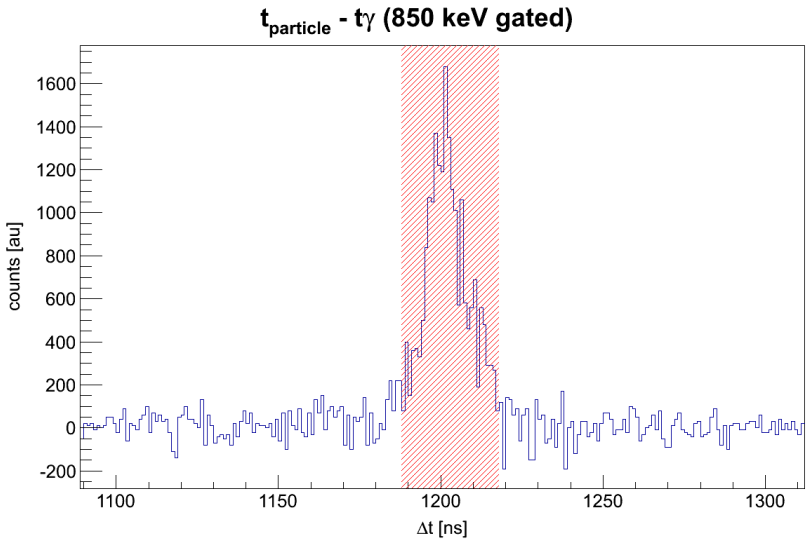

FIGURE 7.26: Particle-γ ray time coincidence plot with a condition on the 850 keV peak with background subtracted. Red marked area represents the time window which is 30 ns.

the γ ray energy after Doppler correction. It is worth to note that the plots are very similar, meaning that the γ times determined by the digital methods following the sampling of the signal and the ones determined with conventional methods are in good agreement. The time condition to be set is in principle arbitrary and the cross-section determined will depend highly on the timing condition -which events will be rejected with the background and which will be accepted-. In order to determine the time window with high accuracy and make sure that no good events are lost, we have done a reverse investigation on timing, in such a way that three conditions have been determined in the energy axis, first covering the 850 keV peak and the others to cover the background having the same number of channels as the first condition has. In this way, one can produce a background subtracted time spectrum where the limits of the prompt peak are easier to assign. This time spectrum and 30 ns time window are shown in Fig. 7.26. We have determined that a minimum of 95.3(7)% of the counts are within our time window.

7.8 Doppler correction

It was mentioned in the previous sections that the velocity of the ions are relativistic and the target is placed in the forward position about 95 mm from the front of the closer detectors, therefore, the Doppler correction is of utmost importance.

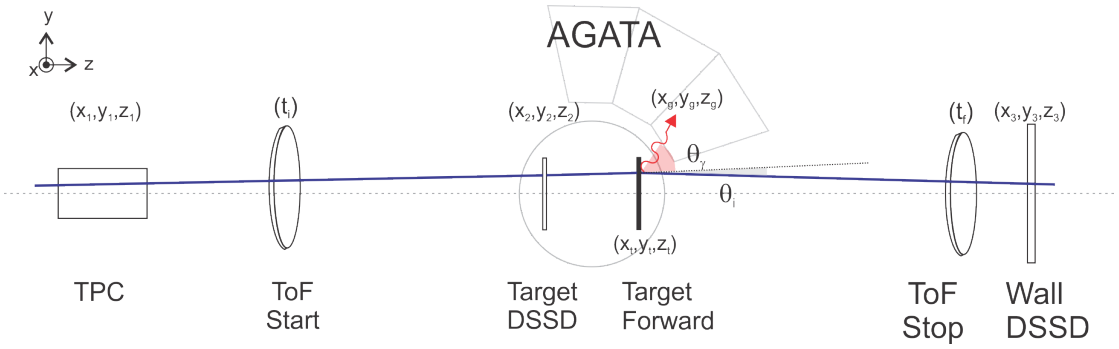

FIGURE 7.27: Schematic view of the reconstruction of the ions and γ ray trajectories. The detectors and positions have been rescaled to fit the drawing.

We need the velocity vectors of each ion fully determined, before and after hitting the secondary target. In order to determine the velocity vector of each ion, one needs its trajectory in 3-dimensional space and its speed. The trajectory is reconstructed using the *xy* positions of the TPC and DSSSD detectors, as it has been already mentioned, and the z positions are fixed for each detector and shown in Fig. 7.14. The y-position of the TPC read-out from the TDCs was problematic since the time gates were wrongly set during this run. But, this parameter can be recovered with the alternative way of measuring the drift times from the delay line, as it was already mentioned in Sec. 7.4.1.1. Thus, the y position was calculated by the sum of the two ends of the delay line and calibrated.

The particle trajectory has to be known to calculate the velocity vector precisely and also to calculate the γ ray emission angle. Therefore, a correction is needed for the actual hit position on the target since it is almost 21 cm away from the nearest position sensitive detector, i.e. Target DSSSD, and this distance considerably long for the proper calculation of the scattering angles. Thus, the corrected positions have been calculated for each trajectory (x'_2, y'_2, z'_2 in Fig. 7.27) and applied on the distance between the two ToF detectors according to the ion positions in the *xy-plane* in the calculation of the particle velocity.

7.9 Isomeric Ratio

The isomeric ratio is the probability to produce ions in their isomeric state with respect to the total production of this nucleus in a given reaction. The production and the selection of the radioactive beam using FRS have been mentioned in Sec. 7.4. In table 7.2 the FRS settings have been listed where the S2 slits can be seen

opened asymmetricaly, i.e. -10, +70 mm. The reason to select the righter-most part of the beam is to select more energetic ^{52}Fe ions, thus to select the ^{52}Fe ions excited in higher spin states [94, 142]. This will increase the probability of the ^{52}Fe nucleus to be produced in the isomeric state ($I^{\pi} = 12^{+}$), and therefore increase the isomeric ratio.

In our case the isomeric ratio was measured experimentally by implanting the ^{52}Fe ions in a 1 cm plastic thick stopper in the close-up position. In order to measure the isomeric ratio, two separate runs were performed since the lifetimes of the isomeric state and ground state are very different, i.e. 45.9 s and 8.3 h, respectively. The implantation of the isomeric state was done for 2 minutes of beam implantation and 2 minutes of decay cycles for 30 minutes. On the other hand, the implantation of the ground state was done for 2 hours of beam and 2.5 hours of decay. The β-decay of the two states have unique patterns in such a way that the isomeric state and the ground state decays into higher and lower spin states of ^{52}Mn, thus the the most intense γ ray transitions are 929.5 keV (see Ref. [144]) and 168 keV (see Ref. [143]), respectively.

In order to calculate the isomeric ratio experimentally, several corrections have to be applied to the areas of the γ ray peaks to find normalized intensities, such as:

- Probability of the ions to decay within a given time
- Absolute γ ray detection efficiency at given energy range
- Dead-time of the setup

Probability of the ions to decay within a given time can be calculated following the exponential decay law. Number of surviving ions after the decay of a radioactive sample consisting of initially N_0 ions and with the decay constant λ within a given time t is determined basically using Eq. 7.16.

$$N(t) = N_0 e^{-\lambda t} \tag{7.16}$$

In the current case, one has to take into account the growing activity along with the exponential decay. If we assume the production rate of a radioactive ion in a reaction as I, number of nuclei that are formed as a result of the reaction as N_1 and the decay constant of the production nuclei as λ_1, then:

$$dN_1 = Idt - \lambda_1 N_1 dt \tag{7.17}$$

and the solution of this equation is given by:

$$N_1(t) = \frac{I}{\lambda}(1 - e^{-\lambda_1 t}) \tag{7.18}$$

Using the combination of the two decay conditions mentioned above, one can determine how many ions decayed in both runs. These were determined to be 90% and 16% for the isomeric and the ground state decays, respectively.

The absolute γ ray detection efficiency was measured using a ^{152}Eu source. The ^{152}Eu source is convenient since it emits γ rays that are in a wide range, i.e. from 121.8 keV to 1408 keV. There were two calibration runs with the ^{152}Eu source that in one the source was positioned at nominal position of the target and in the other the source was positioned at the forward position of the target. The reason of the two measurements was to determine the efficiency decrease due to the plastic stopper. Comparing the two calibration runs, the efficiency decrease due to the plastic stopper found to be 30% and 1% at 122 keV and 964 keV energies, respectively. Thus, the absolute efficiency of AGATA with the plastic stopper was found to be 4.21(13)% and 2.75(8)% at 168.7 keV and 929.5 keV γ energies, respectively.

The dead-time of the setup was different when the beam is on and off. The dead-time is as high as 90% when the beam is on and is as low as 20% when the beam is off. This is because, during the spill is on, the trigger request is FRS and AGATA, thus the dead-time of the setup is given by FRS and AGATA detectors together. While, during the spill is off, the trigger request is only AGATA, and the dead-time of the setup is determined only by AGATA. The dead-time of the implantation period, i.e. 2 minutes of beam-on and 2 minutes of beam-off, is averaged 60%. The dead-time of the setup determined the measurement periods, in order to take full advantage of the low dead-time during the beam is off, especially in the isomeric state decay measurements. In order to collect enough statistics of the isomeric state decay, it was needed to run the beam for 15 minutes. But, the first implanted ions at the isomeric state would decay at the level of 99% within 5 minutes, and many of these events would be lost due to the high dead-time of the setup. Therefore, the optimum implantation and decay measurement

times were decided to be about 2 times of the mean life-time, thus 2 minutes of implantation and 2 minutes of decay. In case of the ground state decay, there is no such constraint, therefore 2 hours of implantation was enough to have sufficient implanted ions. Then the beam has been turned off to collect the decay data with low dead-time for 2.5 hours.

TABLE 7.4: Summary of the parameters needed for the isomeric ratio calculation. See text for details.

$\mathbf{E}_\gamma$	**Area**	**Decayed**	**Live-time**	ε_γ	**Implanted ions**
929.5 keV	1760(190)	0.902(12)	0.40(5)	0.0275(8)	20.02×10^6
168.7 keV	50880(3560)	0.17267(16)	0.80(5)	0.0421(13)	160.86×10^6

Then the intensities of the two transitions from the isomeric and the ground states can be calculated by taking into account the normalization coefficients shown in Table 7.4. The isomeric ratio then can ben calculated as:

$$R = \frac{\text{Implanted ions at the isomeric state}}{\text{Total ions implanted}} = 14(2)\%, \tag{7.19}$$

where R is the isomeric ratio.

7.10 Results

7.10.1 γ ray Angular Distribution

The angular distribution of the $0^+ \rightarrow 2_1^+$ γ rays has been calculated with `DWEIKO` [146]. This is important to know prior to the cross-section determination since it will bring a correction factor to the γ ray intensities. We tested the coherency of the calculations with the experimental results by determining the experimental angular distribution normalizing the detected γ ray in the units of solid angle normalized to the detector solid angle. Such comparison is shown in Fig. 7.29, the red line represents the `DWEIKO` calculations and the blue data points represent the experimental data. It is shown that the calculated angular distribution is in very good agreement until 42 degrees with the experimental data. Due to the close geometry of the setup, i.e. the secondary target at the forward position, the anisotropic distribution, and the relativistic kinematics the γ ray detection

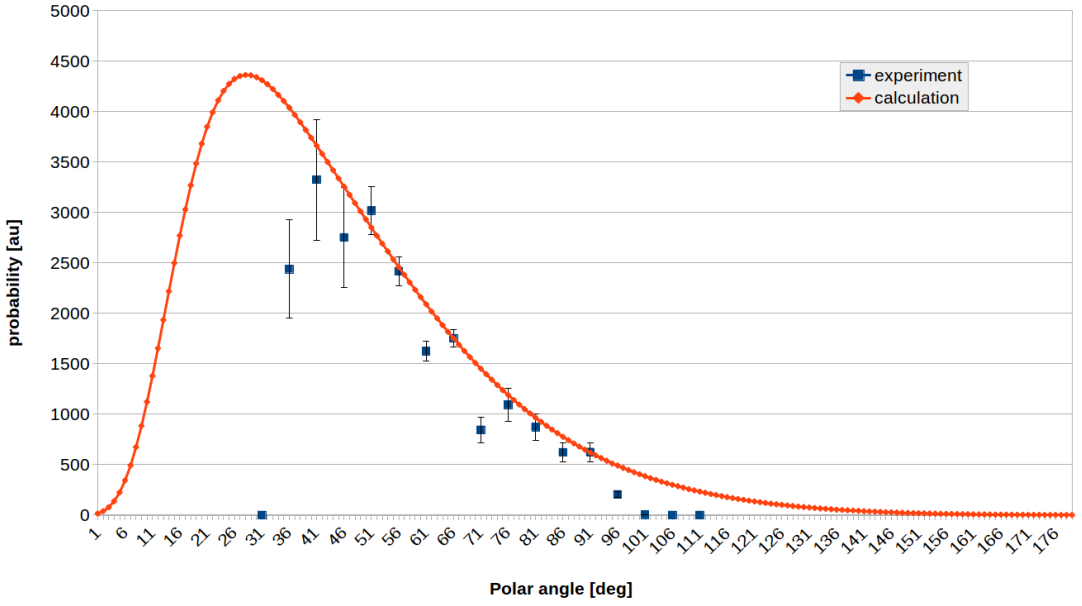

FIGURE 7.28: γ ray angular distribution in the laboratory reference system, calculated with `DWEIKO` (red line) and with the experimental data (blue dots).

efficiency is increased by 22% with respect to the measured for an isotropic distribution.

7.10.2 Experimental cross-sections

The γ ray spectrum has been generated selecting ^{52}Fe in the FRS detectors and the LYCCA arrays, with a 30 ns. time window. The γ ray spectrum shown in Fig. 7.29 is also corrected for the Doppler effect event-by-event. The area of the $2_1^+ \rightarrow 0^+$ transition in the raw spectrum is 3380(200) with the condition of 1.28º in the laboratory reference system in the ion scattering angles.

The relativistic Coulomb excitation cross-section of the ground state to the first 2^+ ($0^+ \rightarrow 2_1^+$) is calculated by considering the corresponding γ ray intensity corrected by the efficiency (ε_γ) for the energies at the given detection angles (C_θ) normalized to the number of ^{52}Fe ions on the ground state arriving to the target and to LYCCA.

One of the key ingredients to determine the experimental cross-section is the intensity of the beam arriving to the target. The ion identification at FRS provides the intensity of the beam at the scintillator position in S4, that is as well the trigger detector for FRS. After the incoming ion identification, there are several elements

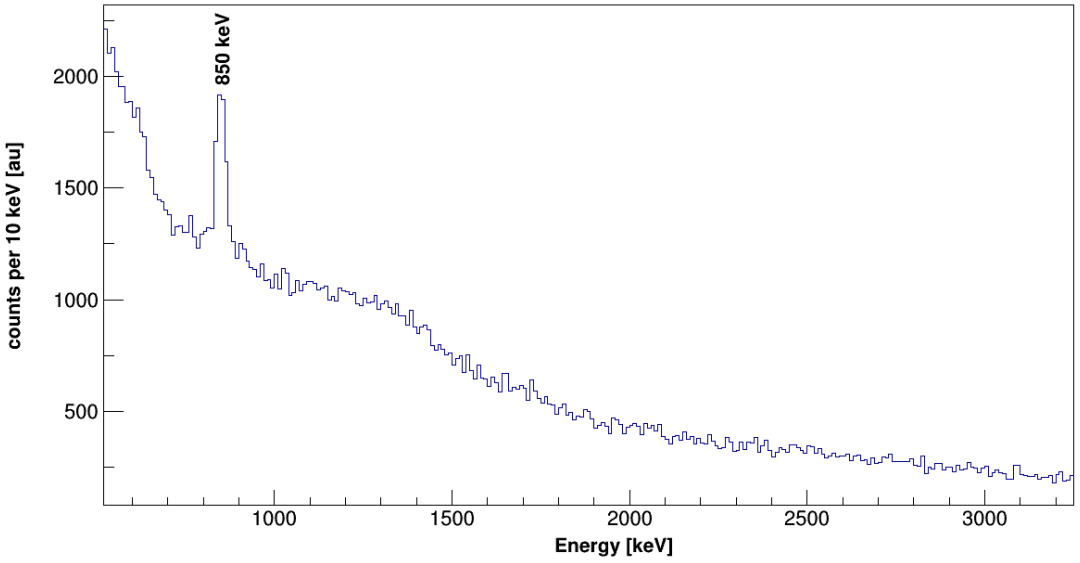

FIGURE 7.29: Doppler corrected γ ray spectrum for the $0^+ \rightarrow 2_1^+$ transition in ^{52}Fe.

(detector material) on the trajectory of the ions, that modifies the composition of the beam. We are not interested, in the present work, on the ions different from ^{52}Fe arriving to the target, and, regarding possible reactions on elements after the target, we exclude on both, the Coulomb excitation evaluation and the beam intensity evaluation, the ions suffering nuclear reactions leading to a product different from ^{52}Fe. Thus, excluding the reactions on the target, the beam intensity is evaluated to be $8.88222(3)\times10^8$, when placing a condition in FRS in ^{52}Fe and in LYCCA as well in ^{52}Fe. The calculated total cross-sections show that reactions in the target will only contribute a maximum of 0.6% to the uncertainty in the intensity of the beam.

Since the beam velocity was relativistic (i.e. the average v/c = 0.51 at the end of the target) the γ rays emitted from the de-excited ions suffer a large Doppler effect. The Doppler shifted energy of the γ rays, for instance for the $2_1^+ \rightarrow 0^+$ transition is spread over a region with 600 keV range depending on the AGATA detection angles (see Fig. 7.30). Therefore the detection efficiency for the transition will vary depending on the angle that it was detected. Such calibration has been done using the ^{152}Eu source considering the real detection energy at each detection angle and effective detection efficiency has been deduced for the 849.5 keV transition as 0.0377(4).

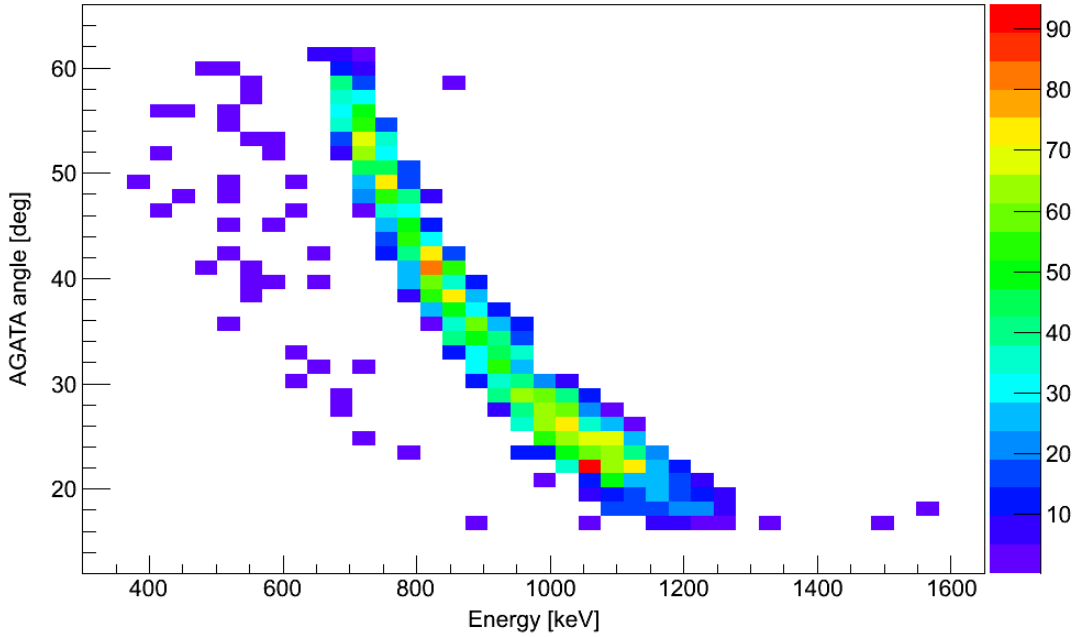

FIGURE 7.30: AGATA angles vs. γ ray energies without Doppler correction with the $2_1^+ \rightarrow 0^+$ transition is gated with background subtraction. The Doppler shifted energy of this transition is at around 1200 keV at small angles (i.e. θ = 16) and is at around 600 keV at large angles (i.e. θ = 60) producing varied detection efficiency.

The total intensity of the $2_1^+ \rightarrow 0^+$ 849.5 keV transition has been evaluated considering the effective efficiency, the effect of the angular distribution (C_θ), the isomeric ratio (C_{iso}) and the feeding ratio (C_F) of $2_2^+ \rightarrow 2_1^+$, see Tab. 7.5. The cross-section is deduced with the γ ray intensity normalized to the number of ions arrived to the target and the number of atoms in the target as 129(9) mb (see Tab. 7.7).

TABLE 7.5: Correction factors applied for the 849.5 keV transition determined for AGATA. C_θ, C_{iso} and C_F represent the angular distribution correction, the isomeric ratio correction and the feeding correction, respectively. See text for details.

Isotope	$\mathbf{I}_i \rightarrow \mathbf{I}_f$ [$\hbar$]	$\mathbf{E}_\gamma$ [keV]	Area	ε_γ	$\mathbf{C}_\theta$	$\mathbf{C}_{iso}$	$\mathbf{C}_F$	**Intensity**
^{52}Fe	$2_1^+ \rightarrow 0^+$	849.5 (1.4)	3380(200)	0.0377(4)	1.22(1)	0.86(2)	1.029(1)	85400(5100)

The transitions observed in the high-energy region of the Doppler corrected γ ray spectrum are shown in Fig. 7.31. The spectrum has large oscillations due to the differential nonlinearity of the AGATA digitizers which are large enough to hide broad γ ray peaks produced by the velocity losses in the target in transitions from short lifetime states. Just in order to make more clear the identification

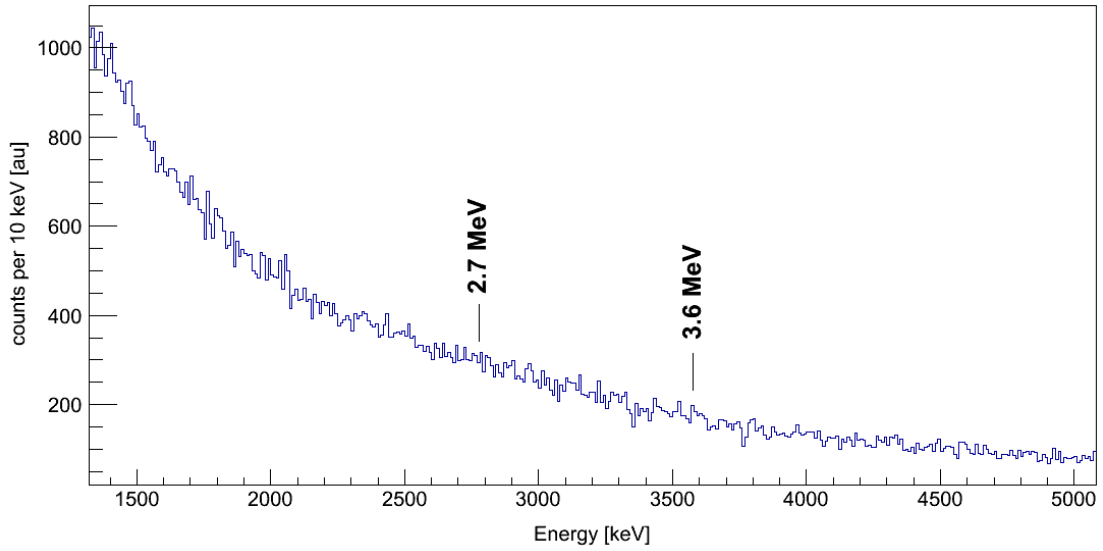

FIGURE 7.31: The high energy range of the Doppler corrected γ ray spectrum.

of the candidate transitions, the background oscillations have been reduced by subtracting the spectrum which has been determined with a condition excluding the ^{52}Fe reaction channel in LYCCA. Such spectrum is shown in Fig. 7.32. In

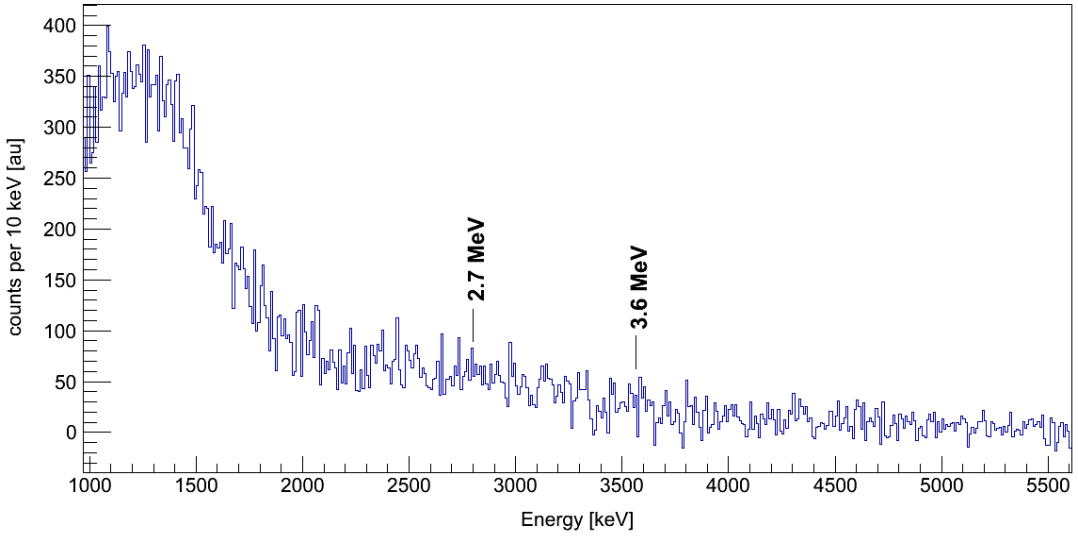

FIGURE 7.32: The high energy range of the Doppler corrected γ ray spectrum with oscillations due to the differential nonlinearity reduced. See text for details.

this spectrum, the $2_2^+ \rightarrow 0^+$ and $2_2^+ \rightarrow 2_1^+$ transitions at 1.9 MeV and 2.7 MeV, respectively, and a candidate for the $14^+ \rightarrow 12^+$ at 3588 keV have been assigned. Nevertheless, the intensities of the transitions have been determined with the original spectrum, obtaining the region of the peaks with the help of the suppressed spectrum. The assignment of the 3588 detected transition as candidate for the 14^+

$\rightarrow 12^+$ de-excitation is based on the expected transition energy, estimated by the LSSM calculations. The areas of $2_2^+ \rightarrow 0^+$ transition and the candidate for the $14^+ \rightarrow 12^+$ transition (see Tab. 7.1) are 400(180) and 120(80) counts, respectively. In Tab. 7.6 the intensities are shown for these transitions.

TABLE 7.6: Summary of the parameters used for the intensity determination with the correction factors applied for the transitions in ^{52}Fe. C_θ, C_{iso} and C_B represent the angular distribution correction, the isomeric ratio correction and the branching ratio correction, respectively. See text for details.

Isotope	$\mathbf{I}_i \rightarrow \mathbf{I}_f$ [$\hbar$]	$\mathbf{E}_\gamma$ [keV]	Area	ε_γ	$\mathbf{C}_\theta$	$\mathbf{C}_{iso}$	$\mathbf{C}_B$	**Intensity**
^{52}Fe	$2_2^+ \rightarrow 0^+$	2770 (5)	400(180)	0.029(4)	1.22(1)	0.86(2)	0.758(22)	17500(7600)
^{52}Fe	$(14^+ \rightarrow 12^+)$	3588 (4)	120(80)	0.025(3)	1.22(1)	0.14(2)	1	28100(19200)

The energy of the 2_2^+ is known at 2759.8(9) keV with a halflife of 0.28^{+9}_{-5} ps in Ref. [143, 145]. In our experiment, the energy of this level has been positioned wrong due to the fact that the fast ions, i.e. v/c = 0.51, emitting γ rays as they slow down through the target. In such conditions, the position of the emission point is not correct for the 2_2^+ level, and the Doppler correction provides a wrong energy. Such phenomenon has also been observed in the Monte-Carlo simulations with the realistic conditions. Nevertheless, the calculated half-lives of 2_2^+ and 14^+ states are on the same order, allowing us to do an internal calibration and assign a more approximate energy at 3575(4) keV for the suggested $14^+ \rightarrow 12^+$ transition.

The Coulomb excitation cross-sections of the ^{52}Fe states deduced in this work are summarized in Tab. 7.7.

TABLE 7.7: Cross-sections of the transitions in ^{52}Fe deduced in this work. The energies in the brackets are after the internal calibration. See text for details.

Isotope	$\mathbf{I}_i \rightarrow \mathbf{I}_f$ [$\hbar$]	$\mathbf{E}_\gamma$ [keV]	σ **[mb]**
^{52}Fe	$0^+ \rightarrow 2_1^+$	849.5(1.4)	79(5)
^{52}Fe	$0^+ \rightarrow 2_2^+$	2770 [2760]	16(7)
^{52}Fe	$(12^+ \rightarrow 14^+)$	3588 [3575]	26(18)

The Doppler corrected γ ray energy spectrum has a distribution of counts around 1.4 MeV, spread along 500 keV. These counts have a partial contribution from the wrongly Doppler corrected $2_1^+ \rightarrow 0^+$ transition due to the inelastic scattering of ^{52}Fe on ^{28}Si of the Target-DSSSD and on the Target-TOF scintillator. This contribution has been investigated by calculating the Doppler correction assuming the γ ray emission point as the Target-DSSSD position (see Fig. 7.33). There is

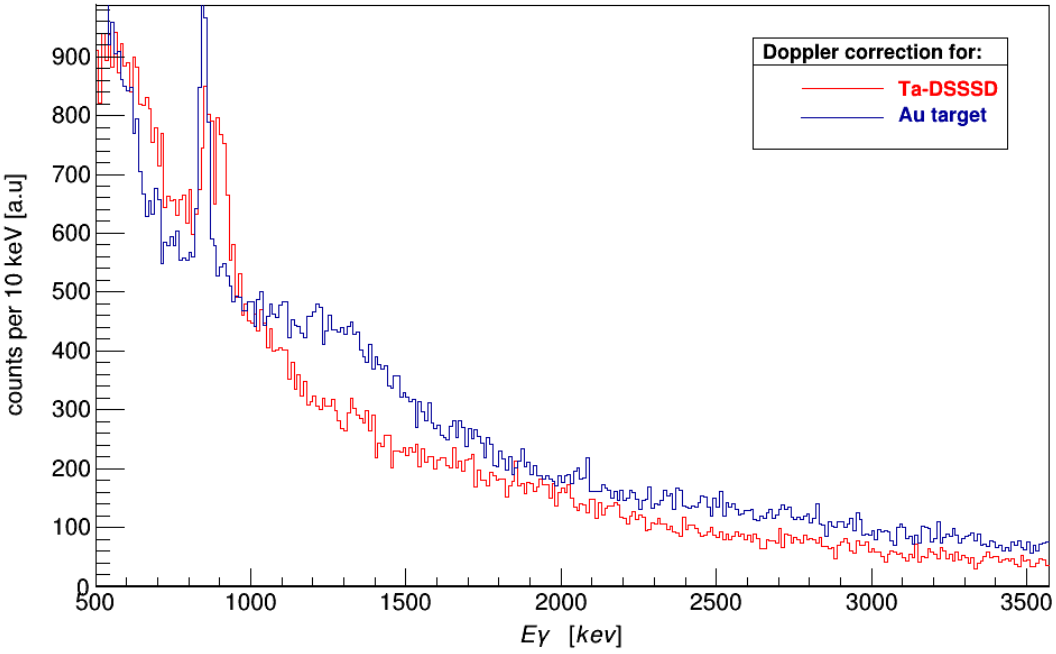

FIGURE 7.33: Doppler correction has been done for the Target-DSSSD position to explain the bump at around 1.4 MeV in the Doppler corrected energy spectrum for the ^{197}Au target. The 849.5 keV peak has a double structure in the spectrum Doppler corrected for the Target-DSSSD position which caused by the inelastic scattering on Target-DSSSD and on Target-TOF detectors.

also a contribution from the background peaks due to the natural radiation and sources present in the experimental area.

7.10.3 ^{197}Au target excitation

As the ^{52}Fe ions hit to ^{197}Au target and suffer Coulomb excitation, the ^{197}Au nuclei can suffer Coulomb excitation as well. The recoiled ^{197}Au nuclei, for the scattering angles we are considering, have energies of the order of tens of keV/u, not enough energy to exit the target and de-excite almost fully stopped. The corresponding transition can be observed in the γ ray energy spectrum without Doppler correction. The Coulomb excitation of ^{197}Au is well known and the $\frac{7}{2}^+ \rightarrow \frac{3}{2}^+$ transition de-excited from the Coulomb excited nuclei occurred with 0.924 branching ratio with an energy transition of 547.5 keV [150]. The area of this transition has been found to be 470(90) with the same 30 ns time window applied for the ^{52}Fe. The deduced cross-section of the target coulomb excitation is shown in Tab. 7.8. The correction factor for the angular distribution has been determined

TABLE 7.8: Correction factors applied for the 547.5 keV transition determined for AGATA. See text for details.

Isotope	$\mathbf{I}_i \rightarrow \mathbf{I}_f$ [$\hbar$]	$\mathbf{E}_\gamma$ [keV]	Area	ε_γ	$\mathbf{C}_\theta$	$\mathbf{C}_{iso}$	**Intensity**	σ **[mb]**
^{197}Au	$\frac{3}{2}^+ \rightarrow \frac{7}{2}^+$	547.6(1)	470(90)	0.0453(5)	1	1	11600(2200)	10.8(2.0)

1 since the angular distribution of the $\frac{7}{2}^+ \rightarrow \frac{3}{2}^+$ is almost isotropic according to the DWEIKO calculations.

7.10.4 Comparison of the experimental cross-sections with the calculations

The cross-sections have been calculated using DWEIKO [133]. DWEIKO calculates elastic scattering differential cross sections, probabilities, and cross sections for inelastic scattering in nuclear collisions at intermediate and high energies. A coupled-channels method together with the optical potentials are used for calculating the inelastic amplitude. [133].

The code accepts the optical model potential parameters [147], the matrix elements and nuclear deformation parameters as the input ingredients. The real and imaginary parts of the optical potential were obtained for our reaction using the Global Optical Potential by T. Furumoto (see Fig. 7.34). The output of the

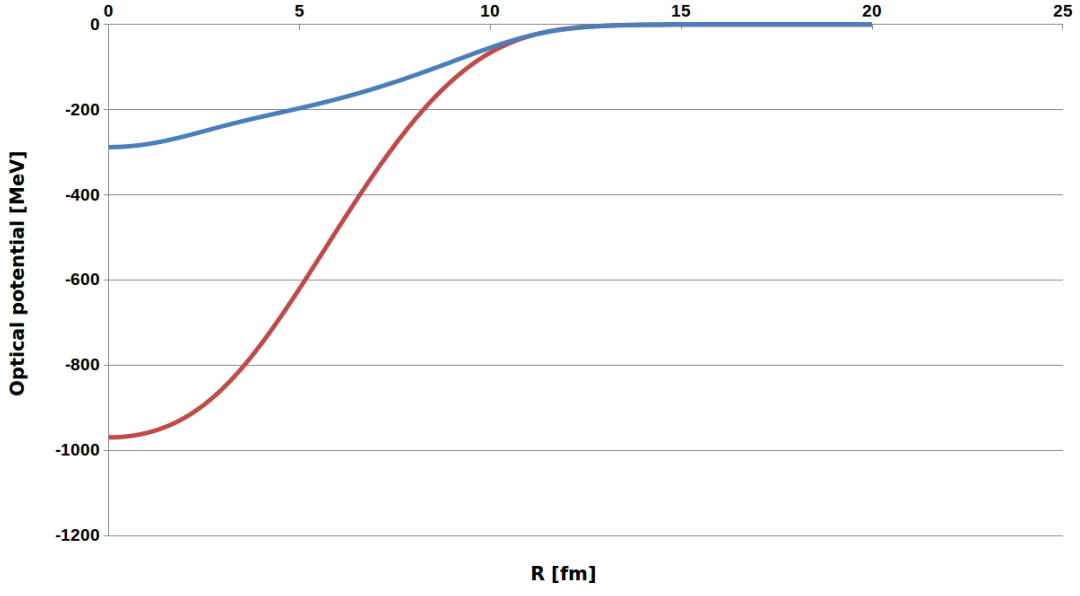

FIGURE 7.34: The real (blue line) and imaginary (red line) parts of the optical model potential obtained using Global Optical Potential by T. Furumoto [147].

code contains the Coulomb excitation cross sections, angular distributions of γ rays, elastic and inelastic scattering cross sections. The integrated elastic scattering cross section for the scattering angles larger than 3° is 215 mb. The total nuclear reaction cross section has been calculated as 4553 mb. Considering this cross section, only 5.6‰ of the ^{52}Fe beam suffer nuclear reactions. Limiting the impact parameter b_{min} = 18 fm, which translates to 1.28° scattering angle in the laboratory system, the total nuclear cross section becomes 0.17 mb.

The relativistic Coulomb excitation cross-section calculations have also been performed by C. Bertulani using a semi-classical method [148, 149]. The calculated cross sections, together with the experimentally determined ones, are presented in Tab. 8.5. The B(E2) value for the $0^+ \rightarrow 2_1^+$ cross section calculation has been taken from the work of K.L. Yurkewicz and collaborators [111] and was determined in an intermediate energy Coulomb excitation experiment performed at NSCL. We

TABLE 7.9: Comparison of the calculated cross-sections with known matrix elements using the `DWEIKO` code, the ones calculated by C. Bertulani, and the experimental ones. The energy in brackets is after the internal calibration.

Isotope	$\mathbf{I}_i \rightarrow \mathbf{I}_f$ [$\hbar$]	$\mathbf{E}_\gamma$ [keV]	σ_{theo}^{DWEIKO} **[mb]**	$\sigma_{theo}^{Bertulani}$ **[mb]**	σ_{exp} **[mb]**
^{197}Au	$\frac{3}{2}^+ \rightarrow \frac{7}{2}^+$	547.5	40.1	28.0	10.8(2.0)
^{52}Fe	$0^+ \rightarrow 2_1^+$	849.5	69.8	46.9	79(5)
^{52}Fe	$0^+ \rightarrow 2_2^+$	2770 [2760]	11	7.8	16(7)

would like to point out the discrepancies between the experimental and calculated cross sections, in particular for the ^{52}Fe $0^+ \rightarrow 2_1^+$ Coulomb excitation process.

7.10.5 Large Scale Shell Model calculations using `ANTOINE`

The interpretation of the data has been done in the framework of the large scale shell model calculations in the full *pf*-shell space using the code `ANTOINE` [109]. Two well known interactions, the KB3G [117] and the GXPF1A [115] have been used to calculate excitation energies and transition probabilities. With both interactions, the calculations have been performed considering the core polarization and quadrupole properties by using effective charges e_p = 1.31, e_n = 0.46 and e_p = 1.5, e_n = 0.5, respectively. The estimated quadrupole transition probabilities and γ ray energies compared to the experimental result are shown in Tab. 7.10. The calculation with the GXPF1A interaction gives an excitation energy of the

TABLE 7.10: Comparison of the experimental results with LSSM calculations with the KB3G and GXPF1A interactions. The energy in brackets is after the internal calibration.

Interaction	$\mathbf{I}_i \rightarrow \mathbf{I}_f$ [$\hbar$]	**ΔE [keV]**	**B(E2) [e^2fm^4]**
KB3G	$12^+ \rightarrow 14^+$	4391	21.6
GXPF1A	$12^+ \rightarrow 14^+$	3753	34.3
Experiment	$(12^+ \rightarrow 14^+)$	3588 [3575]	410(210)

14^+ above the yrast trap, closer to the experimental candidate. Also the calculation with GXPF1A, together with the corresponding effective charges, provides a B(E2) value larger than the one obtained with the KB3G. Nevertheless, the results indicate that the experimental B(E2) is about 10 times larger than the results of the LSSM calculations, suggesting a larger degree of collectivity in the involved states.

The calculations have also been done for the 2_2^+ state using the same effective charges and results compared to the experimental ones are listed in Tab. 7.11. The results are in good agreement with the KB3G interaction in terms of the

TABLE 7.11: Results compared calculations using KB3G and GXPF1A interactions, and experiment. The energy in brackets is after the internal calibration. The B(E2) value has been deduced with more accuracy in the current work.

Interaction	$\mathbf{I}_i \rightarrow \mathbf{I}_f$ [$\hbar$]	**ΔE [keV]**	**B(E2) [e^2fm^4]**	
KB3G	$0^+ \rightarrow 2_2^+$	3109	180.65	
GXPF1A	$0^+ \rightarrow 2_2^+$	2669	211.95	
Previous experiment	$0^+ \rightarrow 2_2^+$	2760	130^{+80}_{-50}	[143, 145]
Current experiment	$0^+ \rightarrow 2_2^+$	2770 [2760]	182(80)	

reduced transition probability, on the other hand the GXPF1 interaction predicts better the excitation energy.

The calculations have been done for the 2_1^+ state using the same effective charges and the results are compared to the experimental ones in Tab. 7.12. The reduced

TABLE 7.12: Results compared calculations using KB3G and GXPF1A interactions, and experiment for the $0^+ \rightarrow 2_1^+$.

Interaction	$\mathbf{I}_i \rightarrow \mathbf{I}_f$ [$\hbar$]	**ΔE [keV]**	**B(E2) [e^2fm^4]**	
KB3G	$0^+ \rightarrow 2_1^+$	928	846.8	
GXPF1A	$0^+ \rightarrow 2_1^+$	883	863.3	
Previous experiment	$0^+ \rightarrow 2_1^+$	849.5	817(102)	[111]
Current experiment	$0^+ \rightarrow 2_1^+$	849.5	945(60)	

transition probability to the first excited state has been found around 15% larger than the previous measurement in Ref. [111].

7.11 Summary and conclusions

In this experiment, the collectivity in ^{52}Fe has been studied using relativistic Coulomb excitation. This reaction mechanism allowed us to determine the reduced matrix elements by measuring the cross sections. The unstable ^{52}Fe beam has been produced with an isomeric ratio of 14(2)%. Extensive Monte-Carlo simulations of the setup with GEANT4 and Agata Simulation Package, relativistic Coulomb excitation cross section calculations with `DWEIKO` and Shell Model calculations with the `ANTOINE` code and the KB3G and GXPF1A interaction have been done and compared with the experimental results. The relativistic Coulomb excitation cross-section calculations show discrepancies that will require further analysis and calculations. A candidate for the high spin 14^+ state above the isomeric 12^+ state has been suggested for the first time. The proposed state has been found more collective than the predictions done with the LSSM calculation with both mentioned interactions, in the full pf-space.

Regarding to the 2_1^+, the comparison of the measured cross-section with the DWEIKO calculations foresee a B(E2) that is about 15% times higher than the value previously determined in Ref. [111] and as well as the shell model estimates. The investigation on this discrepancy is still ongoing.

The energy resolution of the $2_1^+ \rightarrow 0^+$ transition has been found experimentally worse than the simulated predictions. The reason is due to the uncertainty on the geometry of the setup, which has two sources, the first is the uncertainty on the position of the Ge crystals in the set-up, the other is the poorly stretched target foil, making its surface rather curvy, which changes the target position of the order of the millimeter along the beam spot. Our extensive study with Monte-Carlo simulations and with the experimental data showed that our position sensitivity in AGATA deduced from the Doppler correction is of the order of 1000 μm.

Chapter 8

Resumen en castellano

8.1 Introducción

Este trabajo doctoral está compuesto de dos partes:

i) un trabajo de instrumental relacionado con el sistema de detección de neutrones NEDA, incluido el diseño de los detectores por medio de simulaciones Monte-Carlo.

ii) experimentación sobre la estructura nuclear con los sistemas de detección basado a los detectores semiconductores de germanio. En este segunda parte, se presentaran dos actividades experimentales realizadas con las técnicas de espectroscopia rayo-γ, desde la fase de preparación hasta la terminación del análisis de datos con debate de los resultados.

La primera parte está dedicada al desarrollo de los detectores de neutrones de nueva generación con la eficiencia alta, basados en centelladores líquidos, que se utilizaran como trigger o instrumentación complementaria en los experimentos de la estructura nuclear de alta resolución. He estado participando activamente en un proyecto Europeo que su objetivo es construir tal instrumento, llamado NEutron Detector Array (NEDA) acoplado al multi-detector del rayo-γ de la alta pureza, como AGATA [1], EXOGAM2 [2]. NEDA esta actualmente en la fase de producción, es una obra cooperativa de unos países Europeos, incluidos España, Turquía, Italia, Francia, Polonia, Gran Bretaña y Suecia. Nuestro objectivo con NEDA es construir un multi-detector de alta eficiencia para cumplir las necesidades de los experimentos contemporáneos, que se investiga la estructura de los

núcleos exóticos que se encuentran lejos de la valle de la estabilidad β. Uno de los métodos mas exitosos para producir tales núcleos exóticos es utilizar las reacciones *fusión-evaporación* con haces estables o radioactivos y blancos estables. Los núcleos mas exoticos deficientes neutrones se producen en los canales muy débiles de reacción despues de la emisión de dos o mas neutrones del núcleos *compound*. Para realizar una espectroscopia-γ de alta resolución de tales sistemas exóticos, por ejemplo como en el caso de ^{92}Pd [3], se requiere la identificación de canales de reacción, adicionalmente a la eficiencia alta y selectividad, y la determinación de la multiplicidad de neutrones.

En la parte instrumental de esta tesis, se explicara el diseño conceptual temprano del multi-detector de NEDA. Antes de explicar el diseño se introducirá el mecanismo de detección de neutrones utilizando centelladores líquidos. Durante la fase de desarrollo de NEDA, se ha creado un banco de pruebas en los "Laboratori Nazionali di Legnaro" (LNL - INFN). Las pruebas se hicieron utilizando cuatro detectores de prototipo con tamaños idénticos y dos centelladores diferentes: el centellador de líquido convencional y el centellador de líquido deuterado. Uno de los detectores de centelladores de líquidos convencionales fue adquirido y montado por nosotros en IFIC-Valencia. Con estas pruebas, nos propusimos caracterizar los prototipos y probar su funcionalidad con la electrónica de *digital sampling*. De particular interés fueron la determinación de la eficiencia relativa de los dos centellador (G. Jaworski), la resolución en tiempo (V. Modamio) [4], la evaluación de *neutron-cross-section* (T. Hüyük) y las pruebas de las placas rápidas *analog-to-digital* (J. Egea y M. Jasztrab) [5–7].

La segunda parte de esta tesis se dedica a la descripción de la preparación, realización, análisis y discusión de los resultados de dos experimentos. Será precedida por una breve introducción a los detectores semiconductores de germanio de alta pureza y los sistemas de trigger / detector complementario. El primer experimento se realizó con la instalación EXOGAM - Neutron Wall - DIAMANT en GANIL. El análisis de este experimento me permitió ganar experiencia en una instalación que involucra a los detectores de neutrones. El multi-detector de Neutron Wall es el ancestro de NEDA. Más detalles sobre este experimento se darán en la seccion 8.6.

El segundo experimento se realizó en la instalación GSI Fragment Separator con la configuración AGATA - PreSPEC. Este experimento se realizó para estudiar la colectividad en ^{52}Fe por encima del estado isomérico 12^+. Con el fin de poblar los

estados baja altitud por encima del estado isomerico, produjimos el haz inestable ^{52}Fe a energías relativistas y realizamos excitación de Coulomb por el blanco pesado de ^{197}Au. La motivación física, se discutirán el mecanismo de reacción y el análisis del experimento junto con los resultados y su evaluación.

8.2 NEutron Detector Array - NEDA

NEDA es un multi-detector que se utilizará en los experimentos de la estructura nuclear acoplado a los detectores basados en germanio (e.g. AGATA, EXOGAM2). Con el fin de realizar estudios de espectroscopia de rayosγ de alta resolución de núcleos exóticos que se encuentran lejos del valle de estabilidad, la identificación del canal de reacción requiere simultaneamente una alta eficiencia y capacidad para determinar la multiplicidad de neutrones. Se utilizará en diferentes estudios de estructura nuclear tanto de núcleos ricos en neutrones como núcleos deficiente en neutrones. NEDA presentará una alta eficiencia de detección para eventos de uno, dos y tres neutrones con una buena discriminación neutrón-gamma.

En detectores de neutrones como NEDA, uno de los problemas críticos en la determinación de la multiplicidad de neutrones es que la dispersión de los neutrones puede hacer que un único neutron sea detectado en diferentes detectores del sistema, es el llama "cross-talk" de neutrones. Un objetivo importante en el diseño de nuevos filtros de detección de neutrones, tales como NEDA, es minimizar "cross-talk" neutrones y la sensibilidad para detectar 2 o 3 neutrones, realmente emitidos, en comparación con sistemas de detectores ya existentes, por ejemplo Neutron Wall [16, 17] y Neutron Shell [18]. Además, NEDA utilizará la electrónica digital y el procesamiento de señal digital de tecnologia mas avanzada basado en las tarjetas NUMEXO2 [5, 6]. Teniendo esto en cuenta, un esfuerzo considerable se ha invertido recientemente en el estudio de sincronización digital [4], tarjetas de adquisición rápida de datos digitales [7] y la discriminación digital forma pulso [19, 20].

8.2.1 El diseño de los detectores de NEDA

NEDA está diseñado conceptualmente como un multi-detector flexible con unidades de detección idénticas capaces de adaptarse a diferentes configuraciones experimentales. Se eligió un hexágono regular como punto de partida para el diseño de la geometría NEDA, ya que es el polígono más adecuado sea para el agrupamiento de los detectores en geometrias compactas, como para el acoplamiento del contenedor de centellador líquido al tubo fotomultiplicador (PMT) de forma circular, minimizando el área descubierta por el PMT. La longitud lateral del hexágono es de 84 mm, adecuada para los tubos fotomultiplicadores más grandes disponibles normalmente con 5 pulgadas de diámetro (véase Fig. 3.1). El volumen de centellador líquido en el detector es de 3,23 litros. Se utiliza un contenedor de aluminio con un grosor de 3 mm para proporcionar suficiente estabilidad mecánica al detector. A parte de la modularidad, los criterios de diseño de NEDA incluyen:

- Eficiencia: maximizada dentro de la cobertura geometrica
- Distancia de blanco a detector: lo suficientemente grande para la discriminación de neutron-γ por tiempo de vuelo (TOF)
- Granularidad: maximizar la eficiencia de discriminación de los canales de reacción con una multiplicidad de neutrones mayor que 1.

8.2.2 Simulaciones de Monte-Carlo

El objetivo principal de las simulaciones es evaluar el rendimiento de la primera implementación de NEDA combinado con Neutron Wall y AGATA. Las simulaciones Monte Carlo presentadas en este capítulo se realizaron utilizando Geant4 [23] y el paquete de simulación AGATA (ASP) [1, 24]. El rendimiento del sistema propuesto se ha simulado para una fuente de ^{252}Cf que emite neutrones isotrópicamente y para la reacción de fusión-evaporación ^{58}Ni + ^{56}Fe en el que los neutrones se distribuyen según la cinemática de reacción.

8.2.2.1 Generadores de eventos

Para simular el rendimiento de los detectores, se han utilizado dos generadores de eventos diferentes para producir neutrones, uno correspondiente a una fuente de

^{252}Cf y otro que reproduce realisticamente la emisión de neutrones en una reacción de fusión-evaporación. La distribución de energía de los neutrones de una fuente de ^{252}Cf se produce el generador de eventos incorporado de Geant4 usando la expresión utilizada en la Ref. [25]. En cuanto a los eventos de reacción de fusión-evaporación realistas, el código de Monte-Carlo Hauser-Feshbach LILITA_N97 [26] se ha utilizado para calcular los parámetros físicos de la emisión de neutrones evento por evento.

8.2.2.2 Verificación del generador de eventos de reacción fusión-evaporación

Para validar nuestras simulaciones, se ha verificado el generador de eventos comparando una medición con el instrumento Neutron Wall con una simulación de la misma configuración. Se utilizaron datos medidos con el instrumento Neutron Wall en los que se utilizaron un haz de ^{58}Ni a 220 MeV que incidía sobre un blanco de ^{56}Fe con un espesor de 10 mg/cm^2. La elección de esta reacción fue motivada por la existencia de datos utilizados anteriormente para la caracterización de Neutron Wall [17]. Además, las características de esta reacción son bastante similares a las que pretendemos utilizar en futuros experimentos con NEDA. Para validar el generador de eventos se realizó una comparación de las distribuciones experimentales de TOF medidas en el experimento mencionado para los diferentes ángulos polares de Neutron Wall con las simulaciones de Geant4. La Figura 3.4 muestra los espectros TOF medidos y simulados para los seis ángulos θ de Neutron Wall. Los datos experimentales se recogieron utilizando un "Common Stop" para los detectores de neutrones, por lo tanto el eje del tiempo tiene los tiempos de vuelo más largos a la izquierda. El centro de la distribución de se ha tomado como referencia de tiempo (t = 0 ns en los espectros). La renormalización entre datos experimentales y simulados se realizó utilizando la relación entre el número total de neutrones en los espectros experimentales y simulados TOF. Con el fin de mejorar el acuerdo de los datos simulados y experimentales, la energía de centro de masa de las partículas de luz evaporada tuvo que ser incrementada en 800 keV en LILITA_N97. Esta energía fue substraida de la energía de excitación del núcleo después de cada emisión de neutrones, con el fin de mantener la competencia correcta entre los diferentes canales de decaimiento. Como se ve en la figura, el acuerdo es bastante bueno después de añadir energía de 800 keV y, por lo tanto,

concluimos que el generador de eventos puede usarse para determinar las cifras de rendimiento de NEDA para la reacción de fusión-evaporación.

8.2.2.3 Evaluación del "Cross-Talk" de neutrones

En un multi-detector de neutrones con una geometría compacta, como NEDA, la probabilidad de interferencia de neutrones entre detectores es bastante grande. Para el multi-detector de Neutron Wall, la simulación de neutron cross-talk se estima en un 12% en un acuerdo justo con las estimaciones anteriores [16, 17]. Esto conduce a una ambigüedad con respecto al número real de neutrones que interactúan en el sistema. Con el fin de disminuir esta ambigüedad y optimizar la eficiencia de discriminación en el caso de emisión de dos y tres neutrones, se ha incluido una condición en la correlación entre la distancia entre los centroides del detector (Δr) y la diferencia de TOF (Δt) de dos detectores que han generado señal.

8.2.3 Implementación primaria de NEDA para acoplar con AGATA: Diseño y resultados de las simulaciones

Se han propuesto dos configuraciones para la implementación de NEDA, junto con el Neutron Wall, que se utilizará con AGATA en GANIL (véase Fig. 3.8). En la configuración mostrada en la Fig. 3.8-a, Neutron Wall a 180 mm de su posición nominal en la dirección del haz, es decir, las caras delanteras de los detectores pentagonales están a 690 mm de la posición del blanco. Los 50 detectores NEDA se colocan a 510 mm, 17 unidades a 60.5º, 16 unidades a 74º y 17 unidades a 87.5º con respecto a la dirección del haz, para cubrir un ángulo sólido mayor en dicha dirección. En la configuración mostrada en la Fig. 3.8-b, las unidades hexagonales de Neutron Wall se colocan en ángulos θ entre 60º y 90º. La distancia de blanco a detector de Neutron Wall se mantiene su posición original, es decir, 510 mm. Las 51 células unitarias NEDA se sitúan entre $\theta = 0º$ y $\theta = 60º$, cubriendo un ángulo sólido de aproximadamente $\Omega = 0{,}7\pi$ s.r. en la posición hacia delante. La unidad central de detección de NEDA se coloca a 570 mm de la posición de blanco. Los resultados de las simulaciones del sistema descrito, se presentan en la tabla 8.1 y 8.2.

TABLE 8.1: Las eficiencias de detección de un, dos y tres neutrones obtenidas de simulaciones de una fuente ^{252}Cf para las diferentes configuraciones descritas en el texto. Los errores son estadísticos.

Geometria	ε_{1n} [%]	ε_{2n} [%]	ε_{3n} [%]
Neutron Wall (NW)	8.81 (*6*)	0.50 (*4*)	0.021 (*13*)
NW + NEDA	13.55 (*5*)	1.371 (*23*)	0.125 (*12*)
NW-ring + NEDA	14.68 (*5*)	1.743 (*21*)	0.182 (*11*)

TABLE 8.2: Las eficiencias de detección de un, dos y tres neutrones obtenidas de simulaciones de la reacción ^{58}Ni + ^{56}Fe para las diferentes configuraciones descritas en el texto. Los errores son estadísticos.

Geometria	ε_{1n} [%]	ε_{2n} [%]	ε_{3n} [%]
Neutron Wall (NW)	26.00 (*5*)	3.93 (*10*)	0.55 (*14*)
NW + NEDA	28.70 (*5*)	6.37 (*11*)	1.66 (*12*)
NW-ring + NEDA	31.30 (*5*)	7.62 (*11*)	1.89 (*11*)

8.3 Pruebas con detectores de neutrones

En la fase de preparación de NEDA se adquirieron prototipos conteniendo centellador líquido, con las que se consturyeron igual numero de detectores y, en el contexto de éste trabajo doctoral se hicieron las pruebas para caracterizar sus rendimientos de *neutron-cross-talk*. El banco de pruebas se instaló en el Laboratorio "Laboratori Nazinoali di Legnaro", incluyendo la electrónica de procesamiento de señales y el sistema de adquisición de datos. El procesamiento de señales se ha realizado de dos maneras: digital y analógico. El sistema analógico fue igual al utilizado en el caso de la Neutron Wall y sistema digital ha sido desarrollado especialmente para EXOGAM2 y NEDA con una interfaz que es compatible con AGATA usando FADC de alta fecuencia y numero efectivo de bits.

Con el fin de descubrir las características de *neutron cross-talk* de los detectores prototipo, se ha realizado una medición en dos fases. La medición se basa en una idea simple, en la obtención de los resultados de cross-talk de neutrones, con la substracción de dos espectros TOF, uno de los eventos *reales* y el otro de los eventos *real + cross-talk*. El primer espectro se ha adquirido colocando los dos detectores de neutrones enfrentados y alejados. El segundo se ha obtenido colocando los detectores uno junto al otro a igual distancia de la fuente (véase la figura 4.3). Los resultados experimentales sugieren un 15.51% de eventos de neutron cross-talk sobre el número de neutrones detectados. Con el fin de evaluar mejor este resultado, se han realizado las simulaciones Monte-Carlo de las pruebas

de cross-talk. Los neutrones que han sufrido "cross-talk" se determinan de la misma manera que en el banco de prueba, es decir, se sustraen los espectros de ToF de las dos configuraciones. La probabilidad de la detección de los neutrones en ambos detectores con sólo un neutrón emitido, se encontró que el 15.58% de todos los neutrones detectados en las simulaciones. Los resultados de la simulación están en buen acuerdo con los resultados experimentales.

8.4 Detectores de espectroscopia γ y auxiliares

En las últimas décadas, la espectroscopía de rayos-γ utilizando multi-detectores de Ge se ha convertido en una herramienta esencial en los estudios experimentales de estructura nuclear. Sin embargo, la producción disminuye a medida que los núcleos de interés se vuelven más exóticos, la investigación de tales núcleos será más difícil, lo que conlleva la necesidad de contar con detectores más eficientes y con mayor sensibilidad. Para responder a estas necesidades se están construyendo nuevos detectores, sensibles a la posición, basados en el análisis de la forma del pulso (PSA) y el trazado (tracking), cubriendo 4π s.r. ángulo sólido con alta granularidad. Los métodos de supresión de fondo Anti-Compton convencionales [38-41] ya no serán necesarios gracias a estas técnicas y la cobertura geometrica con los detectores de Ge puede ser tan elevada como el 80% [1]. En esta sección, se presentarán dos de los ampliamente conocidos sistemas de detectores segmentados Europeos, basados en detectores semiconductores de Ge hiperpuro: EXOGAM y AGATA. Estos detectores se utilizaron también en los experimentos presentados en esta tesis.

8.4.1 AGATA

AGATA es un sistema de detectores semiconductores coaxiales de Ge Hiperpuro de tipo-n altamente segmentados y encapsulados, con capacidad de PSA y de trazado. AGATA tenrá 180 detectores cuando se complete (ver Fig. 5.1). Los cristales se agrupan en tres para formar clusters (AGATA triple cluster - ATC) y cada grupo se mantiene a temparatura criogenica a traves de un criostato que evapora nitrogeno líquido. enfría por un criostato. El radio interior de AGATA es de 225 mm y el radio exterior es de 315 mm. Cada uno de los cristales tiene el contacto exterior dividido en 36 segmentos, que junto con el contacto interior

que dispone de dos pre-amplificadores con ganancias distintas, proporcionan 38 señales eléctricas independientes.

La primera fase del detector, conocida como Demostrador de AGATA o AGATA Demonstrator (5 clusters) (Fig. 5.3) fue instalada y utilizada satisfactoriamente en los Laboratori Nazionali di Legnaro (LNL) hasta el año 2011. Posteriormente, se trasladó al GSI de Darmstadt en Alemania en 2012 para ser acoplado con los detectores de PreSPEC, como fase previa a FAIR/NUSTAR, Separador de Fragmentos (FRS - FRagment Separator) hasta 2014. Tres clústeres AGATA doble y cinco clústeres triples AGATA (19 cristales) estuvieron operativos durante la campaña GSI en 2012. AGATA se trasladó a GANIL en la segunda mitad de 2014. En GANIL, AGATA se ha utilizado acoplada al espectrometro magnetico VAMOS y se encuentran en preparación las campañas de medida con AGATA acoplada a los detectores NEDA y DIAMANT en 2018 y muy probablemente en 2019 se utlizará con haces radioactivas acoplada a detectores de particulas cargadas ligeras. Actualmente, hay 35 detectores operativos de AGATA en GANIL.

8.4.2 EXOGAM

El multi-detector EXOGAM se encuentra en GANIL y se utiliza para realizar experimentos con haces tanto estables como radioactivos, de las instalaciones GANIL y SPIRAL. El sistema consta de detectores segmentados tipo Clover [57] en una distribución espacial que permite tener una cobertura maximizada en ángulo sólido (véase la figura 5.6-a). Los detectores Clover se encuentran rodeados el escudo Anti-Compton, formado por detectores de centelleo de BGO, y que nos permiten reducir los eventos de fondo y aumentar la relación Pico-Total (P / T), que llega a ser del 47%. La eficiencia de detectores compuestos, como son los detectores tipo Clover, se puede incrementar en el proceso llamado "Add-back", en el que señales producidas simultaneamente por cristales adyantes, se suman, recuperando parcialmente los rayos-γ que solo depositan una parte de su energía y escapan despues de una interacción Compton. Incluyendo este proceso, se sabe que la eficiencia de EXOGAM puede llegar a ser del 20% pra multiplicidad de rayos-$\gamma = 1$. La eficiencia absoluta de EXOGAM en la configuración junto con Neutron Wall y DIAMANT es superior al 10%.

El multi-detector EXOGAM utiliza VXI (VME eXtension for Instrumentation) Módulos para la adquisición y para transferir los datos.

El sistema de decisión "trigger" de EXOGAM tiene dos niveles. El primer nivel proporciona una decisión rápida que permite iniciar la conversión. El segundo nivel, llamada de validación, toma la decisión final sobre la lectura o el rechazo del evento. El sistema de adquisición de datos (DAQ) de EXOGAM está basado en MIDAS (Sistema de Adquisición de Datos de Instancia Múltiple) que se desarrolló inicialmente para EUROGAM y EUROBALL [63].

8.4.3 Neutron Wall

Neutron Wall es un conjunto de detectores de neutrones que se utiliza principalmente para seleccionar e identificar los canales de reacción, asociados con la emisión de neutrones, mediante la detección de los neutrones de las reacciones de fusión-evaporación. Neutron Wall consta de 15 hexágonos y 1 pentágono en forma de bloques de detección y cubre 1π s.r. ángulo sólido a 510 mm desde la posición de blanco hasta las superficies del detector (véase la figura 5.8). Los bloques de detectores hexagonales se subdividen en 3 detectores y cada uno contiene aproximadamente 3.2 litros de centellador líquido, mientras que el bloque pentagonal se subdivide en 5 detectores y cada uno contiene aproximadamente 1,1 litros de centellador líquido. Por lo tanto, el sistema completo consta de 50 detectores y el volumen total del escintilador es de aproximadamente 150 litros.

Los detectores de neutrones son sensibles tanto a los rayos gamma como a los neutrones, que pueden ser discriminados por PSA. El mecanismo de detección de los neutrones nos permite procesar la forma de las señales de los detectores, que dependen del tipo de la partícula detectada, y se explica por los mecanismos de Förster y Dexter [13,15]. Junto con el PSA, el TOF se utiliza para la discriminación neutrón-γ que puede verse en la Fig. 2.6.

8.4.4 DIAMANT

DIAMANT es un multi-detector de partículas ligeras de carga que consiste en 80 detectores centelladores de CsI (Tl) de 3 mm de espesor y leidos por fotodiodos, cubriendo el 90% de 4π s.r. en ángulo sólido (vease Fig. 5.10). La resolución de energía es del 2% a 5.5 MeV para las partículas en interes. DIAMANT tiene 70% y 50% de eficiencia para protones y partículas , respectivamente. Los cristales CsI están cubiertos por una lámina, que su material y espesor depende de la

composición y de la energía del haz, con el fin de evitar el daño de los cristales CsI causado por irradiación con el haz. En nuestro caso se utilizaron 5 μm de Talio.

El procesamiento de la señal de los detectores de DIAMANT se realiza a traves de electrónica basada en VXI. La electrónica de DIAMANT proporciona tres parámetros de salida: tiempo, tipo de partícula y energía. El parámetro de tipo de partículas se obtiene utilizando técnicas de discriminación de forma de impulsos [65 - 68]. La identificación de las partículas se realiza por medio de las matrices PID-Energy (vease Fig. 6.6).

8.5 Actividad experimental en GANIL con EXOGAM y detectores complementarios

El experimento se realizó en GANIL con el haz ^{32}S, acelerado a una energía de 79.8 MeV con una intensidad de 10 pnA por el acelerador CIME, incidiendo sobre un blanco de ^{28}Si con un espesor de 0,500 mg/cm^2 sobre un soporte de 8 mg/cm^2 ^{90}Zr llamado "backing". Este experimento, ha sido relevante para conocer el funcionamiento y el analisis de datos del instrumento Neutron-Wall, durante la fase de diseño NEDA. El objetivo principal de este experimento era poblar núcleos en la vecindad de N = Z en la región de ^{56}Ni. El mecanismo de reacción preferible -con haces y blancos estables- para la población de tales núcleos es la fusión-evaporación. En este mecanismo de reacción, el haz acelerado golpea el blanco estacionario, y si el parámetro de impacto es suficientemente pequeño, el núcleo compuesto puede formarse y, en caso de no sufrir fisión, seguirá un proceso de desexcitación (vease Fig. 6.1). El núcleo compuesto está en un estado muy excitado, por lo tanto, poco después de la formación -en unos 10 $^{-19}$ segundos- evaporará nucleones y pequeños fragmentos, como partículas α. La evaporación de las partículas está siempre compitiendo con la emisión de rayos-γ durante el proceso de enfriamiento y cuando el nucleo producto de la reacción se encuentra en un estado cercano o por debajo barrera para la emisión de partículas, la desexcitación continuará con la emisión de rayos-γ hasta que el núcleo alcance el estado fundamental (vease Fig. 6.2). El sistema de detectores incluia, DIAMANT para las partículas cargadas ligeras, Neutron Wall para los neutrones y finalmente EXOGAM para la detección de los rayos-γ.

El experimento fue diseñado originalmente para estudiar la estructura del nucleo ^{58}Zn, sin embargo, incluso en la etapa temprana del experimento estaba claro que los resultados estaban comprometidos por la pureza insuficiente del haz, que estaba contaminado al nivel del 1% con ^{40}Ar - en un estado de carga que proporcionaba la misma rigidez magnética para la misma energía. Sin embargo, se seleccionó la energía del haz para maximizar la sección eficaz relativa de los núcleos más exóticos posibles con tal reacción, reduciendo tanto como sea posible la energía del haz para reducir los canales con varias partículas evaporadas. Las secciones eficaz de dichos canales se han calculado con el código de modelo estadístico `HIVAP` [69, 70] (vease figura 6.8). La barrera Columbiana se calculó como 36 MeV utilizando la ecuacion 6.1, siendo R la distancia maxima entre dos nucleos, a su vez se puede calcular con la ecucacion 6.2. La relación entre la energía del haz y la energía de excitación del nucleo compuesto se deriva utilizando la conservación de la energía y momento y se calcula la energía del centro de masas del sistema como en la ecuacion 6.3. Así, se deducio el limite de barrera Columbiana, en el sistema de laboratorio, como 2.41 MeV/A para nuestro proyectil, como 2.41 MeV/A, y la energía del haz se elegió como 2.5 MeV/A siendo superior de la barrera. Con esta energia, la sección eficaz de la evaporación de neutrones está maximizada y la evaporación de partículas cargadas reducida el máximo posible.

El análisis de los datos inicia con las calibraciones y alineado tanto de los datos de tiempo como de energía. La alineación del tiempo es muy importante en el análisis de tales instrumentos complejos, de tal manera que todas las partículas y rayos-γ tienen que estar en coincidencia de tiempo. Los datos de todos detectores tienen que ser ordenados y organizados de tal manera que podamos establecer condiciones que nos ayuden a identificar los canales de reacción específicos y la cascada de rayos-γ asociada.

Una vez se realizan las calibraciones y alineaciones, se crean los espectros sencillos de rayos-γ y matrices de coincidencia γ - γ bajo diferentes condiciones en las particulas cargadas y neutrones detectados. El área de una transición rayo-γ en un espectro sencillo con condiciones en partículas cargadas y neutrones depende de varios factores. En primer lugar de su intensidad, también la probabilidad de que los canales de reacción del producto al que pertenece esta transición cumplan las condiciones en partículas cargadas y neutrones. La probabilidad de tener el rayo-γ de un núcleo en coincidencia con un canal de partículas, se determina por la probilidad de la detección de “X” partículas cuando se emiten “N” particulas, que

TABLE 8.3: Las eficiencias de detección de particulas obtenidas en este experimento.

Detector	**Particula**	**Eficiencia** [%]
Neutron Wall	1n	21.1
Neutron Wall	2n	1.4
DIAMANT	1p	65
DIAMANT	1α	35

sigue la distribución binomial (vease ecuacion 6.7). Se han utilizado los rayos-γ conocidos para encontrar la eficiencia de detección de partículas comparando las areas correspondientes a una transición con diversas condiciones, por ejemplo, de cero-protones y un-proton. Una vez se determina la la eficiencia de detección de un proton, se puede predecir el canal de reacción de una transición desconocida utilizando la distribución binomial. Sin embargo, la probabilidad de canales que incluyen neutrones no siguen la distribución binomial debido a las condiciones aplicadas para incrementar precisión de identificación de número de neutrones (vease Sección 8.2). En este experimento, las eficiencias de detección de protones, particulas-α, un-neutrón y de dos-neutrones se meustran en tabla 8.3. Se muestran los espectros con diferentes condiciones de particulas cargadas y neutrones en la figura 6.9. La evolución de las areas de las transiciones con diferentes condiciones es evidente. Se muestra el caso de la transición $7/2^- \rightarrow 3/2^-$ (2577 keV) del ^{57}Ni en la figura 6.10. El nucleo se puebla en el canal de reacción 1n2p. En este caso, en el espectro con condición de coincidencia de 1n1α que el pico desaparece, lo que indica que el canal de este nucleo no incluye particula-α.

Se realizó el análisis de los espectros de coincidencia de γ-γ para construir los esquemas de niveles de los núcleos. Con el fin de construirlos, es necesario determinar las intensidades relativas de los rayos-γ dado que la eficiencia de detección depende de su energia. La calibración de eficiencia relativa de EXOGAM se realizó utilizando la fuente ^{152}Eu y la actividad de ^{56}Co que se produció en la reacción.

Por ejemplo, se generó el espectro de transiciones en coincidencia con la transición $7/2^- \rightarrow 3/2^-$ (2577 keV) del ^{57}Ni imponiendo un condición en el pico correspondiente a 2577 keV en la matriz de coincidencias (vease figura 6.11). Encontramos tres transiciones nuevas en dicho espectro a las energias de 611 keV, 880 keV y 975 keV. Se muestran los espectros de coincidencia con dichos picos en las figura 6.12 y 6.13. Se construió el esquema de niveles de ^{57}Ni (vease fig. 6.14) analizando

los espectros de coincidencia. Las multipolaridades de nuevas transiciones se obtenieron utilizando la distribucion angular del nucleo orientado, i.e. los cocientes ADO [80-82] (vease tab. 6.4). En ésta tecnica se comparan las intensidades de rayos-γ en distitos angulos de detección. El multi-detector EXOGAM nos permite hacer la comparacion a los ángulos polares 90, 135 y 145 grados. Entonces se comparan los cocientes de ADO para tanto los rayos-γ conocidos como los nuevos (vease fig. 6.15). El analisis de ADO nos permitió proponer las multipolaridades de las nuevas transiciones como dipolos con una mezcla de cuadrupolo, excepto quizas para la transición de 611 keV que parece un dipolo menos mezclado o sin mezcla.

Además, el analisis de coincidencia de γ-γ nos permitió construir el esquema de niveles de otros nucleos poblados. Por ejemplo, el esquema de ^{65}Ga se muestra en la figura 6.18 indica que no se han observado nuevas transiciones.

En este experimento, se observaron tres nuevas transiciones en ^{57}Ni y se propusieron cuyas multipolaridades. Los esquemas de niveles de otros nucleos poblados estan de acuerdos con los trabajos existentes.

8.6 Actividad Experimental en GSI con AGATA-PreSPEC: Colectividad en ^{52}Fe

El experimento se realizó en las instalaciones GSI donde es posible acelerar haces de nucleos radioactivos, en este caso el ^{52}Fe a energías relativistas para estudiar la colectividad tanto en el estado ismoerico 12^+ como en el estado fundamental, midiendo la sección eficaz de la excitación Coulombiana relativista.

En la última década, los núcleos de la capa $1f_{7/2}$ han llegado a ser un banco de pruebas importante para los modelos nucleares y las interacciones. Cerca del centro de la capa, los núcleos muestran propiedades colectivas similares a las observadas en núcleos más pesados, tales como bandas de tipo rotacional, terminación de banda y fenómenos de "back-bending". En las últimas dos decadas, gracias al advenimiento de los multidetectores de Ge de alta eficiencia, el conocimiento de la estructura del ^{52}Fe se extendió hasta el estado 10^+, confirmando así la inversión prevista [106, 107] de los estados yrast 10^+ y 12^+. Entre otras, se han medido las dos transiciones γ E4 que conectan el estado 12^+ a dos 8^+ estados. Como ya

se ha señalado en la Ref. [110], ^{52}Fe se comporta como un rotor por debajo de I=6, consistentemente con una banda K=0. Utilizando la prescripción del modelo de rotación, se obtuvo un momento intrínseco cuadrupolar $Q_0 \sim 90$ efm^2 para los estados 2^+ y 4^+ más bajos a partir de los valores teoricos de la B(E2). Un cambio drástico se observa en I=6 donde el momento espectroscópico cuadrupolar Q_S cambia de signo y se vuelve muy pequeño. Los cálculos LSSM muestran que la estructura de las dos bandas K = 0 y K = 6 está en gran parte dominada por una configuración $(f_{7/2})^4$. Como se muestra en la Fig. 7.1 el cambio de régimen en I=6 también se refleja en los números de ocupación; la ocupación de la órbita $p_{3/2}$ tiene una caída marcada en este punto. Es bien sabido que el desarrollo de la coherencia cuadrupolar que da lugar a bandas de tipo rotatorio en la capa fp proviene de la mezcla de las órbitas $f_{7/2}$ y $p_{3/2}$ [96, 97]. En los núcleos más deformados de la región, el número de ocupación $p_{3/2}$ permanece casi constante a frecuencia de rotación, mientras que en el spin máximo que se puede construir con las partículas de valencia en la capa $f_{7/2}$, los números de ocupación $p_{3/2}$, $f_{5/2}$ y $p_{1/2}$ desaparecen para ^{44}Ti (I = 12) y se vuelven insignificantes para ^{48}Cr (I = 16). El $f_{7/2}$ se convierte en la única órbita relevante en estos casos en los que los estados de terminación de banda completamente alineados son de carácter no colectivo. La situación es diferente en ^{52}Fe, donde por encima de I = 6, todas las contribuciones permanecen casi constantes y diferentes de cero en función de spin incluso en I = 12, manteniendo así una colectividad residual que se ha considerado fundamental para explicar las caracteristicas del estado isomerico 12^+ "Yrast-trap" del 52Fe..

Nuestro grupo también publicó [105] la medida de la desexcitación γ E4 de la trampa yrast 12^+ en ^{52}Fe a los dos conocidos estados 8^+. Las intensidades evaluadas reflejan probabilidades de transición E4 muy bajas, si se comparan los datos de ^{52}Fe con los B(E4) observados en otros núcleos de capa. Para interpretar estos resultados se realizaron cálculos en el modelo de capa con el código ANTOINE [109] en el espacio completo del modelo pf. Se han utilizado tres interacciones residuales diferentes, a saber, las interacciones FPD6 [116], KB3G [117] y GXPF1 [118]. Todos los cálculos sobrestiman los valores experimentales para las probilidades reducidas de transición. La mejor descripción se logra mediante la interacción FPD6, ya que FPD6 predice una colectividad 50% mayor que las otras interacciones. Un método frecuentemente empleado para investigar la colectividad de los estados es la medición de las probabilidades de transición. En general, valores elevados de la B(E2) en conexión con estados colectivos.

Un método de obtención de los valores de B(E2) es poblar los estados sobre el estado isomerico utilizando la excitación Coulombiana relativista, dado que su sección eficaz está relacionada con los valores de B(E2) [125, 126]. Para realizar dicha medida, se ha producido un haz radiactivo de ^{52}Fe con una relación isomerica de 14(2)% con la ayuda del separador magnético FRagment Separator (FRS - vease Fig. 7.2) y utilizando un blanco de ^{197}Au de 400 mg/cm^2. El FRS es un espectrómetro de alta resolución capaz de identificar en vuelo el cociente A/Q de cada núcleo, donde A representa el número másico y Q la carga efectiva del ión.

El haz procedente del FRS y a energías relativistas (156 MeV.A) interacciona con el blanco ya mencionado y posteriormente entra en el calorimetro de Lund-York-Cologne (LYYCA). LYCCA es capaz de distinguir los productos de reacción, sus velocidades y el ángulo de dispersión para hacer la corrección Doppler y obtener la sección eficaz.

Una vez realizadas todas las calibraciones, tanto de energía como de tiempo de los detectores de FRS, LYCCA y AGATA, es posible establecer condiciones tanto para el núcleo del haz secundario, procedente del FRS, como para el núcleo producto de la reacción, en nuestro caso, en ambos se selecionó el ^{52}Fe. Despues de dicha selección, es posible generar espectros de las transiciones gamma con las energías corregidas por el efecto Dopler producido por la velocidad y trajectoria del producto de la reacción. La corrección Doppler se optimizó para la transición $2_1^+ \rightarrow 0^+$ dada su intensidad muy elevada. Se observaron tres transiciones del ^{52}Fe a las energías 849.5 keV, 2721 keV y 3586 keV (véase las figuras 7.29 y 7.32), siendo la de 849.5 keV es de la $2_1^+ \rightarrow 0^+$. El esquema de niveles del ^{52}Fe se conoce bien hasta el estado isomerico 12^+. Así que la transición de 2770 keV corresponde a la desexcitación del estado 2_2^+ al estado fundamental 0^+, que se observó previamente a la energía de 2760 keV [145]. En nuestro experimento la transición se encuentra a una energía desplazada del valor conocido en la litertatura a causa de la correción Dopler.

La correción Dopler a estas energías es muy sensible a la vida media del estado, a causa del desplazamiento del punto de emision del rayo-gamma. La transición a la energía de 3588 keV es nuestro candidato para la transición $14^+ \rightarrow 12^+$. A causa de su elevada energía, el comportamiento de esta transición se espera muy similar a la de $2_2^+ \rightarrow 0^+$, se puede realizar una calibracion internal para posicionar los picos a la energía correcta.

En la tabla Tab. 8.4 se muestran las secciones eficaz que se encuentran en este experimento con las energías corregidas en paréntesis.

TABLE 8.4: Las secciones eficaz deducidas en este trabajo. Las energías calibradas se muestran en paréntesis.

Isotopio	$\mathbf{I}_i \rightarrow \mathbf{I}_f$ [$\hbar$]	$\mathbf{E}_\gamma$ [keV]	σ [**mb**]
^{52}Fe	$0^+ \rightarrow 2_1^+$	849.5(1.4)	79(5)
^{52}Fe	$0^+ \rightarrow 2_2^+$	2770 [2760]	16(7)
^{52}Fe	$12^+ \rightarrow 14^+$	3588 [3575]	26(18)
^{197}Au	$\frac{3}{2}^+ \rightarrow \frac{7}{2}^+$	576.6(1)	10.8(2.0)

Se muestra en la Tabla 8.5, una comparación de los resultados de la seccion eficaz experimentales para las transiciones conocidas con los de calculos que realizaron utilizando codigo DWEIKO [133] y los que realizaron por C. Bertulani [148, 149]. El resultado correspondiente a la transición $0^+ \rightarrow 2_2^+$ se encuentran en

TABLE 8.5: Comparación de los resultados de la seccion eficaz experimentales para las transiciones conocidas con los de calculados con DWEIKO.

Isotope	$\mathbf{I}_i \rightarrow \mathbf{I}_f$ [$\hbar$]	$\mathbf{E}_\gamma$ [keV]	σ_{theo}^{DWEIKO} [**mb**]	$\sigma_{theo}^{Bertulani}$ [**mb**]	σ_{exp} [**mb**]
^{197}Au	$\frac{3}{2}^+ \rightarrow \frac{7}{2}^+$	547.5	40.1	28.0	10.8(2.0)
^{52}Fe	$0^+ \rightarrow 2_1^+$	849.5	69.8	46.9	79(5)
^{52}Fe	$0^+ \rightarrow 2_2^+$	2770 [2760]	11	7.8	16(7)

buen acuerdo con el cálculo de sección eficaz realizado con la B(E2) obtenida en una medida previa [145]. Por otro lado, los resultados de $0^+ \rightarrow 2_1^+$ del ^{52}Fe y de $\frac{3}{2}^+ \rightarrow \frac{7}{2}^+$ del ^{197}Au no concuerdan con los cálculos de sección eficaz realizados con las B(E2) conocidas.

Por último, con el fin de interpretar los resultados, nuestra colaboradora teórica Prof. Silvia Lenzi de La Universidad e INFN de Padova Italia, realizó los calculos del modelo de capa a gran escala (LSSM) utilizando ANTOINE [109] y las interacciones KB3G [117] y GXPF1A [115] considerando los efectos de polarización del core y las propiedades quadrupolares, usando cargas efectivas $e_p = 1.31$, $e_n = 0.46$ y $e_p = 1.5$, $e_n = 0.5$, respectivamente (vease Tabla 8.6). Según los resultados, la interacción GXPF1A predice mejor que la interacción KB3G la energía de excitación de nuestro candidato para el estado 14^+. Los resultados indican en cualquier caso que la B(E2) experimental es aproximadamente 10 veces mayor que los resultados de los cálculos LSSM, lo que sugiere un mayor grado de colectividad en los estados involucrados.

TABLE 8.6: Comparación del resultado experimental y los de calculos de LSSM con las interacciones KB3G y GXPF1A.

Interacción	$\mathbf{I}_i \rightarrow \mathbf{I}_f$ $[\hbar]$	**ΔE [keV]**	**B(E2) [e^{2}fm^4]**
KB3G	$12^+ \rightarrow 14^+$	4391	21.6
GXPF1A	$12^+ \rightarrow 14^+$	3753	34.3
Experiment	$12^+ \rightarrow 14^+$	3588 [3575]	410(210)

Los cálculos se han hecho también para el estado 2_2^+ usando las mismas cargas efectivas y la comparación de los resultados con el experimental se muestran en Tab. 8.7. La interacción KB3G predice mejor el valor de B(E2) mientras la

TABLE 8.7: Comparación de los resultados calculados utilizando las interacciones KB3G y GXPF1A con el de experimento.

Interacción	$\mathbf{I}_i \rightarrow \mathbf{I}_f$ $[\hbar]$	**ΔE [keV]**	**B(E2) [e^{2}fm^4]**
KB3G	$0^+ \rightarrow 2_2^+$	3109	180.65
GXPF1A	$0^+ \rightarrow 2_2^+$	2669	211.95
Experiment	$0^+ \rightarrow 2_2^+$	2770 [2760]	182(80)

interacción GXPF1A predice mejor la energía de excitación.

Bibliography

[1] The AGATA Collaboration, Nucl. Instr. and Meth. Sec. A **668** (2012) 26-58.

[2] J. Simpson, et al. Acta Physica Hungarica: Heavy Ion Physica **11** (2000) 159-188.

[3] B. Cederwall *et al.*, Nature **469** (06 January 2011) 68-71.

[4] V. Modamio *et al.*, Nucl. Instr. and Meth. Sec. A **775** (2015) 71-76.

[5] F.J. Egea Canet *et al.*, IEEE Transactions on Nuclear Science **62** Issue 3 (2015) 1056-1062.

[6] F.J. Egea Canet *et al.*, IEEE Transactions on Nuclear Science **62** Issue 3 (2015) 1063-1069.

[7] F. J. Egea *et al.*, IEEE Transactions on Nuclear Science **60** (2013) 3526-3531.

[8] K. Shibata, et al., J. Nucl. Sci. Technol. **48**(1), 1-30 (2011).

[9] K. Shibata, et al., J. Korean. Phys. Soc., 59(23), 1046-1051 (2011).

[10] O. Iwamoto, et al., J. Korean. Phys. Soc., 59(23), 1224-1229 (2011).

[11] G. Chiba, et al., J. Nucl. Sci. Technol., 48(2), 172-187 (2011).

[12] G. Knoll, *Radiation Detection and Measurement*, 4$^{\text{th}}$ ed. (Wiley, New Jersey - USA 2010).

[13] G.H.V. Bertrand *et al.*, NIM A **776** (2015) 114-128.

[14] P.-A. Söderström, J. Nyberg and R. Wolters, NIM A **594** (2008) 79-89.

[15] T. Förster, Annalen Der Physik **437** (1948) 55.

[16] Ö. Skeppstedt *et al.*, Nucl. Instr. and Meth. Sec. A **421** (1999) 531-541.

[17] J. Ljungvall *et al.*, Nucl. Instr. and Meth. Sec. A **528** (2004) 741-762.

[18] D. Sarantites *et al.*, Nucl. Instr. and Meth. Sec. A **530** (2004) 473-492.

[19] P.-A. Söderström *et al.*, Nucl. Instr. and Meth. Sec. A **594** (1) (2008) 79-89.

[20] X. Luo *et al.*, Nucl. Instr. and Meth. Sec. A **767** (2014) 83-91

[21] G. Jaworski *et al.*, Nucl. Instr. and Meth. Sec. A **673** (2012) 64-72.

[22] J.J. Valiente-Dobon et al., Annual Report 2014 (2015) 95-96.

[23] S. Agostinelli *et al.*, Nucl. Instr. and Meth. Sec. A **506** (2003) 250-303.

[24] E. Farnea *et al.*, Nucl. Instr. and Meth. Sec. A **621** (2010) 331-343.

[25] P.R.P. Coelho *et al.* Nucl. Instr. and Meth. Sec. A **280** (1989) 270-272.

[26] J. Gomez del Campo and R.G. Stockstad, Oak Ridge National Laboratory Report No. TM7295 (1981), unpublished.

[27] A. Di Nitto, *et al.*, LNL Annual Report 2012 (2013), 82.

[28] M. Kildir *et al.*, Phys. Rev. C **46** (1992) 2264.

[29] A.J. Koning and J.P. Delaroche, Nucl. Phys. A **713**, (2003), 231-310.

[30] Hodgson Rep. Prog. Phys. **47** (1984) 613.

[31] R.D. Hoffman, *et al.* Tech. Rep., LLNL, 222275, 2006.

[32] A. Di Nitto *et al.*, Eur. Phys. J. A **47**, (2011) 83-97.

[33] A. Di Nitto *et al.*, J. Phys. Conf. Ser. **267** (2011) 012053

[34] J. Simpson, Z. Phys. A **358** (1997) 139-143.

[35] J. Cederkäll *et al.*, Nucl. Instr. and Meth. Sec. A **385** (1997) 166-170.

[36] W.W.T. Crane, G.H. Higgins and S.G. Thompson, Phys. Rev. **97** (1955) 242.

[37] The BARTEK NDE 202 module manual, https://nsg.physics.uu.se/sites/default/files/nde202_manual.pdf.

[38] P.J. Twin, Workshop on Nuclear Structure at High Spin, Risø, Denmark, 1981, p. 135.

[39] P.J. Twin, Proc. Conf. on Instr. for Heavy Ion Nucl. Res., in: D. Schapira (Ed.) Nucl. Sci. Research Conf. Series, vol. 7, Harwood, p. 231.

[40] R.M. Lieder, H. Jäger, A. Neskakis, T. Venkova, Nucl. Instr. and Meth., 220 (1984) 363.

[41] J.P. Sharpey-Schafer, J. Simpson, Prog. Particle Nucl. Phys. 21 (1988) 293.

[42] J. Eberth, J. Simpson, Progress in Particle and Nuclear Physics 60 (2008) 283.

[43] FAIRBaseline Technical Report, GSI, 2006.

[44] P.-A. Söderström at al., Nuclear Instruments and Methods Sec. A **638** (2011) 96.

[45] A. Georgiev and W. Gast, IEEE Nucl. Sci. **40** (1993) 770.

[46] P.-A. Söderström. Detection of fast neutrons and digital pulse shape discrimination between neutrons and γ-rays. In A. Covello, F. Iachello, R. Ricci, and G. Maino (editors), *Proceedings of the International School of Physics Enrico Fermi*, volume **169** Nuclear Structure far from Stability: new Physics and new Technology, page 551. SIF, Bologna and IOS Press, Amsterdam, 2008.

[47] E. Farnea, et al. Nucl. Inst. and Meth. Sec. A **621** (2010) 331.

[48] A. Pullia, F. Zocca, G. Pascovici, IEEE Transactions on Nuclear Science (2006) 2869.

[49] F. Zocca, et al., IEEE Transactions on Nuclear Science (2009) 2384.

[50] G. Pascovici, et al., WSEAS Transactions on Circuit and Systems 7 (2008) 470.

[51] R. Venturelli, D. Bazzacco, LNL Annual Report 2004 (2005), 220.

[52] B. Bruyneel, Characterization of Segmented Large Volume, High Purity Germanium Detectors, Ph.D. thesis, Universität zu Köln, Cologne, Germany,2006 (/http://kups.ub.uni-koeln.de/1858/).

[53] T. Kröll, D. Bazzacco, Nucl. Instr. and Meth. Sec. A **565** (2006) 691.

[54] A. Olariu, et al., IEEE Transaction on Nuclear Science **NS-53** (2006) 1028.

[55] D. Bazzacco, Nuclear Physics A **746** (2004) 248c-254c.

[56] I. Foster, C. Kesselman, The Grid: Blueprint for a New Computing Infrastructure, Morgan Kaufmann Publishers, Inc., San Francisco, USA, 1999.

[57] G. Duchene et al., Nuclear Instruments and Methods in Physics Research A **432** (1999) 90.

[58] W. Catford, Personal Web Page on the University of Surry site, 2002, (http://personal.ph.surrey.ac.uk/ phs1wc/tiara/puri/puri-paper/node8.html)

[59] F. Azaiez, Nuclear Physics A **654** (1999) 1003c - 1008c.

[60] EXOGAM Document server at Daresbury, http://npg.dl.ac.uk/documents/edoc000/#ExoGam

[61] Euroball Trigger Card, http://npg.dl.ac.uk/documents/edoc327/edoc327.html

[62] P.J.Coleman-Smith et al., A modular approach to a VXI Resource Manager, on NSS90. http://npg.dl.ac.uk/documents/edoc057/edoc057.pdf

[63] EXOGAM Data Acquisition, http://npsg.dl.ac.uk/documents/edoc413.

[64] M. Aiche, et al., Nucl. Instr. and Meth. Sec. A **391** (1997) 329-337.

[65] J. Gál et al., Nucl. Instr. and Meth. Sec. A **399** (1997) 407.

[66] J. Gál, G. Bíbok, K. Juhsáz, Scientific Instrumentation **3**, 3(1988)85.

[67] J. Gál et al., Nucl. Instr. and Meth. Sec. A **366** (1995) 120.

[68] T.K. Alexander, F.S. Goulding, Nucl. Instr. and Meth. 13(1961)244.

[69] W. Reisdorf, Z. Phys. A **300**, 227 (1981).

[70] W. Reisdorf and M. Schädel, Z. Phys. A **343**, 47 (1992).

[71] K.S. Krane, *Introductory Nuclear Physics* (Wiley, New York - USA 1988).

[72] B. Jäckel et al., Nuclear Instruments and Methods A **261**(3), 543 (1987).

[73] A. Gadea, et al. Phys. Rev. Let. **97**, 152501 (2006).

[74] S.M. Lenzi, et al. Phys. Rev. Let. **87**, 122501 (2001).

[75] P.E. Garrett, et al. Phys. Rev. C **72**, 014307 (2007).

[76] M. Honma, et al. Phys. Rev. C **65**, 061301 (2002).

[77] R. Machleidt and H. Müther, Phys. Rev. C **68** 034005 (2001).

[78] A. Zuker, et al. Phys. Rev. Let. **89**, 142502 (2002).

[79] E. K. Johansson, et al. Phys. Rev. C **80**, 014321 (2009).

[80] H.A. Tolhoek and J.A.M. Cox, Physica **19** (1953) 101-119.

[81] M. Piiparinen, et al., Nuclear Physics A **605** (1996), 191-268.

[82] M. Ionescu-Bujor, et al. Physical Review C **73** 024310 (2006).

[83] D. Rudolph, et al. The European Physical Journal A - Hadrons and Nuclei **4**, Issue 2, 115 - 145.

[84] M. Weiszflog, et al., The European Physical Journal A **11**, 2538 (2001)

[85] D. Rudolph, et al. Physical Review Letters **80**, 3018 (1998).

[86] N. Bendjaballah and J. Delaunay, Nuclear Physics A **244** Issue 2 (1975) 322-328.

[87] D. Rudolph, et al. European Physical Journal A **4** (1999) 115.

[88] NSR Reference Paper, Nucl. Instr. and Meth. Sec. A **640**, (2011) 213

[89] C.-H. Yu, et al. Physical Review C, **62**, 041301(R).

[90] A. Galindo-Uribarri, et al. Physics Letters B **422** Issues 1-4 (1998) 45-51.

[91] J. Gellanki, et al. Physical Review C, **80** (2009) 051304(R).

[92] A.K. Singh, et al. Physical Review C, **59** (1999) 2440.

[93] Zs. Podolyak, et al., Physics Letters B 632, Issues 2-3, 203-206 (2006).

[94] D. Rudolph, et al. Phys. Rev. C **78**, 021301(R) (2008).

[95] E. Caurier et al., Phys. Rev. Lett. 75, 2466 (1995).

[96] G. Martinez-Pinedo et al., Phys. Rev. C5 4, R2150 (1996).

[97] S.M. Lenzi et al., Phys. Rev. C 56, 1313 (1997).

[98] W.P. Alford et al., Nucl. Phys. A 243, 269 (1975).

[99] W. Bohne et al., Nucl. Phys. A 245, 107 (1975).

[100] Y. Iritani et al., J. Phys. Soc. Jap. 43, 1119 (1977).

[101] D. Evers et al., Phys. Rev. C15, 1690 (1977).

[102] P. Decowski et al., Nucl. Phys. A 302, 186 (1978).

[103] Huo Junde, Nucl. Data Sheets 71, 659 (1994).

[104] C.A. Ur et al., Phys. Rev. C 58, 3163 (1998).

[105] A. Gadea et al., Phys. Lett. B 619, 88 (2005).

[106] D.F. Geesaman et al., Phys. Rev. C 19, 1938 (1979).

[107] D.F. Geesaman et al., Phys. Rev. Lett. 34, 326 (1975).

[108] A. Poves and A. Zuker, Phys. Rep. 70, 235 (1981).

[109] E. Caurier, F. Nowacki; Acta Physica Pol. B30, 705 (1999).

[110] R.B.M. Mooy and P.W.M. Glaudemans, Z. Phys. A 312, 59 (1983).

[111] K.L. Yurkewicz, et al., Phys. Rev. C 70 (2004) 034301.

[112] M. Axiotis et al., Phys.Rev. C 76, 014303 (2007).

[113] J. Ekman et al., Phys.Rev. C 66, 051301(R) (2002).

[114] E.K. Johansson et al., Eur. Phys. J. A 27, 157 (2006).

[115] D. Rudolph et al., Phys. Rev. C 78, 021301 (2008).

[116] W.A. Richter, et al., Nucl. Phys. A 523 325 (1991).

[117] A. Poves, E. Caurier, F. Nowacki, Nucl. Phys. A 694, 157 (2001).

[118] M. Honma, et al., Phys. Rev.C 65, 061301(R) (2002).

[119] B. Castel and L. Zamick, Z. Phys. A - Atoms and Nuclei **315** (1984) 99

[120] I.Stefanescu et al., Phys. Rev. Lett. 90, 122701 (2007)

[121] M.Pfützner et al., Nucl. Phys. A 626, 259 (1997)

[122] J. Hüfner, K. Schäfer and B. Schürmann, Physical Review C **12** Number 6, 1888-1898 (1975).

[123] B. Blank, et al., Physical Review C **50**, Number 5, 2398-2407 (1994).

[124] H.-J. Wollersheim, Acta Physica Polonica B **42** (2011) 705-716.

[125] A. Winther and K. Alder, Nuclear Physics **A319** (1979) 518-532.

[126] T. Glasmacher Annu. Rev. Nucl. Part. Sci. 1998. 48:1-31.

[127] N. Iwasa, et al., Nuclear Instruments & Methods In Physics Research Section B **126** (1997) 284.

[128] Th. Schwab, GSI Report No. **91-10** (1991)

[129] O.B. Tarasov, D. Bazin, Nuclear Instruments & Methods In Physics Research Section B **376** (2016) 185-187.

[130] R. Janik, et al., Acta Physica Universitatis Comenianae **XLVIII-XLIX**, Number 1&2(2007-2008), 85-93.

[131] The GSI Fragment Separator website (https://www-win.gsi.de/frs/technical/FRSsetup/detectors/tpc.asp) Accessed on: August 28, 2016.

[132] H. Bethe and J. Ashkin, Experimental Nuclear Physics, J. Wiley, New York (1953), 253.

[133] C. Bertulani, et al., Comput. Phys. Commun. 152 317 (2003).

[134] P. Golubev, et al., Nucl. Instr. and Meth. Sec. A **723**, 55 (2013).

[135] D. Ralet, *et al.*, Nucl. Instr. and Meth. Sec. A **768** (2015) 32-39.

[136] D. Beck, et al. URL: https://www-acc.gsi.de/wiki/Timing/Timing System-ButisInterface

[137] R. Venturelli, et al. Adaptive grid search as pulse shape analysis algorithm for gamma-tracking and results. LNL Annual Report (2004).

[138] A. Lopez-Martens, et al. Nucl. Instr. and Meth. Sec. A **533** 454 (2004).

[139] D. Ralet, Ph.D. Thesis, Technische Universität Darmstadt (2015).

[140] R. Avigo, Ph.D. Thesis, University of Milan (2016).

[141] H. Bethe and J. Ashkin, *Experimental Nuclear Physics*, E. Segre, J. Wiley, 1953.

[142] D. Rudolph on 7^{th} international Conference on Radioactive Nuclear Beams (RNB 7): Cortina d'Ampezzo, Italy, July 3-7, 2006.

[143] NSR Reference Paper Nucl. Instr. and Meth. Sec. A **640**, 213 (2011)

[144] D. F. Geesaman, et al., Physical Review C 19, 1938 (1979).

[145] Y.Iritani, J.Kasagi and H.Ohnuma, J. Phys. Soc. Jap. **43**, 1119 (1977)

[146] C. Bertulani, et al., Comput. Phys. Commun. **152** 317 (2003).

[147] T. Furumoto, et al., Physical Review C **85**, 044607 (2012).

[148] A.N.F. Aleixo, C.A. Bertulani, Nuclear Physics A **505** (1989) 448-470.

[149] C. A. Bertulani, et al., Physical Review C **68**, 044609 (2003).

[150] F.K. McGowan, et al., Annals of Physics **63** 549-561 (1971).